

**Investigating the Neuroprotective Potential of Repaglinide
and Development of Novel PEGylated Nanocarriers for the
Management of Metabolic Disorder linked Alzheimer's
Disease**

THESIS

Submitted in partial fulfilment
of the requirements for the degree of
DOCTOR OF PHILOSOPHY

by

GEETIKA

Under the Supervision of

Prof. RAJEEV TALIYAN



BITS Pilani
Pilani | Dubai | Goa | Hyderabad

**BIRLA INSTITUTE OF TECHNOLOGY & SCIENCE, PILANI
2023**

BIRLA INSTITUTE OF TECHNOLOGY & SCIENCE, PILANI

CERTIFICATE

This is to certify that the thesis entitled “**Investigating the Neuroprotective Potential of Repaglinide and Development of Novel PEGylated Nanocarriers for the Management of Metabolic Disorder linked Alzheimer’s Disease**” was submitted by **Geetika**, ID. No. **2017PHXF0442P** for the award of Ph.D. Degree of the Institute embodies original work done by her under my supervision.

Signature of supervisor

Name in capital letters : **Prof. Rajeev Taliyan**

Designation : Professor,
Department of Pharmacy
BITS-Pilani, Pilani Campus, Rajasthan, India

Date :

Table of Content

<i>Contents</i>	<i>Page. No.</i>
<i>Acknowledgments</i>	i-iii
<i>List of Abbreviations</i>	iv-ix
<i>List of Figures</i>	x-xviii
<i>List of Tables</i>	xix-xxi
<i>Abstract</i>	xxii-xxviii
<i>Chapter 1. Introduction</i>	01-10
<i>Chapter 2. Literature review</i>	11-33
<i>Chapter 3. Hypothesis and Objective</i>	34-36
<i>Chapter 4. Material and Methods</i>	37-65
<i>Chapter 5. Results & Discussion</i>	66-157
<i>Chapter 6. Summary and conclusion</i>	158-161
<i>Chapter 7. Future Scope</i>	162-163
<i>Chapter 8. Bibliography</i>	164-191
<i>Appendix I List of Publications and Presentations</i>	192-195
<i>Appendix II Biographies</i>	196

Acknowledgments

“Gratitude is the fairest blossom which springs from the soul.”

- Henry Ward Beecher

Words cannot describe my appreciation to those who not only encouraged me during this period in my life but also helped me directly and indirectly to the completion of my Ph.D. thesis. First and foremost, I would like to express my most sincere gratitude and deepest feelings to my supervisor **Prof. Rajeev Taliyan**, Professor, BITS, Pilani, Pilani campus for his guidance, timely advice, and encouragement throughout my research work and professional development. I would not be able to find apt words to express my gratitude for the parental love of him and his family to me throughout the period of my research. This thesis becomes possible due to his continuous support and the freedom he gave for carrying out this work. I am and will always remain profoundly grateful to him throughout my life.

I am grateful to Prof. K. Ramgopal Rao Vice Chancellor, and Prof. Souvik Bhattacharyya, former Vice Chancellor of BITS, Pilani-Pilani campus. Prof. Sudhir Kumar Barai, Director, BITS, Pilani, Pilani Campus, Col Soumyabrata Chakraborty, registrar, BITS, Pilani, Pilani Campus, Prof. Navin Singh, Dean, Administration and Prof. Shamik Chakraborty, Associate Dean, Prof. Jitendra Panwar former Associate Dean, AGSRD for their support.

I would like to extend my thanks to Dr. Sunil Kumar Dubey, General manager, Emami Pvt. Ltd and former Ph. D supervisor at BITS-Pilani for providing their valuable support and guidance in the initial stages of my research. I appreciate his insights, suggestions, and feedback, which helped me to refine my work.

I am indebted to Dr. Anil B. Gaikwad, Head, Department of Pharmacy, and Prof. Hemant R. Jadav, Prof. Atish T. Paul former Head, Department of Pharmacy, BITS, Pilani, Pilani Campus for their continuous support. I express my sincere thanks to Prof. R. Mahesh and Dr. S. Murugesan, for their motivation, constant support, and encouragement.

I would like to express my sincere thanks to Prof. Anil Jindal Convenor, Departmental Research Committee, Dr. Gautam Singhvi and Dr. M. M. Pandey, Doctoral Advisory Committee members for their valuable feedback, suggestions, and constructive criticism, which helped me to improve my research work.

My special thanks to the faculty members Prof. Anupama Mittal, Prof. Deepak Chitkara, Prof. Aniruddha Roy, and Dr. Sandeep Sundriyal, for their encouragement, valuable comments, and suggestions. My special thanks to Dr. Richa Shrivastava, and Dr. Shilpi Garg Former Nucleus member of AGSRD for her continuous help regarding the ICMR-SRF fellowship.

Acknowledgments

I express my heartiest thanks to Ms. Moumita Basak, Mr. Arihant K Singh, and Mr. Karan Banoth for always being there to listen to my frustrations, share my joys, and offer me words of wisdom when I needed them most. Your friendship has been a source of comfort and strength to me, and I am grateful for the countless laughs and memories we have shared. I wish all of them a very bright future. The special thanks go to Dr. K.V Krishna who served as a mentor throughout my graduate studies. He has been a source of inspiration and guidance, providing invaluable support and advice on both academic and personal matters. His enthusiasm for research and commitment to excellence has been truly motivating. He challenged me to think deeply and critically about my research and always encouraged me to aim higher. I am grateful for the time and effort he invested in me, which undoubtedly helped me to develop as a researcher and person. His contributions to my success are immeasurable, and I will always be indebted to him for his kindness and generosity."

I would like to thank all my lab members for their motivation, companionship, and support during my research work. I am extremely lucky to have a great company of research scholars of the pharmacy, biological sciences, and chemistry departments. I have learned a lot from everyone during my Ph.D. journey.

I would like to, especially thank, Dr. Sushil K Yadav, Sr. Vet. In charge, of Central Animal Facility for his continuous support during my work. I would also like to thank the staff members of the animal house, Mr. Vishal, Mr. Shyam, Mr. Mukesh, and Mr. Shiva Kumar for taking care of the animals and for assistance during the experimental work.

I am thankful to the administrative staff, Mr. Puran Ji, Lt. Sajjan Ji, Mr. Laxman Ji, Mr. Ram Suthar Ji, Mr. Naveen Ji, Mr. Tarachand Ji, Mr. Surender ji Mr. Mahender Ji, Mr. Abhishek Ji, Mr. Sandeep Ji, and Mr. Suman Ji for their continuous support. My sincere thanks to all the people whom I miss to acknowledge, who have helped me directly or indirectly for the smooth completion of this task.

I would like to acknowledge, the Indian Council of Medical Research for providing a senior research fellowship and special thanks to the Alzheimer's Association society, controlled release society for being a part of these committees. I would like to acknowledge lipid for providing gift samples of phospholipids.

I would like to express my sincere gratitude to the institutions and organizations that recognized my research work and awarded me with the DST-SERB ITS award and CSIR travel award. These awards not only served as a recognition of my efforts but also motivated me to pursue excellence in my research.

Acknowledgments

I would like to express my heartfelt gratitude to my parents for their unwavering support, love, and encouragement throughout my academic journey. They have always been my pillars of strength, providing me with the motivation to overcome any obstacles that came my way. Their sacrifices, guidance, and faith in me have been instrumental in shaping me into the person I am today. I am indebted to them for instilling in me the values of hard work, determination, and perseverance, which have been critical in accomplishing this feat. Thank you, Mom and Dad, for being my constant source of inspiration and for always believing in me.

I am incredibly grateful for the support of my brother and sister-in-law. Their unwavering encouragement, love, and guidance have been a constant source of strength throughout my Ph.D. journey. Their willingness to listen and offer advice, no matter the time of day, has been truly invaluable. Their constant belief in my abilities and their unending support made it possible for me to achieve this milestone. I am forever thankful for their unwavering support, and I look forward to the many years of collaboration, celebration, and shared successes to come.

I would like to express my gratitude to the animals who were used in this research. Their contribution has been invaluable in advancing scientific knowledge and developing new treatments. While it is with a heavy heart that we must acknowledge their sacrifice, it is with the hope that their contribution will lead to better health and well-being for all living creatures. Their willingness to participate in this work is a testament to the resilience and generosity of the animal kingdom, and I am honored to have had the opportunity to work with them. I would like to pay homage to those experimental animals who have sacrificed their lives in making my endeavour successful. May GOD grant them eternal peace.

Finally, I would like to express my sincere gratitude to the Almighty God for His blessings, guidance, and protection throughout my academic journey. His unwavering support has been my constant source of strength, and without His divine intervention, this accomplishment would not have been possible. I am grateful for His infinite mercy and grace that have sustained me during challenging times and given me hope for a better future. May His blessings be upon me and my loved ones always.

“Success is not final; failure is not fatal:
it is the courage to continue that counts.”

“Thank you”

Geetika

List of Abbreviations

%	:	Percentage
% CDR	:	Percentage cumulative drug release
% CV	:	Percentage coefficient of variance
% DL	:	Percentage drug loading
% EE	:	Percentage entrapment efficiency
% F	:	Percentage fraction of drug released
% RE	:	Percentage relative error
% RH	:	Percentage relative humidity
% RSD	:	Percentage relative standard deviation
% RTD	:	Percentage remaining to be degraded
% RSD	:	Percentage relative standard deviation
% v/v	:	Percentage volume by volume
% w/v	:	Percentage weight by volume
% w/w	:	Percentage weight by weight
λ_{\max}	:	Wavelength of maximum absorbance
<	:	Less than
>	:	More than
\leq	:	Less than equal to
\geq	:	More than equal to
=	:	Equal to
~	:	Approximately equal to
\pm	:	Plus or minus
$^{\circ}$ C	:	Degree centigrade
mg	:	Milligram
g	:	Gram
cm	:	Centimeter
μ m	:	Micrometer
nm	:	Nanometer
mL	:	Milliliter
μ L	:	Microliter
mg/mL	:	Milligram per milliliter
μ g/mL	:	Microgram per milliliter

ng/mL	:	Nanogram per milliliter
α	:	Alpha
β	:	Beta
β^1	:	Beta prime
k'	:	Capacity factor
τ	:	Tau protein
ACN	:	Acetonitrile
AD	:	Alzheimer's Disease
AIC	:	Akaike information criterion
AMT	:	Adsorption mediated transport
ANOVA	:	Analysis of variance
API	:	Active pharmaceutical ingredient
APP	:	Amyloid precursor protein
AT	:	Accelerated temperature
ATR-FTIR	:	Attenuated total reflection-Fourier transform infrared spectrometer
AUC	:	Area under curve
AUMC	:	Area under first moment curve
BBB	:	Blood-brain barrier
BBD	:	Box-Behnken design
BCS	:	Biopharmaceutical classification system
BDNF	:	Brain-derived neurotrophic factor
BSA	:	Bovine serum albumin
CA1	:	Cornu ammonis - 1
CAF	:	Central Animal Facility
CBF	:	Cerebral blood flow
CED	:	Convection enhanced delivery
CMC	:	Critical micellar concentration
CMT	:	Carrier mediated transport
C_{max}	:	Maximum concentration
CNS	:	Central nervous system
Conc.	:	Concentration

CPCSEA	:	Committee for the purpose of control and supervision of experiments on animals
CR	:	Controlled release
Cl	:	Clearance
CSF	:	Cerebrospinal fluid
DCM	:	Dichloromethane
DG	:	Dentate gyrus
DLS	:	Dynamic light scattering
DM	:	Diabetes Mellitus
DMSO	:	Dimethyl sulfoxide
DoE	:	Design of experiments
DTNB	:	5,5'-dithiobis-(2-nitrobenzoic acid)
DSC	:	Differential scanning calorimetry
EDTA	:	Ethylene diamine tetra acetic acid
EMA	:	European medical agency
ELISA	:	Enzyme-linked immunosorbent assay
EOAD	:	Early onset of Alzheimer's Disease
FESEM	:	Field emission scanning electron microscopy
GC-HS	:	Gas chromatography – Headspace
GSH	:	Glutathione
h	:	Hour
HCl	:	Hydrochloric acid
HETP	:	Height equivalent to theoretical plates
HPLC	:	High-performance liquid chromatography
HQC	:	Higher quality control sample
IAEC	:	Institutional animal ethical committee
ICH	:	International Council for harmonization
ICV	:	Intracerebroventricular
IDF	:	International Diabetes Federation
IPA	:	Isopropyl alcohol
IR	:	Insulin resistance
IS	:	Internal standard
i.v.	:	Intravenous

IL-6	:	Interleukin-6
k_0	:	Zero order rate constant
k_1	:	First order rate constant
k_H	:	Higuchi release constant
k_{KP}	:	Korsmeyer–Peppas release constant
k_{HC}	:	Hixon Crowell release constant
K_{deg}	:	Degradation rate constant
LLE	:	Liquid-liquid extraction
LLOQ	:	Lower limit of quantification
LDLR	:	Low-density lipoprotein receptor
LOAD	:	Late onset of Alzheimer’s Disease
LOD	:	Limit of detection
LOQ	:	Limit of quantification
LQC	:	Lower quality control
LRP	:	Lipoprotein receptor-related protein
MAP	:	Microtubule-associated protein
MALS	:	Multi-angles light scattering
MDA	:	Malondialdehyde
MeOH	:	Methanol
MetS	:	Metabolic Syndrome
min	:	Minute
MQC	:	Medium quality control
MRT	:	Mean residence time
MRP	:	Multidrug resistance-associated protein
mPEG	:	Methoxy-(polyethylene glycol)
mPEG-PLA	:	Methoxy-(polyethylene glycol)-(polylactide)
mPEG-PCL	:	Methoxy-(polyethylene glycol)-(polycaprolactone)
MWCO	:	Molecular weight cut off
MWM	:	Morris water maze
N	:	Number of theoretical plates
n	:	Diffusional exponent indicating the drug release mechanism in Korsmeyer–peppas model
NDDS	:	Novel drug delivery system

NFT	:	Neurofibrillary tangles
NMR	:	Nuclear magnetic resonance spectroscopy
NPs	:	Nanoparticles
NVU	:	Neurovascular Unit
<i>p</i> value	:	Significance level in statistical tests
PA	:	Passive avoidance task
PBCA	:	Polybutyl cyanoacrylates
PCL	:	Polycaprolactone
PCS	:	Photon correlation spectroscopy
PDI	:	Polydispersity index
P-gp	:	P-glycoproteins
pH	:	Negative log to the base 10 of hydrogen ion concentration
pKa	:	Acid dissociation constant
PLA	:	Poly (D, L-lactide)
PLGA	:	Poly (D, L-lactide-co-glycolide)
PVA	:	Polyvinyl alcohol
p-tau	:	Phosphorylated tau
QC	:	Quality control
QLS	:	Quasi light scattering
QELS	:	Quasi-elastic light scattering
R ²	:	Regression coefficient
R _f	:	Retention factor
R _s	:	Resolution
R _t	:	Retention time
REP	:	Repaglinide
RMT	:	Receptor-mediated transport
RP-HPLC	:	Reversed-phase high-performance liquid chromatography
rpm	:	Rotations per minute
RT	:	Room temperature
SBC	:	Schwarz information criterion
SD	:	Standard deviation
SDS	:	Sodium dodecyl sulphate
sec	:	Second

SEM	:	Scanning electron microscopy
SLN	:	Solid-lipid nanoparticles
SLA	:	Spontaneous locomotor activity
SOD	:	Superoxide dismutase
$t_{1/2}$:	Half-life
$t_{50\%}$:	Time to reach 50% of initial concentration
$t_{90\%}$:	Time to reach 90% of initial concentration
T_{max}	:	Time to reach maximum concentration
TBA	:	Thiobarbituric acid
TDW	:	Triple distilled water
T2DM	:	Type 2 Diabetes mellitus
TEM	:	Transmission electron microscopy
ThT	:	Thioflavin T
TNF- α	:	Tumor necrosis factor- α
USFDA	:	United States Food and drug administration
V_d	:	Apparent volume of distribution
VSMC	:	Vascular smooth muscle cells
ZP	:	Zeta potential

List of Figures

S. No.	Caption	Page No.
Fig.1.1	: Potential risk factors of metabolic disorders	1
Fig.1.2	: Illustration of links between T2DM and AD	5
Fig.1.3	: Mode of action of repaglinide in peripheral (pancreatic cell)	8
Fig.2.1	: Insulin production pathway	14
Fig.2.2	: Neuronal signaling mechanism in a state of insulin sensitivity and insulin resistance.	16
Fig.2.3	: Mammalian target of rapamycin (mTOR) pathway	17
Fig.2.4	: Regulation of GSK-3 β by insulin signaling pathway	18
Fig.2.5	: Schematic representation of various nanocarrier systems for the drug delivery	32
Fig. 2.6	: The illustration of (a) Polymeric nanoparticles and (b) polymer lipid hybrid nanoparticles	33
Fig.3.1	: Mets and dysregulated brain glucose metabolism lead to neurodegeneration which is complicated by ER stress, mitochondrial stress, and the apoptosis process.	35
Fig.4.1	: Ishikawa fishbone diagram to identify the potential attributes in HPLC method development.	41
Fig.4.2	: Experimental schedule of animal model development and treatment	49
Fig.4.3	: Pictorial representation of Passive avoidance apparatus	52
Fig.4.4	: Schematic representation of polymer synthesis	55
Fig.4.5	: Schematic representation of PNPs preparation procedure	56
Fig.4.6	: Schematic representation of PLHNPs preparation procedure	57
Fig.4.7	: The flowchart to perform Gastro-intestinal stability studies	62
Fig.4.8	: Illustration of SPIP model for in situ permeation study in wistar rat model.	63
Fig.4.9	: Illustration of Parallel artificial membrane permeability assay-blood brain barrier (PAMPA-BBB)	65
Fig.5.1	: The half-normal plot and Pareto chart indicate factors that influence response variables of the RP-HPLC method, (A) retention time, (B) Peak tailing, and (C) theoretical plates. The Positive influencing factors were shown in orange whereas the negative shown in blue.	67

Fig.5.2	: The 2D-contour plots and 3D-response surface plots show the relationship among the factors on (A) retention time, (B) theoretical plates, and (C) the Tailing factor.	69
Fig.5.3	: Perturbation chart	70
Fig.5.4	: Repaglinide peaks (A) Std repaglinide 20µg/mL, (B) system-suitability, (C) Selectivity, (D) photo, (E) Thermal, (F) Acid	71
Fig.5.5	: Solubility studies in different solvents	73
Fig.5.6	: HPLC Chromatograms for (A) Blank plasma (plasma sample without IS and REP) (B) Calibration standard (C) LLOQ (50ng/mL) (D)LQC ((E) MQC and (F) HQC of REP.	77
Fig.5.7	: <i>In vivo</i> estimation of parameters to confirm the insulin resistance in rats (A) FBGL; (B) HbA1c; (C) insulin and (D) HOMA-IR; of HFD+STZ induced wistar rats, data are represented in (mean ± SEM, n=6 rats per group). * Indicates, **** $P < 0.0001$ by t-test.	80
Fig.5.8	: <i>In vivo</i> estimation of parameters to confirm the insulin resistance in rats (A) TC; and (B)TG of HFD+STZ induced wistar rats, data are represented in (mean ± SEM, n=6 rats per group). * Indicates, **** $P < 0.0001$ by t-test.	81
Fig.5.9	: <i>In vivo</i> estimation of parameters to confirm the insulin resistance in rats (A) p-tau; and (B) Aβ level of HFD+STZ induced wistar rats, data are represented in (mean ± SEM, n=6 rats per group). * Indicates, **** $P < 0.0001$ by t-test.	81
Fig.5.10	: Cell viability assay of REP on neuroblastoma SH-SY5Y cell line.	82
Fig.5.11	: (A) and (B) screening of STZ concentration; (C) The effect of REP on STZ-treated SHSY-5Y neuroblastoma cell lines	83
Fig.5.12	: (A) Screening of H ₂ O ₂ concentration and (B) neuroprotective effect of REP on H ₂ O ₂ treated SH-SY5Y neuroblastoma cell lines	84
Fig.5.13	: <i>In vivo</i> estimation of neurochemical parameters to understand the effect of REP after the treatment (A) Aβ level; (B) p-Tau; and (C) BDNF; in brain homogenate of HFD+STZ induced wistar rats, data are represented in (mean ± SEM, n=6 rats per group). * Indicates $P < 0.05$; ** $P < 0.01$, *** $P < 0.001$, **** $P < 0.0001$ by one-way ANOVA followed by Tukey's post hoc multiple comparison tests.	85

Fig.5.14 : <i>In vivo</i> estimation of proinflammatory cytokines to understand the effect of REP on (A) TNF- α ; (B) IL-6 level in brain homogenate of HFD+STZ induced wistar rats, data are represented in (mean \pm SEM, n=6 rats per group). * Indicates $P < 0.05$; ** $P < 0.01$, *** $P < 0.001$, **** $P < 0.0001$ by one-way ANOVA followed by Tukey's post hoc multiple comparison tests	86
Fig.5.15 : <i>In vivo</i> estimation of proinflammatory cytokines to understand the effect of REP on (A) GSH; (B) SOD; (C) Nitrite; (D) MDA level in brain homogenate of HFD+STZ induced wistar rats, data are represented in (mean \pm SEM, n=6 rats per group). * Indicates $P < 0.05$; ** $P < 0.01$, *** $P < 0.001$, **** $P < 0.0001$ by one-way ANOVA followed by Tukey's post hoc multiple comparison tests	87
Fig.5.16 : Estimation of transfer latency by performing behavioral parameters using passive avoidance task.	87
Fig.5.17 : Estimation of (A) mean escape latency, (B) time spent in the same quadrant, and (C) representation of track plot for Morri's water maze task. Data are represented in (mean \pm SEM, n=6 rats per group).	88
Fig.5.18 : Effect of REP on the ATF6 expression. values are represented in mean \pm SEM and *** Indicates $P < 0.001$, **** $P < 0.0001$ by one-way ANOVA followed by Tukey's post hoc multiple comparison test	89
Fig.5.19 : Western blot analysis exhibited (A) Bcl-2, Bax, Caspase-3, and GAPDH expression in lysate from rats brain; (B) quantitative analysis of protein expression	90
Fig.5.20 : Plasma concentration-time profile of REP, and PNPs. Values were represented in mean \pm SEM, n=4.	90
Fig.5.21 : : Confirmation of the amphiphilic di-block polymer (PEG-PCL) was done by (A) GPC, and (B) $^1\text{H-NMR}$.	92
Fig.5.22 : The 2D and 3D-response surface plot showing the relationship among the factors on (A) particle size, (B) PDI, and (C) entrapment efficiency of Drug: polymer; Surfactant amount (AB factor), Drug: polymer; Sonication time (AC factor), Surfactant, sonication time (BC factor) of the PNPs	95

Fig.5.23	: The (A) desirability index and (B) overlay plot of PNPs with Drug: polymer; Surfactant amount (AB factor)	96
Fig.5.24	: The compatibility study of REP, BPNPs, and PNPs performed by (A) ATIR, (B) DSC, and (C) pXRD.	98
Fig.5.25	: (A) Particle size and (B) zeta potential of optimized PNPs	99
Fig.5.26	: Morphological characterization of PNPs by (A) SEM and (B) TEM	100
Fig.5.27	: Graphical representation of (A) cryoprotectant screening; (B) amount (%w/v) of selected cryoprotectant.	101
Fig.5.28	: <i>In vitro</i> release profile of REP and PNPs using dialysis bag method for 48h.	101
Fig.5.29	: Stability study of PNPs in simulated gastrointestinal fluids	103
Fig.5.30	: Representative plots of the steady-state concentration (C_{out}/C_{in}) VS time for (A) REP, (b) PNPs, and (c) Effective permeability coefficient and apparent absorption rate constant. Values were represented as mean \pm SEM ($n=3$)	105
Fig.5.31	: Cell viability assay of REP, BPNPs, and PNPs on neuroblastoma SH-SY5Y cell line.	106
Fig.5.32	: The quantitative estimation of coumarin 6, and coumarin 6 loaded PNPs in cellular uptake study by confocal microscopy at 4h and 8h.	107
Fig.5.33	: The effect of REP and PNPs on STZ-treated SHSY-5Y neuroblastoma cell lines.	108
Fig.5.34	: Neuroprotective effect of REP and PNPs on H ₂ O ₂ treated SH-SY5Y neuroblastoma cell lines	108
Fig.5.35	: Plasma concentration-time profile of REP, and PNPs. Values were represented in mean \pm SEM, n=4.	109
Fig.5.36	: Biodistribution study of REP and PNPs in major organs after oral administration (4mg/kg) in wistar rats.	110
Fig.5.37	: <i>In vivo</i> estimation of neurochemical parameters to understand the effect of REP and PNPs after the treatment (A) BDNF; (B) p-Tau; (C) A β level in brain homogenate of HFD+STZ induced wistar rats, data are represented in (mean \pm SEM, n=6 rats per group). * Indicates $P < 0.05$; ** $P < 0.01$, *** $P < 0.001$, **** $P < 0.0001$ by one-way ANOVA followed by Tukey's post hoc multiple comparison test	111

Fig.5.38	: <i>In vivo</i> estimation of neurochemical parameters to understand the effect of REP and PNPs after the treatment (A) TNF- α ; and (B) IL-6 level in brain homogenate of HFD+STZ induced wistar rats, data are represented in (mean \pm SEM, n=6 rats per group). * Indicates $P < 0.05$; ** $P < 0.01$, *** $P < 0.001$, **** $P < 0.0001$ by one-way ANOVA followed by Tukey's post hoc multiple comparison test	112
Fig.5.39	: Effect of oxidative stress parameters (A) MDA; (B) Nitrite; (C) GSH on REP and PNPs. The data are represented in (mean \pm SEM, n=6 rats per group). * Indicates $P < 0.05$; ** $P < 0.01$, *** $P < 0.001$, **** $P < 0.0001$ by one-way ANOVA followed by Tukey's post hoc multiple comparison test.	112
Fig.5.40	: Estimation of transfer latency by performing behavioral parameters using passive avoidance task.	113
Fig.5.41	: (A) Representation of track plot for the novel object recognition task and (B) Time spent in exploring the object. The data are represented in (mean \pm SEM, n=6 rats per group). * Indicates $P < 0.05$; ** $P < 0.01$, *** $P < 0.001$, **** $P < 0.0001$ by one-way ANOVA followed by Tukey's post hoc multiple comparison test.	113
Fig.5.42	: Estimation of (A) mean escape latency, (B) time spent in the same quadrant, and (C) representation of track plot for Morri's water maze task. Data are represented in (mean \pm SEM, n=6 rats per group).	114
Fig.5.43	: (A) Neuronal regeneration on HFD+STZ rats at dentate gyrus (DG) and Cornus ammonis (CA) region of the hippocampus and (B) %neuronal count in DG and CA region. Data are represented in (mean \pm SEM, n=6 rats per group).	116
Fig.5.44	: The 2D and 3D-response surface plot showing the relationship among the factors on (A)PDI, and (B) entrapment efficiency of Drug: polymer; Surfactant amount (AB factor), Drug: polymer; Sonication time (AC factor), Surfactant, sonication time (BC factor) of the PLHNPs	120
Fig.5.45	: The (A) desirability index and (B) overlay plot of PNPs with Drug: polymer; Surfactant amount	121

Fig.5.46	: The compatibility study of REP, BPLHNPs, and PLHNPs performed by (A) ATIR, (B) DSC, and (C) pXRD	123
Fig.5.47	: Characterization of polymer lipid hybrid nanoparticles by (A) PS and (B) ZP	124
Fig.5.48	: Morphological characterization of polymer lipid hybrid nanoparticles by (a) SEM and (b) TEM	125
Fig.5.49	: Graphical representation of (A) cryoprotectant screening; (B) amount (%w/v) of selected cryoprotectant	125
Fig.5.50	: <i>In vitro</i> release profile of REP and PLHNPs using dialysis bag method for 48h.	126
Fig.5.51	: Stability study of PLHNPs in simulated gastrointestinal fluids.	127
Fig.5.52	: Representative plots of the steady-state concentration (C _{out} /C _{in}) VS time for (A) REP, (b) PLHNPs, and (c) Effective permeability coefficient and apparent absorption rate constant. Values were represented as mean± SEM (n=3)	128
Fig.5.53	: Cell viability assay of REP, BPLHNPs, and PLHNPs on neuroblastoma SH-SY5Y cell line.	129
Fig.5.54	: The quantitative estimation of coumarin 6, and coumarin 6 loaded PNP in cellular uptake study by confocal microscopy at 4h and 8h.	130
Fig.5.55	: The effect of REP and PLHNPs on STZ-treated SHSY-5Y neuroblastoma cell lines	131
Fig.5.56	: Neuroprotective effect of REP and PLHNPs on H ₂ O ₂ treated SH-SY5Y neuroblastoma cell lines.	132
Fig.5.57	: Plasma concentration-time profile of REP, and PLHNPs. Values were represented in mean ±SEM, n=4.	132
Fig.5.58	: Biodistribution study of REP and PLHNPs in major organs after oral administration (4mg/kg) in wistar rats	134
Fig.5.59	: <i>In vivo</i> estimation of neurochemical parameters to understand the effect of REP and PLHNPs after the treatment (A) A β level; (B) p-Tau; (C) BDNF level in brain homogenate of HFD+STZ induced wistar rats, data are represented in (mean ± SEM, n=6 rats per group). * Indicates $P < 0.05$; ** $P < 0.01$, *** $P < 0.001$, **** $P < 0.0001$ by	135

	one-way ANOVA followed by Tukey's post hoc multiple comparison test	
Fig.5.60	: : <i>In vivo</i> estimation of neurochemical parameters to understand the effect of REP and PLHNPs after the treatment (A) IL-6; and (B) TNF- α level in brain homogenate of HFD+STZ induced wistar rats, data are represented in (mean \pm SEM, n=6 rats per group). * Indicates $P < 0.05$; ** $P < 0.01$, *** $P < 0.001$, **** $P < 0.0001$ by one-way ANOVA followed by Tukey's post hoc multiple comparison test	136
Fig.5.61	: Effect of oxidative stress parameters (A) MDA; (B) GSH; (C) Nitrite on REP and PLHNPs. The data are represented in (mean \pm SEM, n=6 rats per group). * Indicates $P < 0.05$; ** $P < 0.01$, *** $P < 0.001$, **** $P < 0.0001$ by one-way ANOVA followed by Tukey's post hoc multiple comparison test.	137
Fig.5.62	: Estimation of transfer latency by performing behavioral parameters using passive avoidance task.	138
Fig.5.63	: (A) Representation of track plot for the novel object recognition task and (B) Time spent in exploring the object. The data are represented in (mean \pm SEM, n=6 rats per group). * Indicates $P < 0.05$; ** $P < 0.01$, *** $P < 0.001$, **** $P < 0.0001$ by one-way ANOVA followed by Tukey's post hoc multiple comparison test	139
Fig.5.64	: Estimation of (A) mean escape latency, (B) time spent in the same quadrant, and (C) representation of track plot for Morri's water maze task. Data are represented in (mean \pm SEM, n=6 rats per group).	140
Fig.5.65	: (A) Neuronal regeneration on HFD+STZ rats at dentate gyrus (DG) and Cornus ammonis (CA) region of hippocampus and (B) %neuronal count in DG and CA region. Data are represented in (mean \pm SEM, n=6 rats per group).	141
Fig.5.66	: Characterization of Polymeric nanoparticles and polymer lipid hybrid nanoparticles by (a) particle size, (b) zeta potential.	143
Fig.5.67	: <i>In vitro</i> release profile of Polymeric nanoparticles and polymer lipid hybrid nanoparticles	144
Fig.5.68	: Effective permeability coefficient and apparent absorption rate constant of PNPs and PLHNPs after using SPIP wistar rat model	145

Fig.5.69	: <i>In vitro</i> cell culture studies on neuroblastoma cell line SHSY-5Y for estimation of cell viability by MTT cytotoxicity assay	146
Fig.5.70	: The quantitative estimation of coumarin 6, coumarin 6 loaded PNPs, and coumarin 6 loaded PLHNPs in cellular uptake study by (A) confocal microscope, (B) flow cytometer, and the cell sorter	147
Fig.5.71	: Plasma concentration-time profile of REP, PNPs, and PLHNPs. Values were represented in mean \pm SEM.	148
Fig.5.72	: Biodistribution study of REP, PNPs, and PLHNPs on brain, heart, liver, and kidney.	149
Fig.5.73	: Neurobiochemical parameters improvement on HFD+STZ induced animal model on treatment of REP, PNPs and PLHNPs, (A) A β level, (B) p-Tau level (C) BDNF level, (D) FBGL and data are represented in (mean \pm SEM, n=6 rats per group). * Indicates $P < 0.05$; ** $P < 0.01$, *** $P < 0.001$, **** $P < 0.0001$ by one-way ANOVA followed by Tukey's post hoc multiple comparison test.	150
Fig.5.74	: Effect of inflammatory parameters on HFD+STZ induced animal model on the treatment of REP, PNPs, and PLHNPs, (A) IL-6, and (B) TNF- α . The data are represented in (mean \pm SEM, n=6 rats per group). * Indicates $P < 0.05$; ** $P < 0.01$, *** $P < 0.001$, **** $P < 0.0001$ by one-way ANOVA followed by Tukey's post hoc multiple comparison test.	151
Fig.5.75	: Effect of oxidative stress parameters on HFD+STZ induced animal model on the treatment of REP, PNPs, and PLHNPs, (A) MDA, (B) GSH, and (C) nitrite. The data are represented in (mean \pm SEM, n=6 rats per group). * Indicates $P < 0.05$; ** $P < 0.01$, *** $P < 0.001$, **** $P < 0.0001$ by one-way ANOVA followed by Tukey's post hoc multiple comparison test.	152
Fig.5.76	: The estimation of transfer latency by performing behavioral parameters using passive avoidance task.	152
Fig.5.77	: (A)The representation of the track plot for the novel object recognition task and (B) Time spent in exploring the object	153

Fig.5.78	: (A) The representation of track plot for Morri's water maze task; (B) mean escape latency and (C) Estimation of time spent in the same quadrant	153
Fig.5.79	: <i>In vivo</i> estimation of neurochemical parameters to understand the effect of REP after the treatment (A) BDNF; (B) p-Tau; (C) A β level in brain homogenate of HFD+STZ induced wistar rats, data are represented in (mean \pm SEM, n=6 rats per group). * Indicates $P < 0.05$; ** $P < 0.01$, *** $P < 0.001$, **** $P < 0.0001$ by one-way ANOVA followed by Tukey's post hoc multiple comparison test	155
Fig.5.80	: <i>In vivo</i> estimation of proinflammatory cytokines to understand the effect of REP on (A) TNF- α ; (B) IL-6 level in brain homogenate of HFD+STZ induced wistar rats, data are represented in (mean \pm SEM, n=6 rats per group). * Indicates $P < 0.05$; ** $P < 0.01$, *** $P < 0.001$, **** $P < 0.0001$ by one-way ANOVA followed by Tukey's post hoc multiple comparison test	156
Fig.5.81	: <i>In vivo</i> estimation of proinflammatory cytokines to understand the effect of REP on (A) GSH; (B) SOD; (C) Nitrite; (D) MDA level in brain homogenate of HFD+STZ induced wistar rats, data are represented in (mean \pm SEM, n=6 rats per group). * Indicates $P < 0.05$; ** $P < 0.01$, *** $P < 0.001$, **** $P < 0.0001$ by one-way ANOVA followed by Tukey's post hoc multiple comparison test	157

List of Tables

S.No.	Caption	Page No.
Table.1.1	: List of PEGylated nanocarriers for the treatment of Alzheimer's disease	10
Table.2.1	: The effect of other drugs on C _{max} and AUC of Repaglinide	29
Table.2.2	: List of drugs for the treatment of Alzheimer's disease	31
Table.4.1	: List of instruments/ equipment with manufacturer's name used to conduct the experiments.	38
Table.4.2	: List of software used to conduct the experiments	39
Table.4.3	: QTMP elements for an efficient liquid chromatographic method for estimation of repaglinide	40
Table.4.4	: Design matrix for screening of method variables by seven-factor eight-run Taguchi design	41
Table.4.5	: Design matrix for optimization of the chromatographic method by Box-Behnken Design (BBD)	42
Table.4.6	: Buffer compositions from pH 1 – 9	45
Table.4.7	: Composition of High-fat diet	49
Table.4.8	: Experimental design for the screening of REP in T2DM-associated AD condition	50
Table.4.9	: Experimental design for the screening of REP with nanocarrier systems in T2DM-associated AD condition	50
Table.4.10	: Experimental design for the additive/synergistic effect of best nanocarrier system in T2DM-associated AD condition	50
Table.4.11	: The primer sequence was used for qRT-PCR analysis.	54
Table.4.12	: Instrumental parameters of GC-HS for estimation of residual organic content in nanoparticles	56
Table.4.13	: Quality target product profile (QTPP) of REP-loaded PNPs and PLHNPs	57
Table.4.14	: Risk estimation matrix (REM) for initial risk assessment of different material attributes and process parameters by qualitative analysis.	58
Table.4.15	: Lyophilization Cycles for lyophilization of REP-loaded PNPs and PLHNPs	60

Table.4.16	: Composition of Perfusion solution for SPIP.	64
Table.5.1	: System suitability Parameter	71
Table.5.2	: Precision and accuracy for the analysis of repaglinide	72
Table.5.3	: Representing force degradation of repaglinide in various stress conditions (Mean \pm SD).	73
Table.5.4	: RP-HPLC method optimization for estimation of REP in biomatrix	75
Table.5.5	: Optimization of Liquid-liquid Extraction (LLE) method for sample preparation	76
Table.5.6	: Linearity table of different biomatrix system	77
Table.5.7	: Precision (% CV) and accuracy (% bias) of REP in rat plasma samples at QC levels (n=6)	78
Table.5.8	: Absolute recoveries (%) of repaglinide in rat plasma samples from QC levels	78
Table.5.9	: Stability studies for repaglinide in rat plasma at QC levels	79
Table.5.10	: Pharmacokinetic parameters of REP	91
Table.5.11	: The Statistical values for each of the model sources for both the responses, along with remarks generated by the Design-Expert® software (version 13.0, Stat-Ease Inc.) under the heading of summary of fitness of each model.	93
Table.5.12	: Statistical validation parameters of the selected models for individual responses	94
Table.5.13	: Experimental design model validation	96
Table.5.14	: Mathematic release models for the estimation of <i>in vitro</i> release parameters	102
Table.5.15	: Stability studies	104
Table.5.16	: Pharmacokinetic parameters of REP and PNPs	109
Table.5.17	: Preliminary Screening of phospholipids & stabilizers for preparation PLHNPs. Data are represented as mean \pm SEM	118
Table.5.18	: The Statistical values for each of the model sources for both the responses, along with remarks generated by the Design-Expert® software (version 13.0, Stat-Ease Inc.) under the heading of summary of fitness of each model.	119

Table.5.19	: Statistical validation parameters of the selected models for individual responses	119
Table.5.20	: Experimental design model validation of PLHNPs by QbD	122
Table.5.21	: Mathematic release models for the estimation of <i>in vitro</i> release parameters	126
Table.5.22	: Long-term stability studies of PLHNPs	128
Table.5.23	: Pharmacokinetic parameters of REP and PLHNPs	133
Table.5.24	: Comparative analysis of Pharmacokinetic parameters of PNP and PLHNPs	148

Abstract

Background

Metabolic syndrome (MetS) is a condition which includes clusters of metabolic disorders like glucose intolerance, hypertension, dyslipidemia, obesity, insulin resistance, and that together raise the risk of coronary heart disease, diabetes, and stroke. Among all, type 2 DM (T2DM) is the most common cause of mortality and morbidity caused by MetS. According to the International Diabetes Federation, around 537 million people are living with DM, and this number is expected to rise to 783 million by 2045. T2DM is prominently characterized by hyperglycemia due to insulin resistance (IR). It is also associated with various macro and microvascular complications such as diabetic neuropathy, retinopathy, cardiomyopathy, and nephropathy. IR is mediated by reduced insulin receptor expression and dysregulation of signaling cascades such as phosphoinositide 3-kinase (PI3K)/ Glycogen Synthase Kinase-3 β (GSK-3 β). In the recent past, MetS abnormalities linked to progressive brain insulin resistance (BIR) with consequent impairment of central insulin signaling processes, accumulation of neurotoxins, neuronal stress, and resulting in a progressive course of neurodegeneration is also termed Type 3 DM. The dysregulated PI3K/GSK-3 β in the brain can increase the production and secretion of amyloid-beta (A β) and generates hyperphosphorylated tau which prompts neurodegenerative disorders such as Alzheimer's (AD).

Recently, comorbid conditions including DM linked with AD is mounting at an alarming rate and has become a major health issue in developing and developed countries. Although, several treatment options are available for T2DM management which can temporarily delay or reduce the symptoms of the disease including the classes of drugs- Dipeptidyl Peptidase-4 (DPP-4) inhibitors, Sodium-glucose Cotransporter-2 (SGLT2) inhibitors, etc. but they are effectively unable to control the diabetic complications and co-morbidities. However, recent pre-clinical and clinical studies have indicated the benefits of the meglitinides class of drugs not only in DM but also in comorbid conditions like AD and Huntington's disease (HD). Repaglinide (REP) a meglitinides class drug is believed to act by targeting ATP-binding cassettes and stimulating the release of insulin from the β -cells of the pancreas. REP exerted a neuroprotective effect against kainic acid-induced neuronal cell death in the CA3 region of hippocampal and rotenone-induced Parkinson's disease. Further, recent studies have reported that REP exerted a strong neuroprotective effect in HD which may possibly work via multiple intracellular channel modulators, maintaining calcium homeostasis, gene expression, enzymatic activities, and targets neuronal calcium receptors by specifically attaching to them

in a calcium-dependent manner. Recent evidence also indicated that REP down-regulates the expression of downstream regulatory element antagonist modulator (DREAM), (a calcium-binding protein) that regulates calcium homeostasis and is involved in the pathogenesis of HD and AD. It has been reported that REP increases neuronal survival via upregulating activating transcription factors-6 (ATF6) gene (endoplasmic stress sensor) that may possibly work via activating autophagy and inhibiting endoplasmic stress-induced apoptosis along with inhibition of the DREAM. Thus, there is a huge possibility that REP regulates neurodegeneration via modulating the necrotic and apoptotic cell death protein expression of pro-apoptotic protein, anti-apoptotic protein, calcium homeostasis, and may eventually reduce neuronal cell death. Moreover, clinical reports suggest that repeated doses of REP need to be administered to exhibit pharmacological action as it has a poor pharmacokinetic profile, low solubility, low absorptivity, high protein binding, and substantial first-pass metabolism. This evidence clearly indicated the possible benefit of REP in DM and co-morbid conditions but the lack of strong evidence of its efficacy in AD and pharmacokinetic challenges are emergent needs to be circumvented along with its efficacy to be ascertain.

Therefore, the current research work was conducted in adherence to the following major objectives, (i) To evaluate the neuroprotective potential of REP in MetS associated with AD using *in vitro* and *in vivo* studies, (ii) To improve the efficacy and circumvent pharmacokinetic limitations of REP by developing brain targeted nano drug delivery system; (iii) To examine the best nanocarrier system for targeting REP to the brain by the oral route; (iv) To explore the additive and/or synergistic neuroprotective potential of REP with Memantine (MEM, NMDA receptor antagonist), if any.

Methodology and Results

In vitro and *in vivo* studies were conducted to understand the neuroprotective potential, molecular targets, identifying proteins, and activating cellular signaling pathways of the REP. In the cellular *in vitro* studies, primarily cytotoxicity assay was performed on SHSY-5Y neuroblastoma cells. It was observed that the REP shows cellular viability of ~80-85% at 1mM concentration and no morphological changes in the cells were found. Additionally, to mimic the neurodegenerative condition similar to AD, the SHSY-5Y cells were treated with streptozotocin (STZ, 2.5mM) as it accelerates neuronal aging, A β aggregation and depolarized the mitochondrial membrane, increases apoptosis, and decrease glucose uptake. The results have shown that REP increased the cell viability of STZ-treated SHSY-5Y cells by ~1.2-fold and significantly ($p < 0.01$) decreased the oxidative stress in H₂O₂-treated cells, indicating the possible neuroprotective potential of REP. Further, to check the efficacy of REP in AD, *in vivo*

studies were performed using a high-fat diet (HFD) fed STZ-induced murine model. The HFD was fed for 16 weeks followed by administration of STZ (30mg/kg; *i.p*) in wistar rats for induction of DM-linked AD. The significant ($p < 0.001$) increase in the level of AD pathogenesis modulators i.e; A β , hyperphosphorylated tau proteins, and pro-inflammatory cytokines (TNF- α , IL-6), oxidative marker (Malondialdehyde (MDA), Nitrite (NO)) and decreased brain-derived neurotrophic factor (BDNF), antioxidants (Glutathione (GSH), Superoxide dismutase (SOD)) enzymes level was observed in brain homogenate of HFD fed STZ rats (disease rats) as compared to normal rats. After treatment of REP (4 mg/kg, *p.o*) for 4 weeks in DM-linked AD wistar rats, a significant ($p < 0.01$) decrement in A β , tau proteins, TNF- α , IL-6, MDA, NO, and increment in BDNF, SOD, GSH level was observed compared to disease control rats. Further, behavioral studies (passive avoidance task (PAT), and Morri's water maze (MWZ)) were conducted in HFD-fed STZ rats to understand the effect of REP on memory cognitive dysfunctions in AD. A significant improvement ($p < 0.01$) in the retention memory and spatial memory was observed after the REP treatment compared to HFD-fed STZ. Additionally, the apoptosis marker proteins (Bcl-2, Bax, Caspase-3) and ATF6 gene expression in brain homogenate were measured to understand the mechanistic approach of REP. The decreased intensity of Bcl-2, ATF-6 and increase in the intensity of Bax, Caspase-3 represents activation of apoptosis in HFD+STZ induced rats compared to normal control but after treatment with REP a significant ($p < 0.05$) increase in Bcl-2, ATF-6 expression, and decrement in Bax, Caspase-3 expression indicates a reduction in neuronal cell death then the disease rats. Moreover, the pharmacokinetic (PK) studies confirmed the short half-life ($t_{1/2}$) 2.65 ± 1.54 h), high clearance rate (163.84 ± 17.39 mL/h/kg), and low volume of distribution (2209.63 ± 603.29 mL/kg) of REP after performing the study on wistar rats. Therefore, to circumvent the observed problems *i.e.*, low absorptivity, high protein binding, first-pass metabolism, and poor pharmacokinetic and pharmacodynamic of REP, the targeted nano drug delivery systems were developed and biologically evaluated.

Primarily, an amphiphilic di-block co-polymer (mPEG-PCL) was synthesized using a ring-opening polymerization reaction and was characterized thoroughly using Nuclear Magnetic Resonance (NMR), Gel permeation chromatography (GPC). Further REP was loaded into the polymer using nanoprecipitation method and formulated polymeric nanoparticles (PNPs). In developed PNPs, the role of various process parameters such as drug: polymer, sonication time, and stabilizer amount on response factors like particle size (PS), polydispersity index (PDI), and entrapment efficiency (EE) were studied to optimize the PNPs using Quality by design (QbD) approach response surface (Box Behnken) methodology. Further, the REP-loaded PNPs

showed a high redispersibility index with trehalose and organic residual content in PNPs was estimated using headspace gas chromatography (GC-HS). The morphological characterization of PNPs was characterized by scanning electron microscopy (SEM) and transmission electron microscopy (TEM) and showed that REP-loaded PNPs have isometric shape with the regular surface. Moreover, *in vitro* release study indicated that REP-loaded PNPs (~70% in 48h) followed the Korsmeyer-Peppas model with a Fickian diffusion release pattern. Additionally, REP-loaded PNPs enhance intestinal absorption by ~ 1.3 folds and improve brain permeation by ~ 1.2 folds compared to free REP. Furthermore, cellular studies confirmed that REP-loaded PNPs significantly enhance cell viability, and cell uptake, decrease STZ induce neurodegeneration and oxidative stress in SHSY-5Y cells compared to free REP. Further, in *in vivo* pharmacokinetic study the PNPs loaded with REP showed significant increments in t_{max} (2.4-fold), C_{max} (1.2-fold), $t_{1/2}$ (5.9-fold) and decrement in cL (1.2-fold) as compared to REP. In the biodistribution study, REP-loaded PNPs improve the mean residence time in the brain more than free REP. Likewise, in pharmacodynamic studies, the REP-loaded PNPs significantly ($p < 0.01$) attenuated the A β , tau proteins, TNF- α , IL-6, MDA, NO levels and improves the BDNF, SOD, GSH levels compared to REP. Furthermore, the behavioral studies (PAT, MWZ, Novel object recognition (NOR)) also showed a significant ($p < 0.01$) improvement in the retention, spatial, and recognition memory after being treated with REP-loaded PNPs compared to free REP. Also, improvement in health neuronal count was observed in the REP-loaded PNPs compared to REP after performing hematoxylin and eosin (H&E) staining in the cornu ammonis (CA) and dentate gyrus (DG) regions of hippocampal.

Additionally, polymer lipid hybrid nanoparticles (PLHNPs) were formulated with soy phosphatidylcholine (SPC) as a phospholipid, poly (lactic-co-glycolic acid) (PLGA) as a biodegradable polymer, 1,2 distearoyl-sn-glycerol-3-phosphoethanolamine-N- amino (polyethylene glycol)-2000] (DSPE-PEG 2000) a lipid polymer and Pluronic F127 as a stabilizer. The PLHNPs were prepared using a nanoprecipitation self-assemble process and to optimize the formulation, the effect of various process parameters (Drug: polymer; amount of lipid and sonication time) on response factors (PS, PDI, and EE) were studied using the QbD approach response surface methodology (Box Behnken). The morphological characterization of REP-loaded PLHNPs was carried out by SEM and TEM and showed a core-shell structure with a spherical shape and smooth surface. The REP-loaded PLHNPs showed the release of REP in a controlled manner (~58% in 48h) followed by the Korsmeyer-Peppas model with a Fickian diffusion release pattern. Further REP loaded PLHNPs showed stability in the gastrointestinal environment, also enhance the intestinal permeation rate (~ 3.3 folds), and

improved the brain permeation (~1.6 folds) compared to REP. Moreover, in *in vitro* cellular studies, REP-loaded PLHNPs exhibit significant improvement in cellular uptake (~21%), enhance cell viability, reduce STZ-induced neurodegeneration, and decrease the oxidative stress in neuroblastoma SHSY-5Y cells compared to free REP. Moreover, *in vivo* pharmacokinetic studies indicated significant ($p < 0.05$) improvement in t_{\max} (4.4-fold), C_{\max} (1.9-fold), $t_{1/2}$ (9.1-fold), and decrease in the cL rate (1.8-fold) compared to free REP in wistar rats. Further, in biodistribution studies, it decreases the brain clearance rate (~ 5.6-fold) and increases the area under the curve (~10.1 fold) when compared with the free REP. Likewise, in pharmacodynamic studies, the REP-loaded PLHNPs significantly ($p < 0.01$) attenuated the A β , tau proteins, TNF- α , IL-6, MDA, NO levels and improves the BDNF, SOD, GSH levels compared to REP. Furthermore, the behavioral studies (PAT, MWZ, NOR) also showed a significant ($p < 0.01$) improvement in the retention, spatial, and recognition memory after treated with REP-loaded PLHNPs compared to REP. Also, improvement in the neuronal count was observed in the REP-loaded PLHNPs compared to REP after performing H&E staining in the CA and DG regions of the hippocampal.

Furthermore, a comparative evaluation was conducted between PNP and PLHNP to examine the best nanocarrier system for targeting REP to the brain by oral route. It was observed that both the nanocarriers were efficient to deliver REP in the brain but PLHNP exhibits significant changes like delaying the release of REP more efficiently and showed good stability in the simulated gastrointestinal fluids compared to PNP. Additionally, PLHNP showed significant enhancement in effective intestinal permeability by ~3.13-fold, absorption rate (K_a) by ~1.69-fold, and improved brain permeability compared to PNP. The *in vitro* cellular uptake study of PLHNP showed ~ 1.2 % more uptake than PNP. Furthermore, PLHNP formulation significantly prevents the neuronal cell death induced by STZ and H₂O₂ in SHSY-5Y cells as evidenced by increased cell viability by 0.97-fold than the PNP. Moreover, pharmacokinetic studies also indicate the significant improvement of t_{\max} by 1.8-fold, C_{\max} by 1.4-fold, $t_{1/2}$ by 1.5-fold, and CL 1.4-fold by PLHNP when compared to PNP. Likewise, in pharmacodynamic studies, PLHNP strongly attenuated the level of A β , tau-protein, pro-inflammatory cytokines (IL-6, TNF- α), MDA, NO and increased the antioxidant enzyme level (GSH), BDNF when compared to PNP. Furthermore, behavioural studies (PA, MWM, and NOR test) also indicated highly significant improvement in the cognitive dysfunctions by PLHNP when compared to PNP, and H&E staining also confirmed, a more healthy neuronal count in PLHNP when compared with PNP. Hence, the comparative study confirmed that oral administration of PLHNP efficiently promotes the brain delivery of REP more than the PNP, due to its core-

shell nanoparticulate structure which imparts GI stability, enhanced permeation, and reduced immunogenicity. The polymeric core in PLHNPs encapsulates the REP and SPC monolayer surrounding the core which reduces the outward diffusion and enhances the stability of REP. The outer layer of DSPE-PEG 2000 prolongs the circulation time of nanocarriers by avoiding reticuloendothelial system (RES) uptake, which is indispensable for increasing the brain's uptake of nanocarriers. PEGylation facilitates the ligand–receptor interactions at the brain endothelium to ease the entry of REP into the brain.

Additionally, the additive and/or synergic neuroprotective potential of REP in combination with MEM was also examined using the HFD+STZ model. The mechanistic co-delivery approach of REP will be a more rational approach for providing novel and better therapeutic solutions for effective AD management. The low dose of MEM (5mg/kg; *p.o*) and REP (4mg/kg; *p.o*) were administered in HFD+STZ neurodegenerative rats and measured the level of neurochemicals (A β , tau protein, BDNF), proinflammatory cytokines (TNF- α , IL-6) and oxidative stress biomarkers (GSH, SOD, NO, MDA). After 3 weeks of treatment with REP+MEM, a significant ($P<0.01$) amelioration in the level of A β , tau protein, TNF- α , IL-6, and an increase in the level of BDNF has been observed when compared to free REP. The results confirmed an additive effect when REP was combined with MEM. Strikingly, when the combination of REP and MEM was compared with the PLHNPs -REP loaded formulation group, no additional significant differences in attenuation of Oxidative, neuroinflammatory, and AD markers were observed. Therefore, these results clearly indicated that the REP-loaded PLHNPs might exert a neuroprotective effect similar to the combination of REP and MEM group and proved an attractive translational possibility of REP-loaded PLHNPs formulation for clinical benefits in AD patients comorbid with BIR.

- In overall conclusion, for the first time, our research work confirmed the neuroprotective potential of REP in MetS-induced AD. Therefore, REP paved the way and suggested a therapeutic clinical repurposed drug for treating AD, co-morbid in MetS patients.
- Furthermore, targeted drug delivery systems like PNPs and PLHNPs -REP loaded formulations have been developed that improved the various pharmacokinetic problems i.e., short half-life, high clearance rate, high protein binding, low absorptivity, and first-pass metabolism as well as improved the efficacy of REP. Moreover, the comparative studies between developed and optimized PNPs and PLHNPs loaded REP nanocarriers, concluded that the PLHNPs exerted more significantly targeted brain delivery than the PNPs due to its core-shell structure and PEGylation on the outer surface which facilitates the ligand–receptor interactions at the brain endothelium to ease the entry of REP into the brain.

- In line with these, we also observed that REP-loaded PLHNPs have a potential neuroprotective effect similar to that exerted by the combination of low-dose MEM with REP.
- Therefore, in nutshell, our study provides mechanistic-based strong evidence for REP and REP-loaded PLHNPs formulation that can be repurposed and used therapeutically for treating not only DM but also MetS-linked neurodegenerative- AD.

1. Introduction

1.1 Metabolic syndrome (MetS) and Insulin resistance (IR)

Metabolic syndrome (MetS) also known as syndrome X and insulin resistance syndrome, is a set of metabolic disorders that comprised central obesity, atherogenic dyslipidemia, hypertension, glucose intolerance, and insulin resistance (IR) [1]. These metabolic disorders are the risk factors for the development of cardiovascular disease and type 2 Diabetes mellitus (T2DM). Additionally, Mets may also raise the risk of microvascular (nephropathy, retinopathy, and neuropathy) and endocrine complications [2]. According to the International Diabetes Federation (IDF), one-quarter of the world's adult population has MetS. The prevalence of Mets ranges from 20-25% in the adult population and 19.2% in children. [3]. Recent statistical data indicates a significant prevalence of metabolic syndrome in India, impacting a substantial portion of the adult population.

In the wake of urbanization, excessive calorie intake, rising obesity, and sedentary lifestyles were evolving MetS into serious concerns in the public. In the next 5 to 10 years, MetS imposes a 5-fold increase in the risk of T2DM and a 2-fold increase in the risk of cardiovascular disease [4]. MetS is a state of persistent low-grade inflammation that also results from a complicated interplay between genetic and environmental factors. Visceral adiposity, atherogenic dyslipidemia, genetic susceptibility, hypercoagulable condition, high blood pressure, chronic stress, endothelial dysfunction, and insulin resistance are the multiple variables that increase the susceptibility of the syndrome [5,6].

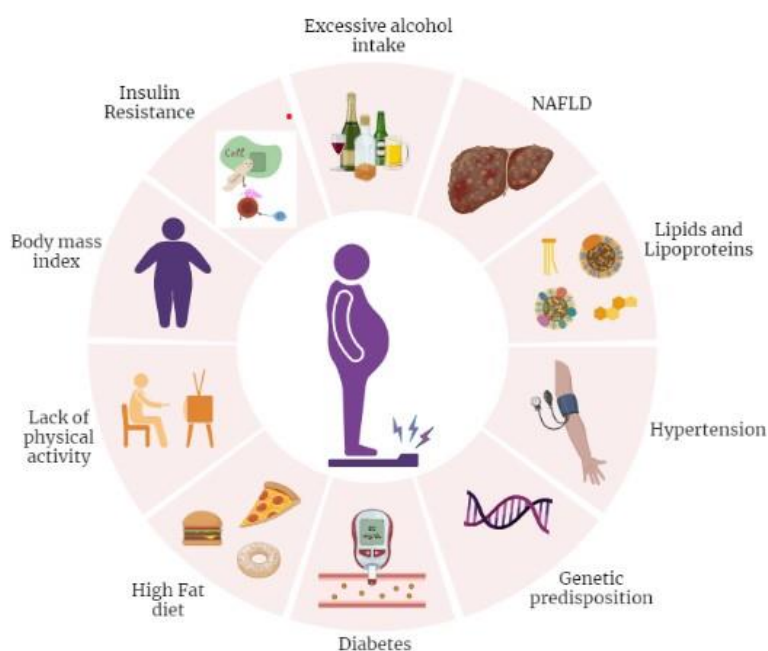


Fig.1.1: Potential risk factors of metabolic disorders

Metabolic processes ensure a continuous supply of energy and nutrition to all the body segments. Any disturbance in the normal metabolic mechanism leads to the development of serious pathophysiological complications. With the rapidly growing industrialization and urbanization, the instance of the occurrence of these disorders has increased with excessive fat intake and unhealthy lifestyle habits [7]. According to the World Health Organization (WHO), the obesity index has tripled since 1975. However, in 2016 about 39% of adults aged 18 years or above were found to be obese. According to various datasheets and charts, in 2019 around 38.2 million children under 5 years were overweight or obese [8].

Moreover, the term 'MetS' comprises T2DM and a cluster of closely connected clinical characteristics like Insulin resistance (IR), obesity (especially abdominal adiposity), hypertension, and a common form of dyslipidemia (increased triglycerides and low high-density lipoprotein (HDL)-cholesterol with or without elevation of low-density lipoprotein (LDL)-cholesterol) are defining characteristics of MetS [9]. Coronary, cerebral, and peripheral artery disease are related to a considerably elevated incidence when the metabolic syndrome is present [10]. Therefore, atherosclerotic cardiovascular disease (ASCVD) is responsible for more than 75% of hospitalizations for diabetic complications and 80% of diabetic mortality.

T2DM is a component of MetS that was described in 1988 and is the most common cause of mortality and morbidity caused by MetS. T2DM is prominently characterized by hyperglycemia due to glucose intolerance and insulin resistance (IR) [6,11]. According to the International Diabetes Federation (IDF), around 537 million adults (20-79 years old) are living with DM, and predicted to rise to 643 million by 2030 and 783 million by 2045[12]. Additionally, around 541 million adults have impaired glucose tolerance, which places them at risk of T2DM. Moreover, diabetes is responsible for 6.7 million deaths in 2021 which means 1 every 5 seconds. T2DM is also associated with various macrovascular (coronary artery disease, peripheral artery disease, stroke) and microvascular complications (nephropathy, retinopathy, and neuropathy) [13,14].

In the early 1970s, it has been reported that IR was the characteristic feature of T2DM and clinical development of this disease is indicated by the progressive inability of β -cells. The pancreatic β cells compensate for the prevailing insulin resistance by sufficient hyperinsulinemia [15,16]. IR often develops before the onset of diabetes and is frequently observed in unaffected first-degree relatives. Both the severity of hyperglycemia and the metabolic repercussions of IR contribute to morbidity and mortality. Primarily the defects in insulin action impaired the adipocytes and skeletal muscle cells which indirectly hampered the glucose transporter 4 (GLUT4) translocation and resulted in impaired insulin-mediated glucose

transport. As the β cells fail to compensate for the prevailing IR, impaired glucose tolerance causes hyperglycemia [17].

Likewise, insulin resistance impaired the ability of insulin in the brain and dysregulates the brain's physiological functions. Margolis and Altszuler are the first scientists who suggested that insulin can cross the blood-brain barrier (BBB) by showing the increased level of insulin in the cerebrospinal fluid of rats after peripheral infusion of insulin. Further, the results were confirmed in the dog that insulin crosses the BBB after intravenous administration of insulin. But no direct evidence was found that whether the insulin transport system and the insulin receptors protein are responsible for it [18,19].

1.2 Insulin action in the brain

All cell types in the brain express insulin receptors, however, the expression of these receptors varies between brain regions. Numerous animal studies indicate that the CA1, and CA3 olfactory bulb, entorhinal cortex, hypothalamus, and dentate gyrus regions of the hippocampus, as well as the cerebral cortex, striatum, and cerebellum, contain the higher expression of the insulin receptors. The extensive distribution of these receptors in the brain indicates that insulin signaling also serves a variety of crucial roles in brain signaling [17]. Alternatively, alterations in insulin signaling in the central nervous system (CNS) may accelerate brain aging, influence plasticity, and be involved in the process of neurodegeneration. Furthermore, the majority of insulin receptors are situated on neurons; they are abundantly expressed in the presynaptic axon terminal of synapses and comprise the postsynaptic density (PSD) [20].

The insulin receptor and the insulin-like growth factor 1 (IGF-1) receptor are broadly distributed in the brain and mediate the biological effects of insulin and IGF-1. Numerous molecules participate in insulin signaling cascades, which are known to play crucial roles in brain functioning [21]. PI3-K/AKT is important for metabolism and lipid and protein synthesis, whereas mitogen-activated protein kinase (MAPK) impacts cell proliferation, survival, and gene expression in the brain [22].

Furthermore, insulin signaling initiates with insulin binding to a tyrosine kinase receptor, which serves as a transmembrane insulin receptor and binds to IGF-1 which activates insulin receptors. The insulin receptors have two subunits i.e., α and β subunits. As insulin binds to the extracellular α -subunit of the insulin receptor, it promotes the dimerization of the intracellular β -subunit [23]. Through activation of intrinsic tyrosine kinases, the α -subunit stimulates autophosphorylation of tyrosine residues on the β -subunit. The auto phosphorylated β -subunit then phosphorylates tyrosine residues on a collection of adaptor proteins belonging to insulin receptor substrate (IRS) families 1 through 4 (IRS1-IRS4) which were expressed in the cerebral

cortex, and hypothalamus respectively [24]. IRSs classify insulin stimulation into diverse routes and deliver intracellular signals that mediate distinct functions. The activation of the insulin–IR–IRS–PI3-K–AKT pathway, controls the phosphorylation of numerous intracellular proteins, including serine/threonine-protein kinase mTOR (mammalian target of rapamycin), glycogen synthase kinase 3 (GSK-3), cAMP-responsive element-binding protein (CREB), filamin A, and nitric oxide synthetases [25].

Insulin resistance is a factor that contributes to the development of T2DM and seems to play a crucial role in cognitive dysfunctions such as impaired attention, motor speed, executive functioning, and verbal memory [26]. Thus, there is a huge possibility that peripheral insulin resistance may also be associated with brain insulin resistance which dysregulates these functions. An increasing amount of evidence suggests that neuronal integrity and functional changes are mediated by aberrant central insulin signaling [27–29]. The alteration in the signaling offers the framework for describing insulin's role in the origin, development, and therapy of several neurodegenerative diseases.

1.3 Brain insulin resistance & Neurodegeneration

Brain insulin resistance (BIR) is the lack of response by brain cells to insulin, which can occur due to multiple reasons ranging from reduction in the number of insulin receptors, the inability of the present receptors, and impairment in the activation of the insulin signaling cascade [30,31]. The dysfunction thus progresses into hampering brain metabolic processes and aggregation of plaques, shrinkage in the size of the hippocampus. The impairment in the cerebral metabolic processes has a disastrous impact on neuroplasticity and neurotransmitter functioning which leads to the seeding of inflammatory cascade [32]. All these alterations cause hampering of cognitive abilities and brain functions. The reduced glucose and energy availability to the brain leads to the development of a hypometabolic state in many areas of the brain which may further progress to atrophy of major neural areas, neuronal and synaptic disconnection [33]. These energy crisis states give birth to an oxidized redox environment, the dampened activity of enzymes, and continuous hyperactivity of inflammatory cascade all of this resulting in metabolic conflict in glycolytic glucose breakdown and pyruvate oxidation resulting in downregulation of oxygen and glucose supply and ceasing of blood flow to frontal and temporal regions of the brain resulting in synaptic dysfunctions [34].

The metabolic disorder which may lead to abnormalities linked to progressive brain insulin resistance with consequent impairment of central insulin signaling processes, accumulation of neurotoxins, neuronal stress, and resulting in a course of neurodegeneration is termed as “Type-3 diabetes mellitus” (T3DM)[23,29]. T3DM corresponds to chronic insulin resistance and

insulin deficiency state in the brain which leads to the progression of neurodegenerative disorders.

Neurodegeneration is an umbrella for the progressive loss of structure or function of neurons, including the death of neurons. Neurodegenerative diseases comprise one of the major public health concerns, mostly in our aging population. The consequences are very significant both in terms of pathology and the cost of caring for patients [35]. However, the causes of most neurodegenerative diseases remain unknown. Many neurodegenerative diseases including Alzheimer's (AD), Spinal muscular atrophy, Parkinson's disease (PD), Lewy body disease, Huntington's disease (HD), and amyotrophic lateral sclerosis (ALS) occur as a result of neurodegenerative processes [36]. Such diseases are incurable, resulting in progressive degeneration and/or death of neurons. The proper clinical diagnosis of neurodegenerative diseases is often difficult given the large overlap in signs and symptoms, although in more than 75% of cases, the clinical diagnosis is confirmed by post-mortem examination. As research progresses, many similarities appear that relate these diseases to one another on a sub-cellular level. Discovering these similarities offers hope for therapeutic advances that could ameliorate many diseases.

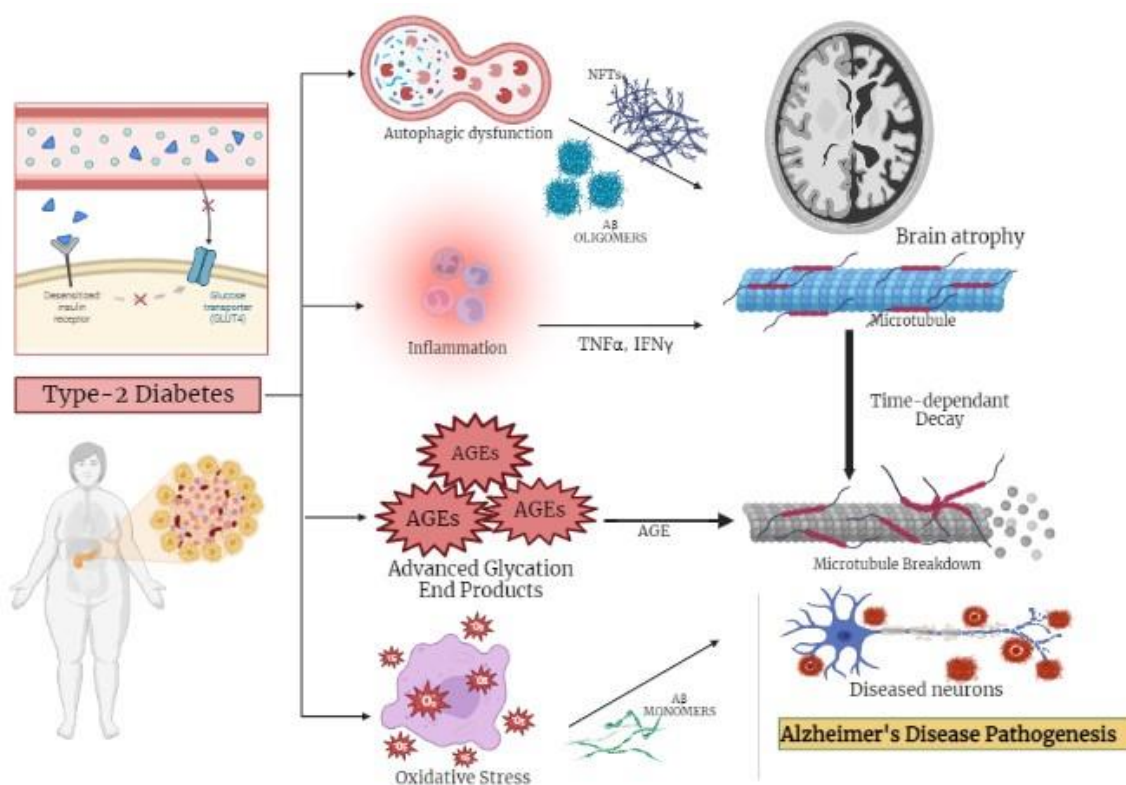


Fig.1.2: Illustration of links between T2DM and AD

Dementia is characterized by a decline in memory, language, problem-solving, and other cognitive skills that affect a person's ability to perform everyday activities. AD is the most common cause of dementia, followed by mixed AD and vascular dementia, Lewy body dementia, and frontotemporal dementia [37]. AD is a chronic and progressive neurodegenerative disease, which has been caused by protein misfolding, and accumulation of A β in the brain. AD accounts for 60 to 80 % of dementia cases and aging is considered as the greatest known risk factor for AD [38].

AD is one of the most commonly occurring neurodegenerative disorders which has an impact on the lives of aged patients. According to the Alzheimer Association, in 2022 it was observed that around 6.5 million Americans aged 65 and older are suffering from this debilitating disorder and seeing its accelerating occurrence. Moreover, this number is projected to rise to 65.7 million by 2030 [39]. The disorder is characterized by severe cortical atrophy and progressive loss of neurons due to the build-up of tau tangles intracellularly and β -amyloid plaques extracellularly. Several investigations have demonstrated a link between AD and impaired insulin signaling in the brain, suggesting that diminished insulin action may play a crucial role in the development of neurodegenerative disease [40,41]. In accordance with this, a clinical trial of intranasal insulin administration to AD patients showed a reduction in cognitive loss and Insulin therapy of cultured neurons can also prevent synaptic loss, a symptom of AD patients. In addition, the expression of GSK-3 is increased in the hippocampus region of AD patients and post-synaptosomal supernatants produced from the AD brain. In contrast, inhibition of GSK-3 attenuates APP processing and reduces neurodegeneration associated with hyperphosphorylated tau in AD[42,43].

Insulin signaling can attenuate the aggregation of amyloid- (A) fibrils and hyperphosphorylation of tau protein that causes amyloid plaques and helical neurofibrillary tangles, which are hallmarks of AD. A reduction in GSK3 phosphorylation could lead to Tau hyperphosphorylation. Increasing GSK-3 activation may also result in an increase in A production (due to an increase in presenilin 1 activity mediated by GSK-3) and demonstrated that GSK3 regulation may play a crucial role in the development of AD pathogenesis [44–46]. Additionally, treatment strategies for AD are still under extensive research. Nowadays, only symptomatic treatments exist and try to counterbalance the neurotransmitter disturbance by using cholinesterase inhibitors and N-methyl-D-aspartate (NMDA) receptor antagonists. To block the progression of the disease, therapeutic agents are supposed to interfere with the pathogenic steps responsible for the clinical symptoms, classically including the deposition of extracellular amyloid β plaques and intracellular neurofibrillary tangle formation.

Thus, there is an unmet need to identify newer molecular targets/mechanisms and novel approaches for the management of AD. Recently, comorbid condition including MetS linked with AD is also mounting at an alarming rate and has become a major health issue in developing and developed countries. Although, treatment options are available for the management of AD comorbid with MetS which can temporarily delay or reduce the symptoms of the disease. Moreover, repurposing of the existing clinical class of drugs such as Dipeptidyl Peptidase-4 (DPP-4) inhibitors, Sodium-glucose Cotransporter-2 (SGLT2) inhibitors, Meglitinide, etc have gained attention due to their anti-diabetic as well as neuroprotective effect. However, recent pre-clinical and clinical studies have indicated the benefits of the meglitinides class of drugs not only in DM but also in comorbid conditions like Parkinson's (PD) and Huntington's disease (HD).

1.4 Meglitinides

Meglitinides or glinides are the class of oral antidiabetic agents used in the treatment of T2DM. Meglitinides directly stimulate the release of insulin from pancreatic β cells and lower the blood glucose concentration [47]. Currently, two analogs are available for clinical use i.e., Repaglinide (REP) and Nateglinide. The chemical structures and mechanisms of these agents were different but the effect on early-phase insulin release is similar, with a rapid rise in insulin concentrations and a short half-life. Early trial evidence supports their effect in the reduction of postprandial glucose and reduction in hypoglycemic episodes.

REP is a carbamoyl methyl benzoic acid derivative approved in 1998 by the United States Food and Drug Administration (US-FDA) for Diabetes mellitus (DM) [48]. REP, a potent short-acting insulin secretagogue that acts by closing ATP-sensitive potassium (KATP) channels in the plasma membrane [49]. It acutely decreases blood glucose levels by stimulating the release of insulin from the β cells of the pancreas. REP closes the K-ATP channels on the plasma membrane and closure of the K channels depolarizes the β cells, resulting in the opening of calcium channels. The subsequent calcium influx was generated after the opening of channels and resulted in the stimulation of calcium-dependent exocytosis of insulin [50].

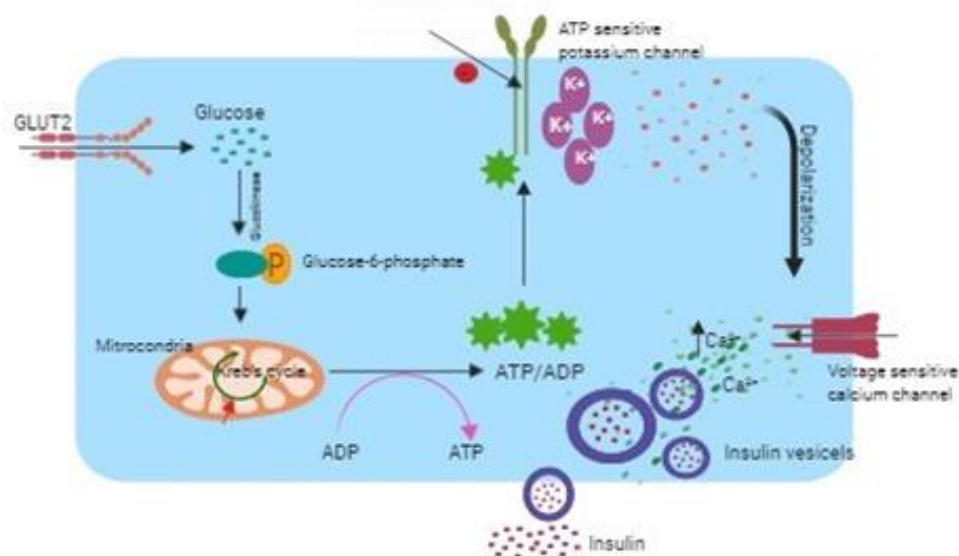


Fig. 1.3: Mode of action of repaglinide in peripheral (pancreatic cell)

REP belongs to non-sulfonylurea insulin secretagogues with a very quick onset and short duration of action. Theoretically, it reduces the incidence of hypoglycemic episodes by stimulating insulin in a glucose-sensitive fashion [51]. The majority of regularly used meglitinides are metabolized in the liver and primarily eliminated via the bile, apart from a small amount of the parent chemical that has been detected in the urine[52]. REP is currently marketed as PRANDIN by Novo Nordisk. PRANDIN tablets for oral administration and used as an adjunct to diet, and physical exercise to lower the blood glucose level in DM patients. Additionally, numerous reports suggest that REP exerted a neuroprotective effect in PD and HD. It observed that REP acts against kainic acid-induced neuronal cell death in the CA3 region of hippocampal and rotenone-induced PD [53]. Further, recent studies have reported that REP exerted a strong neuroprotective effect in HD which may possibly work via multiple intracellular channel modulators, maintaining calcium homeostasis, gene expression, and enzymatic activities, and targets neuronal calcium receptors by specifically attaching to them in a calcium-dependent manner [54]. Recent evidence also indicated that REP down-regulates the expression of downstream regulatory element antagonist modulator (DREAM), (a calcium-binding protein) that regulates calcium homeostasis and is involved in the pathogenesis of HD [55]. It has been reported that REP increases neuronal survival via upregulating activating transcription factors-6 (ATF6) gene (endoplasmic stress sensor) that may possibly work via activating autophagy and inhibiting endoplasmic stress-induced apoptosis along with inhibition of the DREAM. Thus, there is a huge possibility that REP regulates neurodegeneration via

modulating the necrotic and apoptotic cell death protein expression of pro-apoptotic protein, an anti-apoptotic protein, calcium homeostasis, and may eventually reduce neuronal cell death.

Moreover, reports also suggest that REP is rapidly absorbed from the gastrointestinal tract and results in the increment of plasma concentration. The peak plasma concentration level reaches within one hour after administration and represents a short half-life. Further, it was stated that the REP has poor pharmacokinetic characteristics such as low volume of distribution, 30 L (consistent with intracellular fluid distribution), high plasma protein binding (greater than 98 %), rapid metabolism, and low mean absolute bioavailability (53%).

Therefore, to circumvent the pharmacokinetic parameters and improve the efficacy of REP, the nanocarrier systems were explored using nanotechnology. Nanotechnology has revolutionized the field of drug delivery by offering promising solutions for the efficient and effective delivery of therapeutic agents. It has been widely acknowledged that conventional drug delivery systems face significant challenges such as non-specific distribution, low bioavailability, and adverse side effects. These limitations can be overcome by the development of nano-based drug delivery systems that offer several advantages over conventional treatments. One of the major advantages of nanotechnology in drug delivery is the ability to increase drug concentration at the desired site of action. Nanoparticles can be engineered to target specific cells or tissues and release the drug payload at the desired location. This targeted delivery system reduces the side effects associated with conventional treatments, which often result in the accumulation of the drug in non-targeted tissues. By selectively delivering drugs to the target site, the toxicity of the drug is minimized, and the therapeutic effectiveness is improved. Moreover, nanoparticle-based drug delivery systems exhibit a prolonged circulation time in the bloodstream, which enhances drug delivery and efficacy. The use of nanostructures permits the controlled release of drugs at the prescribed dose, enabling sustained drug release over an extended period. This controlled release system not only reduces the frequency of dosing but also ensures that the drug is delivered at the desired site for a more extended period, thereby improving the overall efficacy of the treatment. Another advantage of nano-based drug delivery systems is that they offer improved bioavailability. The small size of nanoparticles allows them to cross biological barriers such as the blood-brain barrier and deliver drugs to the target site, thereby improving the overall bioavailability of the drug. In addition, the high surface area to volume ratio of nanoparticles increases the drug loading capacity, which in turn enhances drug bioavailability.

Nanoparticles have emerged as a promising tool in drug delivery due to their ability to improve the pharmacokinetics and pharmacodynamics of therapeutic agents. They can be designed to carry drugs to specific target sites in the body, protect drugs from degradation or elimination, and control the release of drugs over time.

There are various types of nanoparticles used in drug delivery, Polymeric nanoparticles: These are nanoparticles composed of synthetic or natural polymers, such as poly (lactic-co-glycolic acid) (PLGA), polyethylene glycol (PEG), chitosan, and albumin. Polymeric nanoparticles can be designed to release drugs over a prolonged period and can be functionalized to target specific tissues or cells. Lipid-based nanoparticles: These include liposomes, solid lipid nanoparticles (SLNs), and nanostructured lipid carriers (NLCs). Lipid-based nanoparticles are composed of lipids and can carry hydrophobic or hydrophilic drugs. They are biocompatible, biodegradable, and can be functionalized to target specific tissues or cells. Dendrimers: These are highly branched, synthetic polymers with a defined molecular structure. Dendrimers can carry drugs in their interior and on their surface and can be functionalized to target specific tissues or cells. Overall, nanoparticles offer several advantages in drug delivery, such as improved drug solubility, bioavailability, and targeting, as well as reduced toxicity and side effects. With ongoing research and development, nanoparticles hold great potential to revolutionize the field of drug delivery and improve patient outcomes.

Table.1.1: List of PEGylated nanocarriers for the treatment of Alzheimer's disease.

S.No.	Drug	Formulation	Justification
1.	Memantine	PLGA-PEGylated Nanoparticles	<ul style="list-style-type: none"> • Sustained delivery of the drug into the target tissue • Improve learning capacities
2.	Memantine-HCL	PLGA-PEGylated Nano scaffolds	<ul style="list-style-type: none"> • Reduce level of pro-inflammatory cytokines • Improve permeation
3.	Si-RNA	PEGylated nanoparticles	<ul style="list-style-type: none"> • Maintain the Biological activity of the molecule • Increase stability and biocompatibility
4.	A β ₁₋₄₂ peptide	Polymeric nanoparticles	<ul style="list-style-type: none"> • Increase the blood half-life of the particles. • Increase the peptide adsorption onto the surf

2. Literature Review

2.1 Metabolic syndrome and associated risk factors

Metabolic processes ensure a continuous supply of energy and nutrition to all the body segments. It is defined as the total of all the biochemical reactions occurring in the body. Any disturbance in the normal metabolic mechanism leads to the development of serious pathophysiological complications known as MetS. MetS, also referred to as insulin resistance syndrome, comprises various complications that altogether elevate the risk of occurrence of coronary heart disease, diabetes, stroke, chronic kidney disease, and other serious complications. It can be easily diagnosed by several easily diagnosable signs like obesity, high blood pressure, high blood sugar levels, high blood triglycerides, and decreased HDL cholesterol [58]. MetS incorporate major disorders like obesity, atherogenic dyslipidemia, hypertension, diabetes mellitus, and prothrombotic and proinflammatory states. The key hallmarks of the MetS comprise leptin resistance, downregulated adiponectin level, insulin refractoriness, malfunctioning secretion of insulin, and glucose intolerance [59].

Due to the rapidly growing industrialization and urbanization, the instance of the occurrence of these disorders has increased with excessive fat intake and unhealthy lifestyle habits [14]. According to World Health Organization (WHO), the worldwide obesity index has tripled since 1975. However, in 2016, about 39% of adults aged 18 years or above were found to be overweight and 13% were obese. Worldwide, about 13% of adult people (11% men and 15% women) were found to be obese. In 2019. Around 38.2 million children under 5 years were overweight or obese [8].

2.2 MetS and T2DM

Out of all the metabolic syndromes involved, DM is the most common disorder, with about 422 million people suffering from T2DM, and 2 million deaths accredited to this deadly disorder. It is the prime cause of blindness, heart attacks, kidney failure, stroke, and lower limb amputation [12]. This widespread epidemic of metabolic disorders, especially DM, is attributed to genetic background, diet, exercise, and aging.

DM, as defined by American Diabetes Association “is a group of metabolic disorders characterized by hyperglycemia resulting from defects in insulin secretion, insulin action or both. The chronic hyperglycemia of diabetes is associated with long-term damage dysfunction and failure of different organs, especially the eyes, kidneys, nerves, heart, and blood vessels. DM is primarily classified into 2 types i.e., Type-1 Diabetes (T1DM)s, and Type-2 diabetes [60]. Multiple pathogenic processes are entangled in this pathogenic chain of progression of

diabetes ranging from the autoimmune destruction of pancreatic β -cells along with insulin deficiency to the flawed insulin activity which can occur due to the resistance developed to its action resulting in diminished tissue responses. As the disease continues to progress, insulin secretion is unable to modulate the glucose hemostasis leading to hyperglycemia.

T1DM occurs due to the autoimmune destruction of β -cells by the action of CD4⁺ and CD8⁺ Cells and macrophages entering the islets. All of this results in a shortage of insulin and thus leading to metabolic dysfunctions. The condition is further aggravated by excessive glucagon secretion which occurs due to abnormal pancreatic α -cells [61]. Moreover, T2DM is a consequence of the multitude of causative factors encompassing elevation in obesity, sedentary lifestyles, increased dietary calorie intake and aging population, genetic makeup, etc. However, in T2DM, the primary pathophysiological abnormalities involved are either downregulated insulin secretion occurring due to the malfunctioning of β -cells or the inability of the secreted insulin to downregulate the blood glucose level due to the insulin resistance [60,61]

In the presence of obesity, hyperlipidemia, or hyperglycemic conditions, the presence of a higher concentration of free fatty acids and glucose levels exposes β -cell to various stresses like inflammatory stress, oxidative stress, and amyloid stress predisposing them to lose their integrity. The presence of a surplus of free fatty acids and glucose triggers the apoptotic unfolded protein response pathways which ultimately give birth to ER stress and thus induce β -cell malfunction and cell death [62]. Metabolic and oxidative stress is induced due to obesity-related lipotoxicity, glucotoxicity and glucolipotoxicity further impairing β -cells [59,63]. Aggregation of misfolded proteins and islet amyloid polypeptides occurs as a result of prolonged high glucose concentration, leading to the accumulation of misfolded insulin and islet amyloid polypeptides and increased generation of protein-folding mediated reactive oxygen species. It also leads to modifications in the mobilization of calcium ions from ER which favored proapoptotic signals, aided in the degradation of proinsulin mRNA, and stimulated the release of IL-1, further aggravating local inflammation in islets [62,64]. Thus, all of this mix of pathogenic abnormalities progress to compromise in the integrity of islets, disrupted cell-to-cell communication within islets, impaired modulation of the balance between insulin and glucagon, defects in insulin synthesis and release, and ultimately hyperglycemia [64,65]. Although Diabetes and related disorders are well known to cause deleterious effects throughout the body like cardiovascular diseases, dyslipidemia, atherosclerosis, diabetic nephropathy, diabetic retinopathy, diabetic ketoacidosis, diabetic neuropathy, neurodegenerative diseases have now been added to this list.

2.3 MetS and Insulin

2.3.1 Formation of insulin and its action

The insulin is secreted by the β -cells as pre-proinsulin which undergoes maturation through some conformational modifications with the help of proteins in the endoplasmic reticulum (ER) and leads to the formation of proinsulin. The formed proinsulin is folded and three disulfide bonds are molded in the presence of various ER chaperone proteins [66]. The folded proinsulin is translocated to the Golgi apparatus where it resides in the immature secretory vesicles and divides into C-peptide and insulin [67]. Both of these substrates are stored in the secretory vesicles along with islet amyloid polypeptides (IAPP) and other products [68]. This conversion under normal circumstances completes before the secretion of insulin. However, in changed pathological conditions such as T2DM, insulinoma, or familial hyperproinsulinemia, elevated concentrations of split proinsulin have been detected which cause disturbance in the insulin formation and synthesis process [69]. Moreover, the formed insulin is stored in the vesicles until its release is triggered. The β -cells recognize any fluctuations in the blood glucose levels and in response to that the secretion of insulin will take place. Additionally, glucose transporter 2 (GLUT2) functions as the glucose sensor for the β -cells and simultaneously transports glucose inside β -cells where it is catabolized and as a result intracellular ATP/ADP ratio rises, triggering the closing of plasma membrane-localized ATP-dependent potassium channels which results in membrane depolarization and opening of calcium ion channels, facilitating the entry of calcium ions in the cell, rise in the ionic concentration inside cell further triggers the fusion of secretory vesicles carrying insulin with the plasma membrane, ultimately leading to insulin secretion [64,70].

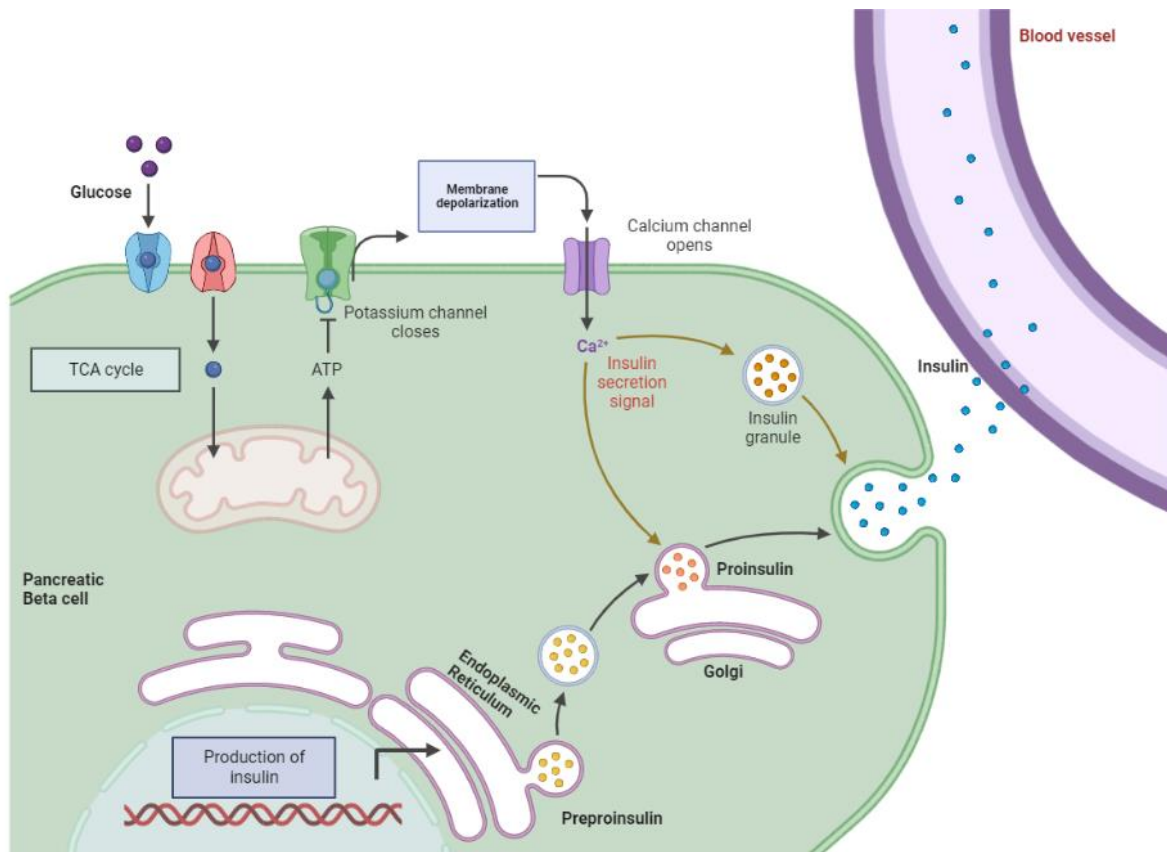


Fig.2.1: Insulin production pathway

2.3.2 Insulin receptors and insulin receptor substrate

The structure of insulin shows that there are a lot of amino acids that are involved in binding to the insulin receptor. The insulin receptor is a tetrameric glycoprotein found at the plasma membrane and made up of two extracellular α -subunits and two β -subunits as transmembrane subunits. Moreover, two isoforms of insulin receptors i.e., type A and type B exists, which bind to insulin and Insulin-like Growth Factor-1 (IGF-1) [71]. The insulin binds to its receptor, which is a dimer on the cell membrane and causes its tyrosine kinase activity to start phosphorylating. The insulin receptor can also form a heterodimer with the IGF-1 receptor and modulate the affinity for insulin of IGF-1 [72]. On the other hand, the phosphorylation of serine residues contributes to the regulation and control of the activity of the receptor, causing it to become internalized. The insulin receptor dimer can bind and phosphorylate several other proteins, activating a signaling cascade that regulates a variety of functions including cell growth, survival, and metabolism [73,74].

Additionally, Insulin Receptor Substrate (IRS) activates the recruits of insulin receptors and phosphorylates many substrates like Growth factor receptor-bound (Grb), Dedicator of Cytokinesis (Dock1), Casitas B-lineage lymphoma (Cbl), and adapter protein with Pleckstrin homology and Src homology 2 domains (APS) adaptor protein [75]. Moreover, IRS and Src

homology/collagen (Shc) are the two main substrates of insulin for activation through a phosphorylation cascade. Furthermore, the four known IRS proteins are also present i.e., IRS-1, IRS-2, IRS-3, and IRS-4. The IRS-1 and IRS-2 have widely overlapped tissue distribution while IRS-3 and IRS-4 are less characterized [76].

2.3.3 Insulin signaling pathways in the brain

Insulin initiates its activity by binding with the α -subunit of the receptor triggering the dimerization and autophosphorylation of the tyrosine residues at the β -subunits forming insulin receptor substrate (IRS-1 and IRS-2) [77,78]. Besides insulin, the insulin growth factor also binds to the insulin receptor which is also capable of inducing the response. This binding is maximum in areas like the cerebral cortex and hippocampus which are in charge of cognitive abilities and behavior [79]. The tyrosine kinase enzyme phosphorylates the tyrosine residues on the IRS-1 and IRS-2 substrate which further triggers its actions. Their actions encompass all the mechanisms crucial for the sustenance of life like modulation of glucose concentration, cellular calcium levels, neuronal survival and growth, functioning of neurotransmitters, and synaptic strength and neurogenesis [80].

2.3.3.1 PI3-AKT pathway

Insulin and IRS work majorly through 2 canonical pathways: PI3-Akt pathway and Ras/MAPK pathway. Phosphorylation of insulin receptors results in the phosphorylation of IRS-1, which then causes the phosphorylation of PI3K. PI3K modulates the conversion of PIP2 to PIP3, facilitating the inclusion of the pleckstrin homology (PH) domain to the membrane which contains proteins like AKT and PDK1. On reaching the membrane, phosphorylation of AKT by PDK1 and mTOR leads to its activation [81]. AKT is primarily the button for stimulating the insulin signaling cascade and protein kinase C ζ (PKC ζ) and PKC λ . AKT on being triggered, phosphorylates the substrate of TBC1D4, modulating the movement of GLUT4 receptors to the cell membrane for the uptake of glucose [77]. This PI3K/AKT signaling is primarily in charge of the functioning of metabolic processes including glucose translocation, utilization, energy metabolism, and neuronal survival [82]. It is also intricate in causing the phosphorylation of GSK-3 and gene transcription.

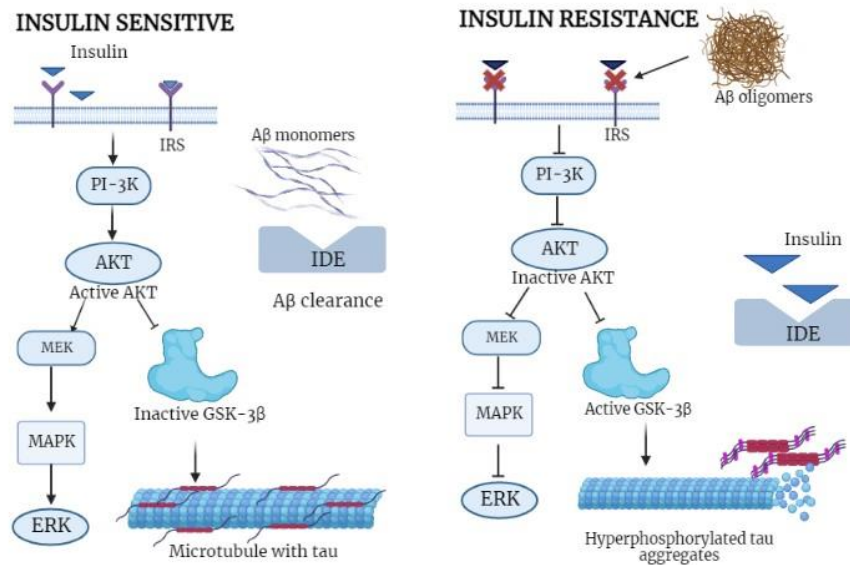


Fig.2.2: Neuronal signaling mechanism in a state of insulin sensitivity and insulin resistance.

2.3.3.2 Mitogen-activated protein kinase (MAPK)

The binding of insulin at the α -substrate of the receptor causes autophosphorylation at the β -subunit resulting in the triggering of guanine nucleotide exchange factor SOS causing the formation of GTP from GDP and causing activation of Ras. The Ras results in the activation of Raf stimulating Raf and then MEK followed by mitogen-activated protein kinase (MAPK)/ERK [81,83]. This MAPK signaling pathway is implicated in the processes like cell growth, proliferation, survival, and differentiation of cells. It is also known to modulate gene transcription by controlling the phosphorylation of various transcription factors. ERK being attached to the cAMP response element binding protein (CREB) activates the same and upregulates the transcription of genes playing a role in the survival of neurons [84]. p38 MAP kinase cascade is also intricately involved in the neuroinflammatory pathway. It is said to be entangled with major pathological features of AD-like excitotoxicity, synaptic plasticity, and phosphorylation of tau [85].

2.3.3.3 Mammalian target of rapamycin (mTOR)

The mammalian target of rapamycin (mTOR) falls in the PI3K pathway. Activation of the mTOR/FRAP pathway by PI3K tunes the phospholipase D resulting in hydrolysis of phosphatidylcholine and elevated concentrations of phosphatidic acid and diacylglycerol [86]. Insulin promotes the synthesis of proteins and halts their degradation by activating mTOR. mTOR has been identified to regulate the mammalian translation machinery by modulating phosphorylation, activating p70 ribosomal S6 kinase (p70^{rsk}), and causing phosphorylation of initiation factor 4E for eukaryotic translation (eIF-4E) inhibitor, PHAS1 or 4E-binding protein 1 [87,88]. p70^{rsk} initiates ribosomal biosynthesis by phosphorylating the ribosomal S6 protein

forming increased translation of mRNAs with a 58 terminal oligopyrimidine tract. mTOR phosphorylates PHAS-1 and causes its dissociation from eIF-2 allowing cap-dependent translation of mRNAs with the highly structured 58-untranslated region [88]. Activation of mTOR by AKT modulates protein and lipid synthesis and other aspects involved in cellular metabolism, growth, survival, and autophagy [77].

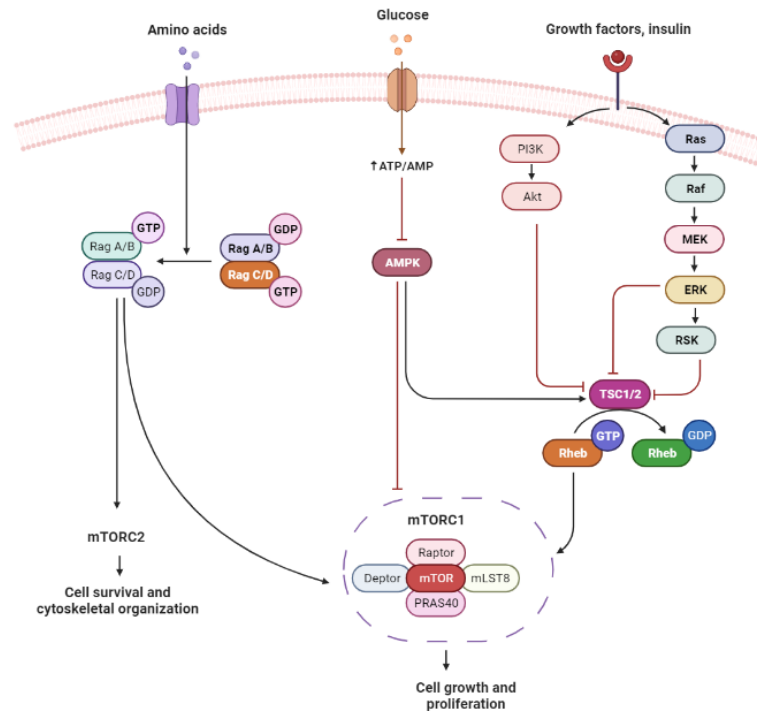


Fig.2.3: Mammalian target of rapamycin (mTOR) pathway

2.3.3.4 GSK-3 β

AKT phosphorylates GSK-3, and on being inactivated it metabolizes glucose. It also regulates the apoptotic process, cellular metabolic activities, and transcription factors aiding in cellular development and increasing neuronal life span [89]. The activation of the GSK-3 β isoform which besides being involved in glycogenesis, neurotrophic factor signaling, Wnt signaling, neurotransmitter signaling, and assembly of microtubules is also responsible for promoting tau phosphorylation, deposition of amyloid beta (A β) and microglia-mediated neuroinflammation when phosphorylated [89–91].

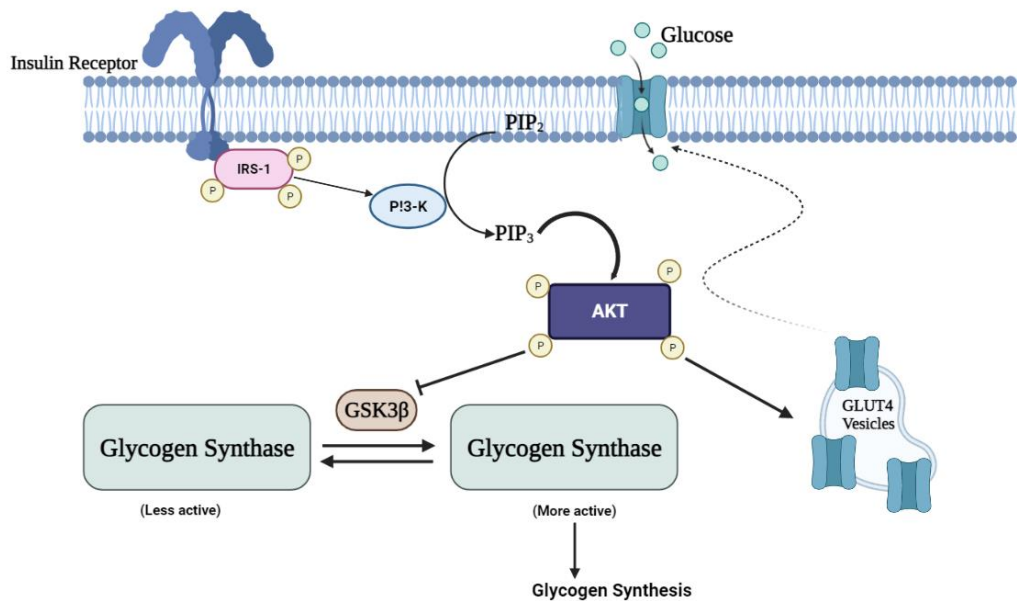


Fig.2.4: Regulation of GSK-3 β by insulin signalling pathway

2.3.3.5. Insulin and Glucose Transporter (GLUT) system

Insulin is the most potent anabolic physiological agent known to stimulate the storage and synthesis of lipids, proteins, carbohydrates, prevent their breakdown, and release into circulation [92]. The first step by which insulin enhances energy storage or use is the controlled transport of glucose into the cell, which is mediated by facilitative glucose transporters. There are 14 glucose transporter proteins encoded in the human genome (GLUT1-GLUT14) that catalyze hexose transport across cell membranes via an ATP-independent, facilitative diffusion mechanism [93]. GLUT2 and GLUT4 are the most extensively researched and crucial glucose transporters for glucose homeostasis. GLUT2 is expressed in the liver, gut, kidney, and pancreatic islet -cells, as well as in the central nervous system's neurons and astrocytes. GLUT2 is necessary for pancreatic cells for glucose-stimulated insulin release. In contrast, GLUT4 is highly expressed in adipose tissue and skeletal muscle; however, these tissues also express a select group of additional transporters [94]. In the absence of insulin or other stimuli, GLUT4 is predominantly intracellular but is rapidly redistributed to the plasma membrane in response to these stimuli. Transgenic mice that express large amounts of GLUT4 in adipose tissue or skeletal muscle are highly insulin-sensitive and glucose tolerant. On the other hand, conditional depletion of GLUT4 in either adipose tissue or skeletal muscle results in insulin resistance and a similar incidence of diabetic animals[95]. In accordance with these findings, it has been revealed that the expression of GLUT4 in the skeletal muscle of T2DM patients is dramatically decreased, indicating that these patients have a diminished capacity to handle glucose [96].

2.3.3.6 Insulin degrading enzyme (IDE)

The IDE, a metalloproteinase secreted by microglia and serves as a common pathway for breaking down insulin and A β . The overexpression of IDE results in the shortage of insulin availability and mutations in the IDE gene leads to a significant elevation in serum insulin levels.

In the late 1940s, it is reported that the IDE have the ability to break down insulin and degrades insulin into inactive fragments. In IDE-deficient mice, insulin breakdown was reduced, and hyperinsulinemia was observed [97]. Furthermore, employing silencing RNA (Ribonucleic acid) to reduce the amounts of human IDE in HepG2 cell-line cultured cells decreased insulin breakdown by up to 76% [98]. Surprisingly, while IDE plays a crucial role in insulin homeostasis, insulin also helps to maintain IDE levels. Insulin treatment of primary hippocampal neurons increased IDE protein levels by 25%, potentially via a feedback mechanism [99]. Despite its affinity for insulin, IDE has been linked to the breakdown of other amyloidogenic peptides. Human cerebrospinal fluid has been found to contain IDE (CSF). Its activity and levels have been discovered to be lower in AD brain tissue, and it is linked to higher A levels [100]. Furthermore, the enzymatic activity of IDE from diverse rat tissues was ranked in the following order: liver > pancreas > kidney > testis > adrenal gland > spleen > ovary > lung > heart > muscle > brain > fat. Furthermore, IDE is not the only enzyme involved in insulin degradation; cathepsin D has also been found to engage in lysosomal insulin degradation [101].

2.3.3.7 Insulin resistance and its possible mechanisms

Insulin resistance is a condition in which cells have a diminished ability to respond to insulin, resulting in a biological effect that is less than expected for a given dose of insulin. Insulin-resistant people require more insulin than normal to maintain normal blood glucose levels (hyperinsulinemia). The majority of insulin-resistant people avoid developing substantial hyperglycaemia through compensatory hyperinsulinemia [102,103]. In a vicious loop, the more insulin generated to lower blood sugar, the greater the insulin resistance. Furthermore, the combination of insulin resistance and hyperinsulinemia considerably enhances the occurrence of the insulin resistance syndrome's closely associated anomalies and clinical diagnoses [102]. Obesity, glucose intolerance, diabetes, hypertension, dyslipidaemia, metabolic syndrome, cardiovascular diseases, and possibly neurodegenerative diseases are all examples of insulin resistance syndrome [104–107].

Insulin resistance is thought to occur at the cellular level in the majority of instances due to post-receptor abnormalities in insulin signaling. Although promising results in animals for a

variety of insulin signaling abnormalities, their significance to human insulin resistance is currently unknown. Down-regulation, inadequacies, or genetic polymorphisms in tyrosine phosphorylation of the insulin receptor, IRS proteins, or PIP-3 kinase are possible pathways, as are GLUT 4 function problems[108].

2.4 Brain insulin resistance (BIR) and Neurodegeneration

Brain insulin resistance is the lack of response by brain cells to the insulin which can occur due to multiple reasons ranging from reduction in the number of insulin receptors, the inability of the present receptors to bind to the secreted insulin to impaired activation of the insulin signaling cascade [30,77]. The dysfunction thus progresses into hampering brain metabolic processes and aggregation of plaques, shrinkage in the size of the hippocampus. The impairment in the cerebral metabolic processes has a disastrous impact on neuroplasticity, and neurotransmitter functioning and thus leads to the seeding of the inflammatory cascade. All these alterations cause hampering of cognitive abilities and mood [78,109]. The reduced glucose and energy availability to the brain leads to the development of a hypometabolic state in many areas of the brain which may further progress to atrophy of major neural areas and neuronal and synaptic disconnection [110]. These energy crisis states give birth to an oxidized redox environment, the dampened activity of respiratory chain enzymes, and continuous hyperactivity of inflammatory cascade all of this resulting in metabolic conflict in glycolytic glucose breakdown and pyruvate oxidation resulting in downregulation of oxygen and glucose supply and ceasing of blood flow to frontal and temporal regions of the brain resulting in synaptic dysfunction [111–113].

Several research reports have found cognitive impairments in patients with DM since the 1920s implemented neurodegeneration [114]. Multiple studies have reported the presence of such severe memory deficits in patients with elevated hemoglobin A1c concentrations [115,116]. Fludeoxyglucose F-18-positron emission tomography (FDG-PET) studies have also highlighted the association of insulin resistance with the reduction in cerebral glucose metabolic rate in the posterior cingulate, precuneus, paired to temporal and frontal cortex regions of the pattern which are primarily important for memory and cognition. Identical patterns were also observed in the subjects carrying the apolipoprotein E ϵ 4 allele (APOE ϵ 4) which is the major AD risk factor [117,118]. A higher concentration of insulin in the circulation hampers the BBB by decreasing the endothelial insulin receptors and reducing the BBB permeability to insulin. Thus, reduced insulin concentrations of insulin were found in the CSF of people with insulin resistance. This directly implicates the reduced concentration of insulin in the brain and hence reduced neural and glial activity and impaired neuronal integrity [119].

Modulation of permeability by T2DM predisposes it to severe damage by facilitating the entry of other prohibited toxic substances [120,121].

2.4.1 BIR and AD

Many researchers have signaled the role of insulin in the progression of neurodegenerative diseases by various mechanisms which include aggravating the disease-specific pathological lesions and also enhancing the vulnerability of neurons to neurodegeneration [107]. It has been known to enhance AD pathological features like an aggregation of β -amyloid plaques, tau tangles, and α -synuclein lesions [106]. Studies have also highlighted the consistency in the brain changes associated with T2DM and AD [122]. Moreover, western immunoblot analysis found upregulated IGF-1R levels surrounding and within amyloid- β plaques and downregulated IGF-1-binding protein-2 in AD temporal cortex. Notably decreased IRS-1 and 2 levels were observed in AD neurons, in connection to upregulated levels of inactivated phospho^{Ser312}IRS-1 and phospho^{Ser616}IRS-1 and phosphoserine epitopes colocalized strongly with the NFTs signaling the impairment of IGF-1R and IR signaling in AD brain [123,124]. Impaired insulin signaling pathways are also involved in cognitive impairment like PI3K activation is connected to the LTP expression in the hippocampal region CA1 [125], and dentate gyrus [126]. Inhibition of PI3K has been implicated in impaired passive avoidance and spatial learning [127]. Insulin also affects learning and memory by modulating the ion channels and neurotransmitter receptors. It primarily regulates the synthesis and activity of neurotransmitters involved in memory and cognition like acetylcholine [128] and norepinephrine [129].

AD and T2DM share a whole lot of pathophysiological features due to which Alzheimer's disease is sometimes also referred to as type-3 diabetes mellitus (T3DM) [130]. Some of the identical features include deposits of A β plaques and fibrils in AD which is quite similar to the deposits of IAPP in pancreatic islets which also forms agglomerates and fibers as diabetes worsens [131]. The presence of oxidative stress and excessive ROS leads to the accumulation of glycated A β and tau which is akin to the buildup of advanced glycation end products and their receptors (RAGE) in kidney, retina, and atherosclerotic plaques in subjects suffering from diabetes [59,132–134]. Other shared pathological features encompass synaptic dysfunction, impaired autophagy, and excessive inflammation [34].

2.5 Pathological mechanisms in AD

One of the most commonly occurring neurodegenerative disorders, Alzheimer's dementia has impacted the lives of about 1 in 9 Americans aged 65 and older. Around 6.5 million Americans

aged 65 and older are suffering from this debilitating disorder and seeing its accelerating occurrence, this number is projected to rise to 65.7 million by 2030 [135]. The disorder is characterized by severe cortical atrophy and progressive loss of neurons due to the build-up of tau tangles intracellularly and β -amyloid plaques extracellularly [133,136,137]. The mitochondrial dysfunction and oxidative stress associated with the disease pathology led to an imbalance in the normal ionic concentrations and an increase in the ROS which further aggravates the pathology.

2.5.1 Deposition of A β plaques and tau tangles

A β , being the primary pathological marker of AD is formed from APP when it is proteolytically cleaved by β and γ -secretase. The elevated accumulation of A β in the AD brain occurs as a result of impaired clearance and increased formation of A β [138,139]. Hyperinsulinemia also elevates the susceptibility to AD by playing a part in A β toxicity. The Insulin degrading enzyme (IDE) is mainly responsible for degrading A β and it was found to be the prime modulator of A β in neuronal and microglial cells. Due to the hyperinsulinemia conditions prevalent in T2DM, the presence of a high concentration of peripheral insulin dampens the degradation of A β by serving as a competitive substrate for the enzyme [140,141]. The mice with deleted IDE genes served showed 50% downregulation in the clearance of A β as well as an increase in the cerebral accumulation of the plaques. Insulin also plays a role in APP transportation and metabolism [97] as it is known to reduce the intracellular accumulation of A β PP significantly by increasing its transportation from the trans-Golgi network which is its site of generation to the plasma membrane, hence increasing its extracellular secretion and also by downregulating its degradation by IDE [142]. The [C-11] Pittsburgh compound B (PiB) positron emission tomography study also investigated asymptomatic, late middle-aged adults from Wisconsin Registry for Alzheimer's prevention and postulated that insulin resistance is directly related to increased PiB uptake in frontal and temporal areas signifying higher amyloid deposition [143]. Many studies found the intranasal administration of insulin to be effective in restoring insulin signaling, elevating the concentration of synaptic proteins, and decreasing A β concentration and microglia activation in 3xTg-AD mice brains [144]. Another study also evidenced the effect of insulin in decreasing the toxic effects of Dutch mutation (DA β_{1-40}) on human brain pericytes in a dose-dependent manner [145].

Likewise, the aggregation of A β is also found to hamper insulin signaling by competing with it for binding and decreasing its affinity to its receptors [141]. Also, it dampens the neuronal transmission of insulin-stimulated signals by desensitizing and downregulating the insulin surface receptors. The intracellular A β PP causes direct disturbance in the PI3K activation of

Akt, resulting in hampered survival signaling, and upregulated GSK-3 β leading to increased tau hyperphosphorylation tau [42].

Insulin was found to be accumulated in the form of oligomers in hyperphosphorylated tau-bearing neurons in AD. The intraneuronal agglomeration of insulin was found to be directly dependent on tau hyperphosphorylation and follows tauopathy progression [146]. Tau was found to be a significant modulator of insulin signaling. Tau functions as a scaffolding protein and interacts with many components involved in the insulin signaling pathway. It was found to bind to the Src homology 3 (SH3) domain of the Src family tyrosine kinases which consists of the p85 α subunit and PI3K, which is a key component in the insulin signaling cascade [147]. Tau was found to bind to the phosphatase and tensin homolog protein (PTEN), which is a negative regulator. The insulin transduction aided in the dephosphorylation of PIP3 (phosphatidylinositol-3,4,5-triphosphate) to form PIP2 (phosphatidylinositol-4,5-diphosphate) and helps in its downregulation and favors insulin signaling [148,149]. The regulatory function of tau in insulin signaling was also confirmed by the study where deletion of tau resulted in hampered hippocampal response to insulin due to changes in the activities of IRS-1 and PTEN [148]. However, the pathological forms of tau developed due to hyperphosphorylation could lead to loss of proper functioning of tau protein resulting in disturbance in insulin signaling and development of brain insulin resistance [148]. Kuga et al. investigated the age-related changes in the hippocampus of middle-aged rats (17 months) and found the elevation in tau phosphorylation, A β content, PTP-1B, and dampened phosphorylation of IRS-1, Akt, GSK-3 β , mTOR, and TrkB contributing to the development of IR and AD onset [150]. On one hand, short-term exposure resulted in rapid hyperphosphorylation of tau at several Ser/Thr residues in human neuroblastoma cells or rat primary cortical neurons whereas prolonged exposure led to reduced phosphorylation [151,152].

IR has been evidenced as a significant connecting link between the A β and tau pathologies. Dependence of temporal-parietal areas of the brain on glycolysis leads to lactate release which is associated with elevated interstitial A β oligomer formation. The A β agglomeration aids in Ser phosphorylation of IRS-1, dampening the downstream insulin signaling and IR as a result of it which further aggravates A β plaque deposition. Chronic insulin resistance also promotes tau hyperphosphorylation leading to the deposition of Neurofibrillary tangles in different regions than A β and together all of these interlinked pathologies worsen the AD progression [153].

2.5.2 Mitochondrial and Endoplasmic reticulum stress leading to AD

Mitochondrial dysfunction, oxidative stress, and inflammation are other bridges between deadly disorders. Mitochondrial dysfunction and oxidative stress are pivotal processes underlying the progression of AD pathologies and their interaction with all causative factors [133]. Reduction in proper mitochondrial functioning is found to be directly influenced by insulin concentration. Mitochondrial impairment or mutations in mtDNA leads to disastrous repercussions which encompass alterations in the β -oxidation pathway, modifications in ATP productions due to variations in oxidative phosphorylation complexes, and upregulated ROS release. It is known to be disastrous to the cell's metabolism and tissues involved and interferes with their proper functioning due to aggravated tissue inflammation which is the main feature of AD and T2D [154]. The alterations in the mitochondrial function were also validated when the isolated brain mitochondria, cerebral cortex homogenates, wild-type hippocampus, triple transgenic AD, and T2D mice were investigated and a notable reduction in the mitochondrial respiration, membrane potential, and energy levels was observed. The study also found a significant reduction in autophagy-related protein 7 (ATG7) and glycosylated lysosomal membrane protein 1 (LAMP1) concentration in the cerebral cortex and hippocampus of T2D and 3xTg-AD mice. Reduced concentrations of nuclear respiratory factor 1 (NRF1) and NRF2 are found in both brain regions of T2D and 3xTg mice along with the downregulated mitochondrial encoded nicotinamide adenine dinucleotide dehydrogenase subunit 1 (ND1) and postsynaptic density protein 95 (PSD95) and synaptosomal-associated protein (SNAP25) in the hippocampus of T2D and 3xTg mice validate the impairment in mitochondrial function, biogenesis and autophagy in AD and T2D [155].

T2DM is associated with inherited or acquired downregulation of mitochondrial oxidative phosphorylation capacity, reduced ADP-stimulated oxidative phosphorylation, mitochondrial plasticity, and reduced mitochondrial content in skeletal muscle cells and hepatocytes. The developed insulin resistance is related to the decrease in insulin-triggered mitochondrial activity due to the blunted mitochondrial plasticity. Mitochondrial abnormalities are speculated to speed up the progression of insulin resistance and organ dysfunction by increased release of reactive oxygen species [156]. Mitochondria's role was also demonstrated in the modulation of insulin via IDE.

Additionally, the catabolic degradation of the abnormal and misfolded proteins and parts of damaged organelles is a common feature observed in AD as well as T2DM [157]. In AD, aggregation of amyloid plaques and tau tangles led to autophagy dysfunction and downregulation of gene expressions [136]. However, the involvement of autophagy

impairment is also witnessed in diabetes and is speculated that it results in its progression into subsequent neurodegeneration [158]. Another proof of the involvement of impaired autophagy in T2D comes from the disturbance in the P13K/mTOR pathway which is involved in autophagy modulation [157].

Moreover, the Endoplasmic reticulum (ER) combats the unfolded proteins accumulated in the lumen by initiating 3 different intracellular signaling cascades. The developed ER stress aggravates obesity and diabetes pathology, which are dangerous risk factors for AD and hasten the progression of AD. One of the studies, suggested the triggering of presenilin-1 by ER stress by activating the transcription factor 4 (ATF4) and thus elevating the A β secretion by γ -secretase which was halted by quercetin by altering the UPR signaling [159]. ER stress arising as a result of diabetes, plays a pivotal role in aggravating insulin resistance by modulating the oxygen-regulated protein 150 (ORP150) expression, which is a molecular chaperone safeguarding against ER stress [104].

Disruption in the communication links between the ER and mitochondria known as mitochondria-associated ER membranes (MAMs) stems from obesity-related mitochondrial dysfunction. The obesity-like conditions result in the elevation of calcium overload, oxidative stress, and reduced mitochondrial oxidative capacity. [160]. ER stress also arises due to the aggregation of AGEs which further leads to the initiation of multiple disease pathologies. In order to keep the misfolded protein in their foldable states and to check the release of 3 UPR mediators, including inositol-requiring enzyme alpha-1 (IRE1), PERK, ATF6 during ER stress, GRP78 collaborates with abnormal protein aggregates [161]. Under conditions of persistent ER stress, the PERK/eIF2/ATF4 axis triggers the transcription of genes involved in cell death resulting in CHOP protein [162].

Moreover, there are currently no medications that can cure, or halt disease progression. Cholinesterase inhibitors (ChEIs) and N-methyl-D aspartate (NMDA) receptor antagonists are the only approved treatments for AD. Memantine, the sole antagonist of NMDA receptors, that can be administered in both ways as a monotherapy and as an adjuvant to ChEIs. The ChEIs (donepezil, rivastigmine, galantamine, and tacrine) are indicated for mild to moderate AD; only donepezil is approved for the severe stage. These drugs reversibly bind the enzyme acetylcholinesterase and increased the quantities of the neurotransmitter acetylcholine, which is involved in cognition, learning, memory, and other cognitive processes. Although tacrine is accessible, it is not advised due to its significant risk for hepatotoxicity and medication interactions (cytochrome P450), which necessitate frequent monitoring. Although these

treatments can temporarily alleviate symptoms, they cannot alter the progression of the disease. As the disease progresses and more neurons are destroyed, the treatments become less effective. To improve the prognosis of neurodegenerative illnesses, novel therapeutic techniques, such as neuroprotection and neuro restoration, are required. In clinical trials registered with clinicaltrials.gov, a National Institutes of Health record of publicly and privately financed clinical studies, 244 anti-medicine Alzheimer's were evaluated between 2002 and 2012. Among the 244 medicines, only one (memantine) successfully completed clinical trials and went on to earn FDA clearance. Many variables, including the high expense of drug research, the relatively long period required to observe if an investigational treatment changes disease progression, and the BBB-protected structure of the brain, contribute to the difficulty of creating effective treatments for AD.

2.5 Meglitinide class of anti-diabetic drug

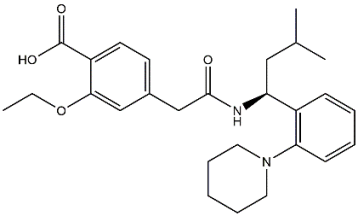
The class of oral anti-diabetic medications i.e., meglitinides or glinides is used to treat T2DM and is also known as an insulin secretagogue. Meglitinides reduce blood glucose levels by directly stimulating the release of insulin from pancreatic cells via the closing of potassium channels [30]. Further, repaglinide (REP) and nateglinide are the two analogs of meglitinides that are available for clinical usage. Although these drugs' chemical compositions and processes differ, their effects on the early phase of insulin release are comparable, with a sharp spike in insulin concentrations. Moreover, early trial data support their role in lowering postprandial glucose and lowering episodes of hypoglycemia.

2.5.1 Repaglinide

REP is a carbamoyl methyl benzoic acid derivative approved in 1998 by the United States Food and Drug Administration (US-FDA) for Diabetes mellitus (DM) [48]. REP, a potent short-acting insulin secretagogue that acts by closing ATP-sensitive potassium (KATP) channels in the plasma membrane [49]. REP is currently marketed as PRANDIN by Novo Nordisk. PRANDIN tablets for oral administration and used as an adjunct to diet, and physical exercise to lower the blood glucose level in DM patients. Nowadays, REP is marketed as an oral tablet under numerous brand names such as Prandin, Eurepa, Novonorm, Rapilin, Regan, and Repide with a daily repeated dosage of 0.5-2 mg

2.5.2 Properties of REP

General Name : Repaglinide
IUPAC Name : 2-ethoxy-4-({[(1S)-3-methyl-1-[2-(piperidin-1yl)phenyl] butyl] carbamoyl} methyl) benzoic acid

CAS registry number	: 135062-02-1
Empirical Formula	: C ₂₇ H ₃₆ N ₂ O ₄
Structure	: 
Molecular weight	: 452.6 g/mol
Therapeutic class	: Meglitinide class of Anti-diabetic drugs
Appearance	: White to off-white powder
Solubility	: Less soluble in water
Melting point	: 130 °C
pKa	: 3.68
Partition coefficient (Log P)	: 5.9
BCS Classification	: Class II
Proprietary names	: Prandin, Novonorm, Enyglid
Marketed as	: 0.5 mg, 1mg, 2mg film-coated tablets, and 0.5 mg capsules

2.5.3 Therapeutic indications and dosage of REP

REP is a member of the Meglitinides class of non-sulfonylurea insulin secretagogues with a very quick onset and short duration of action. Theoretically, it reduces the incidence of hypoglycemic episodes by stimulating insulin in a glucose-sensitive fashion[51]. The majority of regularly used meglitinides are metabolized in the liver and primarily eliminated via the bile, apart from a small amount of the parent chemical that has been detected in the urine. REP is intended for individuals with type 2 diabetes whose hyperglycemia is no longer adequately controlled by diet and exercise. Additional REP negatively affects respiratory tract infections and headaches. In Europe, REP is contraindicated in patients with severe liver dysfunction, and not recommended for patients over the age of 75[163].

2.5.4 REP and Neuroprotection

REP is a short-acting insulin secretagogue. It acutely decreases blood glucose levels by stimulating the release of insulin from the β cells of the pancreas. REP closes the ATP-sensitive potassium (K-ATP) channels on the plasma membrane and closure of the K channels depolarizes the β cells, resulting in the opening of calcium channels. The subsequent calcium

influx was generated after the opening of channels and resulted in the stimulation of calcium-dependent exocytosis of insulin [50]. Various reports suggest that REP exerted a neuroprotective effect on PD and HD. It observed that REP acts against kainic acid-induced neuronal cell death in the CA3 region of hippocampal and rotenone-induced PD. Further, recent studies have reported that REP exerted a strong neuroprotective effect in HD which may possibly work via multiple intracellular channel modulators, maintaining calcium homeostasis, gene expression, and enzymatic activities, and targets neuronal calcium receptors by specifically attaching to them in a calcium-dependent manner. Recent evidence also indicated that REP down-regulates the expression of downstream regulatory element antagonist modulator (DREAM), (a calcium-binding protein) that regulates calcium homeostasis and is involved in the pathogenesis of HD and AD. It has been reported that REP increases neuronal survival via upregulating activating transcription factors-6 (ATF6) gene (endoplasmic stress sensor) that may possibly work via activating autophagy and inhibiting endoplasmic stress-induced apoptosis along with inhibition of the DREAM. Thus, there is a huge possibility that REP regulates neurodegeneration via modulating the necrotic and apoptotic cell death protein expression of pro-apoptotic protein, an anti-apoptotic protein, calcium homeostasis, and may eventually reduce neuronal cell death.

2.5.5 Problems associated with REP

REP is rapidly absorbed from the gastrointestinal tract and results in an increment of plasma concentration. The peak plasma concentration level reaches within one hour after administration. The pharmacokinetics of REP was characterized by a mean absolute bioavailability of 53%. In clinical trials, the pharmacokinetic parameters of REP were characterized by a low volume of distribution, 30 L (consistent with intracellular fluid distribution), and high plasma protein binding (greater than 98 %). REP is rapidly and completely metabolized after intravenous or oral administration via oxidative biotransformation and direct conjugation with glucuronic acid[164]. The CYP2C8 and CYP3A4 are two isoenzymes which mainly involve the dealkylation and oxidation of REP to the dicarboxylic acid (M2) and aromatic amine (M1) metabolite. REP is mainly excreted in the bile and faces along with its metabolites, and no metabolites have been observed with significant hypoglycemic effects[165].

The exposure of REP is elevated in patients with hepatic insufficiency and elderly patients with T2DM. The pharmacokinetic parameters such as the area under the curve (AUC) were increased by 9.7-folds in patients with hepatic insufficiency compared to healthy volunteers whereas, in the elderly T2DM patients, a 3.7-fold increment was observed. A significant 2-fold

increase in half-life ($t_{1/2}$) was observed as compared to patients with normal renal function after a 5-day treatment of REP (2 mg x 3/day)[166].

2.5.6 REP interactions with another drug

REP is metabolized by CYP2C8 and CYP3A4 enzymes, therefore drugs that are inhibitors and/or inducers of these CYP isoenzymes may change their pharmacokinetics. Thus, various drugs are involved to affect the pharmacokinetics of REP and should be considered when delivering together[167]. The followings are some drugs that substantially change the pharmacokinetic parameters when co-administered with the REP (Table.2.1).

Table 2.1: The effect of other drugs on C_{max} and AUC of Repaglinide

Drug	CYP inhibitor/inducer	Dose strength (mg)	Dosing	Pharmacokinetic parameter impairment	
				C_{max}	AUC
Cyclosporine	-	-	100mg BID	1.8-fold ↑	2.5 fold ↑
Fenofibrate	-	-	200 mg QD	0%	0%
Itraconazole	inhibit CYP3A4	-	100 mg BID	1.5 fold ↑	1.4 fold ↑
Ketoconazole	inhibit CYP3A4	2	200 mg QD	16% ↑	15% ↑
Nifedipine	-	2	10 mg TID	0%	0%
Clarithromycin	inhibit CYP2C8	-	250 mg BID	40% ↑	67% ↑
Clopidogrel	-	0.25	300 mg (day1) 75 mg QD (Day 2-3)	1.3 fold ↑	2.9 fold ↑
Deferasirox	-	0.5	30 mg/kg QD	62% ↑	2.3 fold ↑
Rifampin	induce CYP3A4 and/or CYP2C8	4	For 4 days 600 mg QD for 6-7 days	17-79% ↓	32-80% ↓
Simvastatin	-	2	20 mg QD for 4 days	26% ↑	0% ↑
Trimethoprim	CYP2C8	-	160 mg BID for 2 days 160 mg QD for 1 day	41% ↑	61% ↑
Gemfibrozil + Itraconazole	-	-	Gem: 600mg BID for 3 days Itra: 100mg BID for 3 days	2.8 fold ↑	1.9 fold ↑

Therefore, to circumvent these issues nanocarrier systems were used, as nanotechnology offers multiple benefits in treating or managing the disease by site-specific and target-oriented delivery of precise active pharmaceutical ingredients.

2.6 Nanocarrier systems

Nowadays, nanotechnology showed a bridge to the barrier of biological and physical sciences by applying nanostructures and nanophases; particularly in nanomedicine and nano-based drug delivery systems [168]. Nanomedicines have achieved popularity as a result of their ability to encapsulate medications or bind therapeutic chemicals to nanostructures and deliver them to target tissues more accurately with a controlled release [56]. Nanostructures permit the release of integrated drugs at the prescribed dose since they persist in the circulatory system for a prolonged time [57]. A significant number of nanostructured systems have been approved by FDA or European Medical Agency (EMA) that are in the clinic to treat or diagnose several diseases [169].

PEGylated nanoparticle-based drug delivery systems offer several fundamental advantages in comparison to conventional treatments, which often exhibit a longer circulation duration, lower toxicity, specifically targeted release, and improved bioavailability. The enormous potential of nanoparticulate systems, in synergy with new developments in the discovery of novel functional molecules, can improve the treatment. PEGylated nanoparticle-based drug delivery systems have emerged as a promising approach for targeted drug delivery due to their unique physicochemical properties and biocompatibility. PEGylation refers to the attachment of polyethylene glycol (PEG) to the surface of nanoparticles, which has been shown to improve their pharmacokinetics and biodistribution.

The use of PEGylated nanoparticles for drug delivery has several advantages over traditional drug delivery methods. Primarily, PEGylation can increase the circulation time of nanoparticles in the bloodstream, which allows for more efficient drug delivery to the target site. Second, PEGylation can reduce the toxicity and immunogenicity of nanoparticles, as well as prevent their clearance by the reticuloendothelial system (RES). It can also improve the solubility and stability of hydrophobic drugs, allowing for their efficient delivery to the target site.

Several types of PEGylated nanoparticles have been developed for drug delivery, including liposomes, dendrimers, and polymeric nanoparticles. Liposomes are spherical vesicles composed of a lipid bilayer that can encapsulate hydrophilic and hydrophobic drugs. PEGylated liposomes have been used for the delivery of a wide range of drugs, including

anticancer agents, antibiotics, and immunosuppressants. Dendrimers are highly branched macromolecules that can be synthesized with precise molecular weight and size. PEGylated dendrimers have been shown to have excellent biocompatibility and low toxicity, making them attractive candidates for drug delivery. Polymeric nanoparticles are composed of biocompatible polymers that can encapsulate drugs and release them in a controlled manner. PEGylated polymeric nanoparticles have been used for the delivery of drugs such as paclitaxel, doxorubicin, and insulin. One of the key advantages of PEGylated nanoparticles is their ability to target specific cells or tissues. Targeted drug delivery involves the use of nanoparticles that can selectively accumulate in diseased tissues, such as tumours or inflamed tissues, while sparing healthy tissues. This is achieved by decorating the surface of nanoparticles with ligands that can recognize and bind to specific receptors or antigens on the surface of target cells. PEGylation can improve the targeting efficiency of nanoparticles by reducing their uptake by non-target cells and prolonging their circulation time in the bloodstream.

Table.2.2: List of drugs for the treatment of Alzheimer’s disease

Class of Drug	Name of Drug	Limitations
Cholinesterase Inhibitors	Donepezil	Poor solubility, High protein binding, Liver toxicity, symptomatic relief, and gastrointestinal disturbance Temporarily improving cognitive symptoms Drug-drug interactions. High administration frequency
	Rivastigmine	
	Galantamine	
NMDA receptor antagonists	Memantine	Symptomatic relief in moderate to severe Alzheimer's Disease Inability to significantly alter the disease progression or reverse cognitive decline.
Monoclonal Anti-body	Lecanemab	Slowing down disease progression, potential safety concerns, limited availability for routine clinical use, high cost
	Aducanumab	

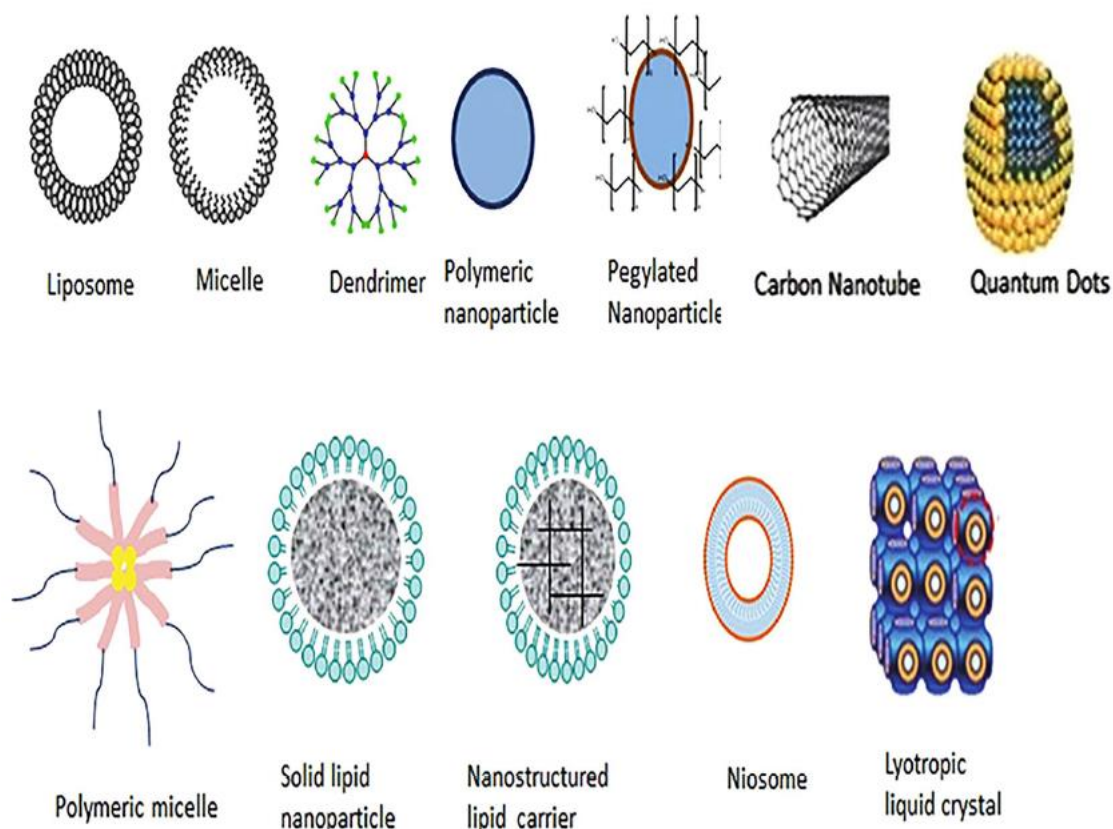


Fig.2.5: Schematic representation of various nanocarrier systems for the drug delivery

2.6.1 Polymeric Nanoparticles

Polymeric nanoparticles (PNPs) have been extensively employed as a biodegradable material due to their beneficial characteristics in terms of elaboration and design, excellent biocompatibility, and bio imitative properties. PNPs have a small size which allows them to permeate easily through biological barriers and capillaries[170]. The surface of PNPs can be functionalized with PEGylation to enhance systemic circulation, bioavailability, and tissue targeting efficiency. Though, the PNPs can shield the active ingredient from degradation and deliver it to the intended site but increase the risk of toxicity due to the slow degradation rate of polymers and lack of loading capacity due to the high molecular weight of polymers (Fig.2.5). Moreover, PNPs may not be easily biodegradable in the body, leading to their accumulation in tissues and potential toxicity issues. The properties of PNPs can vary from batch to batch, making it challenging to reproduce results. Also, the stability of PNPs is a crucial factor in drug delivery systems. However, polymeric nanoparticles can be sensitive to changes in temperature, pH, and other environmental factors, which can affect their stability and ultimately their efficacy.

The PNPs may have a limited capacity to carry therapeutic agents, leading to a need for a high dose of the drug to achieve the desired therapeutic effect. The release rate of the drug from

PNPs may not be as controllable as other drug delivery systems, leading to potential variations in therapeutic efficacy [171].

2.6.2. Polymer Lipid Hybrid Nanoparticles (PLHNPs)

PLHNPs comprise a core-shell structure consisting of three main components i.e., a core of biodegradable polymer which efficiently loads the hydrophobic drug molecules, then a lipid monolayer surrounding the core to enhance the stability and reduces the outward diffusion of the drug and outer corona of a lipid polyethylene glycol layer to enhance systemic circulation and protect against immune recognition. The presence of a core-shell structure exhibits complementary characteristics to polymeric nanoparticles [172]. The PLHNPs have high structural integrity, stability, and controlled release capability which can be attributed to the polymer core. Furthermore, PLHNPs exhibit high biocompatibility and bioavailability due to the lipid and lipid-PEG layers [173]. PLHNPs are a type of hybrid nanoparticle that combines the advantages of both PNPs and lipids-based nanoparticles. The lipid shell of PLHNPs can prevent the burst release of drugs that can occur with PNPs. The lipid shell can control the release of drugs over a longer period, allowing for sustained drug delivery. Additionally, the lipid shell can also protect the drug from degradation and clearance by the immune system, leading to higher bioavailability. Moreover, the PLHNPs has ability to enhance cellular uptake and drug penetration. The lipid shell of PLHNPs can fuse with the cell membrane, allowing for efficient cellular uptake. Additionally, the lipid shell can also facilitate drug penetration across the blood-brain barrier, which is often a major obstacle for drug delivery to the brain. It also has the ability to target specific cells or tissues. Whereas the polymeric core of PLHNPs can be functionalized with ligands or antibodies that can recognize and bind to specific cells or tissues. This targeted delivery can increase the efficacy of treatment while minimizing off-target effects, leading to increased efficacy and bioavailability of drugs.

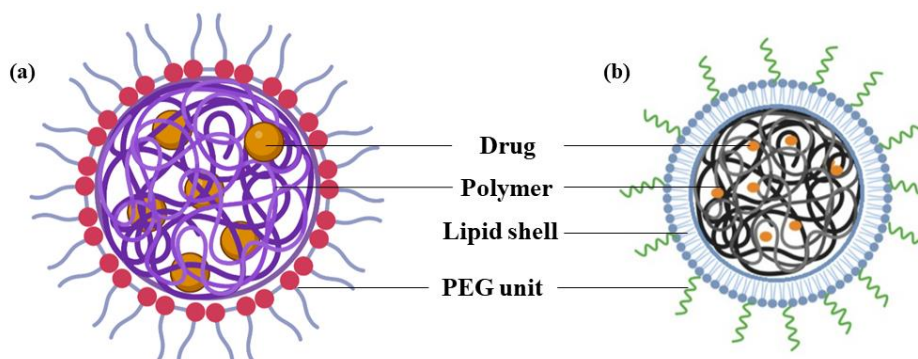


Fig.2.6: The illustration of (a) Polymeric nanoparticles and (b) polymer lipid hybrid nanoparticles

3.1 Gaps in the existing research

Recent studies have shown that people with MetS are at a higher risk of developing brain insulin impairment due to dysregulation of the insulin signaling pathway which eventually may cause devastating cardiovascular and T2DM disorders. Metabolic disorders may generate endoplasmic reticulum stress, inflammation, and mitochondrial stress which modulate the apoptosis process, activate the ROS, and may possibly lead to neurodegeneration. The neurodegeneration also activates via the dysregulation of the insulin receptor signaling pathway that increased the PI3K, GSK-3 β activity, hyperphosphorylation of tau proteins, and amyloid- β accumulation as well as increased neurofibrillary tangle formation and all of them believe to be direct contributors to AD pathogenesis.

Despite numerous pharmacological interventions, an effective therapeutic strategy for complete recovery from this debilitating, MetS with AD co-morbidity seems to be far away. Thus, exploring novel therapeutic strategies is an unmet need for effective clinical management of MetS associated with AD. In the majority of cases, the progressive accumulation of damaged and misfolded proteins due to their ineffective clearance impaired the processes and accelerates the progression of the disease.

In this regard, REP (anti-diabetic drug) has gained attention in recent past due to its neuroprotective potential in CNS disorders including HD and PD. However, the molecular mechanism and its efficacy in MetS comorbid with AD are not yet explored. Although, the existing evidence has demonstrated that REP targets neuronal calcium receptors by specifically attaching to them in a calcium-dependent manner. Interestingly, REP seems to modulate calcium hemostasis, apoptosis, and ER stress but the reason behind this is still elusive and remains to be an interesting topic of investigation that needs to be explored.

Despite the therapeutic potential of REP, various reports have highlighted its poor pharmacokinetic profile (poor solubility, short half-life, first pass metabolism) and limited brain availability, which could significantly hamper its efficacy. Therefore, there is a critical need to develop novel strategies to enhance the bioavailability and brain targeting of REP for improved therapeutic outcomes. In this context, the exploration of nanocarrier systems represents a promising approach for enhancing the delivery and efficacy of REP. However, there is still a significant gap in the research regarding the optimal formulation and design of nanocarrier systems for efficient REP delivery for the management of Mets linked AD.

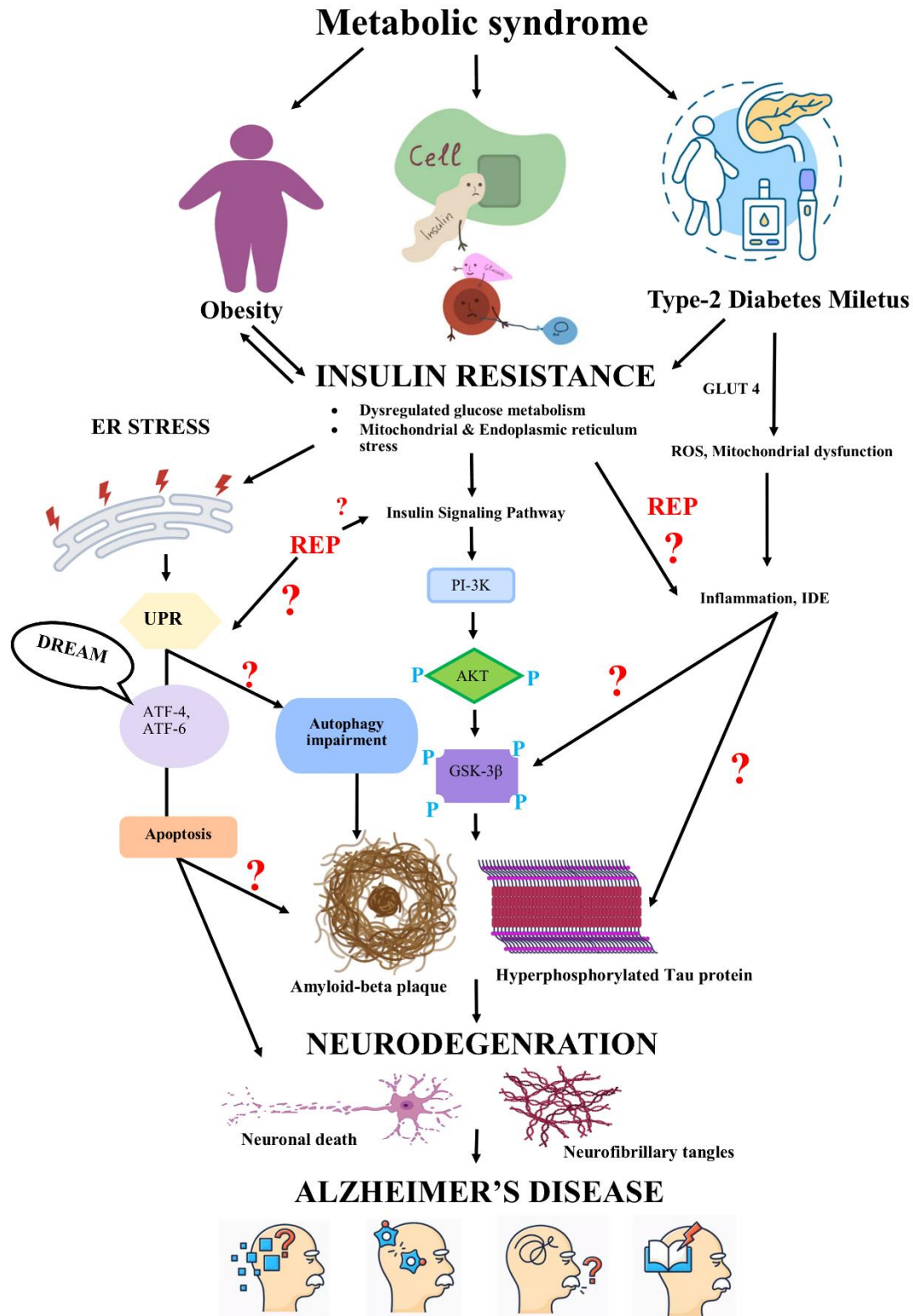


Fig.3.1: Mets and dysregulated brain glucose metabolism leads to neurodegeneration which is complicated by ER stress, mitochondrial stress, and the apoptosis process. Moreover, the molecular mechanism of REP and its efficacy in T2DM comorbid with AD is yet to be explored. GLUT-4, Glucose transporter type 4; UPR, unfolded protein response; ATF, Activating transcription factor; ROS, Reactive oxygen species; IDE, Insulin degrading enzyme; PI3K, Phosphoinositide 3-kinases; GSK-3 β , glycogen synthase kinase-3 beta.

3.2. Objectives of the proposed research

Based on the identified gaps in the existing research, the objective of the proposed research was categorized and prioritized into the areas that require further investigation and development.

Objective I : To evaluate the neuroprotective potential of REP in MetS associated with AD.

Objective II : To improve the efficacy and circumvent pharmacokinetic limitations of REP by developing brain targeted nano drug delivery system.

Objective III : To examine the best PEGylated nanocarrier system for targeting REP to the brain by oral route.

Objective IV : To explore the potential additive and/or synergistic neuroprotective effect of REP with Memantine (MEM, NMDA receptor antagonist).

4. Materials and methods

4.1. Materials

4.1.1. *In vitro* Cell line

Human neuroblastoma SH-SY5Y cells were obtained from National Centre for Cell Science (NCCS), Pune, India. The cells were preserved in Dulbecco's modified Eagle's medium high glucose (DMEM-F12) comprising 20% (v/v) Fetal bovine serum (FBS), and 1mL/L of antibiotic (Penicillin-streptomycin) media. The cells were incubated at $37 \pm 1^\circ\text{C}$ with a 5% CO_2 humidified atmosphere in the incubator.

4.1.2 Animals

The central animal facility, BITS-Pilani, Pilani campus, India (417/PO/ReBi/2001/CPCSEA) provided the wistar rats (200–220 g) for conducting the animal study. All animal experiments were accomplished as per Institutional Animal Ethic Committee (IAEC) guidelines of BITS-Pilani, Pilani campus, India (protocol number IAEC/RES/22/05/Rev-1/28/25). The animals were retained in polyacrylic cages under controlled conditions (12 h light/dark cycle, $22 \pm 1^\circ\text{C}$ with 60% relative humidity) and fed with the normal diet with purified water *ad libitum*.

4.1.3 Drugs and chemicals

REP was provided by Tokyo Chemical Industry Co., Ltd. (Tokyo, Japan). FBS, DMEM, and penicillin–streptomycin solution was purchased from Gibco Life Technologies (U.S.A.). Dried toluene, triethylamine, bovine serum albumin (BSA), sodium chloride, monobasic potassium phosphate, sodium hydroxide, pancreatin, sodium phosphate, benzyl alcohol, dimethyl sulfoxide (DMSO), ethyl acetate and diethyl ether were acquired from SISCO research laboratories (SRL, India). Methoxy Poly (ethylene glycol) (Mn, 5000), tin (II) 2-ethyl hexanoate, ϵ -Caprolactone, trehalose, pepsin, methyl thiazolyl diphenyl-tetrazolium bromide (MTT), 5,5'-dithiobis-(2-nitrobenzoic acid) (DTNB), xylazine, ketamine, sodium dodecyl sulphate (SDS), ascorbic acid and Thiobarbituric acid (TBA) were procured from Sigma-Aldrich. Phospholipon 90 H, soy lecithin, egg phosphatidylcholine, soy phosphatidylcholine, Distearoyl-sn-glycerol-3-phosphoethanolamine-Poly (ethylene glycol) (DSPE-PEG₂₀₀₀) were provided by Lipoid. Poloxamer 407 was supplied by BASF (India). Porcine polar brain lipid (PBL) was acquired from Avanti polar. Dialysis tubing (10kDa) and Phosphate buffered saline; pH 7.4 (PBS) were obtained from Himedia (Mumbai, India). Insulin, Tumour Necrosis Factor alpha (TNF- α), and Interleukin-6 (IL-6) ELISA kits were procured from Ray Biotech Inc. Brain-Derived Neurotrophic Factor (BDNF) ELISA kit was purchased from Boster Biological Tech. Ltd, USA. Amyloid beta ($\text{A}\beta_{1-42}$) and phosphorylated tau protein (pTau) ELISA kits were

acquired from Elab Science. Trizol reagent was purchased from Invitrogen, USA. SYBR green / ROX qPCR master mix kit was from Bio-Rad. Deionized ultra-pure water was obtained from the in-house Millipore Milli-Q Plus system with an electrical resistivity of 18.2 MΩ.cm (at 25°C) (Millipore Bedford Corp., Bedford, MA, USA). HPLC grade solvents methanol, acetonitrile, and isopropyl alcohol were obtained from Merck Millipore (MA, U.S.A.).

4.1.4 Antibodies and Primers for the study

The Primary and secondary antibodies like anti-Bax, anti-Bcl-2, anti-caspase-3, GAPDH, and anti-rabbit IgG antibody used in the present study were procured from cell signaling technology, Danvers, Massachusetts, USA. The ECL kit for visualization was procedure from Thermo fisher scientific. Primers Activating transcription factor-6 (ATF-6) and GAPDH were purchased from Imperial Life Sciences limited.

4.1.5 Instrument / Equipment used

All the instruments /equipment used in the present studies were mentioned in Table. 4.1.

Table 4.1: List of instruments/ equipment with manufacturer's name used to conduct the experiments.

Instrument / Equipment name	Manufactures/ company name
Ultrasonic microtip processor	Vibra-Cell™, Sonics®, USA
Magnetic stirrer with a hot plate and temperature controller	Tarsons, India or Remi, India
Rota vacuum evaporator	Rotavapor R210, Buchi, Switzerland
Ultrasonic bath sonicator	Toshiba, India
Temperature-controlled centrifuge	Eppendorf biotech company, Germany
Ultra-centrifuge, Freezer (-20 °C, -80 °C), CO ₂ incubator, Biosafety cabinet	Thermo Scientific, USA
Triad Freeze Dry System	Labconco, USA
Malvern Zetasizer, nanoZS,	Malvern, UK
Field emission Scanning microscope	FEI limited, USA
Confocal Laser Scanning Microscope	Carl Zeiss
Nanodrop	Synergy, Biotek
SDS-PAGE	Bio-Rad
High Resolution-Transmission Electron Microscope	Technai FEI, USA
Inverted microscope	Zeiss, India
Microplate reader	Bio Tek ELX50, Epoch
UV spectrophotometer	UV-1800 Shimadzu, Japan

Tissue Homogenizer	:	Kinematica™ Homogenizers, Germany
Actophotometer, Passive Avoidance instrument, Morri's water maze, Novel object recognition apparatus	:	Inco Ambala, India
Bruker alpha-one FTIR spectrophotometer	:	Bruker Optik, Germany
DSC-60 plus	:	Shimazu, Kyoto, Japan
Powder X-Ray Diffraction	:	Rigaku-mini flex
Thermal Cycler	:	Bio-Rad
Centrifuge	:	Eppendorf
Elisa Palate reader	:	Bio Tek, Agilent-United state
High-performance liquid chromatography	:	Shimadzu, Kyoto, Japan

4.1.6 Software used

All the instruments /equipment used in the present studies were mentioned in Table. 4.2.

Table 4.2: List of software used to conduct the experiments

Software		Company name
Design Expert® software	:	Stat-Ease Inc., Minneapolis, USA
Phoenix Win Nolin	:	Certera™ Pharsight, USA
ANY- maze 7.1 Video tracking system	:	Stoelting, USA
Graph Pad Prism	:	Dotmatics, California

Methods

4.2 Analytical method for estimation of REP

4.2.1 Instrumentation and chromatographic conditions

The method was developed using a Shimadzu HPLC system (LC-2010HT, Shimadzu Corporation, Japan) equipped with a pulse-free solvent delivery system comprised of two pumps. The system also consists of a high-efficiency five-line degasser, block heating-type column oven, sample cooler, intelligent autosampler, and UV-visible detector. The chromatographic peaks were collected and analyzed using LC solutions software. The separations were carried out on waters Nova-pack C₁₈ column (3.9 x 150 mm, 4µm particle size) in isocratic mode. The aqueous phase was filtered through a 0.22 mm nylon membrane filter and ultrasonically degassed. The column was maintained at a temperature of 30°C, and a

20µL sample was injected into it. The detector was operated at a maximum wavelength of 243 nm for data acquisition of REP.

4.2.2. Preparation of standard solutions

Primary stock solutions of REP (1000µg/mL) were prepared by dissolving the accurately weighed amount in acetonitrile. The primary stock solution was diluted using the mobile phase for the preparation of the standard stock solution. Further dilutions were made to prepare different concentrations for the calibration curve[174].

4.2.3. Optimization of RP-HPLC method by Quality by Design approach

4.2.3.1 Quality target method profile (QTMP) and critical analytical attributes (CAAs)

QTMP is the preliminary stage of the analytical quality by design (A-QbD) approach, and it is a collection of all the possible factors which define the characteristics criteria of the target analytical method (Table 4.3).

Table.4.3: QTMP elements for the efficient liquid chromatographic method for estimation of repaglinide

Method Parameters	Objective	Justification
Target analyte	Repaglinide	Development of an analytical method for estimation of active analyte from the pharmaceutical dosage form
Type of method	Reverse phase chromatography	A reliable method with a non-polar stationary phase that provides better retention of the molecule
Sample nature	Liquid	The analyte should be in the liquid phase for ensuring complete miscibility
Instrument requirement	HPLC equipped with a quaternary pump system with UV detector	The quaternary pump provides accurate mixing of mobile phase solvent and high resolution, whereas UV detector helps in the detection of analyte at a suitable wavelength
Sample preparation	Dilution in a linear method	The dilution of analyte solution must be accurate and assuring its proper elution
Quality attributes	% assay Theoretical plate count Tailing factor	These attributes help to develop a method that meets the quality standard

To attain the QTMP targets, numerous possible CAAs were chosen, which are corresponding to QTMP, i.e., retention time (RT) represents the separability of the compound, tailing factor (TF), and theoretical plate count (PC) reflect the efficiency of the method [17].

4.2.3.2. Risk assessment and factor screening studies

Risk assessment is a crucial step prior to the optimization of the chromatographic solution. It is used to identify the possible parameters which have immense potential to affect the identified CAAs and are defined as critical material parameters (CMPs). To achieve the CMPs, the

Ishikawa fishbone cause-effect diagram was conceptualized to outline the relationship(s) between CMPs and CAAs (Fig 4.1).

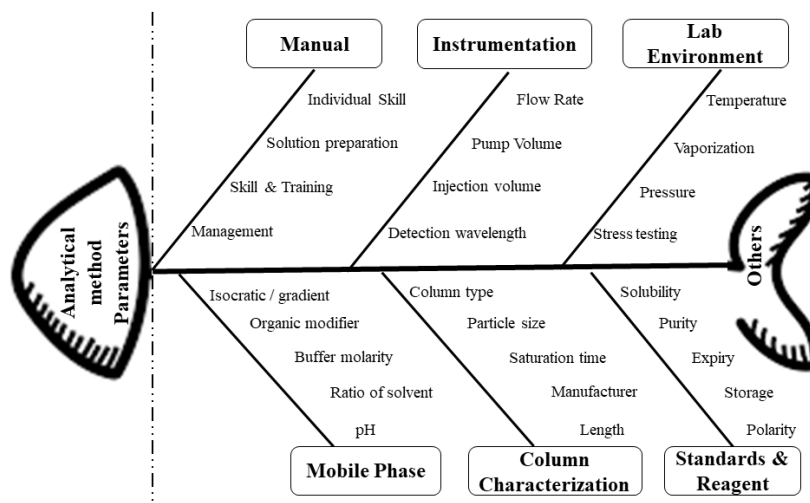


Fig.4.1: Ishikawa fishbone diagram to identify the potential attributes in HPLC method development.

The factors such as flow rate, the volume of acetonitrile, injection volume, pH, and column temperature have a substantial effect on the CMP. Further, the factor screening was done by using L8 (2⁷) Taguchi design with 7 factors and 8 runs allotted with low and high scores (Table 4.4).

Table. 4.4: Design matrix for screening of method variables by seven-factor eight-run Taguchi design

Run	Mobile Phase	Flow rate (mL/min)	Injection volume (µL)	Column temperature (°C)	Buffer strength (mM)	Buffer pH	Organic modifier
1	-1	-1	-1	+1	+1	+1	+1
2	+1	+1	-1	-1	+1	+1	-1
3	+1	+1	-1	+1	-1	-1	+1
4	-1	-1	-1	-1	-1	-1	-1
5	+1	-1	+1	-1	+1	-1	+1
6	-1	+1	+1	+1	+1	-1	-1
7	+1	-1	+1	+1	-1	+1	-1
8	-1	+1	+1	-1	-1	+1	+1

Levels of factor study		Low (-1)	High (+1)
Mobile Phase	(Organic: aqueous)	50:50	60:40
Flow rate	(mL/min)	0.8	1.0
Injection volume	(µL)	10	20
Column temperature	(°C)	30	40
Buffer Strength	(mM)	10	20
Buffer pH		3.0	5.0
Organic modifier		Methanol	Acetonitrile

It was used to identify the key independent variables that completely affect the chosen CAAs, *i.e.*, RT, TF, and PC [176]. The statistical analysis was performed using Design Expert® software 11 (M/s Stat-Ease Inc., Minneapolis, MN, USA).

4.2.3.3. Factor Optimization studies

The three method parameters were selected based on their significant effect on the CAAs and measured as CMPs. The (A) mobile phase ratio (Acetonitrile: Buffer solution), (B) flow rate, and (C) pH of buffer were chosen for further optimization study using response surface by Box-Behnken design (BBD) at three equidistant levels, *i.e.*, low (-1), intermediate (0) and high (+1) with 17 experimental runs (Table 4.5). All other parameters were kept constant at their optimum levels during the experimentation, and a standard concentration was maintained. The data obtained were analyzed against three response factors, *i.e.*, RT, TF, and PC [177].

Table.4.5: Design matrix for optimization of the chromatographic method by Box-Behnken Design (BBD)

RUN	FACTOR			RESPONSE		
	Mobile Phase (organic phase)	Flow rate (mL/min)	Buffer pH	Retention time (RT)	Tailing (TF)	Theoretical plates (TP)
1	0	+1	0	4.52	1.01	3747
2	0	-1	+1	7.21	1.31	3645
3	0	-1	0	5.15	1.12	4259
4	+1	-1	0	4.63	1.15	4597
5	+1	0	-1	2.80	1.09	4097
6	-1	0	-1	5.49	1.31	4189
7	0	-1	-1	3.96	1.17	4878
8	0	+1	-1	3.28	1.03	3458
9	0	-1	0	5.30	1.10	4567
10	0	0	0	4.89	1.05	3987
11	+1	0	+1	6.94	1.07	3579
12	0	-1	0	5.47	1.13	4309
13	-1	+1	0	6.45	1.26	3681
14	-1	0	+1	7.12	1.28	3668
15	+1	+1	0	4.17	1.04	3585
16	0	+1	+1	6.53	1.07	3357
17	-1	-1	0	6.71	1.29	4621

Factor description with code and actual levels

Critical method Parameters (CMPs)		Code Levels		
		Low (-1)	Intermediate (0)	High (+1)
Mobile Phase	(organic: aqueous)	50:50	60:40	70:30
Flow rate	(mL/min)	0.8	0.9	1.0
pH of Buffer		3.00	3.50	4.00

4.2.3.4. Optimization of data analysis and model validation

The data analysis, optimization of data, and model validation were done using Design Expert® software 11. The second-order polynomial (i.e., quadratic) model was used to assess the main and interaction effect. The fitting of data was conducted to establish the factor-response relationship in terms of analysis of variance (ANOVA), lack of fit, coefficient of correlation (R^2), adjusted R^2 (R^2 -adj), and predictive R^2 (R^2 -pred). The regression model is poorly attuned when the lack of fit is significantly higher than the random pure error ($P > 0.05$), and when the lack of fit is significantly lower than the random pure error ($P < 0.05$), the regression model is fitted well. The developed factor-response relationships were analyzed and decoded graphically via the consequent 3D-response surface plots and the respective 2D-contour plots. The model validation was done using mathematical optimization tools, which respond to optimum chromatographic solutions for various CAAs, including minimizing RT, TF, and maximizing PC. Afterward, the optimization was carried out using the graphical approach to ratify the optimal chromatographic solution within the design space outlined [178].

4.2.4 Method validation

The validation of the analytical method was achieved in terms of various parameters such as linearity, accuracy, precision, detection, and quantification limit as per the International Conference on Harmonization of Technical Requirements for Pharmaceuticals for Human Use (ICH) guidelines Q2 (R1).

A system suitability test was performed to confirm the function of the chromatography system on a day-to-day basis. It was evaluated by injecting the same sample concentration six times to check the efficiency of the column, retention time (RT), peak area, tailing factor (TF), and reproducibility. The acceptance criteria of system suitability were limited to $RSD \leq 2\%$ for the peak area and retention time, whereas it should be < 2 of the analytes for TF.

Selectivity studies were performed to understand the interference of formulation excipients and degradants. The peak purity of REP was evaluated using the UV spectra recorded dual-wavelength UV-visible detector, and the interference of excipients used in the polymeric nanocarrier system was evaluated by mixing of polymer with drugs [179].

Linearity is the capability of a test to acquire test results directly proportional to the analyte concentration. The linearity was determined by injecting a solution of different concentrations (100–9000 ng/mL) of REP six times per concentration, and the results of samples were plotted by nominal concentrations on the x-axis versus peak area ratios on the y-axis. The analyte's

detection and quantification were determined by calculating the lowest concentration that can be detected and quantified. The lowest analyte concentration, which can be detected or differentiated (LOD) and quantified (LOQ), was determined by the signal-to-noise ratio. The accuracy, intra, and inter-day assay precision were estimated by analyzing six replicate samples at three different QC levels, i.e., Low-quality control (LQC), Medium quality control (MQC), and High-quality control (HQC).

The accuracy, intra-day, and inter-day assay precision were determined within a day or three consecutive days [180,181].

The carryover effect is a reappearance of the analyte in the next run due to the sample overload. It was estimated by injecting three continuous higher-concentration samples of the calibration curve followed by a blank sample.

The robustness of the developed analytical method was estimated by changes in chromatographic conditions such as a change in flow rate ± 0.2 , column oven temperature $\pm 5^\circ\text{C}$, composition, and mobile phase ratio ± 2 . The recovery was evaluated as a response to each condition concerning the standard solution.

4.2.5 Force degradation studies

The forced degradation studies were measured to estimate the stability-indicating properties of the validated method. In this study, REP was subjected to degradation under different stress conditions, including acidic, basic, thermal, photolytic, and oxidation. In brief, the drug solution was dispersed in a 0.1 M Hydrochloride solution and sodium hydroxide solution. The drug solution was added in 30% hydrogen peroxide solution for oxidation stress, whereas for solid-state degradation study under thermal, ultraviolet (UV), and fluorescent light. The REP (5mg) was kept under thermal (60°C), UV, and fluorescent light for 48 hr. and approximately the sample was withdrawn at 24 hr. and 48 hr. The samples were analyzed with a validated RP-HPLC method after dissolving 1mg REP in 1mL acetonitrile solution and further diluting the stock solution with mobile phase appropriately [182].

4.2.6 Solubility studies

Solubility studies of REP in different aqueous and organic solvents were estimated using the shake flask method. Aqueous solvents include water and different buffers in the pH range of 1 – 9 (Table 4.6). An excess amount of REP was added in a 2 mL microcentrifuge tube with each solvent and placed for shaking in an orbital shaking incubator for about 24 h at 37°C . It was ensured that throughout the study time, an excess amount of REP was present in all the tubes. Further, samples were centrifuged at 10,000 rpm for 20 min after 24 h and the supernatant was

diluted and analyzed by the developed HPLC method. The buffer solutions were prepared as per previously reported methods [183,184].

Table 4.6: Buffer compositions from pH 1 – 9

Composition of solution A	Composition of solution B	pH	Volume of solution A	Volume of solution B
Glycine – 0.5 g	Dibasic sodium phosphate	1.0	100*	-
Sodium chloride – 3.68 g	(anhydrous) – 16.35 g	2.0	70	30
1 M Hydrochloric acid – 94 mL	Dihydrogen potassium phosphate (anhydrous) –	3.0	58	45
Milli Q water up to 1000 mL	2.80 g	4.0	56	48
	Sodium chloride – 0.15 g	5.0	55	49
	Milli Q water up to 1000 mL	6.0	50	50
		7.0	30	83
		8.0	-	100 [¥]
		9.0	-	100 [¥]

*pH to be adjusted with the dilute hydrochloric acid solution

¥pH to be adjusted with dilute sodium chloride solution

4.3 Bio-analytical method for quantification of REP in rat plasma and tissues

4.3.1 Instrumentation and chromatographic conditions

RP-HPLC analysis was performed on the Shimadzu HPLC system (LC-2010HT, Shimadzu Corporation, Japan) consisting of a quadrupole pump system, UV-visible detector, block heating-type column oven, and intelligent autosampler for sample injection. The detector was operated at a maximum wavelength of 243nm. Repaglinide and diclofenac diethylamine (internal standard) were separated on Waters Nova-Pak C18 column (3.9 x 150 mm, 4 mm particle size) with a mobile phase containing acetonitrile and phosphate buffer (pH 3.5; 0.01 M) (40:60% v/v) at a flow rate of 0.8 mL/min in an isocratic mode and at a column oven temperature of 30 ± 0.5 °C. The injection volume was 40 µL and the retention time for diclofenac diethylamine and repaglinide were 5.7 and 10.6 min respectively. The data integration and hardware control were carried out by utilizing LC solution software.

4.3.2 Collection of plasma and tissue homogenates

The blood was collected from the retro-orbital plexus in heparinized disposable tubes and centrifuged at 7500 rpm for 20 min to separate the plasma and stored at -80 ±10 °C until analysis. For tissue homogenate, tissue (brain, heart, liver, and kidney) was promptly harvested and rinsed thoroughly with ice-cold saline further and blotted with filter paper. A precisely

weighed quantity of each tissue sample was homogenized using a tissue homogenizer (Kinematica™ Polytron™ PT 1600E) at 15000 rpm in 1:2 w/v of phosphate buffer saline solution. Afterward, centrifugation was carried out at 10000 rpm for 20 min, to obtain clear supernatant then collected supernatant of respective tissues was stored at -80 ± 10 °C until analysis[185].

4.3.3 Preparation of standard solutions

The standard solution of REP was prepared in acetonitrile to attain a concentration of 5 mg/mL. Further, serial dilution of REP (5 mg/mL) was prepared with acetonitrile to make a 500 µg/mL working stock solution. The calibration standards and QC samples were prepared by spiking with 2 µL of respective working standards in blank rat plasma or tissue samples. The final calibration standards were prepared in the range of 50-20000 ng/mL in the plasma matrix. The QC samples were prepared by utilizing QC standards at four concentration levels, such as limit of quantification (LOQ, 50 ng/mL); low QC (LQC, 100 ng/mL), medium QC (MQC, 2000 ng/mL) and high QC (HQC, 15000 ng/mL). The working and stock standards were kept in refrigerated conditions at -20 °C.

4.3.4 Sample preparation

The extraction of the sample was done by using extraction techniques like protein precipitation (PP), liquid-liquid extraction (LLE), and solid phase extraction (SPE). In protein precipitation (PP) the organic solvents (methanol, acetonitrile) were used for extraction, but plasma interference was observed. In LLE various solvents were screened such as n-hexane, dichloromethane, and ethyl acetate and with ethyl acetate, no plasma interference and a good recovery of IS with REP was recovered.

4.3.5 Method validation parameters

The validation of the bioanalytical method was achieved in terms of various parameters in accordance with the US FDA and European Medical Agency (EMA) guidelines.[186–189]

System suitability is a test for system performance in which the same concentration of the sample was injected six times to understand the column efficiency, resolution, and reproducibility on a day-to-day basis.

Selectivity was done to estimate the chromatographic interference from the bio matrix[190]. In this blank rat plasma and tissue sample was compiled randomly from the rats and analyzed to check the hindrance of the matrix and the method was selective when the peak ratio to IS was less than 5 times of Lower limit of quantification (LLOQ) and less than 20 times of the IS[179]. The linearity and calibration curve of an analyte was prepared in the range of 50-20000ng/mL. The minimum six calibration curves were generated in plasma and tissue samples by plotting

nominal plasma concentrations on X-axis versus peak area ratios (drug/IS) on the Y-axis. To accomplish the error of accuracy and coefficient of variation, the validation criteria (CV) should be $\pm 15\%$ for all calibrations, except for the LLOQ ($\pm 20\%$). [191] However, the limit of detection (LOD) and limit of quantification (LOQ) were measured as a signal-to-noise ratio, and Accuracy, and precision (intra-day and inter-day) assays were estimated by analyzing six replicate samples at three different Quality control (QC) levels, i.e., Lower quality control (LQC), Medium quality control (MQC), High quality control (HQC).

The accuracy, intra-day, and inter-day assay precision were determined within a day or between three consecutive days. The acceptance criteria for intra and inter-day precision was limited to $\leq 15\%$ (RSD, %), and accuracy was within $\pm 15\%$ except for LLOQ, where it should not exceed $\pm 20\%$ for precision and accuracy.

Recovery was estimated by the ratio of the compound concentration (relative) or peak area of extraction ion chromatogram (absolute) in plasma [192].

The stability studies of REP in the plasma matrix of the six replicates at QC levels (LQC, MQC, HQC) and LLOQ were estimated under the following conditions: (1) in autosampler at 4°C for 24 h; (2) benchtop (at ambient temperature ($25\pm 3^{\circ}\text{C}$) for 9 h; (3) over three freeze-thaw cycle at -80°C . Stability studies were calculated by comparing the stability samples, with freshly spiked samples. Stability samples were considered to be stable if assay values were within the adequate limits of accuracy (i.e., $\pm 15\%$ Bias) and precision (i.e., 15% R.S.D.), except LLOQ (i.e., 20% of CV) [193].

4.4. *In vitro* experimental Procedure

4.4.1 Cell viability assay by MTT

The SHSY-5Y (P24) cells were cultured with 1.5×10^4 cells/well cell density [20]. After 24 h of seeding the cells were treated with test compounds at the concentration range of 0.25-100 $\mu\text{g}/\text{mL}$ to screen out the effective concentration with time. Then cells were washed with sterile PBS solution in triplicate and 20 μL of MTT (5mg/mL) solution was added to form formazan crystals [194]. Further, culture grade DMSO (200 μL) was added to dissolve the crystals, and using a microplate spectrophotometer (Epoch, Biotek, Winooski, USA) the absorbance was measured at 570 nm, and 630 nm (reference wavelength).

4.4.2 STZ Treated neuroblastoma cell-based study

The assay was performed to understand the neuroprotective nature of test compounds on the SHSY-5Y cells induced with streptozotocin (STZ). Initially, the effective concentration of STZ

was examined to originate metabolic stress into the cells[195]. The SHSY-5Y cells (3×10^4 cells/well) were seeded into 96 well plate and allowed to attach at 37 C in a 5% Co₂ incubator. Further, the cells were treated with STZ at a concentration of 1-20 mM for 6 and 12 h to investigate the effective concentration and time[196]. Afterward, cells were treated with REP to estimate the cell viability and evaluate the protective effect of REP [197].

4.4.3. Reactive oxygen species-scavenging activity by hydrogen peroxide

The assay was performed to determine the intracellular ROS production, initially neuroblastoma SHSY-5Y cells were seeded into 96 well plate with a cell density of 15×10^3 cells/well and allowed to be attached for 12 h at 37 °C in a 5% Co₂ incubator. Further cells were exposed to H₂O₂ at a concentration of 1-20 mM for 12 and 24 h to examine the effective concentration and then treated with a test compound to evaluate the neuroprotective effect by estimating the percent cell viability [198].

4.4.4. Cellular uptake assay of nanoformulation

(a) Microscopy: The SH-SY5Y (P29) cells were seeded on a glass coverslip with a cell density of 2×10^4 in the 6-well plate. The coumarin-6 (C6) loaded PNPs and PLHNPs (150 μL) were incubated with the cells in DMEM-F12 medium at 37 °C for 4 or 8 h. The cells were washed thrice with PBS (pH 7.4) and nuclei were counterstained with 4',6-diamidino-2-phenylindole (DAPI, 1μg/mL, 30 min). Further, the cells were washed, resuspended in PBS, and mounted onto a glass slide after fixing with 4% paraformaldehyde solution and observed under a Carl ZEISS LSM 880 Axio confocal microscope (Jena, Germany).

(b) Flow cytometry: The quantitative estimation of cellular uptake was performed by flow cytometer. The SH-SY5Y cells (P30) were seeded in the 6 well plate and C6-loaded PNPs and PLHNPs (150 μL), were added. The loaded nanocarriers were incubated for 4 h and 8 h in DMEM-F12 medium at 37 °C and harvested by 0.25% trypsin solution. The cells were resuspended in PBS and a total of 10×10^3 events were noted in FACS (flow cytometer and the cell sorter), FACSAria SORP (Becton, Dickinson, San Jose, CA, USA) [199].

4.5. In vivo experimental Procedure

4.5.1. Induction of MetS and BIR linked with AD

The wistar rats (200-250 mg/kg) were acclimatized for seven days and afterward, diet manipulation was done with a High-fat diet (HFD) (Table 4.7). The HFD was fed for 16 weeks and then a low dose of STZ (30 mg/kg, *i.p*) was injected [22,200].

Table. 4.7: Composition of High-fat diet

Sr. No	Ingredient	Amount (gm)
1	Powdered Normal Pellet Diet	365
2	Lard	310
3	Casein	250
4	Cholesterol	10
5	Vitamins & Mineral mix	60
6	dl-methionine	03
7	Yeast powder	01
8	Sodium Chloride	01

The wistar rats subjected to HFD with STZ exhibited characteristic features of IR were confirmed after 72 h of STZ administration and the assessment of body weight, fasting blood glucose level (FBGL), total cholesterol (TC), triglycerides (TG), glycosylated hemoglobin level (HbA1c), and insulin level were measured using commercially available kits. Fig. 4.2

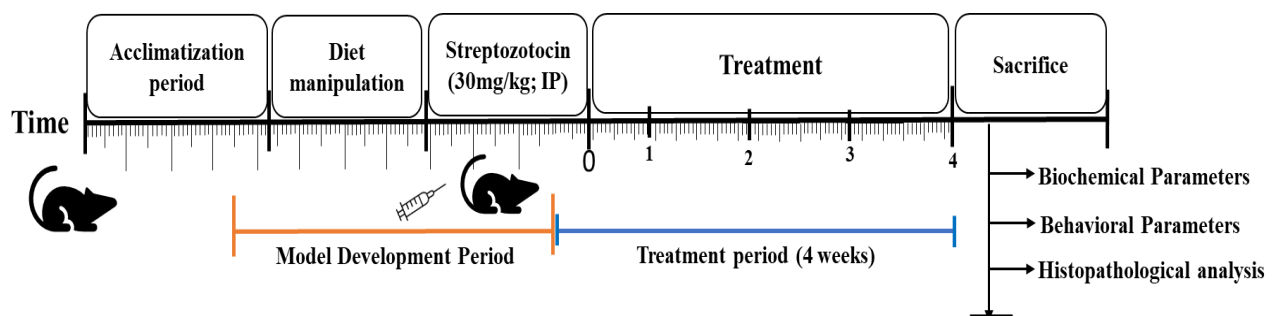


Fig.4.2: Experimental schedule of animal model development and treatment

4.5.2. Experimental Protocol for *in vivo* study

Initially, the animals were divided into four groups as in Table 4.8 to assess the neuroprotective effect of REP. The treatment was carried out for 4 weeks and biochemical parameters were examined and compared with an anti-Alzheimer drug as a standard.

Table 4.8: Experimental design for the screening of REP

Group 1	: Normal pellet diet fed rats (Normal control)
Group 2	: High-fat diet-streptozotocin diabetic rats (disease control), administer with Milli- Q water

Group 3	: High-fat diet -streptozotocin-diabetic rats, administered with REP suspension (REP; 4mg/kg, <i>p.o</i>)
Group 4	: High-fat diet -streptozotocin-diabetic rats, administered with memantine (MEM; 5mg/kg, <i>p.o</i>)

Further, for the determination of different nanocarrier systems, the group were divided as per the following Table 4.9

Table 4.9: Experimental design for the screening of REP with nanocarrier systems in MetS-associated AD condition

Group 1	: Normal pellet diet fed rats (Normal control)
Group 2	: High-fat diet-streptozotocin diabetic rats (disease control), administer with Milli- Q water
Group 3	: High-fat diet -streptozotocin-diabetic rats, administered with REP suspension (REP; 4mg/kg, <i>p.o</i>)
Group 4	: High-fat diet -streptozotocin-diabetic rats, administered with PNPs; 4mg/kg, <i>p.o</i>
Group 5	: High-fat diet -streptozotocin-diabetic rats, administered with PLHNPs; 4mg/kg, <i>p.o</i>

Additionally, to estimate the additive/synergistic effect via *in vivo* study the animals were divided into the following groups Table 4.10.

Table 4.10: Experimental design for the additive/synergistic effect of best nanocarrier system in MetS-associated AD condition

Group 1	: Normal pellet diet fed rats (Normal control)
Group 2	: High-fat diet-streptozotocin diabetic rats (disease control), administer with Milli- Q water
Group 3	: High-fat diet -streptozotocin-diabetic rats, administered with REP suspension (REP; 4mg/kg, <i>p.o</i>)
Group 4	: High-fat diet -streptozotocin-diabetic rats, administered with REP suspension (4mg/kg, <i>p.o</i>) and MEM (5mg/kg, <i>p.o</i>)
Group 5	: High-fat diet -streptozotocin-diabetic rats, administered with PLHNPs; 4mg/kg, <i>p.o</i>

4.5.3. Blood Collection and serum isolation

The blood was collected from the retro-orbital plexus method. In brief, each wistar rat was hand restrained, the neck was gently scuffed and the eye was made to bulge then a glass capillary was inserted. The blood was allowed to flow by capillary action into the heparinized disposable tubes. The tubes were centrifuged at 7500 rpm for 20 min at 4 °C to separate out the plasma and stored at -80 ±10 °C [179,201].

4.5.4. Estimation of serum metabolic parameters

The serum BGL, TG, TC, LDL, and Insulin levels were measured using commercially available kits as per the manufacturer's guidelines. Further, the homeostasis model assessment insulin resistance (HOMA-IR) was estimated using the below-mentioned formula

$$HOMA - IR = (Insulin \times glucose) / 405$$

4.5.5. Estimation of neurochemicals biomarkers

The brain was harvested after the treatment period and rinsed with an ice-cold isotonic saline solution. The hippocampal region was extracted and homogenized with ice-cold phosphate buffer saline (0.1M, PBS, pH 7.4). The homogenate was centrifuged at 10000 rpm for 20 min at 4 °C and the supernatant was separated for further analysis. The ELISA kits of brain-derived neurotrophic factor (BDNF), Amyloid-β, and p-tau level were used as per the manufacturer's instructions for the evaluation of REP.

4.5.6. Estimation of Oxidative stress parameters

MDA was estimated using the wills method. In this method, the thiobarbituric acid reacts with MDA, and the amount of MDA was determined using a spectrophotometer at 532 nm. Moreover, the abundance of nitrite in brain homogenates indicates the production of NO which was measured by colorimetric assay with Griess reagent. The equal amount of samples with Griess reagent was mixed and incubated in the dark for 10 min at room temperature followed by determination of absorbance at 540 nm. Further, the GSH level was estimated by previously described methods with modifications. In brief, the supernatant of brain homogenate was precipitated with 4% sulfosalicylic acid at 4 °C for 1 h. Afterward, samples were centrifuged at 1200 g for 15 min. and in 1 ml of the supernatant, 2.7 ml of phosphate buffer (0.1M, pH 8), and 0.2 ml of 5,5' dithiobis (2-nitrobenzoic acid) (DTNB) were added. Using a spectrophotometer, the developed yellow color was quantified at 412 nm [202].

4.5.7. Estimation of proinflammatory cytokines

The pro-inflammatory cytokines (TNF-α, IL-6) were estimated by using brain homogenates and the levels were determined by ELISA kits.

4.5.8. Behavior assessment for cognitive and motor functions

4.5.8.1 Passive avoidance task

The passive avoidance task was executed as per the previously described reports. In brief, the apparatus consists of an illuminated compartment and a dark compartment (Fig.4.3). Both compartments were separated by a guillotine door and equipped with a shock scrambler grid floor. Primarily, the acquisition trial was performed on each animal by placing them into the illuminated compartment for habituation of the 60s and after that, the guillotine door was

opened to record the initial latency to enter the dark compartment. Animals with an initial latency period of more than 60s were excluded from further investigation. As the animal entered the dark compartment the guillotine door was closed and an electric foot shock of 50V, 50HZ, and 0.2mA was delivered for 3s through the foot grid. The animal was taken out from the dark chamber and returned to its cage. The retention latency was evaluated after 24h same as in the acquisition trial, but no foot shock was delivered. The latency time was measured up to 300s and chambers were cleaned and dried between the trials with 70% v/v alcohol [203].

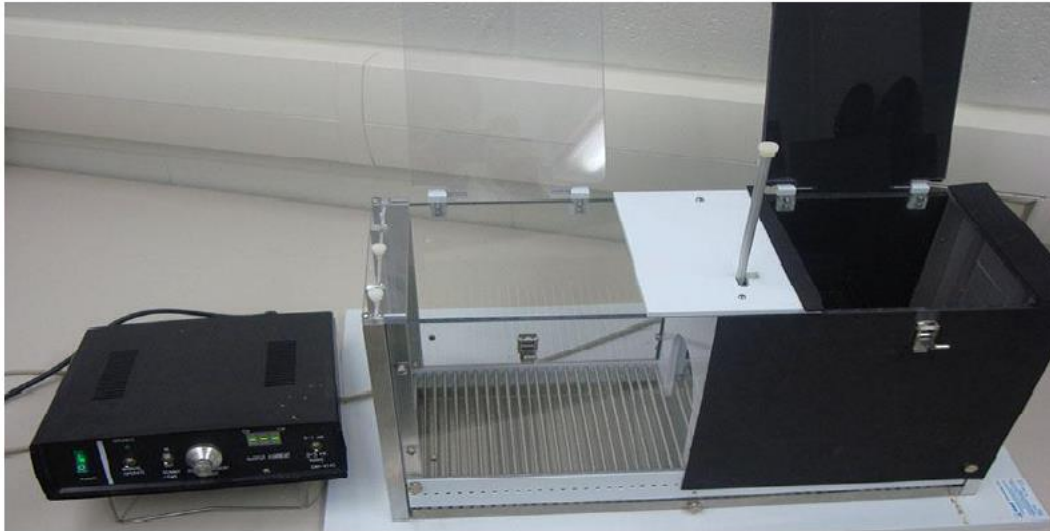


Fig.4.3: Pictorial representation of Passive avoidance apparatus

4.5.8.2 Spatial navigation task

In the spatial navigation task, Morris Water Maze (MWM) comprised of a circular water tank (120 cm diameter, 60 cm height) filled with water (27 ± 1 °C) to a depth of 40 cm and divided into four equal quadrants such as south-west (SW), south-east (SE), north-east (NE) and north-west (NW). The escape platform (10 cm X 5 cm) was positioned in the center of one of the randomly selected quadrants; 2 cm below the water surface and remained in the same position throughout the entire experiment. Before the training phase, the animals were allowed to swim freely in the pool for 60 s without the platform. Animals were subjected to four trials per session for consecutive four days, with each trial having a time limit of the 60s. The animals remained on the hidden platform for the 30s after climbing onto it and before moving on to the next trial. In case animals failed to locate the hidden platform for the 60s, then were placed gently on the platform for 60s. Thereafter, the video tracking software Any-maze 7.1 was used to calculate the time required to locate the hidden platform [204].

4.5.8.3 Probe trial

The escape platform (10 cm X 5 cm) was positioned in the center of the randomly selected quadrants of the pool below 2 cm to the water surface and kept in the same position throughout the entire experiment (south-east for this study) (Fig. 5.9). The animals were permitted to swim freely into the pool for 60 s without a platform before the training started. Animals received a training session consisting of 4 trials per session (once from each starting point) for 4 days, each trial having a ceiling time of 60s. After climbing onto the hidden platform, the animals remained there for 30 s before commencement of the next trial. If the animal failed to locate the hidden platform within the maximum time of 60 s, it was gently placed on the platform and allowed to remain there for the same interval of time. The time taken to locate the hidden platform (latency in seconds) was calculated using ANY-maze video tracking system (Stoelting, USA).

4.5.8.4 Novel object recognition

The rodent's ability to recognize the new object in their environment was assessed by novel object recognition (NOR) task. The NOR task consists of three stages habituation, familiarization, and test stage. In habituation phase, the animals have free access to explore the open field arena for 5 min in the absence of an object on two consecutive days. In familiarization phase, two identical sample objects were placed in the open field arena and animals were placed for the 5min. Whereas during the test phase (24 h later to familiarization phase), the two objects; one identical to the sample and another novel object were placed in the open-filed arena [205]. The objects were placed in the opposite and symmetrical corners of the arena during the familiarization and test phase and time spent was recorded for 5 min to explore the novel or familiar object. The task was performed by using ANY- maze 7.1 software.

4.5.9 Quantitative Real-time Polymerase Chain Reaction (qRT-PCR)

Total RNA from the rat's brain tissue sample was isolated with the TRIzol reagent, according to the manufacturer's protocol. Further RNA was reverse transcribed to complementary DNA (cDNA) by using a Revert Aid First strand cDNA synthesis kit [206]. Moreover, the SYBR green / ROX qPCR master mix kit was used for amplification according to the manufacturer's procedure using the CFX connect Optics Module by Bio-Rad[207]. The PCR conditions for the transcription level of ATF6 were 98 °C for 8 min followed by 32 cycles at 94 °C for 25 sec, 50 °C for 35 sec and 72 °C for 1 min. The relative expression level of activating transcription factor 6 (ATF6) mRNA was calculated keeping glyceraldehyde-3-phosphate dehydrogenase

(GAPDH) as a housekeeping gene and determined by the $2^{-\Delta\Delta t}$ method[208]. The sequence of specific primers is listed in Table.4.11.

Table.4.11: Primer sequence used for qRT-PCR analysis.

Gene name		Primer sequence
ATF6	Forward primer	TGGATTTGATGCCTTGGGAGT
	Reverse primer	AGGAACGTGCTGAGTTGAAGA
GAPDH	Forward primer	TTGCCATCAACGACCCCTTCA
	Reverse primer	AGCACCAGCATCACCCATT

4.5.10 Western blot analysis

The total proteins from the hippocampal region of the brain were extracted in a RIPA lysis buffer supplemented with protease, trypsin, and phosphatase inhibitors. Further, the amount of protein in the sample was detected using a BCA protein assay[207,209]. The collected lysate was separated using 12% SDS-PAGE gel using the electrophoresis technique and then transferred onto the PVDF membrane[210]. The blots were probed overnight with anti-bodies anti-Bax, anti-Bcl-2, ant-caspase-3, and GAPDH at 4 °C. Further, a secondary antibody (anti-rabbit IgG antibody) was used and signals were visualized using an ECL kit.

4.5.11 Assessment of histological changes

In histopathological analysis, brain samples were harvested immediately and fixed with formalin solution (10% V/V). Then samples were embedded into paraffin wax and sectioning them to 5 µm sections. The prepared sections were stained with hematoxylin and eosin stain (H&E) and hippocampal regions (dentate gyrus and cornu ammonis) were examined under the Zeiss microscope. The deteriorating neurons were evaluated in terms of percentage by using ImageJ software.

4.6. Pharmacokinetic profile

The pharmacokinetic study was performed in wistar rats (200-250g) to measure the pharmacokinetic parameters of REP and nanocarrier system. The rats were acclimatized for 7 days and prior to the study and rats (n=4) were fasted overnight. Then REP was administered at a dose of 4 mg/kg, *p.o* with the dosing volume of 1 mL to each overnight fasted rat, and blood was collected in heparinized disposable tubes from retro-orbital plexus at pre-set time intervals. Moreover, the blood was centrifuged at 7500 rpm for 20 min to separate out the plasma and stored at -80 ± 10 °C for further analysis [179,201]. The plasma concentration-time profile was plotted, and the pharmacokinetic parameters were investigated by Phoenix Win Nolin Certera™ (Pharsight, U.S.A; version 8.0) with non-compartmental modeling.

4.7 Biodistribution

The biodistribution of REP and nanocarrier systems was investigated in the wistar rat, the animals were anesthetized (ketamine/ xylene) and sacrificed at predetermined time intervals (0.25h, 2h, 6h, 12h, and 24 h four rats/time point) by cervical dislocation. Further, the highly perforated organs (brain, and liver) were collected promptly and thoroughly rinsed in ice-cold saline to remove blood, and other content and blotted dry with filter paper [211]. Further, the samples were prepared and analyzed with an in-house developed bioanalytical method.

4.8 Development and optimization of Formulations

4.8.1 Synthesis and characterization of di-block amphiphilic polymer:

The di-block polymer was synthesized by a ring-opening method. The m-PEG (M ~ 5000 Da) was dissolved in toluene, and ϵ -caprolactone was added dropwise. Afterward, tin (II) 2-ethyl hexanoate was mixed, and the reaction was processed under a nitrogen atmosphere at 110 °C for 24 h [26]. Further, the reaction mixture was concentrated using a rotary evaporator, and the product was dissolved in dichloromethane, then chilled methanol was added to the obtained precipitate. Later wash the precipitate thrice with chilled diethyl ether and dry it properly (Fig.4.4) [27]. The synthesized polymer was evaluated and characterized by ¹H NMR and by gel permeation chromatography (GPC).

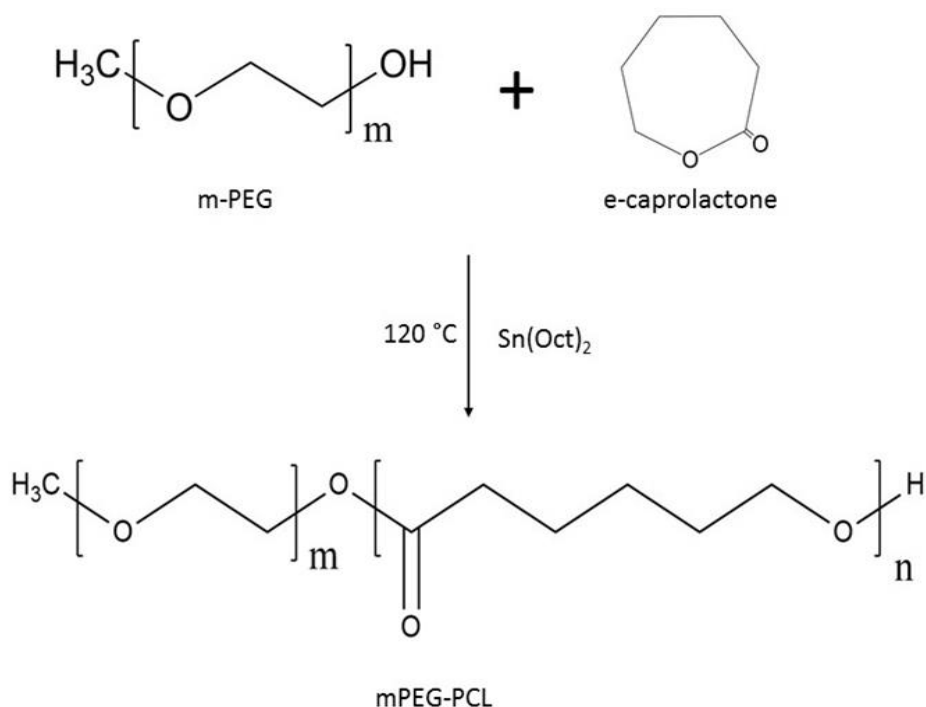


Fig. 4.4: Schematic representation of polymer synthesis

4.8.2 Fabrication of polymeric nanoparticles (PNPs)

The polymeric nanoparticles were formulated by the nanoprecipitation technique with modifications[174]. In brief, 2.5mg of REP, mPEG-PCL polymer was dissolved in 2 mL of acetonitrile (ACN) (Organic phase) followed by dropwise addition of 10 mL poloxamer 407 solutions (aqueous phase) under magnetic stirring for 3 h at 37 °C [174] (Fig. 4.5).

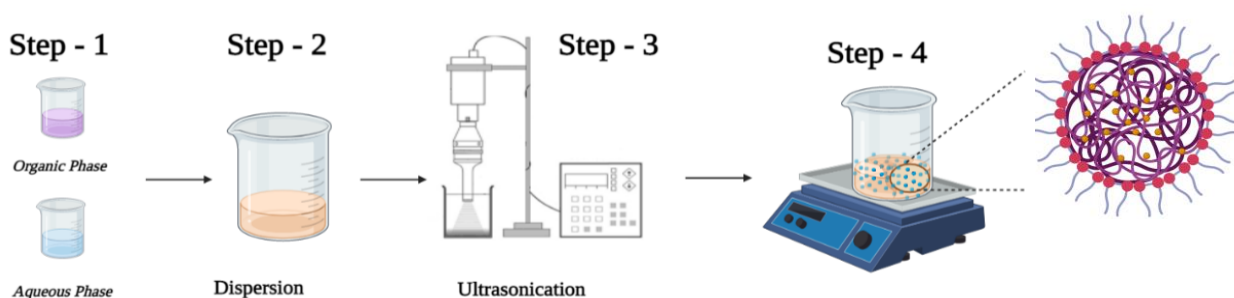


Fig. 4.5: Schematic representation of PNPs preparation procedure

The remaining amount of organic solvent was removed using a rotary evaporator and analyzed by headspace-gas chromatography (HS-GC) (Table 4.12).

Table 4.12: Instrumental parameters of GC-HS for estimation of residual organic content in nanoparticles

Headspace Parameters		Operating Parameters	
Oven temp	: 95 °C	Column	: Rtx-624 (30m X 0.32 mm X 1.8 μm)
Gas Pressure	: 10 psi	Pressure	: 7.2 psi
Pressurizing time	: 1 min	Injection mode	: Split
GC cycle time	: 23 min	Injection port temp	: 180 °C
Shaking Level	: 3	Flow control mode	: Linear velocity
Sample Line Temp	: 110 °C	Column flow	: 1.5 mL/min
Transfer Line Temp	: 120 °C	Total flow	: 91.5 mL/min
Load time	: 0.5 min	Linear velocity	: 22.3 cm/sec
Equilibrium Time	: 25 min	FID Temp	: 260 °C

4.8.3 Fabrication of Polymeric lipid-hybrid nanoparticles (PLHNPs)

The PLHNPs were fabricated by a one-step self-assembly method.[212] In brief, a lipid monolayer was prepared by phospholipid, and DSPE-PEG 2000 after dissolving in a 4% v/v ethanol-water solution. Further, the lipid solution was added dropwise into the deionized water containing 1% w/v stabilizer at 65 °C to maintain the dissolution situation of both the lipids and

prepared an aqueous lipid dispersion medium. Additionally, the weighed amount of REP (1 mg) and poly lactic-co-glycolic acid (PLGA,10mg) were dissolved in the acetonitrile (ACN). The organic phase containing drug and polymer was poured dropwise into the aqueous lipid dispersion medium (phospholipid, DSPE-PEG 2000, stabilizer) under probe sonication followed by continuously stirring at 400 rpm for 3 h and allowed to self-assemble.[213,214] Further, the rotary evaporate was used to remove the organic solvent residue in the PLHNPs and analyzed by headspace-gas chromatography (HS-GC) (Fig.4.6)

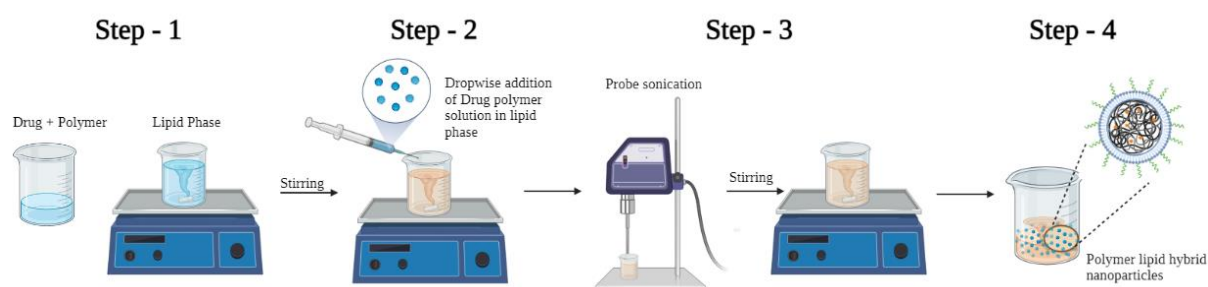


Fig. 4.6: Schematic representation of PLHNPs preparation procedure

4.8.4 Optimization of formulation using quality by design approach

4.8.4.1. Quality Target Product Profile (QTPP)

A QTPP assists in predicting the essential characteristics of the drug product that can be attained to ensure the safety, quality, and efficacy of the drug product. QTPPs are the pivotal elements of the QbD approach and have a crucial role in defining the objectives to develop the drug products (Table.4.13).

Table.4.13: Quality target product profile (QTPP) of REP-loaded PNP and PLHNPs

Target Product Profile	Target	Justification
Dosage	Powder	For ease oral application
Route of administration	Oral	Patient compliance
Appearance	White	Flowable and odorless
Particle size	<150 nm	Enhance permeation to BBB
PDI	< 0.5	Uniform distribution of particle size
Entrapment efficiency	Maximum with desired size range	Maximum entrapment improves permeation and increases drug loading
Release	Control release compared to free drug	Prolong the effect and enhance the efficacy

4.8.4.2. Critical Quality Attributes (CQA)

CQAs are derived from the QTPP and help to identify the key factors which alter the quality of the product. Furthermore, CQAs determine the range or limit for the acceptability to attain the expected product quality. In addition, CQAs emphasize the characteristics which affect the

overall quality and are categorized based on severity. This implies the risk assessment scale and ranks based upon the gauge of severity to predict its impact on safety as well as efficacy. Further, depending on the QTPP of the PNPs and PLHNPs, CQAs were allocated for the formulation.

4.8.4.3. Identification of critical material attributes (CMAs) and process parameters (CPPs)

The CMA and CPPs are two crucial parameters that directly contribute to the variability and efficacy of the CQAs. CMAs are linked with the formulation composition whereas CPPs are allied with the manufacturing and formulation process. CMAs are identified based on the theoretical modeling and design of experiments in the quality risk assessment process, while CPPs are recognized with the process and unit operation.

4.8.4.4. Initial risk assessment

Initial risk assessment assists in recognizing the material attributes and process parameters which effectively affect the product CQAs. Based on the initial experimental data and prior knowledge, a risk assessment tool could be used to identify the order and rank of parameters that could potentially impact the quality of the final product. Initially, the interdependence rating was executed on a three-level scale between CQAs, CMAs, and CPPs and categorized as “high” (H), “medium,” (M), or “low” (L). Afterward, a rating was performed related to the selected CQAs, CMAs, and CPPs, and risk estimation results were calculated and ranked according to severity scores (Table.4.14) [215].

Table.4.14: Risk estimation matrix (REM) for initial risk assessment of different material attributes and process parameters by qualitative analysis.

Critical quality attribute	Material attributes and process parameters						
	Polymeric nanoparticles (PNPs)						
	Drug polymer ratio	Amount of stabilizer	Stirring speed	Stirring time	Organic solvent	Sonication time	Sonication amplitude
Particle size	High	High	High	Medium	Low	High	High
PDI	High	Medium	High	Medium	Low	Medium	Medium
Entrapment efficiency	High	High	Medium	High	High	High	Medium
	Polymer lipid hybrid nanoparticles (PLHNPs)						
	Drug polymer ratio	Lipid polymer ratio	Lipid DSPC-PEG _{2K} ratio	Amount of stabilizer	Stirring time	Stirring speed	Sonication time
Particle size	High	High	Medium	High	Medium	High	High
PDI	High	Medium	Low	Medium	Medium	High	Medium
Entrapment efficiency	High	High	High	High	High	Medium	High

4.8.4.5. Experimental design

The statistical optimization of PNPs and PLHNPs was achieved by response surface methodology via Box-Behnken experimental design (BBD) using Design Expert® software 13 (M/s Stat-Ease Inc., Minneapolis, MN, USA). Based on the CMAs and CPPs experimental factors and factor levels were selected. The BBD consists of center points and a set of points lying in the midpoint of the cube, defining the region of interest. The statistical design was generated to optimize the system with 17 experimental runs and comprised three independent variables with their low (-1), medium (0), and high (+1) levels. All other parameters were kept constant during the experimentation.

4.8.4.6. Optimization of data analysis and model validation

The optimization of data analysis and model validation was done by Design Expert® software 13. The interaction of the factors was assessed by the second-order polynomial (quadratic) equation which is created by the experimental design

$$Y=b_0+b_1A+b_2B+b_3C+b_{12}AB+b_{13}AC+b_{23}BC+b_{11}A^2+b_{22}B^2+b_{33}C^2$$

Here Y denotes response; b_0 indicates constant; b_1 , b_2 , and b_3 represent linear coefficients, b_{11} , b_{22} , and b_{33} are quadratic coefficients, and b_{12} , b_{13} , b_{23} signify interaction coefficients. Further A, B, and C represent the coded intensity of independent variables. The terms A^2 , B^2 , and C^2 define the interaction and quadratic terms, respectively. The fit of data was evaluated by the factor-response relationship in terms of analysis of variance (ANOVA), lack of fit, coefficient of correlation (R^2), adjusted R^2 (R^2 -adj), and predictive R^2 (R^2 -pred). The regression model fitted well when the lack of fit is $P < 0.05$ (lower than the pure error), but the model is attuned poorly when the lack of fit is $P > 0.05$ (lower than pure error). Furthermore, the factor-response relationships were computed and depicted graphically via 2D-contour plots and 3D-response surface plots [215].

4.9. Lyophilization process optimization

The benchtop lyophilization process was used to optimize the lyophilization of PNPs and PLHNPs. In brief, various cryoprotectants (i.e., sucrose, trehalose, mannitol, glucose, and lactose) and different ratios (2%, 5%, and 10% w/v) of selected cryoprotectant was screened out to identify the suitable cryoprotectant. Further, batch lyophilization was carried out on the selected cryoprotectant and three sequential steps were used to accomplish the process i.e; lyophilization cycle freezing (14 h), primary drying (34 h), and secondary drying (8 h) (Table.4.15) [216].

Table.4.15: Lyophilization Cycles for lyophilization of REP-loaded PNPs and PLHNPs

Steps/segment	Temperature (°C)	Hold time (h)	RAMP (°C/min)
Freezing*			
1	10	1.00	5.00
2	0	2.00	2.00
3	-10	1.00	1.00
4	-30	2.00	1.00
5	-55	8.00	0.25
Primary Drying**			
1	-55	8.00	0.25
2	-20	6.00	0.25
3	-10	6.00	0.25
4	4	6.00	0.25
5	20	8.00	0.25
Secondary Drying***			
1	25	8.00	0.25

*Vacuum-off ; ** Vacuum-200 m Torr; *** Vacuum- 100 m Torr

4.10. Physicochemical characterization

4.10.1 Particle size, Poly dispersibility index, and Zeta potential: Dynamic light scattering (DLS) method was used to measure the z-average PS, PDI, and zeta potential (ZP) of the formulated PNPs and PLHNPs using a Malvern Nano ZS (Malvern Instruments Ltd., UK). The prepared nano-dispersion was diluted in a ratio of 1:10 with filtered milli-Q water and sample analysis was carried out at 25°C, 173°backscattering with 1.330 dispersants refractive index for determination of PS, PDI.

4.10.2 Entrapment efficiency (EE): The EE of PNPs and PLHNPs was determined by the ultracentrifugation technique. The dispersant was centrifuged at 40,000 RPM for 35 min at 10 °C after this the centrifuged pellet was diluted with ACN, and bath sonicate for 15 min. The samples were examined by the RP-HPLC method and EE was calculated by using the below-mentioned formula.

$$EE\% = \frac{\text{Amount of REP in nanocarrier}}{\text{Theoretical amount of REP loaded during preparation}} \times 100$$

4.10.3 Morphological characterization: The surface morphological characterization of PNPs and PLHNPs was determined by field emission-scanning electron microscopy (FE-SEM) and high-resolution transmission electron microscopy (HR-TEM). In FE-SEM the nano dispersion of PNPs and PLHNPs (500µL) were diluted in Milli Q water and dried samples were positioned on carbon tape affixed to a metal stub and sputtering was done with gold for the 90s using a Quorum Technologies Q150TES sputter coater (East Sussex, England) to avoid charge accumulation. Further, coated nanoparticles were examined by an FE-scanning electron microscope (Hillsboro, Washington) at 20,000× magnification, 20 kV high vacuum, a spot size of 9.0, and a scale of 0.2–3 µm. Moreover, in HR-TEM analysis (Hitachi (H-7500) the nano

dispersion of PNPs and PLHNPs have splayed on a carbon-coated copper grid and was stained for visualizing with 2% uranyl acetate.

4.10.4 Attenuated Total reflectance-Fourier Transform Infrared (ATR-FTIR): The ATR spectra of REP, BPNPs (placebo polymeric nanoparticles), PNPs, BPLHNPs (placebo polymer lipid hybrid nanoparticles) and PLHNPs were subjected to infrared analysis to measure the interference. The individual samples (4 mg) were placed on ZnSe sample crystal and scanned from 4000 cm^{-1} to 600 cm^{-1} using a Bruker alpha-one FTIR spectrophotometer (Bruker Optik, Germany).

4.10.5 Differential scanning calorimetry (DSC): DSC-60 plus (Shimadzu, Kyoto, Japan) was used to analyze DSC analysis. The thermograms of REP, BPNPs, PNPs, BPLHNPs, and PLHNPs were acquired by adding 4 mg of sample (each) into an aluminum pan, using an empty pan as a reference. The individual samples were heated between $30\text{ }^{\circ}\text{C}$ - $350\text{ }^{\circ}\text{C}$ temperature range with the rate of $10\text{ }^{\circ}\text{C}/\text{min}$ under $50\text{ mL}/\text{min}$ nitrogen purge.

4.10.6 powder X-rays diffraction (pXRD): The pXRD was used to evaluate the crystallinity of the compounds. Crystallinity is deemed undesirable in pharmaceuticals because it shows slow to incomplete dissolution. Thus, pXRD analysis of REP, BPNPs, PNPs, BPLHNPs, and PLHNPs was performed by the diffractometer (Rigaku-mini flex). The voltage was set to 30 kV over a 2θ range from 10° to 60 at a scanning speed of $1^{\circ}/\text{min}$ with Cu ($\lambda = 1.54$) tube as an anode.

4.11 *In vitro* drug release study

In vitro release study of REP, PNPs, and PLHNPs were carried out by using the dialysis bag method. REP, PNPs, and PLHNPs (equivalent to $500\text{ }\mu\text{g}$ of REP, $n=3$) were inserted into an overnight dipped dialysis bag (MWCO of 10 kDa, Himedia Laboratories. Pvt. Ltd.,). The bag was sealed from the sides with the thread and dipped in 50 mL of biorelevant dissolution media (phosphate buffer saline, pH 7.4 containing 0.1% sodium dodecyl sulphate) under a shaking water bath (120 rpm , $37 \pm 0.5\text{ }^{\circ}\text{C}$).^[217] The 1mL aliquot of the release media was withdrawn at preset intervals and replenished with the same volume. Further, samples were filtered and analyzed by the RP-HPLC method.^[174] The drug release mechanism and kinetic were calculated by mathematical models using a DD solver (an Excel add-in). The best-fit model of the release profile was determined based on the lowest Akaike index criteria (AIC) value and high regression coefficient (R^2).

4.12 Stability in simulated biological fluids

The stability of PNPs and PLHNPs in a simulated gastrointestinal tract (GIT) was investigated by three phases mouth phase, gastric phase, and intestinal phase. In order to mimic the

conditions, all the solutions and/or samples were pre-incubated in a bath shaker at 37°C at 100 rpm. Simulated saliva fluid (SSF) was prepared by using 30 mg/mL mucin and other salts to modulate the mouth phase conditions. The PNPs and PLHNPs were associated with SSF at a mass ratio of 1:1 and the mixture were placed in a bath shaker for 10 min with adjusted pH of 6.8. Whereas in the gastric phase, simulated gastric fluid (SGF) consisted of 3.2 mg/mL pepsin, 0.1mM hydrogen chloride, and 2 mg/mL sodium chloride. The sample was taken from the mouth phase and mixed with the SGF at a mass ratio of 1:1 and the mixture was placed in a bath shaker for 2 h.[218] In intestinal Phase, the sample was taken from the gastric phase and diluted in a mass ratio of 1:1 with simulated intestinal fluid (SIF) which is composed of 0.5M CaCl₂, 7.5 M NaCl, 50mg/mL bile extract, and 24 mg/mL pancreatin. The mixture was placed in a bath shaker for a further 2h to mimic the conditions [219].

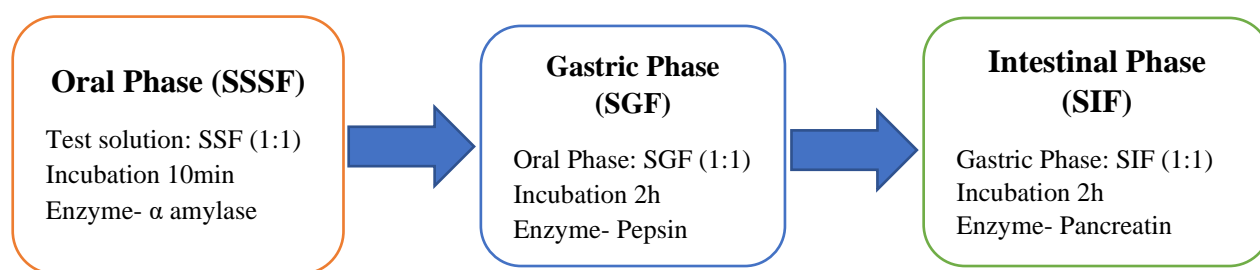


Fig.4.7: The flowchart to perform Gastro-intestinal stability studies

4.13 Stability study of lyophilized formulation

The stability study of freeze-dried PLHNPs was performed as per the International Council for Harmonization of Technical Requirements for Pharmaceuticals for Human Use (ICH, Q1A, R2). The stability of lyophilized PNPs and PLHNPs was assessed at 25°C ± 2°C/ 65 ±5% RH in the stability chamber for 3 months and PS, PDI, ZP, and % EE were estimated every 30 days [220].

4.14 Protein absorption assay

The protein absorption efficiency of PNPs and PLHNPs was assessed by Biuret assay. In brief, BPNPs and BPLHNPs (5mg) were placed in 4% bovine serum albumin (BSA) solution and incubated in a shaking bath incubator for 24 h at 37±0.5°C [221]. Afterward, the nanocarriers were centrifuged at 35000 rpm for 30 min and reagent (biuret reagent, 4 mL) was added in 1 mL of nanocarriers supernatant. The solution was incubated in a shaking bath for 30 min at 120 rpm and later, analyzed using a UV–vis spectrophotometer at 540 nm for assessment of unabsorbed proteins.[222]

4.15 *In situ* absorption and permeation assay

4.15.1. Single pass intestinal perfusion (SPIP) model

The animals were retained in polyacrylic cages under controlled conditions (12 h light/dark cycle, $22 \pm 1^\circ\text{C}$ with 60% relative humidity) and fed with the normal diet with purified water *ad libitum*. The wistar rats were acclimatized for at least seven days and then divided randomly into groups *viz.* REP, PNPs, and PLHNPs. Furthermore, rats were fasted for approximately 12-16 h, with free access to water, and anesthetized by intraperitoneal administration of xylazine (0.02g/kg) and ketamine (0.10g/kg). The rats were laid on a heating pad or kept under the lamp to maintain a body temperature of $37 \pm 1^\circ\text{C}$ [223,224]. Afterward, the laparotomy was performed, through a middle incision of approximately 4 cm in the abdomen to isolate the proximal jejunum portion (15-20 cm) of the small intestine (Fig.4.8). Furthermore, the proximal jejunum area was cannulated from both ends by using a plastic tubing of 3 mm o.d.

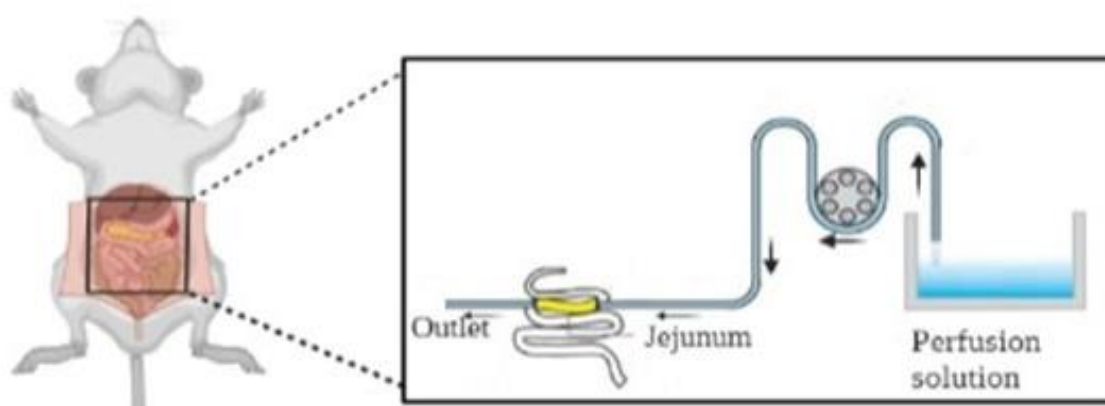


Fig 4.8: Illustration of SPIP model for in situ permeation study in wistar rat model.

The intestinal segment was gently washed with prewarmed ($37 \pm 1^\circ\text{C}$) blank perfusion solution (Table.4.16) for nearly 30-45 min at a 0.5 mL/min flow rate or until the solution was clear. Thereafter, the perfusion solution containing REP/ PNPs/PLHNPs was infused for 1 h (approximately) with a 0.2 ml/min flow rate to achieve a steady state or equilibrium state with the intestinal membrane [225]. As it reached a steady state, the perfusion solution was collected at the pre-determined time interval of every 15 min and withdrawn samples were immediately frozen at -80°C until further analysis.

Table.4.16: Composition of Perfusion solution for SPIP.

Ingredients	Amount
Potassium chloride	5.4 mM
Sodium chloride	48 mM
di-Sodium hydrogen phosphate	28 mM
Sodium dihydrogen phosphate	43 mM
Mannitol	35 mM
D-glucose	10 mM
Polyethylene glycol-4000	1g/L

At last, rats were euthanized by intracardiac injection, and infused intestinal segments length (L) and diameter were carefully measured [225–228]. The effective permeability coefficient (P_{eff}) value was calculated by below formula.

$$P_{eff} = -\frac{Q \cdot \ln C'_{out}/C'_{in}}{A}$$

where Q is the perfusate flow rate (mL/min), C'_{out}/C'_{in} signifies the corrected ratio of outer concentration to inlet perfusate, and A denotes intestine surface area (cm²). However, the apparent first-order absorption rate constant (K_a) was calculated using the following formula.

$$K_a = \frac{[1 - C'_{out}/C'_{in}]Q}{\pi r^2 l}$$

Here, r and l indicate the radius and the length of the perfused intestinal segment.

The quantitate detection of both the eluents *i.e.*, phenol red and REP was done by modifying the developed RP-HPLC method. The Shimadzu HPLC system (LC- 2010HT, Shimadzu Corporation, Japan) equipped with a pulse-free solvent delivery system and UV–visible detector was used. The separation of eluents was carried out on waters Nova-pack C18 column (3.9 × 150 mm, 4 μm particle size) [174]. The detector was set at a maximum wavelength of 243 nm and 398 nm for eluent data acquisition (REP and phenol red respectively). The obtained perfusate samples were centrifuged (10,000 rpm for 30 min), filtered (0.22μm), and diluted with acetonitrile appropriately.

4.15.2. Parallel artificial membrane permeability assay-blood brain barrier (PAMPA-BBB)

The PAMPA assay was mainly conducted to investigate passive permeability. In brief, samples were prepared at the concentration of 1.0 mM in dimethyl sulfoxide (DMSO) and diluted with Phosphate Buffer Saline (PBS); at pH 7.4 to make secondary dilutions for the donor compartment. Further, the filter membrane was layered with porcine polar brain lipid (PBL, 5 μL) extract solution and the receiver well contained 400 μl PBS. Consequently, the plates were

placed over each other as a sandwich where the PBL-coated membrane was positioned between and maintained to prevent the formation of air bubbles at the lower side (Fig.4.9). Then the plate was incubated without agitation for 18h at room temperature [229,230]. Furthermore, the samples were collected from the donor and acceptor compartment, diluted adequately, and quantified by the RP-HPLC method. The assay was carried out in triplicates and the permeability coefficient (Pe) was estimated using an equation.

$$Permeability (Pe) = \frac{-2.303}{A(t - \tau_{SS})} \times \left(\frac{V_a \times V_d}{V_a + V_d} \right) \times \log \left[1 - \left(\frac{V_a + V_d}{(1 - R) \times V_d} \right) \times \left(\frac{C_d(t)}{C_d(0)} \right) \right]$$

where Pe notes as effective permeability coefficient (cm/s), A indicates filter area (0.24 cm²), VD and VA are the volumes in the donor and acceptor phases, t stands for incubation time (s), τSS signifies time (s) to reach steady-state, CD(t) indicates the concentration of the compound in the donor phase at time t, CD(0) implies as the concentration of the compound in the donor phase at time 0, and R estimates membrane retention factor.

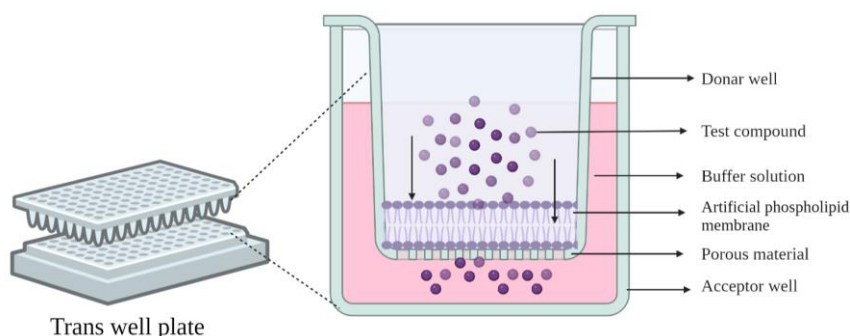


Fig. 4.9: Illustration of Parallel artificial membrane permeability assay-blood brain barrier (PAMPA-BBB)

4.16 *In vitro* & *In vivo* analysis

The *in vitro* cell culture-based studies (cell viability, cell uptake, STZ and hydrogen peroxide assays) and *in vivo* (pharmacodynamic, pharmacokinetic and biodistribution) studies were performed as mentioned in the section 4.4, 4.5, 4.6 and 4.7 respectively.

4.17 Data analysis

All results were expressed as mean ± standard error mean (S.E.M.). The experimental data were analyzed using a graph pad with a one-way analysis of variance (ANOVA) followed by Tukey’s test at a defined significant level of $p < 0.05$.

5.1 Quantitative determination of REP by HPLC method

5.1.1.1 Preliminary method development studies

The RP-HPLC method development was done by checking various parameters such as mobile phase composition, mobile phase ratio, column, column temperature, flow rate, etc., to obtain a good peak shape with less run time, less tailing, high theoretical plates, and resolution. In this study, various solvents were tried as mobile phases like methanol, acetonitrile, and water containing 10mM formic acid, glacial acetic acid, and potassium dihydrogen phosphate by changing the flow rates in the range of 0.8 mL/min to 1.0mL/min. These varied combinations implied that acetonitrile with 10mM of potassium dihydrogen phosphate as the aqueous phase suited the most as the mobile phase. It offered superior chromatographic separation with peak symmetry and a minimum tailing factor, better resolution, and a high theoretical plate count.

5.1.1.2 Risk Assessment Studies

The risk evaluation matrix studies were established by examining the relationship between various input process parameters and analytical attributes, as illustrated in the Ishikawa fishbone diagram. It helps to identify possible risk factors and improve the quality defects for the further screening process. The critical variable was defined as per the risk management method, based on the risk associated with each variable. The influential factors, including the mobile phase ratio, pH of the aqueous phase, flow rate, column temperature, injection volume, buffer strength, and organic modifiers, were significant and selected for the subsequent factor screening studies.

5.1.1.3 Factor Screening study: Taguchi design model

The screening study of factors was performed on the selected CMPs by using the Taguchi design model. The Taguchi design was performed on the already disclosed seven factors, i.e., CAAs, which influence the retention time, tailing factor and theoretical plates count. The Taguchi design was evaluated by a half-normal plot and Pareto charts (Fig.5.1), which assisted to understand the effects.

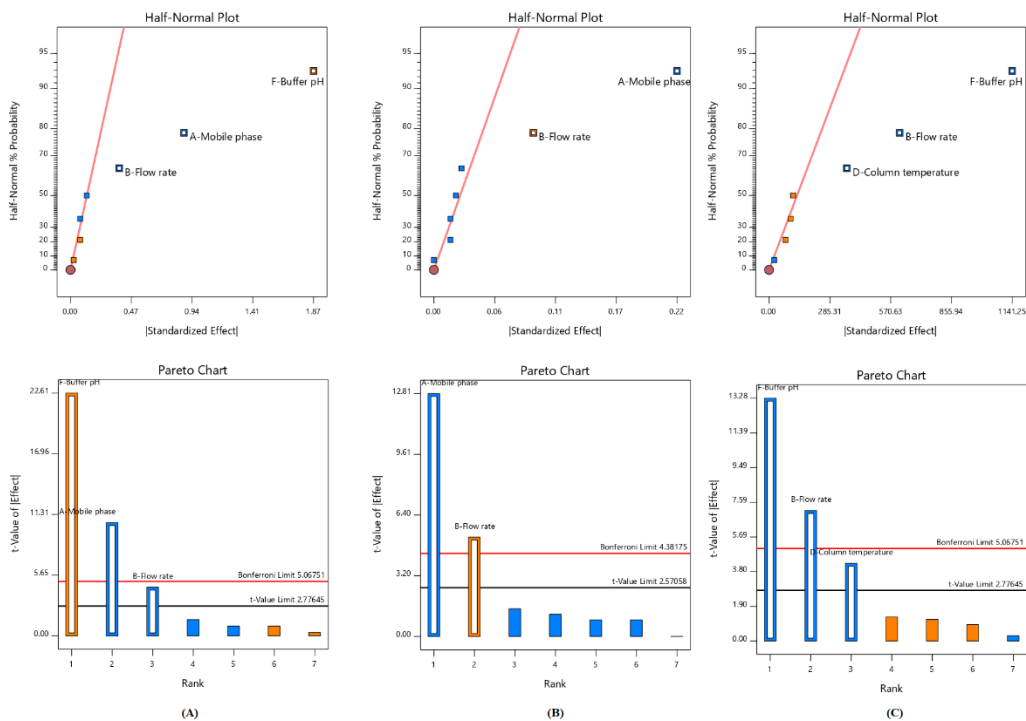


Fig.5.1: The half normal plot and Pareto chart indicating factors that influence response variables of the RP-HPLC method, (A) retention time, (B) Peak tailing, (C) theoretical plates. The Positive influencing factors were shown in orange whereas the negative shown in blue.

The factors exhibited a significant effect ($p < 0.05$) on the mobile phase, flow rate, and pH of the buffer. It was observed that the retention time was positively influenced by the pH of the buffer, showing an increase in the pH of the buffer, increase in the retention time, whereas the mobile phase ratio exhibited an analogous positive relationship with retention time. A positive effect of flow rate and a negative effect of the mobile phase was observed concerning the tailing factor. Similarly, in the theoretical plate count, a negative effect of flow rate and pH of the buffer was observed, which crosses the Bonferroni limit as it was observed in the Pareto charts and half-normal plot representing the impact of CMP on CAA. From Pareto ranking studies, it was observed that the mobile phase ratio, pH of the buffer, and flow rate were highly effective on the selected CAA, which was further used for the optimization studies.

5.1.1.4 Method optimization and response surface analysis

The method optimization studies were performed using response surface BBD, and data were analyzed by selecting the second-order polynomial model for illustrating the main and interactive effects. In BBD three influential variables constructed from the risk assessment and factor screening studies *viz* mobile phase ratio (A), flow rate (B), pH of buffer (C) was further

investigated at three equidistance levels, i.e., low (-1), medium (0) and high (+1). A fixed concentration of REP was used throughout the study, and a BBD matrix containing 17 runs was analyzed. The significance of the impact of various CPPs on the selected CAAs, i.e., RT (R1), TF (R2), and PC (R3) were observed by using Design Expert. The selected influential factors were critically examined using a quadratic polynomial model fitting, as shown in equation 1.

$$Y = \beta_0 + \beta_1X_1 + \beta_2X_2 + \beta_3X_3 + \beta_4X_1^2 + \beta_5X_2^2 + \beta_6X_3^2 + \beta_7X_1X_2 + \beta_8X_1X_3 + \beta_9X_2X_3 \dots (1)$$

Where Y represents the measured response associated with each factor level combination, β_0 indicates the intercept of the produced polynomial model, and β_1 to β_3 represents the coefficient of the linear model term. The X_1 , X_2 , and X_3 are the coded levels of independent variables, and X_1^2 , X_2^2 , X_3^2 , X_1X_2 , and X_1X_3 stand for the quadratic term, interaction, respectively. Analysis of the factor response relationship was done using a 3D response surface and corresponding 2D counterplots for each CAAs. The full quadratic equation for RT (R1), TF (R2), and PC (R3) were generated by the response surface regression process as equations 2, 3,4 respectively.

$$R1 = +4.87 - 0.903*A - 0.292*B + 1.53*C - 0.050*AB + 0.6275*AC + 0.00*BC + 0.496*A^2 + 0.133*B^2 + 0.251*C^2 \dots (2)$$

$$R2 = +1.05 - 0.0987*A - 0.0434*B - 0.0087*C - 0.020*AB + 0.0025*AC + 0.025*BC + 0.115*A^2 + 0.0215*B^2 + 0.251*C^2 \dots (3)$$

$$R3 = +3973.95 - 37.62*A - 417.63*B - 296.63*C - 1800*AB + 0.75*AC + 283.0*BC + 99.53*A^2 + 44.26*B^2 - 186.97*C^2 \dots (4)$$

Here, the equations 2,3, and 4 illustrate that a positive value shows an impact that favors optimization, while negative values depicted an inverse relationship observed between the factors and response. It is evident by the coefficient of the equation and response surface plot, the RT, TF, and PC count are highly dependent and have a high degree of interaction with the selected independent variables. Furthermore, a 2D counter plot and 3-D response surface show a CMP's effect on the CAA's retention time (Fig.5.2).

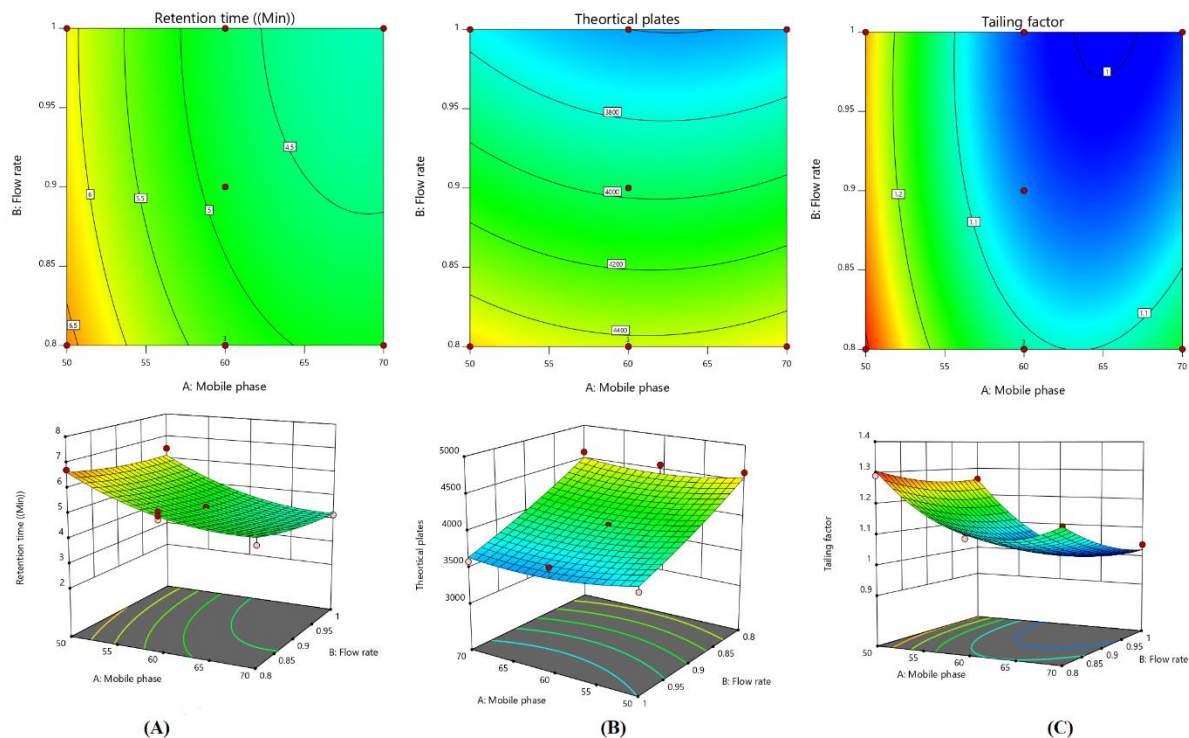


Fig.5.2: The 2D-contour plots and 3D-response surface plots show the relationship among the factors on (A) retention time, (B) theoretical plates, and (C) Tailing factor.

Through the decrease in the ratio of mobile phase (organic) and flow rate, the increases in retention time were observed. The curvilinear rises in retention time up to the intermediate levels followed the gradual decreases at the high level and the model was found significant with an insignificant lack of fit with $0.9832 R^2$, $0.9616 R^2$ -adj, and $0.8303 R^2$ -pred. In the case of the tailing factor, the model was found to be significant ($p < 0.0001$), and the lack of fit was insignificant ($p < 0.529$) with $0.9879 R^2$, $0.9724 R^2$ -adj, and $0.9104 R^2$ -pred. The 3D response surface and 2D counterplot represent an increase in the mobile phase ratio with flow rate, and a decrease in the tailing factor was observed. Subsequently, in theoretical plate count, the model was found to be significant ($p < 0.0001$), and lack of fit was insignificant ($p < 0.7895$) with $0.9663 R^2$, $0.9230 R^2$ -adj, and $0.8582 R^2$ -pred.

5.1.1.5 Optimized method conditions

The optimum chromatographic conditions were examined by performing numerical and graphical optimization with the different CAAs to achieve the desired goal, i.e., minimum RT, TF, and

maximum of the PC for attaining the maximum desirability function, i.e.,0.997, which is close to 1 with final optimization conditions (Fig.5.3).

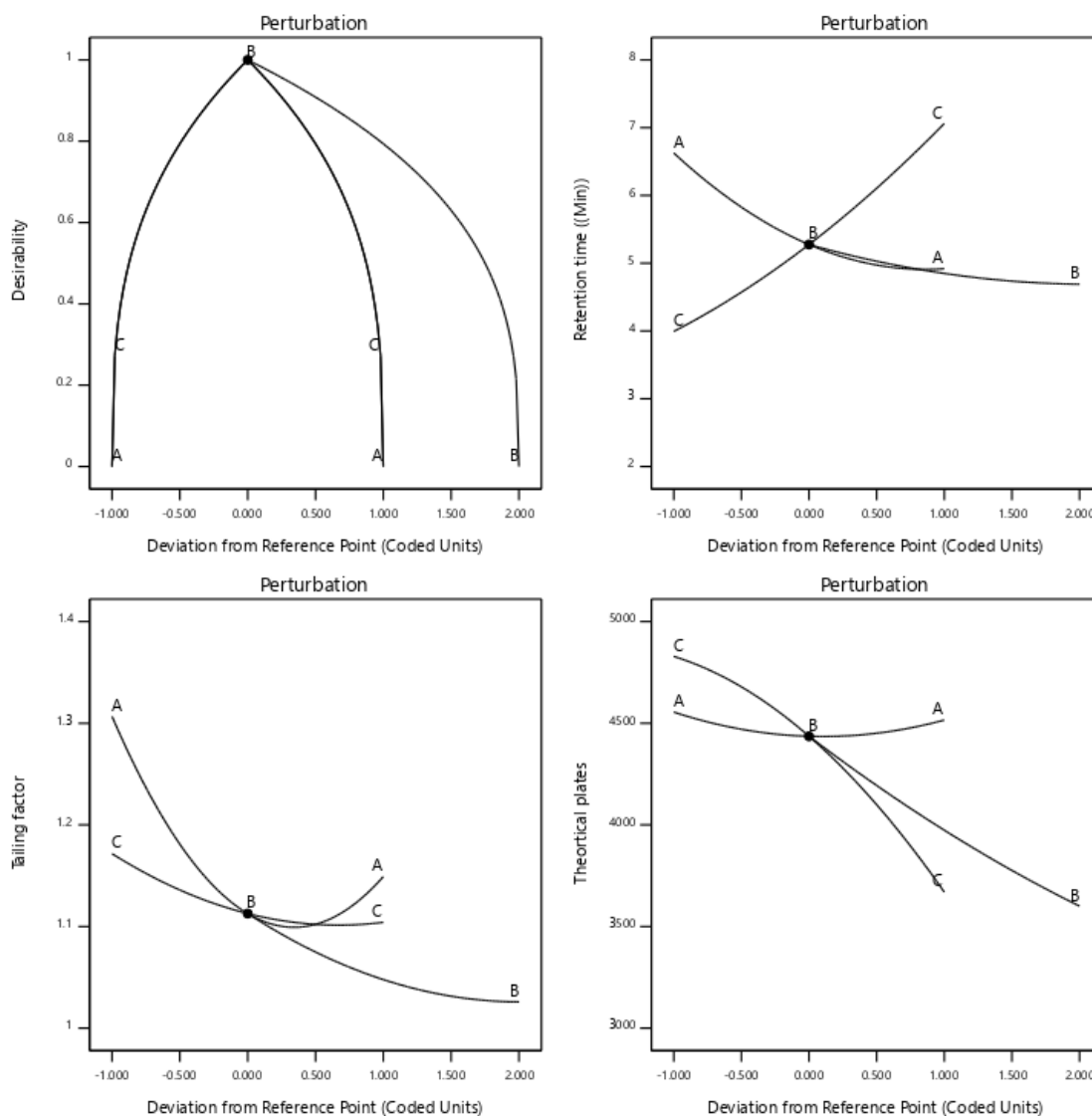


Fig.5.3: Perturbation chart

The results demonstrate the effect of an optimum ratio of mobile phase (medium), flow rate (minimum), and pH of buffer (medium) to get maximum PC, minimum RT, and TF. The developed RP-HPLC chromatographic optimized method was shown a mobile phase composition comprising the 60:40 v/v ratio of acetonitrile and 10mM potassium dihydrogen phosphate at pH (3.5), the flow rate of 0.8 mL/min, evaluated the desirability value of 0.997 at 5.2 min of retention time, 1.1 tailing factor and 4437 theoretical plates.

5.1.2 Analytical Method validation of REP

The developed RP-HPLC method was validated in various parameters such as system suitability, selectivity, linearity, precision, accuracy, carryover, and robustness as per recommended ICH guidelines Q2 (R1) for analytical validation. The system suitability was measured by analyzing six replicates of the same concentration solution and observed that the % RSD of the peak area and RT were within the accepted criteria (Table 5.1).

Table.5.1: System suitability Parameter

Parameter	Results*
Retention time	5.25 ± 0.08
HETP	46.97 ± 2.73
Theoretical plates	4437 ± 10.52
Tailing factor	1.11 ± 0.03

* Data represented as Mean ± SD, n=6

In the selectivity study, no extra peak interference was observed corresponding to formulation excipients compared to the standard REP solution (Fig.5.4).

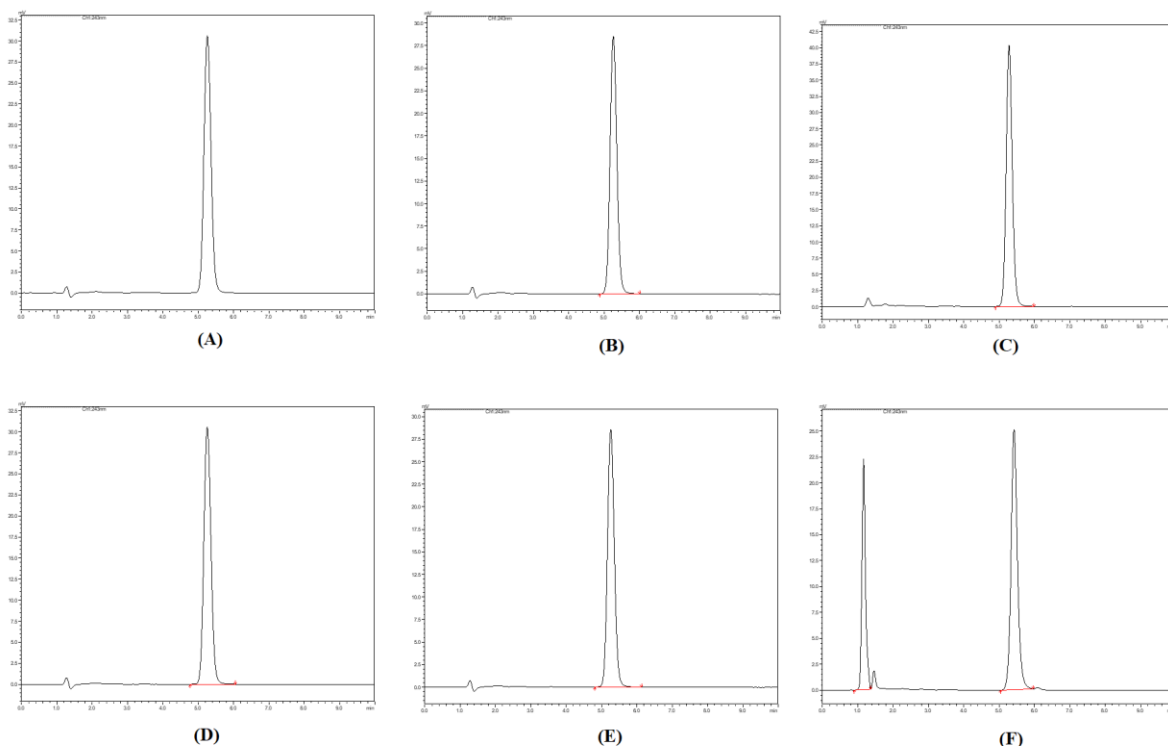


Fig.5.4. Repaglinide peaks (A) Std repaglinide 20µg/mL, (B)system-suitability, (C) Selectivity, (D) photo, (E) Thermal, (F) Acid

Linearity of REP was performed by six calibration curves for different concentrations (100-9000 ng/mL). All the calibration curves were linear and reproducible with a high value of the correlation

of coefficient ($r^2=0.999$). The method linearity was validated by analysis of variance and revealed significant linearity of regression with nonsignificant linearity deviation ($p < 0.05$) of the REP. The LOD and LOQ values of repaglinide were determined by the signal-to-noise ratio, and results were observed at 243 nm λ_{max} with an injection volume of 20 μ L. The LOD and LOQ were found to be 30 ng/mL and 100 ng/mL, respectively. The accuracy of the analytical method determined the degree of closeness between the obtained value to the true value and expressed in terms of % bias. Whereas precision measured the effect of random errors on the repeatability of the method and expressed it as % RSD. The accuracy, intra-day, and inter-day assay precision attained data from QC (LQC, MQC, HQC) samples of REP were enlisted in Table.5.2, and all the obtained values were within the range of recommended guidelines.

Table.5.2: Precision and accuracy for the analysis of repaglinide

Level	Nominal Concentration (ng/mL)	Intra-day		Inter-day	
		Precision (%CV)	Accuracy (% Bias)	Precision (%CV)	Accuracy (% Bias)
LQC	250	1.69	-6.86	1.48	-7.10
MQC	2500	0.13	-4.96	1.99	-1.04
HQC	8000	0.08	-3.10	1.65	1.46

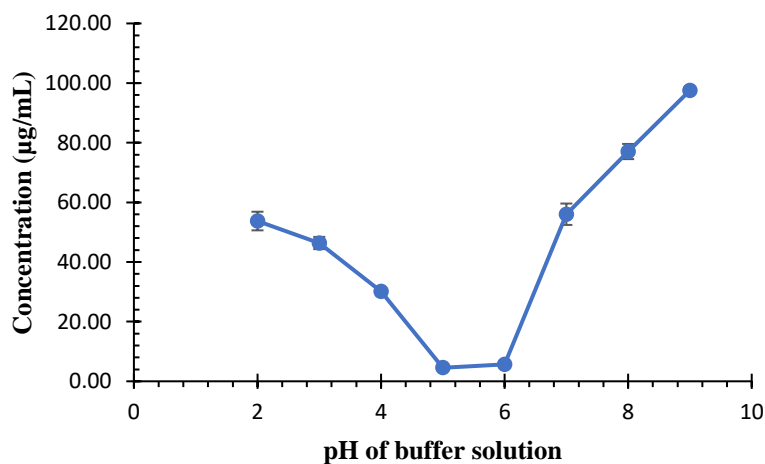
The carryover was assessed by injecting a blank sample after three continuous injections of high concentration sample of linearity range, and no peak of analyte was observed in the blank sample, which represents that the developed method has a zero-carryover effect. The robustness of the developed method was evaluated by changing the chromatographic conditions and observing that the developed method was robust, and results indicate that all the values were within the range of recommended guidelines.

The forced degradation study was performed in different stress conditions i.e., hydrolytic (acidic, basic), oxidation, thermal, and photolytic (UV, and fluorescent light) as per ICH Q1A (R2) recommended conditions. The observed results reveal that the REP degrades in acidic and basic conditions whereas it depicted a high degree of stability when subjected to thermal and photolytic conditions after 48h. (Table.5.3). In this study, it was found that after providing the stress conditions, no shift in the RT of REP was observed, which indicates that the developed method was selective.

Table. 5.3: Representing force degradation of repaglinide in various stress conditions (Mean \pm SD).

State	Stress conditions	Sample treatment	Repaglinide retention time (min)	Unexpected peaks	% degradation
	Reference	-	5.20 \pm 0.02	-	-
Solution state	Acid hydrolysis	0.1M, HCL; 8h	5.44 \pm 0.08	Yes	45.75 \pm 8.6
	Base hydrolysis	0.1M, NaOH; 8h	5.31 \pm 0.12	Yes	73.99 \pm 9.7
	Oxidation	30% H ₂ O ₂ ; 8h	5.29 \pm 0.07	Yes	21.98 \pm 5.9
Solid State	Thermal Degradation	60°C; 24 h	5.20 \pm 0.01	No	-
		60°C; 48 h	5.22 \pm 0.02	No	-
	UV Light	24 h	5.23 \pm 0.03	No	-
		48 h	5.21 \pm 0.01	No	-
	Fluorescent Light	24 h	5.20 \pm 0.02	No	-
	48h	5.20 \pm 0.04	No	-	

REP is a carbamoyl methyl benzoic acid derivative and a weakly acidic drug. It belongs to the BCS class II drugs and showed low solubility in the aqueous medium. In order to estimate the solubility of the REP solution different pH conditions were investigated as shown in Fig. 5.5. The observed results suggested that REP showed a minimum solubility in the 4-6 pH range. As the pH increased (above 6) the solubility increased and in lower pH conditions (acidic conditions i.e 2-4) the solubility of REP decreased. The biphasic nature of REP is due to the presence of two proton binding sites of REP which gives it ampholytic nature and determined its zwitterionic form. Despite its zwitterionic nature, REP is rather lipophilic as it has a high log *P* value i.e., 3.97. This is probably due to the presence of intramolecular electrostatic attraction of positively charged aromatic amino group and negatively charged carboxylate anion.

**Fig.5.5:** Solubility of repaglinide in aqueous buffer medium at different pH.

The REP analytical method was successfully developed and validated and applicable for the quantification of entrapment efficiency, release profile, and drug loading for in-house developed nanocarriers.

5.1.3 Bioanalytical method development by HPLC

A methodological approach was used to accomplish REP from the biological matrix in less time with simple chromatographic conditions such as symmetric peak, good resolution, no tailing, no fronting, and reproducible recovery. To attain this parameter the chromatographic conditions were selected such as mobile phase selection, mobile phase composition, pH of the aqueous phase, column selection, column temperature, flow rate, and injection volume were optimized (Table.5.4). Though acetonitrile-phosphate buffer (pH:3.5;0.01M) with 40:60 %v/v at 0.8mL/min flow rate in isocratic mode was selected as it provides symmetric peak shape, good intensities, and resolution between the IS and REP with a run time of 15min. As the chromatographic conditions were optimized then extraction recovery of REP was selected to be optimized using appropriate extraction methods such as PP, LLE, and SPE. Various methods for extracting REP from biomatrix have been tried using polar solvents such as acetonitrile, and methanol for protein precipitation extraction technique but the interference of matrix, and poor and inconsistent recovery was observed. Further LLE with ethyl acetate was found to be more appropriate due to consistent recovery, symmetric peak, and no interference of plasma proteins was observed (Table.5.5).

Table.5.4: RP-HPLC method optimization for estimation of REP in biomatrix

S.No.	Chromatographic condition	Parameters	Remarks
1.	Mobile phase composition (ACN: Phosphate buffer pH 3.5)	60:40 50: 50 40:60	Asymmetric peak of IS, less resolution Asymmetric peak and no proper ionization of analytes results in decreased peak intensity Symmetric peaks with proper ionization and resolution between the IS and analyte
Based on the results it was observed that for proper separation of IS and analyte from the biomatrix, it confirmed that ACN: phosphate buffer pH 3.5 with 40:60 % v/v was selected as the mobile phase			
2.	Flow rate (mL/min)	0.8 1.0	Symmetric peak with good resolution between IS and REP Asymmetric peak of IS and merge with matrix hindrance
Through the results, it was observed that for the method developed the flow rate should be 0.8 mL/min			
3.	Column temperature (°C)	40 30	Undesirable peaks were observed which might be the degradation product of analytes Symmetric and clean peak with proper resolution between the analytes
Based on the results, it was concluded that ACN: Phosphate buffer pH 3.5 with 40:60 % v/v was selected as the mobile phase. The flow rate and column oven temperature were optimized at 0.8 mL/min, 30 °C respectively, with symmetric peaks with proper resolution between the analytes.			

Results & Discussion

Table.5.5: Optimization of Liquid-liquid Extraction (LLE) method for sample preparation

Extracting technique	Extracting solvent	Sample volume (μL)	Volume of extraction solvent added (μL)	Vortex time (min)	Centrifugation [speed (rpm), time (min)]	% Recovery	Remarks
Protein Precipitation	Methanol	100	500	5	15000, 30	32.48 ±2.9	Interference of plasma matrix with poor recovery
	Acetonitrile	100	500	5	15000, 30	48.41±2.5	Splitting of peaks, interference of plasma with increase in the recovery but inconsistent recovery
Liquid-Liquid extraction	Methylene chloride (DCM)	100	500	5	15000, 30	27.53±1.6	High interference of plasma matrix with very poor recovery
	n-hexane	100	500	5	15000, 30	42.55±2.4	Slight increase in the recovery but inconsistent and high plasma interference was observed
	Ethyl acetate	100	500	5	15000, 30	72.49 ±2.1	Consistent recovery was observed, no interference of plasma proteins was observed
	n-hexane: ethyl acetate (40:60 v/v)	100	500	5	15000, 30	69.32 ±1.8	No interference of plasma proteins was observed but recovery was reduced

5.1.4 Bioanalytical Method validation of REP

In bioanalytical method validation, the system suitability test was performed to conform system working efficiency and reproducibility with proper resolution. Thus, in defined chromatographic conditions it was observed that the peaks were separated properly with a retention time of less than 15 min. The method was selective as no significant plasma matrix interference at retention time was observed (Fig.5.6).

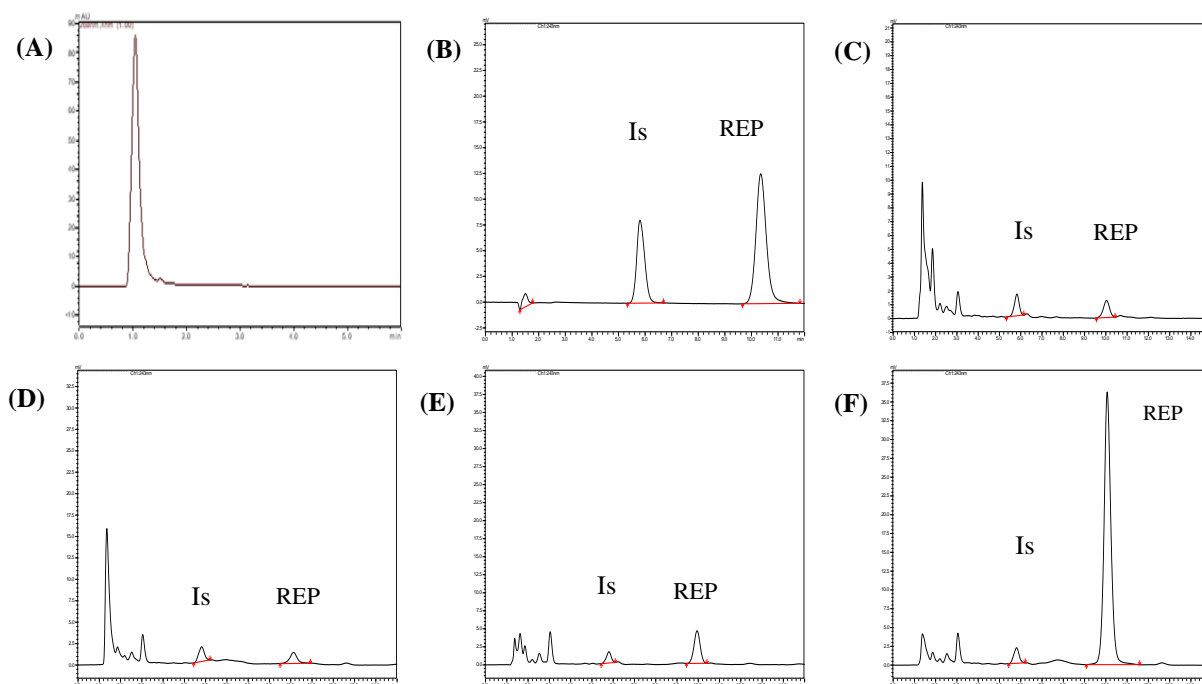


Fig. 5.6: HPLC Chromatograms for (A) Blank plasma (plasma sample without IS and REP) (B) Calibration standard (C) LLOQ (50ng/mL) (D) LQC (E) MQC and (F) HQC of REP.

The calibration curves were constructed using REP calibration standards in plasma, and tissue samples and represent linearity and reproducibility in the range of 50-20000 ng/mL with R^2 values more than 0.999. The accuracy and precision (intra and inter-day) studies were carried out for method validation and results obtained at different concentration levels from the QC sample (LLOQC, LQC, MQC, HQC) were within the recommended range and represented in Table.5.7

Table.5.7: Precision (% CV) and accuracy (% bias) of REP in rat plasma samples at QC levels (n=6)

Level	Nominal Conc. (ng/mL)	Inter-day			Intra-day		
		Measured Conc. (Mean \pm SD, ng/mL)	Precision n (% CV)	Accuracy (% bias)	Measured Conc. (Mean \pm SD, ng/mL)	Precision n (% CV)	Accuracy (% bias)
LLOQ	50	49.18 \pm 10.01	0.20	-1.64	50.94 \pm 5.50	0.108	1.898
LQC	100	104.53 \pm 5.12	0.04	4.53	107.66 \pm 7.19	0.065	10.119
MQC	2000	2010.83 \pm 42.86	0.02	0.54	2023.22 \pm 22.89	0.011	1.161
HQC	15000	15491.29 \pm 61.50	0.04	3.27	15051.18 \pm 72.49	0.048	0.341

The mean recovery values of REP from rat plasma samples are listed in Table.5.8 and absolute recovery was found to be 72.40 ± 2.15 % (n=12). Additionally, no carry-over effect was observed after injecting a higher concentration of standard and confirmed the absence of a carry-over effect.

Table.5.8: Absolute recoveries (%) of repaglinide in rat plasma samples from QC levels

Level	Nominal concentration (ng/mL)	n	Recovery (%)
			Mean \pm SD (n=3)
LLOQ	50	3	70.87 \pm 2.64
LQC	100	3	72.16 \pm 2.95
MQC	2000	3	71.08 \pm 4.21
HQC	15000	3	75.52 \pm 5.0
	Mean	12	72.40 \pm 2.15

n, number of samples; SD, standard deviation; CV, coefficient of variation

The stability studies for REP were performed as per the described procedure in which different stability conditions were provided such as benchtop stability, autosampler stability, freeze-thaw stability. The results represent that REP was stable and might not face any undesirable changes in the routine analysis as no significant degradation was observed (Table.5.9).

The developed and validated analytical, bioanalytical method for quantification of REP using RP-HPLC method is precise, accurate, sensitive, robust, and has high throughput with eco-friendly mobile phase composition. The analytical method of REP was successfully utilized to calculate entrapment efficiency, drug loading, and *in vitro* release kinetics for formulated nanoformulation whereas bioanalytical methods are used for pharmacokinetic and biodistribution studies of REP and REP-loaded nanocarriers.

Table.5.9: Stability studies for repaglinide in rat plasma at QC levels

Stability	Nominal concentration (ng/mL)	Measured Concentration (ng/mL) ± SD	Precision (% CV)	Accuracy (% bias)
Autosampler (48 h)	50	52.17±4.68	8.09	4.34
	100	114.96±5.17	4.49	8.96
	2000	2008.73±11.95	0.99	0.58
	15000	14974.55 ± 152.41	1.06	1.42
Bench-top (24 h, RT)	50	51.54 ± 0.89	1.74	3.098
	100	106.95 ± 1.78	1.66	6.954
	2000	2030.66 ± 22.65	1.11	1.53
	15000	14856.11 ± 277.10	1.86	-0.959
Freeze-thaw (-80 °C, 3 cycle)	50	50.96 ± 2.06	4.051	1.937
	100	108.88 ± 1.87	1.718	8.882
	2000	2072.27 ± 67.34	3.249	3.614
	15000	15048.98 ±80.54	7.929	1.660

5.1.5 Confirmation of Insulin resistance development in wistar rats

5.1.5.1 Effect of NPD and HFD+STZ feeding after 16 weeks on glucose, insulin, HOMA-IR index, and body weight

Prior to estimating the AD progression, we confirmed that the rats fed with HFD (16 weeks)-STZ have become insulin resistant. In order to do this, we checked the body weight and performed serum estimations of Insulin, HOMA-IR HbA1C, and FBGL level (Fig.5.7). It was observed that a consecutive increase in body weight, and significant ($P < 0.001$) amelioration in the level of FBGL, HbA1c, HOMA-IR, insulin of disease control rat as compared with the normal rats. Further, A β and Tau levels were found to be high in disease-control animals starting and significant differences were observed compared to normal control rats. The calculated high level of serum biochemical and neurochemicals indicates the presence of IR condition in HFD-STZ rats.

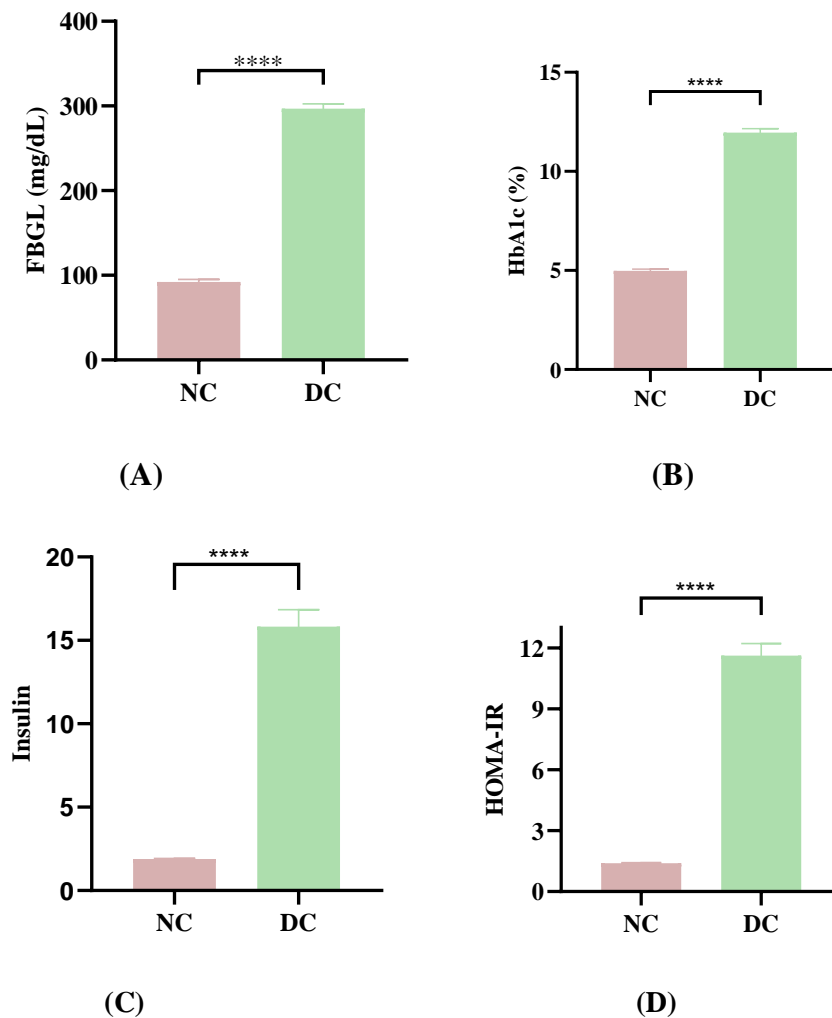


Fig.5.7: *In vivo* estimation of parameters to confirm the insulin resistance in rats (A) FBGL; (B) HbA1c; (C) insulin and (D) HOMA-IR; of HFD+STZ induced wistar rats, data are represented in (mean \pm SEM, n=6 rats per group). * Indicates, **** $P < 0.0001$ by t-test.

5.1.5.2 Effect of NPD and HFD+STZ feeding after 16 weeks on lipid profile

The effect of NPD and HFD with STZ were measured on lipid profile (TC and TG protein) to confirm the development of insulin resistance in the wistar rats as represented in Fig.5.8. The significant ($p < 0.001$) increase in the level of TC and TG in disease control rats compared to normal control rats suggest alterations in the pathophysiology of rats.

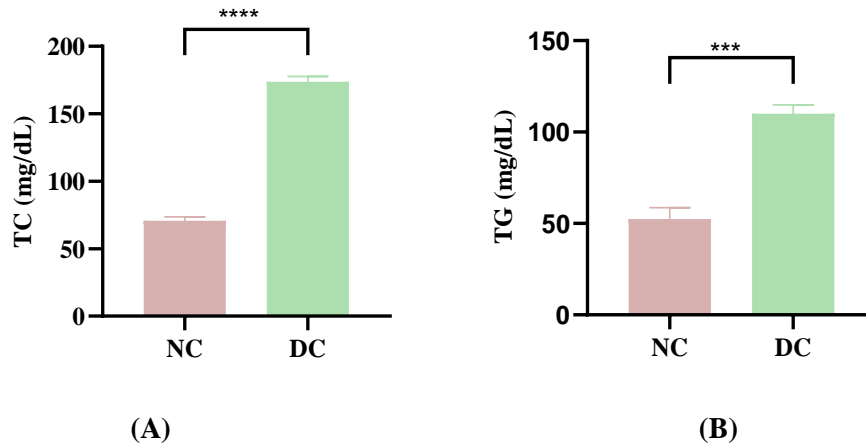


Fig.5.8: *In vivo* estimation of parameters to confirm the insulin resistance in rats (A) TC; and (B)TG of HFD+STZ induced wistar rats, data are represented in (mean \pm SEM, n=6 rats per group). * Indicates, **** $P < 0.0001$ by t-test.

5.1.5.2 Effect of NPD and HFD+STZ feeding after 16 weeks on neurochemicals

The effect of NPD and HFD with STZ was measured on neurochemical parameters ($A\beta$ and tau protein) to confirm the development of insulin resistance in the wistar rats as represented in Fig.5.9. The significant ($p < 0.001$) increase in the level of $A\beta$ and tau protein in disease control rats compared to normal control rats suggest neuronal alterations in wistar rats.

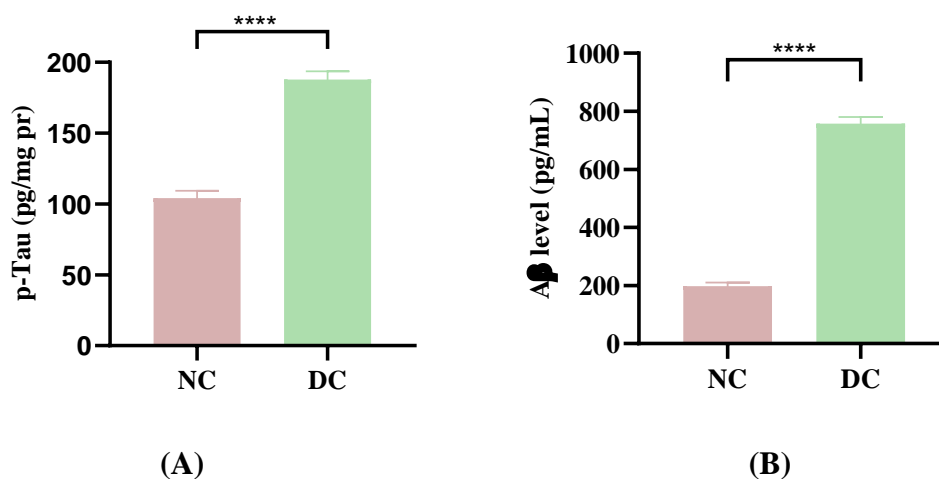


Fig.5.9: *In vivo* estimation of parameters to confirm the insulin resistance in rats (A) p-tau; and (B) $A\beta$ level of HFD+STZ induced wistar rats, data are represented in (mean \pm SEM, n=6 rats per group). * Indicates, **** $P < 0.0001$ by t-test.

5.2 *In vitro* studies on neuroblastoma cell lines (SHSY-5Y)

5.2.1 Cell viability assay

The viability assay indicates the number of live and/or healthy cells in a sample and measures the physical or cellular health in response to chemical agents, therapeutic treatments, or extracellular stimuli is referred to as cell viability assay. Here, cell viability was estimated by MTT assay in which oxidative metabolic activities were measured based on NAD(P)H-dependent dehydrogenase enzyme activity. Primarily, the concentration of REP (0.25-100 $\mu\text{g}/\text{mL}$) was explored on SHSY-5Y cells, and a dose or concentration-dependent toxicity was observed as shown in Fig.5.10. Therefore, the results suggested that at 1 $\mu\text{g}/\text{mL}$ around ~80-85% cells were viable, which was used for further analysis.

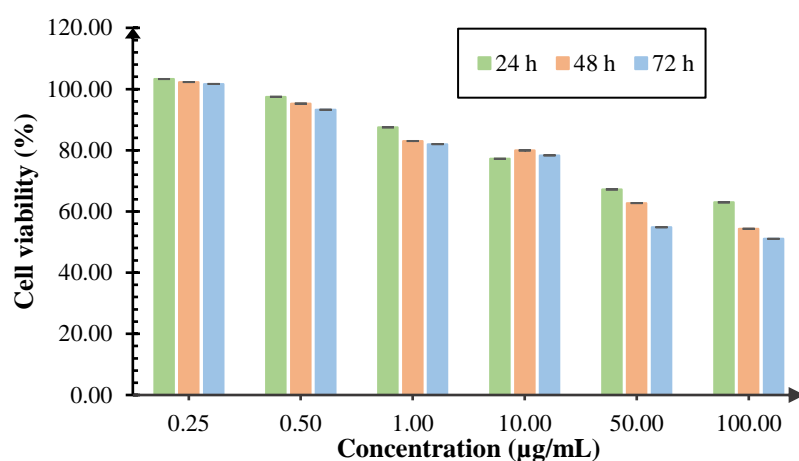


Fig.5.10: Cell viability assay of REP on neuroblastoma SH-SY5Y cell line.

5.1.2 STZ Treated neuroblastoma cell-based study

STZ is a diabetogenic agent which accelerated brain aging, hippocampal atrophy, $\text{A}\beta$ aggregation, and loss of synaptic connections [20]. In neurons, STZ leads to depolarization of the mitochondrial membrane, oxidative stress, increase apoptosis, tau protein phosphorylation, and decrease glucose uptake [231]. Thus, to understand the effect of REP on STZ-treated cells the concentration of STZ was screened out from 1 mM to 20 mM. The concentration-dependent response was observed at 2.5 mM STZ for 12 h and the viability of cells was observed around 60-65% (Fig.5.11). Further, the STZ-induced SHSY-5Y cells were incubated with REP and an increment of around 1.2 folds in the cell viability of the cells was observed which represents a significant ($p < 0.01$) effect on STZ-induced cells. Though the improvement in cell viability represents an effective potential of REP for neurodegenerative disorders.

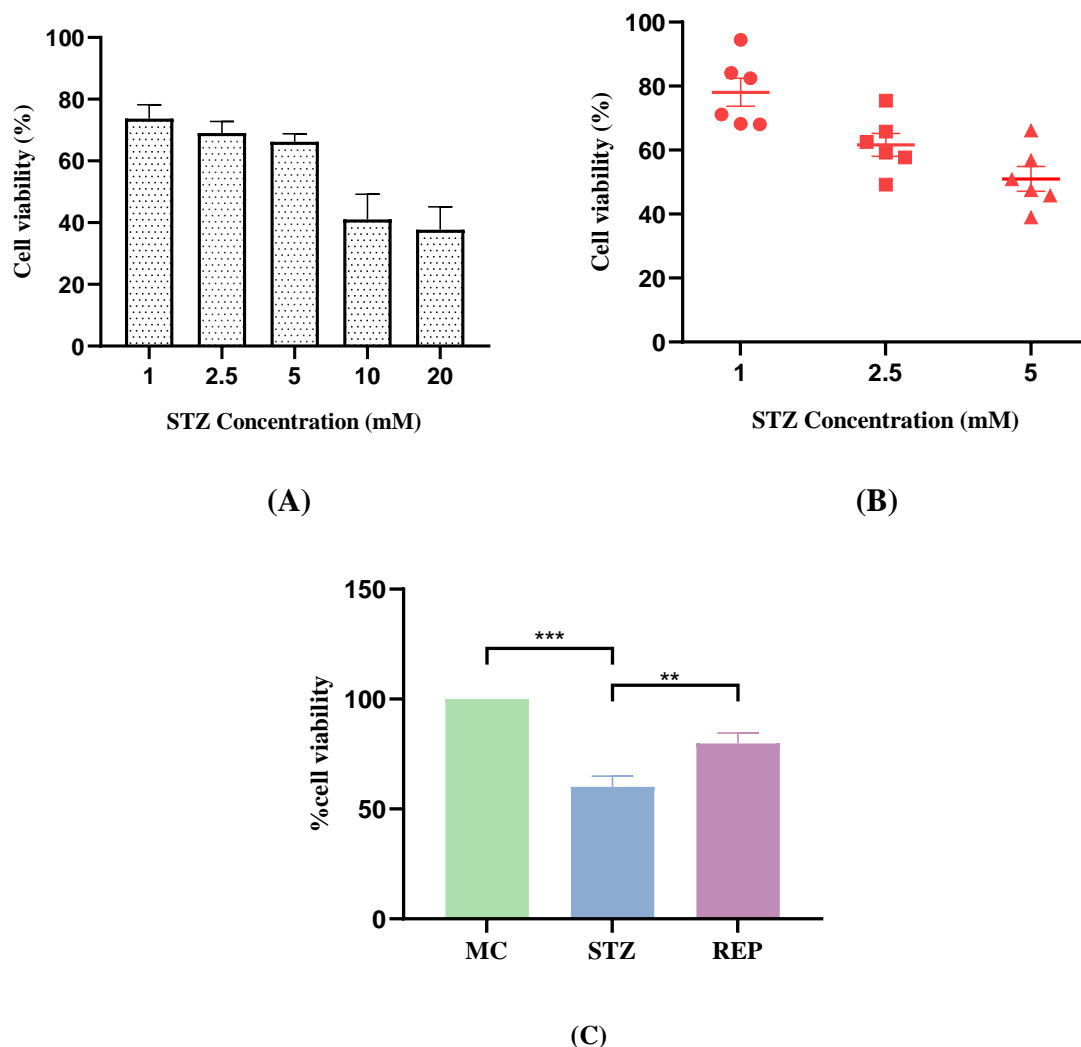


Fig. 5.11: (A) and (B) screening of STZ concentration; (C) The effect of REP on STZ-treated SHSY-5Y neuroblastoma cell lines. and ** Indicates $P < 0.01$, *** $P < 0.001$ by one-way ANOVA followed by Tukey's post hoc multiple comparison test

5.1.3 Reactive oxygen species-scavenging activity by hydrogen peroxide

H_2O_2 is an oxidizing agent which causes cellular damage and halts cell cycle development, resulting in cell death. The optimal H_2O_2 concentration for inducing cell death was determined by performing the preliminary studies in which 0.5-20mM concentrations were screened and observed that at higher concentrations, maximum cells were detached from the surface and float in the media (Fig.5.12). Whereas at low concentrations the viability of cells was around 80-85 % in 24 h. However, at a concentration of 1mM, the viability of cells was observed 70-75% in 24 h but in 12 h the viability reduced and showed around 60% viability. Thus, 1mM concentration of H_2O_2 was selected for further analysis. Afterward, the H_2O_2 -treated SHSY5Y cells (1mM, 12h) were incubated with REP and the study indicates that the REP

represents around 1.3-folds increment in cell viability and showed a significant ($p < 0.01$) effect on H_2O_2 treated cells.

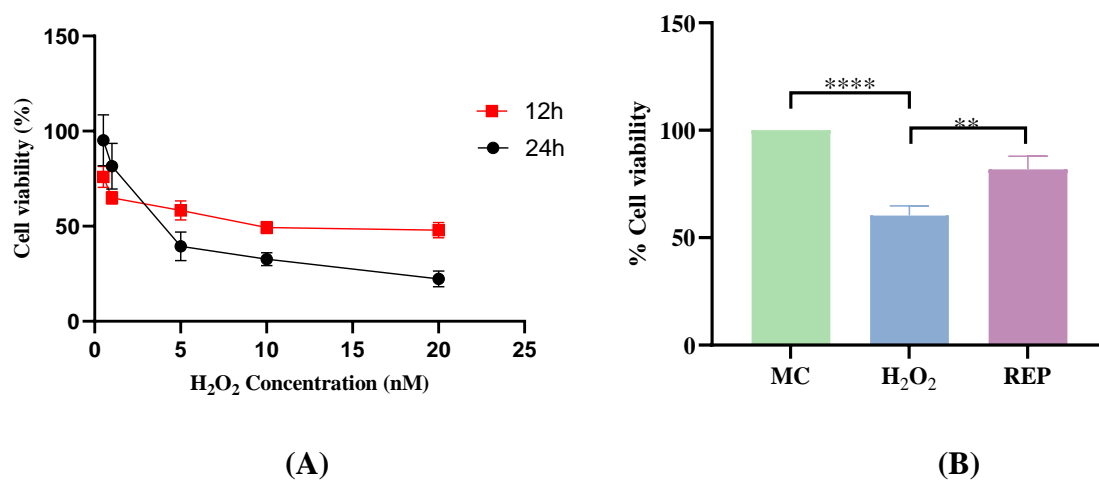


Fig.5.12: (A) Screening of H_2O_2 concentration and (B) neuroprotective effect of REP on H_2O_2 treated SH-SY5Y neuroblastoma cell lines

5.2 In vivo studies

5.2.1 Estimation of Neurochemicals bio markers

Biomarkers are an integral part of drug development and help to measure the effectiveness of an investigational drug. However, it has been well reported that $A\beta$ deposition, hyperphosphorylation of tau proteins, and reduction in the level of BDNF are the characteristic features of neurodegeneration and plays a key role in AD pathogenesis. Thus, the effect of REP on neurochemical parameters (BDNF, $A\beta$, and tau protein) was estimated in HFD+STZ-induced wistar rats after the 4 weeks of treatment (Fig.5.13). It was observed that the DC group rats showed a significant ($p < 0.001$) upregulation in the levels of $A\beta$ and tau proteins than the NC group rats. Whereas the BDNF level was significantly ($p < 0.001$) reduced in DC group rats than the NC group. Therefore, after treatment with REP for 4 weeks a significant ($p < 0.01$) reduction in the level of $A\beta$ and tau proteins was observed as shown in Fig. 5.13 (A &B). Whereas the level of BDNF was improved significantly ($p < 0.01$) compared to DC group rats. Moreover, significant ($p < 0.01$) changes in the level of $A\beta$, tau proteins, and BDNF were also observed compared to MEM. Thus, the observed results suggest that the REP also has the ability to act as a neuroprotective agent and helps in the treatment of various neurodegenerative disorders.

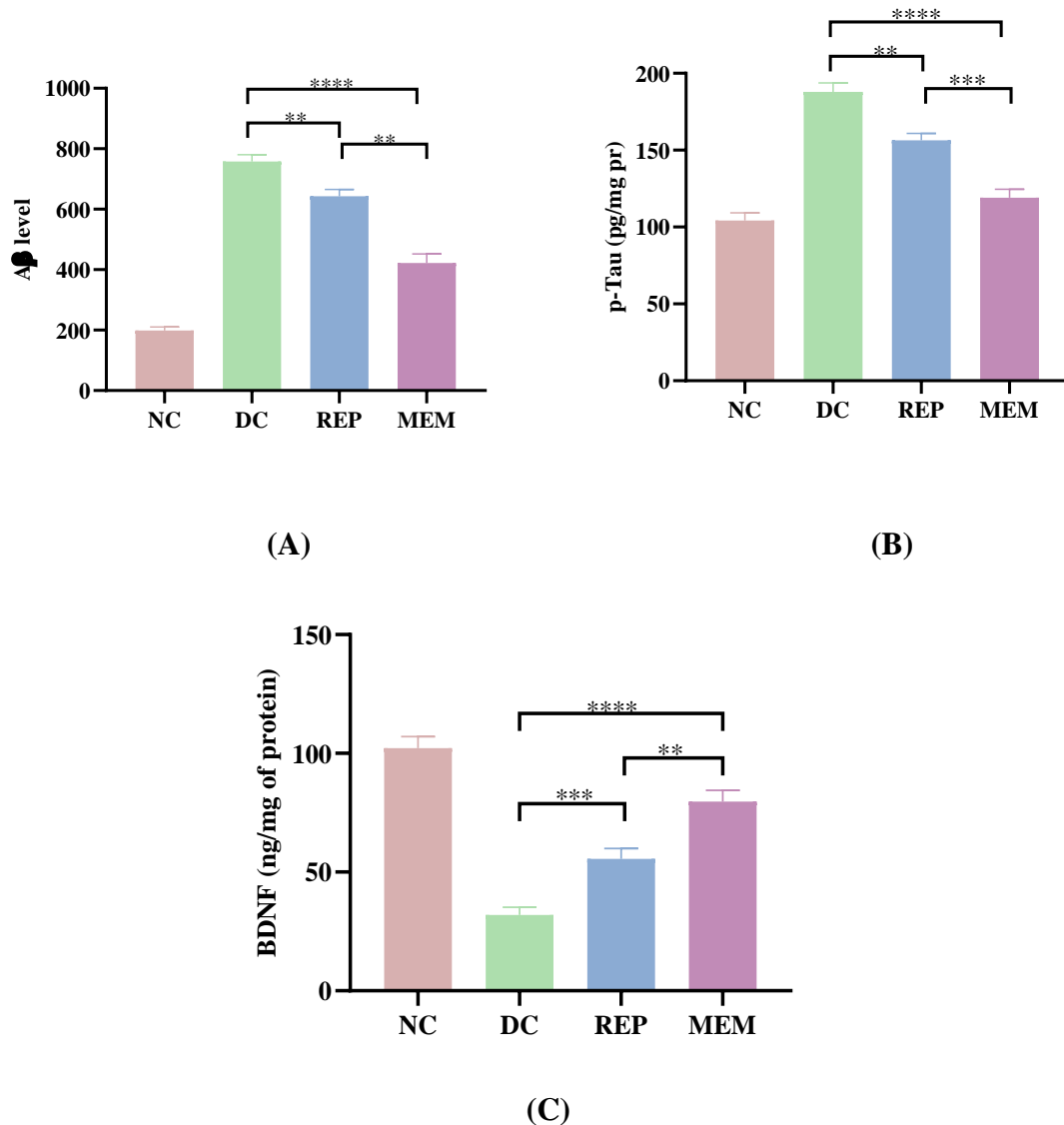


Fig.5.13: *In vivo* estimation of neurochemical parameters to understand the effect of REP after the treatment (A) A β level; (B) p-Tau; and (C) BDNF; in brain homogenate of HFD+STZ induced wistar rats, data are represented in (mean \pm SEM, n=6 rats per group). * Indicates $P < 0.05$; ** $P < 0.01$, *** $P < 0.001$, **** $P < 0.0001$ by one-way ANOVA followed by Tukey's post hoc multiple comparison test

5.2.2 Estimation of Proinflammatory cytokines

The level of inflammatory cytokines (TNF- α and IL-6) were observed (Fig.5.14) and found a significant ($p < 0.0001$) upregulation in the DC group compared to NC rats. After the treatment with REP, a decrement in these levels was observed and showed a significant ($p < 0.001$) suppression as compared to DC. Likewise, the REP showed a significant ($P < 0.05$) change in TNF- α and IL-6 levels compared to MEM.

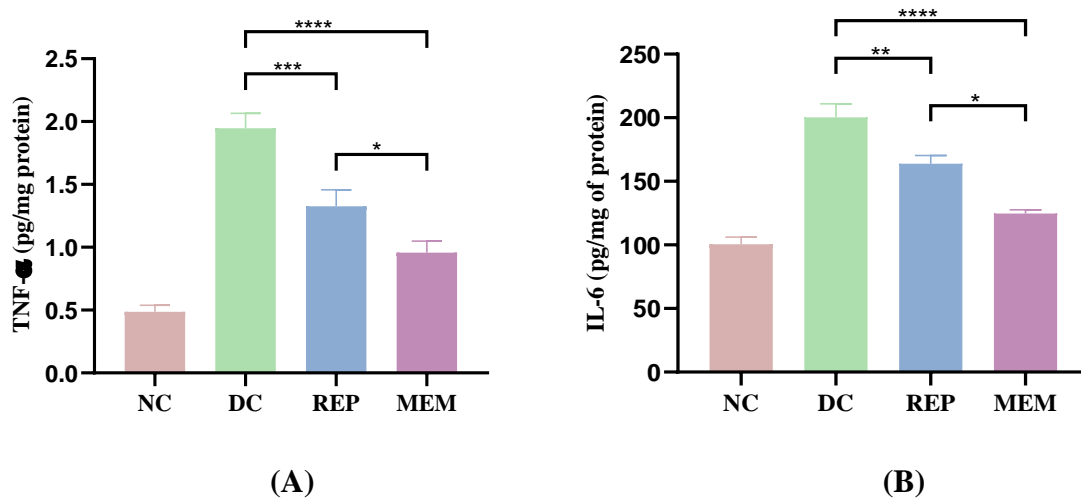
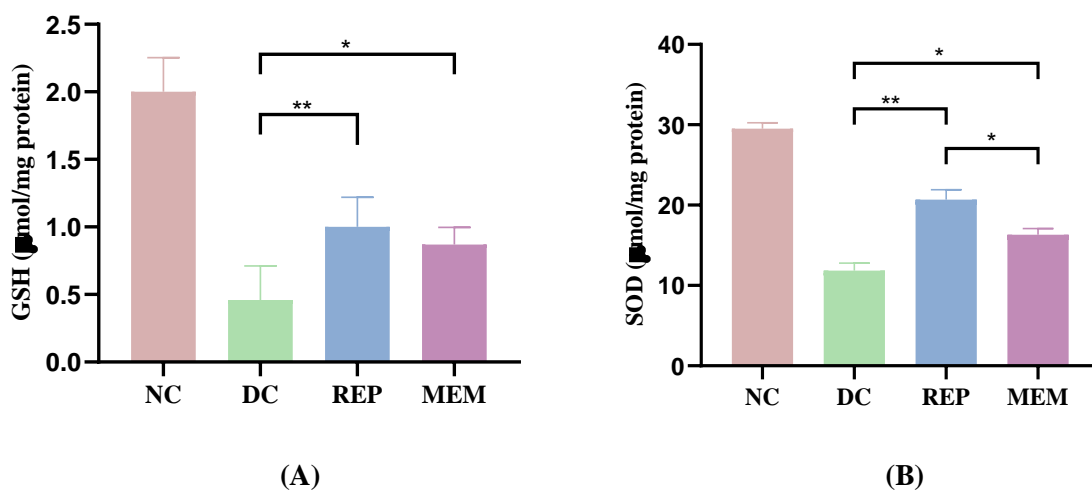


Fig.5.14: *In vivo* estimation of proinflammatory cytokines to understand the effect of REP on (A) TNF- α ; (B) IL-6 level in brain homogenate of HFD+STZ induced wistar rats, data are represented in (mean \pm SEM, n=6 rats per group). * Indicates $P < 0.05$; ** $P < 0.01$, *** $P < 0.001$, **** $P < 0.0001$ by one-way ANOVA followed by Tukey's post hoc multiple comparison test

5.2.3 Estimation of Oxidative stress parameters

In this study, the level of GSH, SOD (antioxidant) MDA, and nitrite (oxidative markers) were determined to understand the role of REP. ROS generation (oxidative stress) plays a significant effect in the production of neurodegeneration. The hippocampus and neocortex regions of the brain were the most vulnerable to oxidative stress-induced impairment. Therefore, the effect of REP on these parameters was measured and results showed that DC group rats significantly ($p < 0.001$) increase the levels of oxidative markers i.e., MDA and nitrile, and decreased the levels of endogenous antioxidants i.e., GSH, and SOD compared to NC group as shown in Fig.5.15 However, after the treatment with REP the reduction in the level of MDA and nitrile was observed compared to DC. Moreover, REP significantly resulted in the attenuation of oxidative markers (GSH & SOD) in comparison to DC.



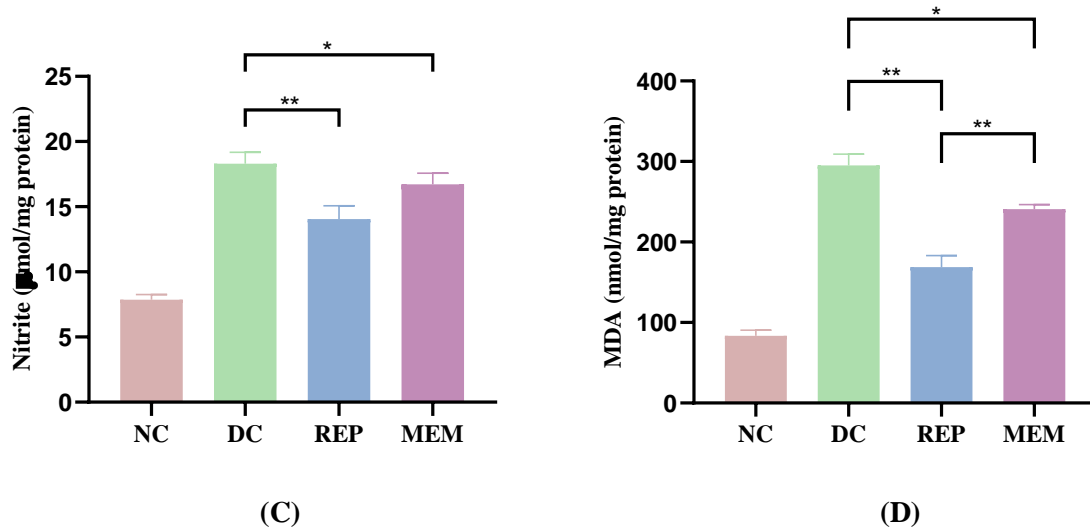


Fig.5.15: *In vivo* estimation of proinflammatory cytokines to understand the effect of REP on (A) GSH; (B) SOD; (C) Nitrite; (D) MDA level in brain homogenate of HFD+STZ induced wistar rats, data are represented in (mean \pm SEM, n=6 rats per group). * Indicates $P < 0.05$; ** $P < 0.01$, *** $P < 0.001$, **** $P < 0.0001$ by one-way ANOVA followed by Tukey’s post hoc multiple comparison test

5.2.4 Behavior assessment by cognitive and motor functions

5.2.4.1 Passive avoidance task

A task in which rodents learn to abstain from a response to avoid the aversive stimulus. The test is used to evaluate the learning and memory in cognitive dysfunctions of the central nervous system. During the acquisition trial, no significant ($P > 0.05$) differences in the initial latency time of all the groups were observed. Whereas in retention latency (after 24h of acquisition trial) analysis a significant ($P < 0.01$) decreased in latency was observed in the HFD+STZ group as compared with NPD (NC) group (Fig.5.16). However, rats treated with REP showed a significant ($P < 0.01$) amelioration in the retention latency compared to the DC group which showed improvement in retention memory.

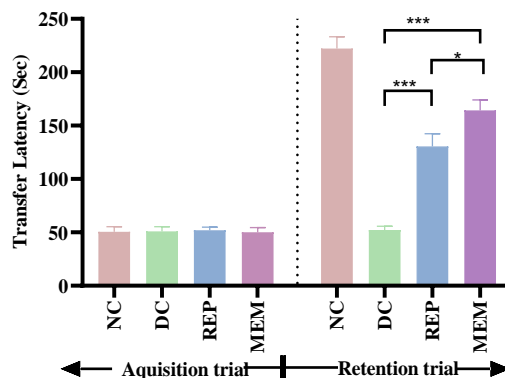


Fig. 5.16: Estimation of transfer latency by performing behavioral parameters using passive avoidance task. Data are represented in (mean \pm SEM, n=6 rats per group). * Indicates $P < 0.05$; *** $P < 0.001$, by one-way ANOVA followed by Tukey’s post hoc multiple comparison test

5.2.4.2 Morris Water maze (MWM)

After four days of training, the mean escape latency in all groups decreased gradually in MWM analysis. However, in the DC group, the mean escape latency was significantly higher in comparison with the NC group. Though there was a significant decrease in escape latency after treatment with REP and attenuated the effect compared to DC, as shown in Fig.5.17. After the hidden platform was removed in the probe trial test, it was found that DC group rats were unable to identify the exact location of the platform and spent less time in that quadrant than the NC group rats. Further, REP was administered for 4 weeks, and it was observed that REP group rats spent more time in the platform quadrant than the DC group rats, indicating that the REP improved the spatial and learning memory. These findings indicate that REP can help to reduce cognitive behavior in rats.

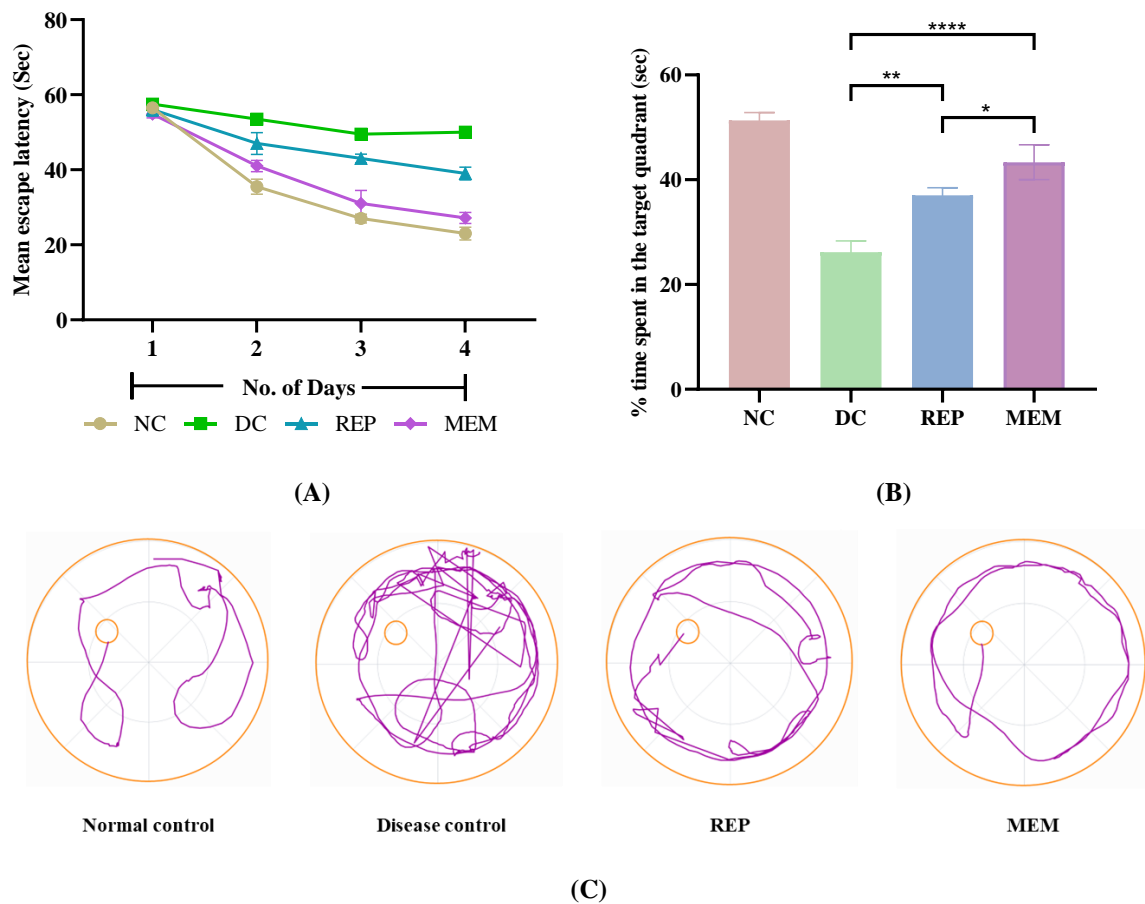


Fig.5.17: Estimation of (A) mean escape latency, (B) time spent in the same quadrant, and (C) representation of track plot for Morris's water maze task. Data are represented in (mean \pm SEM, n=6 rats per group). * Indicates $P < 0.05$; ** $P < 0.01$, **** $P < 0.0001$ by one-way ANOVA followed by Tukey's post hoc multiple comparison test

5.2.5 Quantitative Real-time Polymerase Chain Reaction (qRT-PCR)

The effect of REP was evaluated on the expression of ATF6 as shown in Fig.5.18. and results reveal that the level of ATF6 significantly ($p < 0.01$) reduces in the DC group as compared to the NC group. Moreover, after treated with REP a significant ($p < 0.001$) increment in the level of the ATF6 expression was observed with respect to DC which suggests that REP enhances the level of ATF6 and might help to reduce the apoptosis process. As ATF6 is activating transcription factor that activates the genes for the unfolded protein response during endoplasmic reticulum stress.

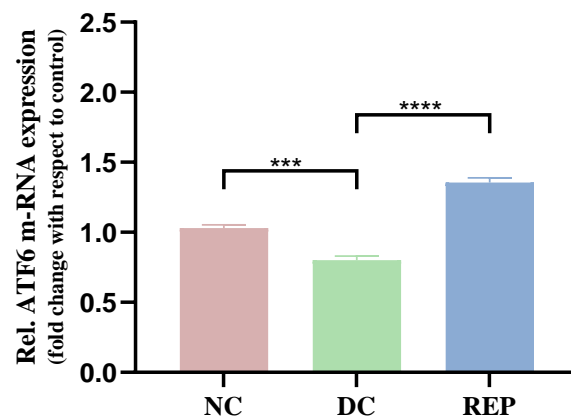


Fig.5.18: Effect of REP on the ATF6 expression. values are represented in mean \pm SEM and *** Indicates $P < 0.001$, **** $P < 0.0001$ by one-way ANOVA followed by Tukey's post hoc multiple comparison test

5.2.6 Western blot analysis

The Bax, and Bcl-2 both are apoptotic and anti-apoptotic protein respectively, whereas caspase-3 is the major effector of apoptosis, and activation of it cause irreversible cell death. Moreover, these proteins' (Bax, Bcl-2, and caspase-3) expression exerts a significant effect on neuron injury. In this study, the effect of REP on the expression of these proteins was measured and it was observed that the expression level of Bax and caspase increased significantly in the DC group compared to the NC group as shown in Fig.5.19. Moreover, the expression of Bcl-2 is reduced and indicates the occurrence of apoptosis in the DC group rats. After treatment with REP, the level of Bax reduces by 1.56-folds and caspase-3 by 1.04-folds compared to the DC group. It was also observed that the expression of Bcl-2 was increased by 1.4-fold compared to the DC group. Further, the overall results revealed that after administration of REP the expression of Bax, and caspase-3 reduced, whereas the expression level of Bcl-2 improved which represents that REP helps to reduce neuron cell death and has the potential to act as a neuroprotective agent.

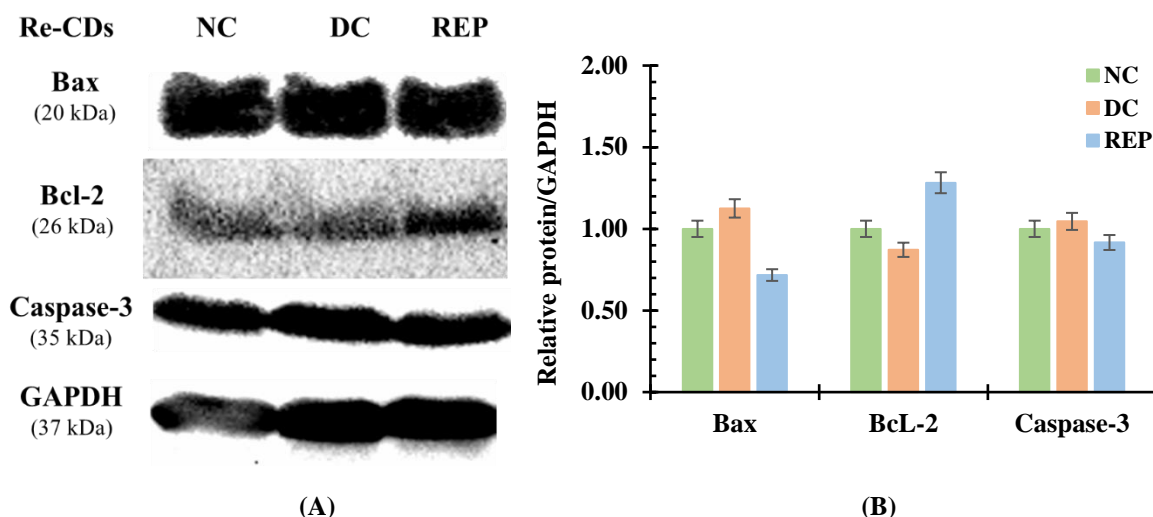


Fig.5.19: Western blot analysis exhibited (A) Bcl-2, Bax, Caspase-3 and GAPDH expression in lysate from rats brain; (B) quantitative analysis of protein expression

5.2.7 Pharmacokinetic study

The pharmacokinetic studies for REP were carried out in wistar rats and a plasma concentration versus time profile was plotted as represented in Fig.5.20. The result showed a quick absorption and peak drug concentration reaches in less than 1h (t_{max}). Though it was noted that the circulation half-life of the REP is very short and also indicates fast distribution and elimination.

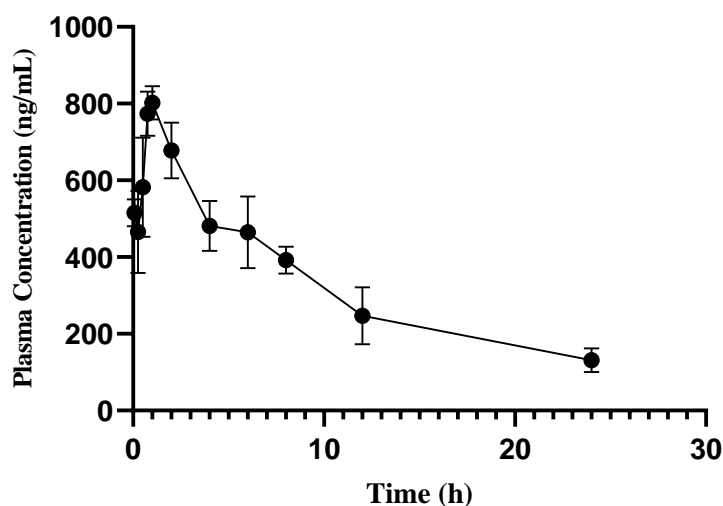


Fig.5.20: Plasma concentration-time profile of REP, and PNP. Values were represented in mean \pm SEM, n=4.

Furthermore, a high clearance rate of REP was observed and through the results, it was very much evident that the REP has a very less AUC as shown in Table.5.10.

Table 5.10: Pharmacokinetic parameters of REP

Parameters		REP
t_{max}	(h)	0.81 ± 0.19
C_{max}	(ng/mL)	800.76 ± 26.57
AUC	(ng.h/mL)	7441.69 ± 763.75
t_(1/2)	(h)	2.65 ± 1.54
CL	(mL/h/kg)	163.84 ± 17.39
MRT	(h)	8.24 ± 0.32
Vd	(mL/kg)	2209.63 ± 603.29

In summary, REP was used to measure its neuroprotective effect by performing *in vitro* and *in vivo* assays as these methods were more reliable and prominent to estimate the effect. *The in vitro* assays suggested that as the concentration of REP increased, the cell viability of cells was reduced suggesting a dose-dependent response. Moreover, the designed *in vitro* studies also indicate the improvement in cell viability after being treated with REP in the STZ and peroxide-induced SHSY-5Y cells. The STZ generates stress in cells and induces phosphorylation of tau protein whereas peroxide produces oxidative stress in the cells.

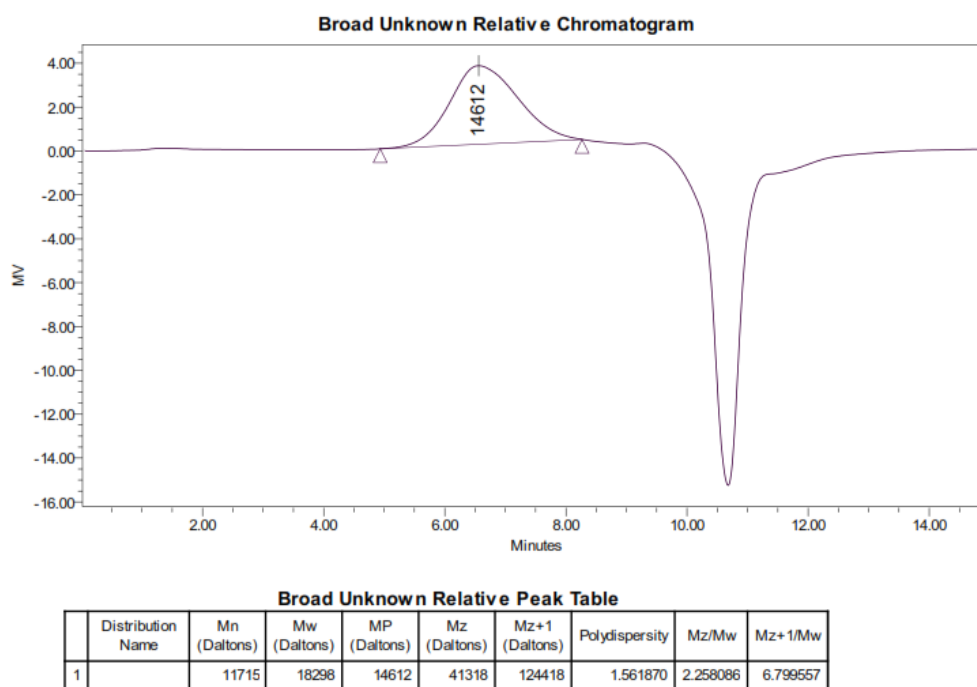
Furthermore *in vivo* studies revealed that after treatment with REP (4 mg/kg, *p.o*) for 4 weeks in HFD-fed STZ wistar rats, a significant ($p < 0.01$) decrement in A β , tau proteins, TNF- α , IL-6, MDA, NO, and increment in BDNF, SOD, GSH level was observed compared to disease control rats. Likewise, the behavioral studies i.e., PAT and MWZ showed a significant improvement ($p < 0.01$) in the retention memory and spatial memory after the REP treatment compared to HFD-fed STZ group rats. Additionally, the apoptosis marker proteins (Bcl-2, Bax, Caspase-3) and ATF6 gene expression in brain homogenate showed a significant ($p < 0.05$) increase in Bcl-2, ATF-6 expression, and decrement in Bax, Caspase-3 expression after treated with REP indicates a reduction in neuronal cell death then the disease rats. Moreover, the PK studies confirmed that the REP has a short half-life ($t_{(1/2)}$ 2.65 ± 1.54 h), high clearance rate (163.84 ± 17.39 mL/h/kg), and low volume of distribution (2209.63 ± 603.29 mL/kg).

Based on the *In vitro* and *In Vivo* results, we further planned to circumvent the observed problems *i.e.*; low absorptivity, high protein binding, first-pass metabolism, and poor pharmacokinetic and pharmacodynamic of REP, the targeted nano drug delivery systems were developed, and biologically evaluated.

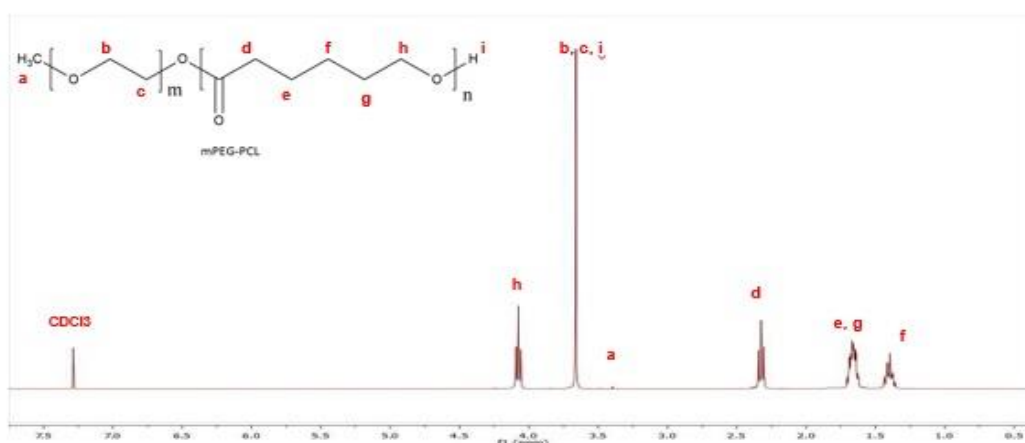
5.3. Development and biological evaluation of Polymeric nanoparticles (PNPs)

5.3.1 Synthesis and characterization of di-block amphiphilic polymer

The mPEG-PCL polymer was synthesized using tin (II) 2-ethyl hexanoate as a catalyst with a simple ring-opening polymerization reaction of ϵ -caprolactone. The characterization of the amphiphilic di-block mPEG-PCL polymer was done by GPC and $^1\text{H-NMR}$ (Fig.5.21). The $^1\text{H-NMR}$ data confirmed the synthesis of mPEG-PCL di-block co-polymer as the spectrum shows peaks at δ 1.39, 1.66, 2.32, and 4.07, which signifies polycaprolactone formation whereas, characteristic peaks at δ 3.66 and 3.39 shows the presence of methylene units of PEG.



(A)



(B)

Fig. 5.21: Confirmation of the amphiphilic di-block polymer (PEG-PCL) was done by (A) GPC, and (B) $^1\text{H-NMR}$. [232]

5.3.2 Fabrication of PNPs

The PNPs were fabricated with synthesized di-block amphiphilic polymer using mPEG as a hydrophilic moiety and a hydrophobic PCL, which have higher biocompatibility and biodegradability. Here, mPEG behaves as a capping agent and acts as a shield for the growing nanoparticles, therefore the particle cannot expand after a certain extent. However, PCL a semicrystalline polymer is used for long-term drug delivery applications due to its slow diffusion and non-toxic nature. Herein, the polymerization of PEG-PCL is used to reduce immunogenicity, toxicity, prolong the blood circulation time and optimize protein activities.

5.3.3 Optimization of PNPs by QbD approach

The optimization of PNPs was done by the QbD approach using the design of experiments, and response surface methodology BBD. The response surface methodology was investigated for determining the difference between variables. Initially, the QTPPs were selected to ensure the safety and efficacy of the final product. The CQAs which are product quality attributes were selected from the QTPPs and influenced the finished product. Though the CQAs were evaluated and based on the parameters of the sequential model sum of the square, model summary statistic the model was suggested (Table 5.11), and quadratic model was recommended for PS (Response 1), PDI (Response 2) and EE (Response 3).

Table 5.11: The Statistical values for each of the model sources for both the responses, along with remarks generated by the Design-Expert® software (version 13.0, Stat-Ease Inc.) under the heading of summary of fitness of each model.

	Response	Source	Sequential p value	R ²	Adjusted R ²	Predicted R ²	Press	Remarks
PNPs	Particle size	Liner	0.0026	0.6524	0.5722	0.3621	22264.95	-
		2FI	0.9089	0.6700	0.4721	-0.3226	46162.34	-
		Quadratic	<0.0001	0.9852	0.9661	0.9227	2696.65	Suggested
		Cubic	0.7306	0.9889	0.9557	-	-	Aliased
	PDI	Liner	0.0114	0.5605	0.4591	0.2061	0.1159	-
		2FI	0.7276	0.6120	0.3792	-0.4692	0.2145	-
		Quadratic	<0.0001	0.9902	0.9776	0.9377	0.0091	Suggested
		Cubic	0.6162	0.9935	0.9739	-	-	Aliased
	Entrapment efficiency	Liner	0.0011	0.6958	0.6256	0.5124	2661.61	-
		2FI	0.9279	0.7088	0.5341	0.1240	4781.29	-
		Quadratic	<0.0001	0.9901	0.9773	0.9424	314.23	Suggested
		Cubic	0.6732	0.9930	0.9719	-	-	Aliased

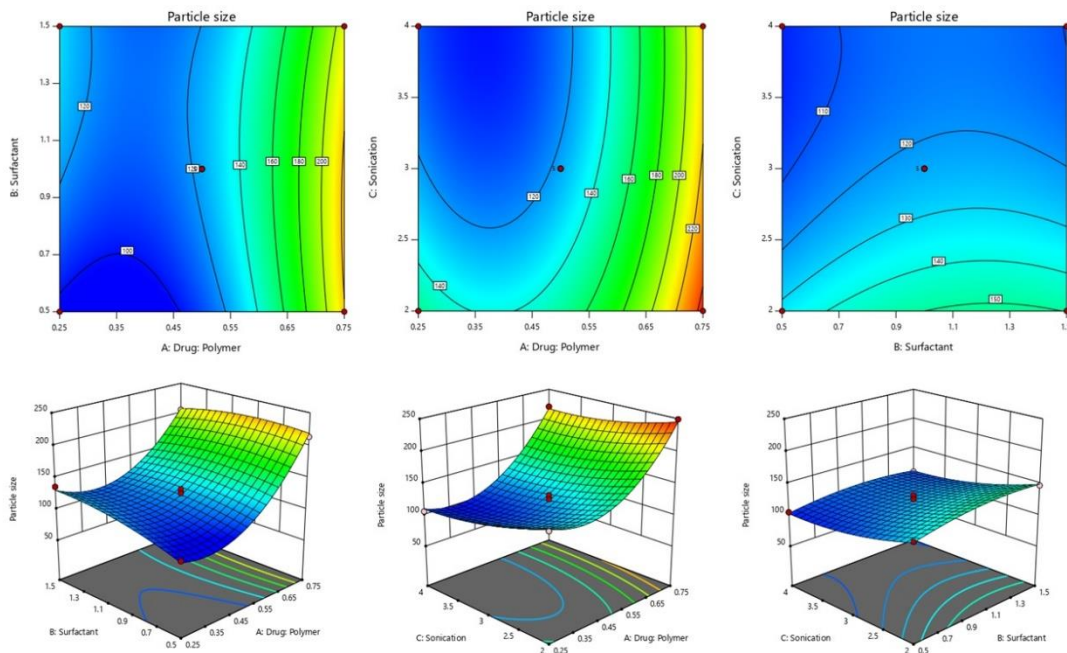
Furthermore, the ANOVA was applied to evaluate the factors which affect the response in quadratic equations (Table 5.12). It was observed that the drug-polymer ratio (Factor 1), surfactant concentration (Factor 2), and sonication time (Factor 3) significantly affect selected

responses in PNPs. The BBD provides information on polynomial equations involved in the interaction, the effects of independent variables, and their responses.

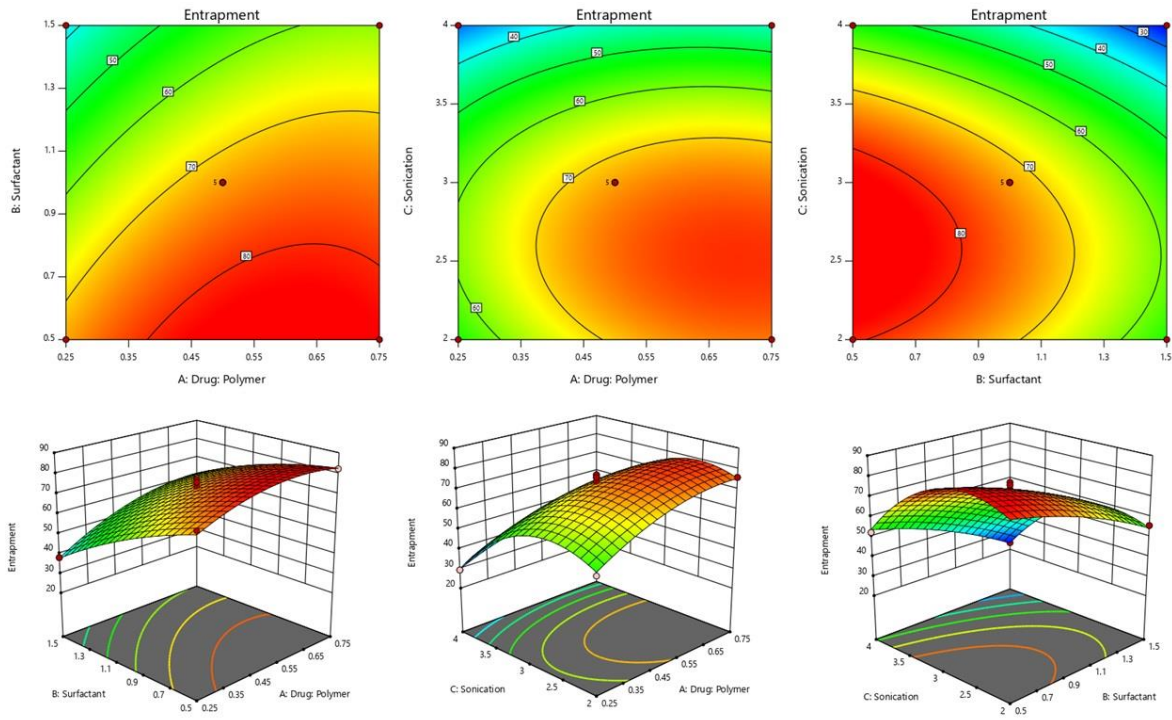
Table 5.12: Statistical validation parameters of the selected models for individual responses of PNPs

Response	Equation	Adequate precision	F-value	p-value Prob >F
Particle size	$+122.27+50.08A+5.91B-17.42C-11.59AB +3.57AC-2.58BC+49.31A^2-8.34B^2+9.82C^2$	22.60	51.67	0.0001
PDI	$+0.11+0.09A-0.006B-0.02C-0.01AB$ $0.03AC+0.01BC+0.11A^2+0.02B^2-0.007C^2$	25.90	78.73	0.0001
Entrapment	$+73.74+8.30A-14.03B-14.45C$ $+3.44AB-2.21AC-1.02BC-6.36A^2-3.68B^2-16.94C^2$	27.62	77.84	0.0001

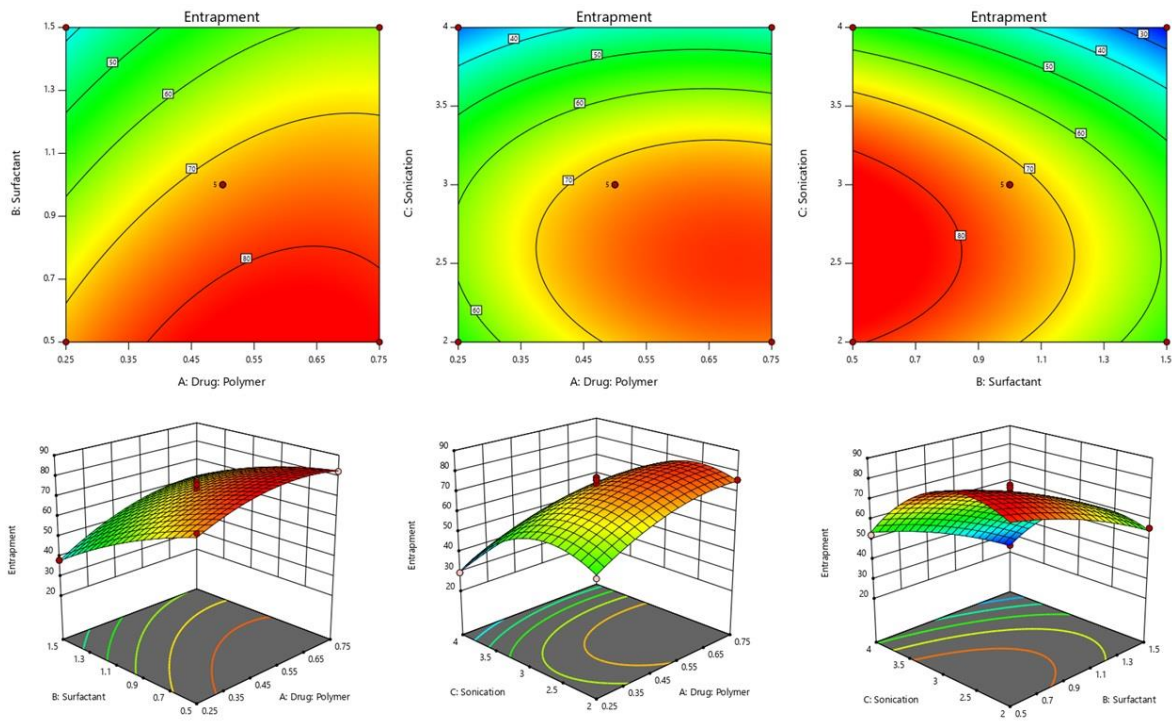
Attentively observing the polynomial equations and surface plots (2d or 3d) results in emphasizing the effects of each variable independently and in combination with other variables on each response. The 3D response surface plots of PS, PDI, and % EE on PNPs were generated and showed a dependency on selected independent variables (Fig.5.22). It was examined that as the drug: polymer ratio increases, the PS, PDI, and % EE increase. Herein, the amount of the drug was kept constant, and changes in the amount of polymer were carried out. As the amount of polymer increased, it resulted in a decrease in PS and PDI due to the change in concentration of hydrophilic moiety of the polymer. Moreover, a reduction in PS, PDI, and % EE is observed as the surfactant concentration and sonication time increase. The increase in surfactant concentration leads to adsorption onto the interface and reduces the surface tension, whereas an increase in the sonication time breaks the particles and reduces the dispersion size.



(A)



(B)



(C)

Fig.5.22: The 2D and 3D-response surface plot showing the relationship among the factors on (A) particle size, (B) PDI, and (C) entrapment efficiency of Drug: polymer; Surfactant amount (AB factor), Drug: polymer; Sonication time (AC factor), Surfactant, sonication time (BC factor) of the PNPs

The overlay plot was created by numerical and graphical methods to predict the composition for optimizing the nanoformulation. The composition of factors was selected from the design space in the overlay plot (Fig.5.23) and the selected criterion for the optimized region was to obtain by minimum PS, PDI, and maximum EE%.

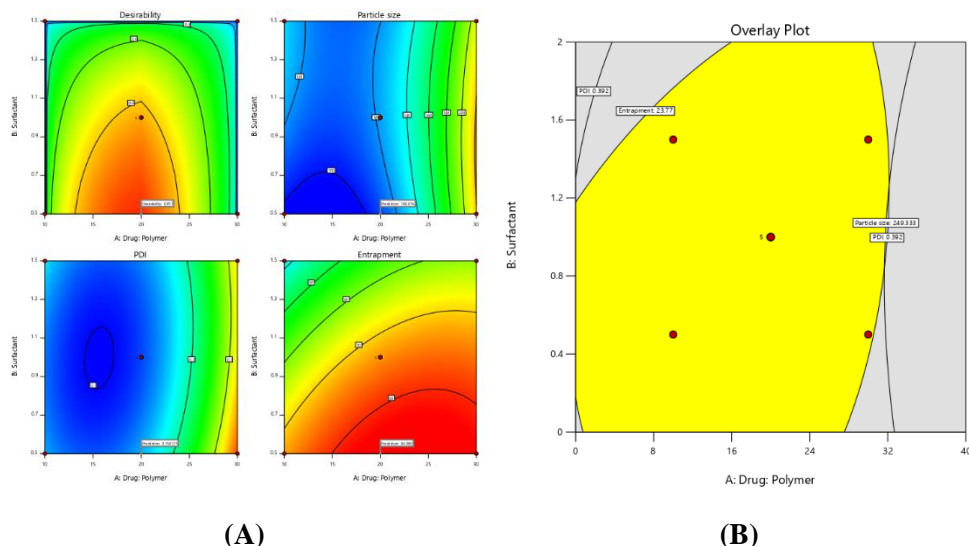


Fig.5.23: The (A) desirability index and (B) overlay plot of PNPs with Drug: polymer; Surfactant amount (AB factor)

Furthermore, the predicted results were validated by comparing them with the actual experimental values obtained from the responses (Table.5.13). The deviation between predicted and experimental values ranged from -4.33 to 5.42 in PNPs. The obtained results demonstrated that the generated design space can reduce the risk of failure and thus indicated that the models are reliable.

Table 5.13: Experimental design model validation

Responses	Polymeric nanoparticles		
	Predicted value	Experimental value	% Residual
Particle size (nm)	108.01	112.53 ± 5.91	-4.33
Polydispersity index (-)	0.166	0.157 ± 0.08	5.42
Entrapment efficiency (%)	84.08	77.78 ± 3.98	4.04

5.3.4 Physicochemical Characterization of nanoparticles

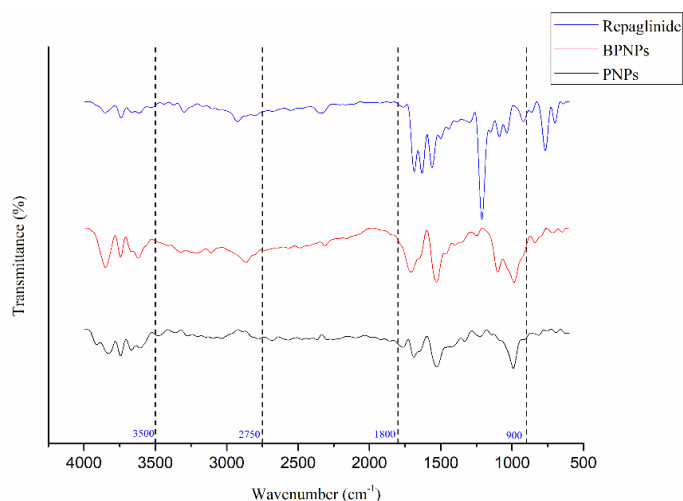
5.3.4.1 Compatibility study

The ATIR spectra analysis of REP, BPNPs, and PNPs depicts the appearance of no new peaks and disappearances of existing peaks which eliminates the probability of any chemical interactions (Fig.5.24 A). The ATIR spectra of REP showed a peak at 3310 cm^{-1} (NH stretching), 2952 cm^{-1} (-CH stretch), 1684 cm^{-1} (-C=O) and C-O stretch at 1040 cm^{-1} , 1209 cm^{-1}

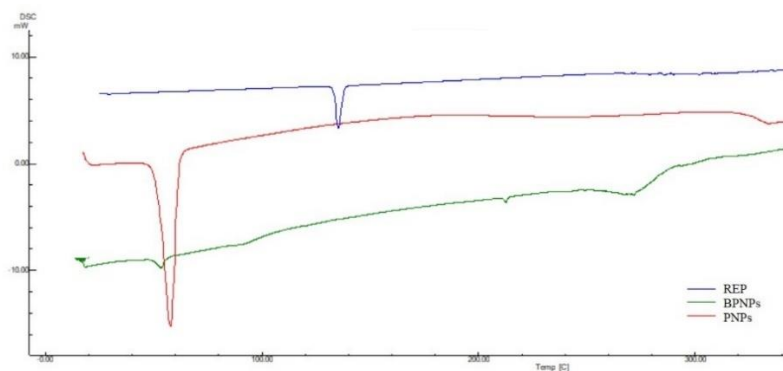
¹ respectively. Whereas in PNP's peaks were observed at 1192 cm⁻¹ (C-O stretch), 1767 cm⁻¹ (C=O), 2970 cm⁻¹ (-CH stretch). Though a slight shift was seen in IR fingerprint region peaks and the absence of an extra peak confirmed no interaction between the excipients used in the formulation of PNP's.

DSC is a thermoanalytical technique for studying the thermal properties and/or phase transitions that can be produced or absorb heat as a function of time and temperature. DSC also evaluates the material properties, inertness, melting point and determines the content and degradation of the substance. The thermogram of REP shows an endothermic peak at 135 °C whereas BPNPs showed a peak at 55 °C, 185 °C and PNP's at 54 °C, 212 °C, and 272 °C respectively. The thermograms depict the shift of the peaks in PNP's which represents the proper incorporation of guest moiety into the host cavity. The absence of characteristic peaks of components indicates the amorphous nature of PNP's (Fig.5.24. B).

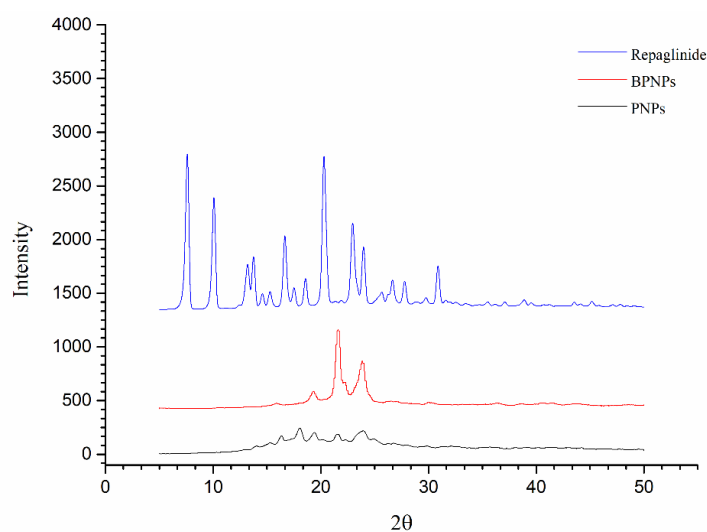
pXRD, a non-destructive technique was used to identify phase transition and measured the diffraction pattern of crystalline material. The crystallinity of REP, BNP's, and PNP's, was investigated by pXRD. The patterns of REP revealed the distinguishable diffraction peaks at diffraction angles 2θ of 7.65°, 10.11°, 12.40°, 13.24°, 13.76°, 14.58°, 16.67°, 17.50°, 18.56°, 20.22°, 22.91°, 23.33°, 25.67°, 26.60°, and 30.88° which confirmed the highly crystalline nature whereas the PNP's and BPNPs also showed an extra peak at 23.37° which indicate the proper encapsulation in the matrix (Fig.5.24.C).



(A)



(B)



(C)

Fig. 5.24: The compatibility study of REP, BPNPs, and PNP performed by (A) ATIR, (B) DSC, and (C) pXRD.

5.3.4.2 Particle size and morphological evaluation

The physicochemical characterization of PNP was estimated by measuring the PS, PDI, ZP, and morphological parameters (FE-SEM, TEM). PS is a pivotal property that influences the drug release pattern, stability, and *in-vivo* behavior of the formulation. For target site-specific delivery, the 50 – 150 nm range is suitable particularly for delivery to the brain. The absolute size of PNP was found to be 112.53 ± 5.91 nm with a polydispersity index of 0.157 ± 0.08 (Fig. 5.25 (A)). Furthermore, ZP is the electric potential of the particle movement in a diffusion layer, which is related to slipping or shear plane. ZP is closely associated with the nanoparticles' stability and surface morphology. It gives vital information about the long-term stability of nanoformulations and their tendency to aggregate. The ZP of the PNP was -6.20 ± 0.82 mV, which suggested that the nanoformulation was stable (Fig. 5.25 (B)).

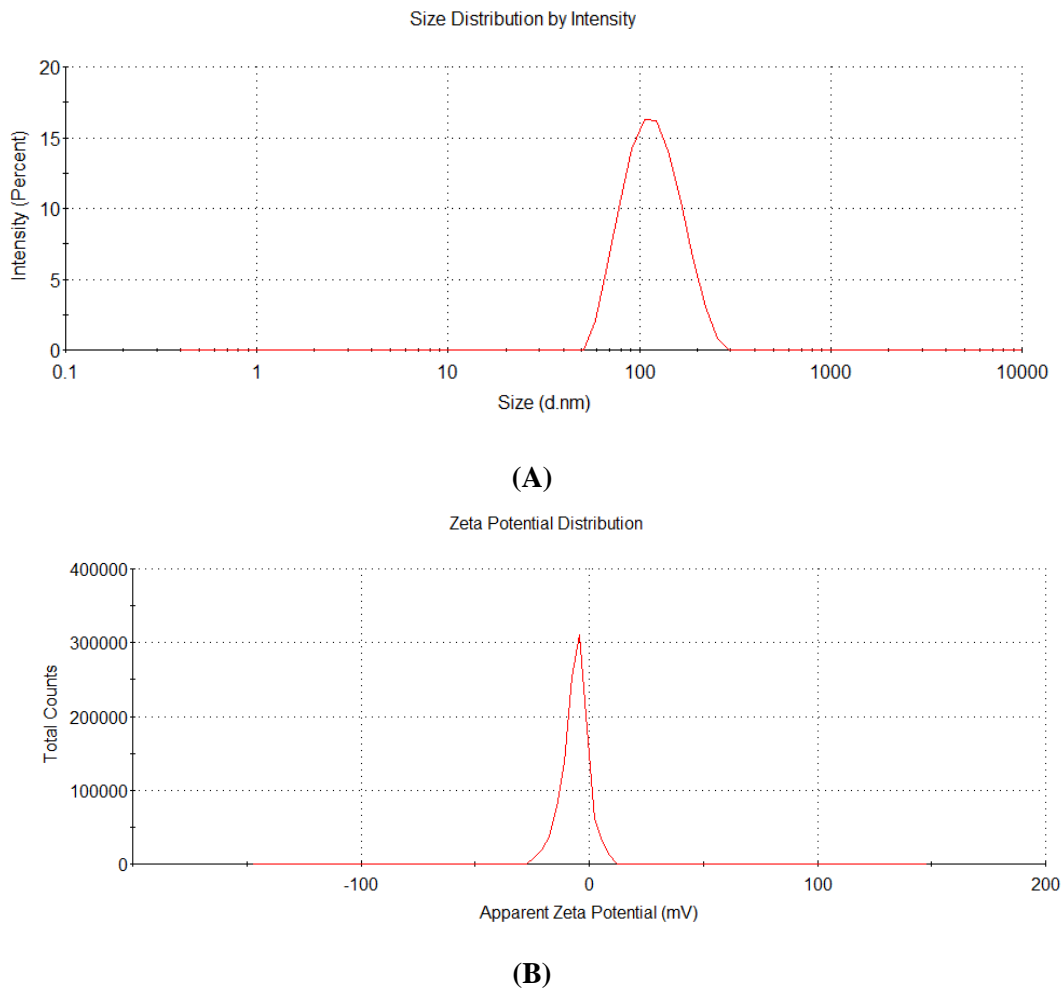


Fig. 5.25: (A) Particle size and (B) zeta potential of optimized PNPs

Moreover, particle morphology significantly influences the percent drug loading, entrapment efficiency, drug release profile, pharmacokinetics, and biodistribution pattern of the nanoparticles. It also has a role in cellular uptake, cellular internalization, receptor binding, and molecular interactions. The FE-SEM and TEM analysis showed that most nanoparticles were isometric, with smooth surfaces and the average size of nanoparticles was the same as obtained by DLS (Fig.5.26).

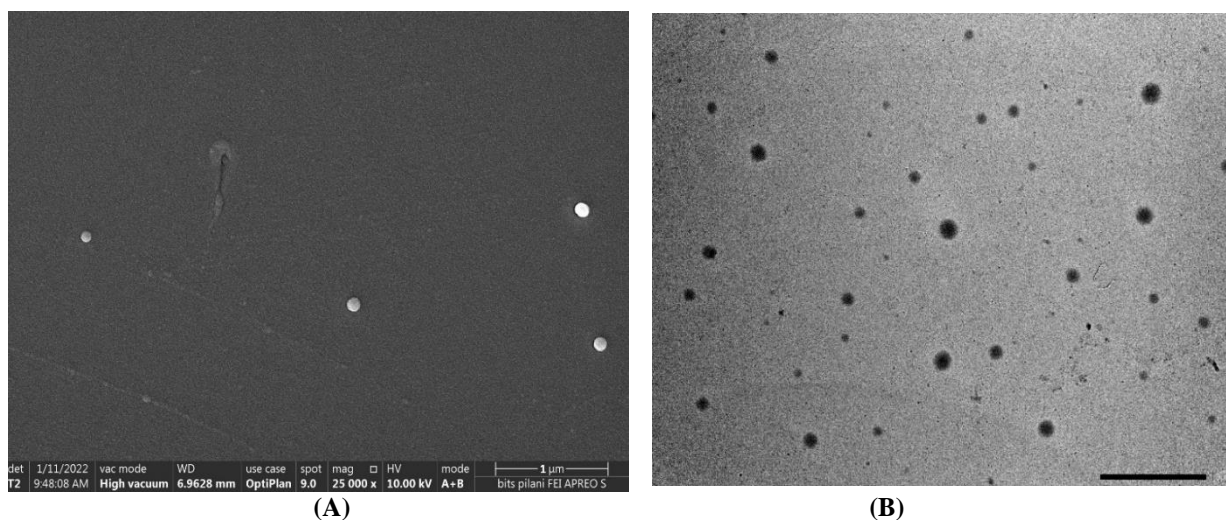


Fig. 5.26: Morphological characterization of PNPs by (A) SEM and (B) TEM

5.3.4.3 Lyophilization process optimization

Lyophilization is a process to improve the long-term stability of nanoformulations for the delivery of the drug. The process generates various stress like destruction, aggregation during the process, and protectants are added to protect nanoparticles from stress. In preliminary studies, various protectants (sucrose, trehalose, lactose, mannitol) were screened based on cake formation and dispersibility. The impact of protectants was observed by performing freeze-thaw studies on the physical stability of PNPs and evaluated by redispersibility index (Fig. 5.27 (A)). Through the preliminary screening, trehalose was finalized due to its excellent redispersibility. The redispersibility is quite high and this might be the consequence of providing bulk rather than being ascribed to the formation of a collapsed network. The lowest concentration of trehalose (5% w/v) was less efficient and attributed to the formation of a poor network, which is the primary requirement for providing cryoprotection against undue stress of freeze-drying (Fig.5.27 (B)).

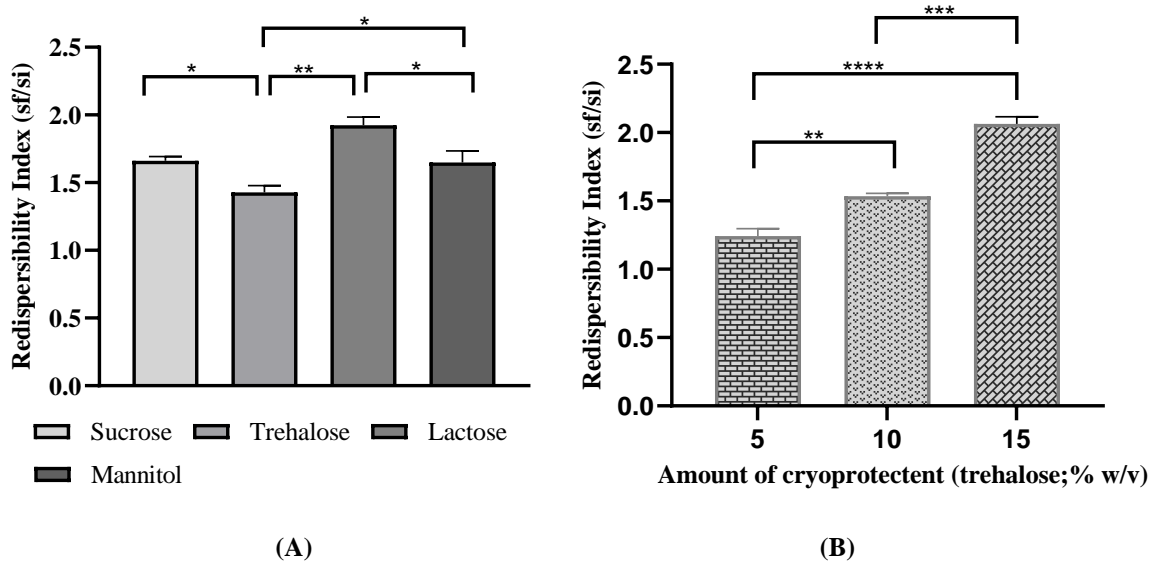


Fig. 5.27: Graphical representation of (A) cryoprotectant screening; (B) amount (% w/v) of selected cryoprotectant.

5.3.5 *In vitro* drug release study

The estimation of *in vitro* drug release is important for nanoformulation, as the rate and extent of active ingredient present at the site of action depend on the release profile of the active ingredient. Hence a sustained/controlled release of drug from nanoparticle is suitable to maintain the therapeutic window. The release profile of REP and PNPs were estimated by the dialysis bag method (Fig. 5.28) and showed a cumulative drug release of ~ 70 % in PNPs within 48h whereas REP showed a burst release profile.

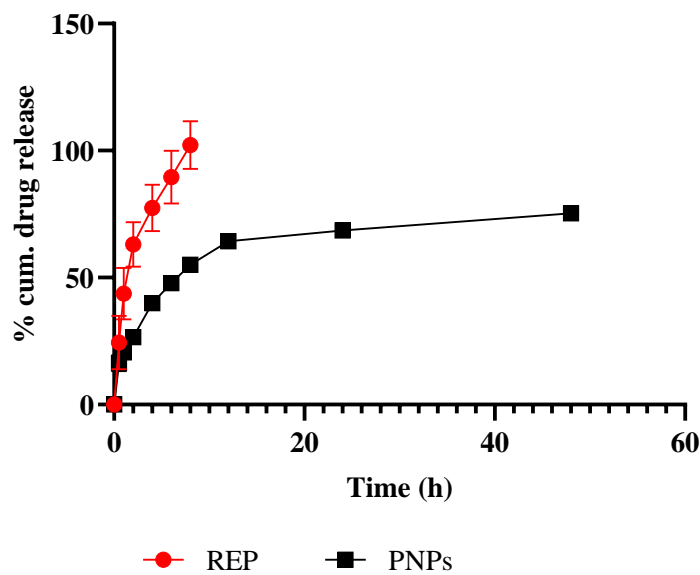


Fig. 5.28: *In vitro* release profile of REP and PNPs using dialysis bag method for 48h.

It was observed that the REP released 100% in ~2h and different mathematical models were used to understand the release pattern of REP using DD-Solver (Table 5.14). The REP shows first-order kinetics whereas PNPs exhibited high regression coefficient values and low AIC values with the Korsmeyer-Peppas model, indicating a best-fit model. The PNPs have a fickian diffusion release pattern ($n < 0.245$), and imply the degradation by the creation of fine pores. The REP diffused through the fine pores and follows the controlled release pattern. The decrease in fluctuations results in better therapeutic efficacy and lower toxicity.

Table 5.14: Mathematic release models for the estimation of *in vitro* release parameters

Model	Parameters	Test Sample	
		REP	PNPs
Zero	K_0	9.03	4.31
	R^2	0.69	0.83
	AIC	108.37	81.66
First	K_1	2.16	0.13
	R^2	0.94	0.97
	AIC	84.90	72.52
Higuchi	K_H	39.52	19.09
	R^2	0.85	0.94
	AIC	96.41	68.33
Korsmeyer-Peppas	k_{KP}	81.82	34.55
	R^2	0.93	0.98
	AIC	73.76	42.79

5.3.6 Protein adsorption of PNPs

Protein adsorption is an important assay to identify the stability of nanocarrier in blood and circulation half-life. The nanoparticles with a hydrophobic surface have a tendency to adsorb protein on their surface, which enhances the opsonization and macrophage recognition. Thus, it led to the enhancement in elimination rate and limit the therapeutic efficacy. The protein adsorption could be minimized by utilizing lipophobic moieties such as polyethylene glycol (PEG) or poly (ethylene oxide) (PEO) on the surface of the nanoparticles. These molecules are non-toxic, safe, and classified as Generally Regarded as Safe (GRAS) by the U.S. FDA. Usually, PEG and PEO enhance the probability of pre-disposing of the drug molecule to the target site by resisting interactions with bloodstream components. The PEG and PEO decrease the clearance rate and increase the blood circulation through the formation of stealth nature of nanoparticles. In the study, PNPs were incubated with 4% BSA (physiological concentration of blood), and protein adsorption was found to be $5.14 \pm 3.24\%$. The low protein adsorption was owing to the presence of PEG units on the surface. The PEG chain over the PNPs surface

prevents the protein from being adsorbed on its surface and, thus, can deceive the mononuclear phagocytic system (MPS) for their uptake.

5.3.7 Stability studies

5.3.7.1 Stability study in simulated biological fluids

Nano formulations are getting much consideration for the controlled delivery of drugs, but the stability of nanoparticles has been a source of concern. Especially, the size of nanoformulation which facilitates target-specific delivery, rapid gastric emptying, and reproducible transit through GIT. Additionally, it protects the encapsulated drug, controlled release profile, reduced toxicity, and immunogenic potential over the conventional system. In preparation of nanoparticles, the surface-capping or stabilizing ligands were used to control the dimensions of particles. Herein, the effect of different simulated gastrointestinal fluids on nanoparticles was measured and represented in Fig. 5.29. The PNPs were found stable but no significant changes in the quality attributes were observed in simulated gastrointestinal fluids. As the formulation comprises of stabilizing or capping agent (Poloxamer), which diminished the van der Waals forces and established repulsion between the colloidal particles. These forces ultimately reduced the aggregation and precipitation of the particles.

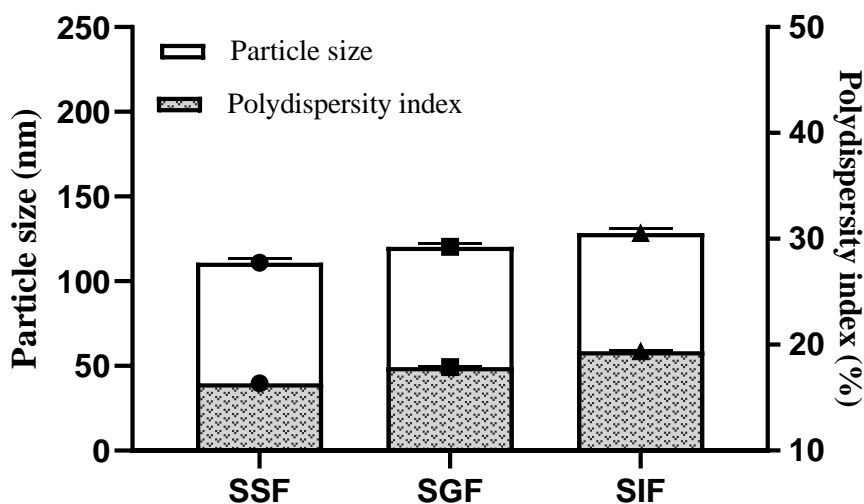


Fig: 5.29: Stability study of PNPs in simulated gastrointestinal fluids

5.3.7.2 Stability of lyophilized nanoformulation

The major parameter to be considered is stability of nanocarrier which should thoroughly characterize its resuspendability. The long-term stability study was carried out in accordance with ICH guidelines for three months and PS, PDI, ZP, and EE % were evaluated. The PNPs were found to be stable and did not show any significant variation in comparison to the initial

sample (Table 5.15). Furthermore, redispersion time for lyophilized PNPs was observed to be less than 1 min and the designed lyophilized PNPs were discovered to be stable at 25 ± 2 °C, 60 ± 5 % RH.

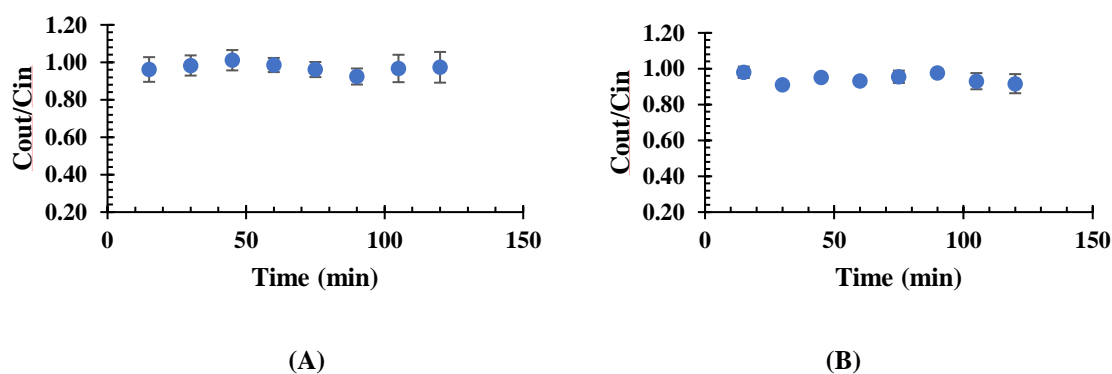
Table 5.15: stability studies*

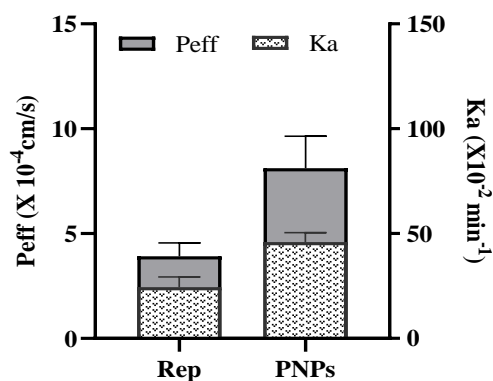
Parameters	Initial	after 1 month	after 2 months	after 3 months
PS (nm)	112.5 ± 5.91	115.8 ± 4.98	116.4 ± 4.26	120.1 ± 3.55
PDI	0.157 ± 0.08	0.153 ± 0.07	0.150 ± 0.03	0.159 ± 0.02
ZP (mV)	-6.20 ± 0.82	-6.81 ± 0.29	-6.63 ± 0.42	-7.05 ± 0.15
% EE	77.78 ± 3.98	77.43 ± 4.09	76.57 ± 3.25	74.49 ± 2.56

*Results were represented as mean \pm SEM, n=3

5.3.8 *In situ* absorption study by Single pass intestinal perfusion (SPIP) model

Intestinal absorption is a crucial factor for defining the bioavailability of oral drugs, as there are many transporters that are available on the intestine which are involved in the pharmacokinetic profile of drugs.[224,227] Thus, for identifying the transport mechanisms (p-glycoprotein), intestinal absorption plays a critical role in the improvement, safety, and effectiveness [233]. This study explored the effect of p-glycoprotein, pH, tight junction regulators, and endocytosis inhibitors on the intestinal absorption of REP. The primarily steady state of REP with intestinal tissue was examined for permeation through the intestine and confirmed by the determination of C_{out}/C_{in} ratios to attain a plateau with time in all the test solutions (Fig. 5.30). During the intervening time, no nonspecific binding of REP to the tubing was discovered and remained stable in the perfusion solution throughout the experiment. The P_{eff} and K_a values were calculated by estimation of an average of C_{out}/C_{in} data, obtained from the different perfusion solutions over a period of 2h with subsequent 15 min intervals. In the study, it observed that the P_{eff} value increased around ~ 2.3 folds of PNPs compared to free REP and showed a significant change in K_a with an increment of ~ 2.3 folds in PNPs with respect to REP indicating that the nanoformulations enhanced the permeation/absorption rate of REP in wistar rats.





(C)

Fig. 5.30: Representative plots of the steady-state concentration (cout/cin) VS time for (A) REP, (B) PNPs, and (C) Effective permeability coefficient and apparent absorption rate constant. Values were represented as mean \pm SEM

5.3.9 Parallel artificial membrane permeability assay-blood brain barrier

The BBB is a highly selective barrier, comprised of specialized tight junctions between brain endothelial cells. In order to target brain delivery and achieve effective treatment, the drugs are required to penetrate the BBB and reach to intended targets. The two mechanisms that are involved in the delivery of drugs through BBB the active and passive. In the active mechanism, various transport proteins are required for drug delivery whereas in the passive mechanism diffusion is the most common approach to cross the barrier. The measurement of brain permeability is necessary for the delivery of drugs to the brain and the most reliable method to determine is a direct method, but it is a technically challenging, and time-consuming process. Nowadays, *in vitro* PAMPA-BBB is the most used method to predict brain permeability due to its high throughput. PAMPA-BBB is designed to precisely mimic the physicochemical microenvironment of the barrier and is based on the passive diffusion of molecules through an artificial membrane made of polar brain lipids (PBL) in dodecane solution. PAMPA is a limited method because it is modeled by an artificial membrane and thus is neither used for active transport nor P-gp efflux. Herein, REP and PNPs were examined to determine the effective permeability (Pe) using measured concentrations and it was observed that the PNPs achieve ~1.2 folds more permeability to the brain than REP. Moreover, using calculated experimental permeability rates (log Pe) the molecules were classified, as low ($-6.14 < \log Pe < -5.66$), medium ($-5.66 < \log Pe < -5.33$), high ($\log Pe > -5.33$), and impermeable ($\log Pe < -6.14$) [229,230,234].

5.3.10 *In vitro* cell culture study

5.3.10.1 Cell viability assay

The viability assay indicates the number of live and/or healthy cells in a sample and measures the physical or cellular health in response to chemical agents, therapeutic treatments, or extracellular stimuli is referred to as cell viability assay. Here, the viability of cells was evaluated by MTT assay, a colorimetric trial used to measure the cellular oxidative metabolic activities based on NAD(P)H-dependent dehydrogenase enzyme activity. The effect of REP, BPNPs, and PNPs, was measured in a range of 0.25-40 $\mu\text{g/mL}$ to recognize the potential of nanoparticles (Fig. 5.31). The cell viability over $\sim 70\%$ indicates the biocompatibility and nontoxicity of the nanoformulation. However, at the higher concentration PNPs and BPNPs showed $\sim 85\%$ cell viability in SH-SY5Y cells and indicated the nontoxic nature of REP-loaded nanoformulations.

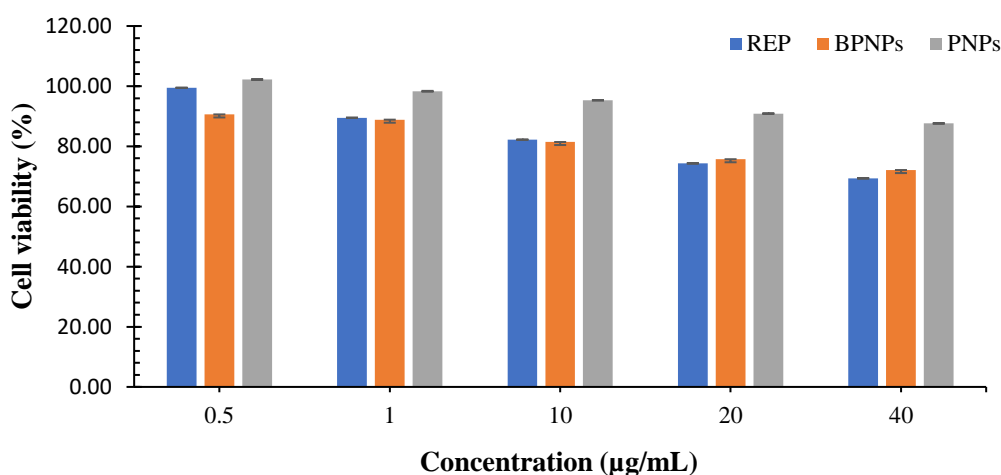


Fig.5.31: Cell viability assay of REP, BPNPs, and PNPs on neuroblastoma SH-SY5Y cell line.

5.3.10.2 Cellular uptake

Nanoparticles are used in drug delivery systems to reduce systemic toxicity, prolong blood circulation, and enhance intracellular uptake. The cellular uptake is influenced by shape, size, surface hydrophobicity, and charge. Herein, the cellular uptake of PNPs was investigated by confocal microscopy and flow cytometry in SH-SY5Y cell lines using C_6 as a model drug. Though it was observed that the cellular uptake of C_6 -loaded PNPs was significantly ($p < 0.001$) higher than the free C_6 in SH-SY5Y cells at 4h and 8h (Fig.5.32). The increased uptake was observed in C_6 -loaded PNPs compared to free C_6 in SH-SY5Y cells at 4 h and 8h respectively. The PNPs exhibited enhanced uptake than free C_6 which might be due to the loading of the drug into a hydrophobic polymer matrix and negative charge also exhibits a strong interaction

with the cell membrane to enhance the intercellular uptake. Though more uptake into the cells ensures more amount of the drug is available at the site of action for therapeutic activity indicating the possibility for reduction of dose and improvement in efficacy.

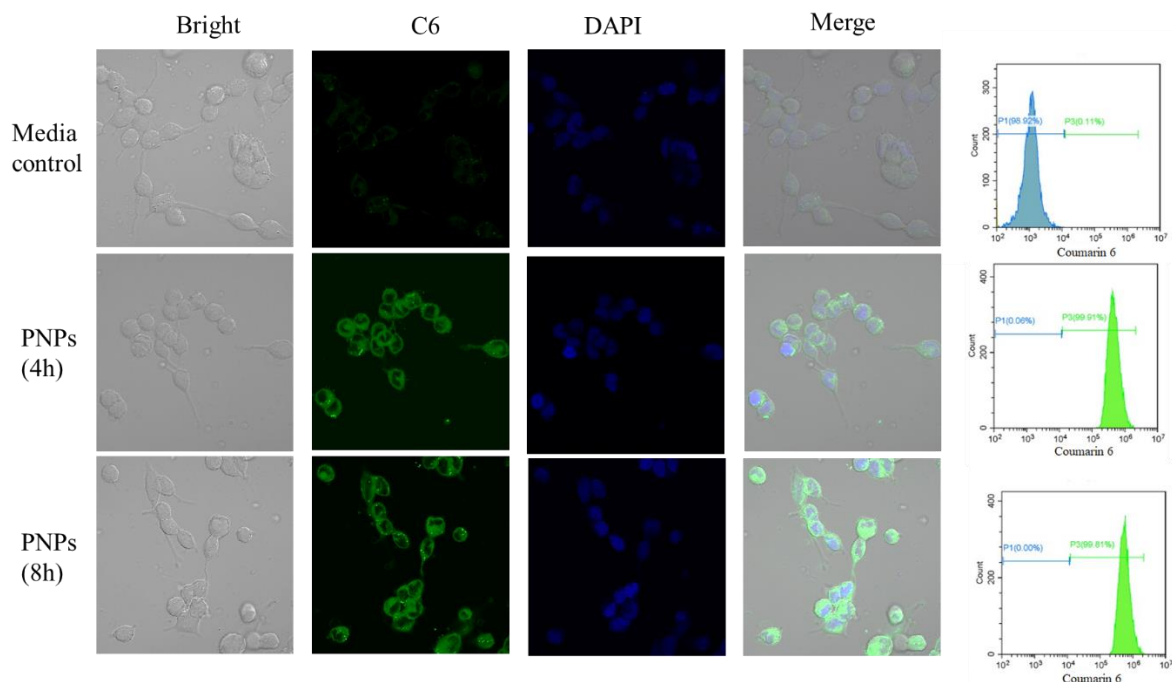


Fig.5.32: The quantitative estimation of coumarin 6, and coumarin 6 loaded PNPs in cellular uptake study by confocal microscopy at 4h and 8h.

5.3.10.3 STZ treated SHSY-5Y cell-based study

Primarily, the concentration of STZ was optimized and observed at a concentration of 2.5mM approximately 60-65% of the cell was viable. Further, the cells were treated with REP and PNPs with the same concentration and incubated for 12 h (Fig.5.33). Afterward, it was observed that the REP shows an increment of ~ 1.2 fold in cell viability which represents a significant effect compared to only STZ-induced cells similarly a ~ 1.42 -fold increment was observed in PNPs treated SHSY-5Y cells compared to REP. However, REP enhances the viability of cells but after loading of REP in PNPs the ~ 1.1 -fold improvement in cell viability was observed in the STZ-induced SHSY-5Y cells.

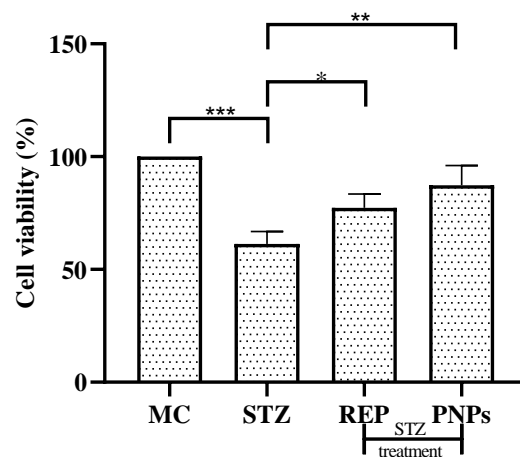


Fig. 5.33: The effect of REP and PNPs on STZ-treated SHSY-5Y neuroblastoma cell lines. data are represented in (mean \pm SEM, n=6 rats per group). * Indicates $P < 0.05$; ** $P < 0.01$, *** $P < 0.001$, by one-way ANOVA followed by Tukey's post hoc multiple comparison test

5.3.10.4 Reactive oxygen species-scavenging activity by hydrogen peroxide

The optimal H_2O_2 concentration for inducing cell death was determined by performing the preliminary studies and it was observed that at 1 mM concentration of H_2O_2 , approximately 60% of the cell were viable after 12 h treatment on SH-SY5Y cells (Fig.5.34). Further, H_2O_2 -treated SHSY-5Y cells (1mM, 12h) were incubated with REP and PNPs to depict the neuroprotective effect on SHSY-5Y cells. Though the study indicates that the REP shows a ~1.3-fold increase in cell viability, similarly PNPs show a significant ($p < 0.01$) effect compared to H_2O_2 . The PNPs also enhance the neuroprotective effect by around 1.4-folds and an increase in cell viability indicates that the REP predominates and at the same time PNPs promote the neuroprotective effect.

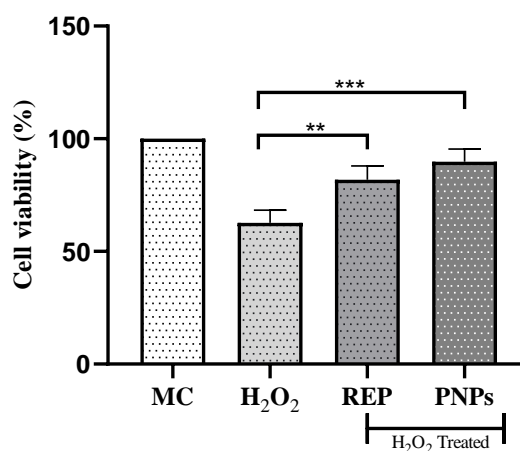


Fig.5.34: Neuroprotective effect of REP and PNPs on H_2O_2 treated SH-SY5Y neuroblastoma cell lines. data are represented in (mean \pm SEM, n=6 rats per group). ** Indicates $P < 0.01$, *** $P < 0.001$, by one-way ANOVA followed by Tukey's post hoc multiple comparison test

5.3.11 Pharmacokinetic study

The pharmacokinetic studies for REP and PNPs were carried out in wistar rats. The plasma concentration versus time profile of REP and PNPs was plotted in Fig.5.35. A bi-exponential decline in the concentration profile was identified, which shows that the data may be fitted into a two-compartmental model. The administration of REP, and PNPs at 4mg/kg; *p.o.*, shows quick absorption, and peak plasma concentration in PNPs reached at ~ 2 h approximately (Table 5.16). It was observed that the PNPs exhibited ~2.1 fold, increase in $t_{1/2}$ than REP solution, indicating slow distribution and elimination. However, AUC was observed to be higher in PNPs (21960.01 ± 907.09 ng. h/ml) than in pure REP solution, which indicates the long-circulating ability of the nanoformulation in plasma. The clearance (Cl) of PNPs indicates ~1.2 fold, a decrease to pure REP solution.

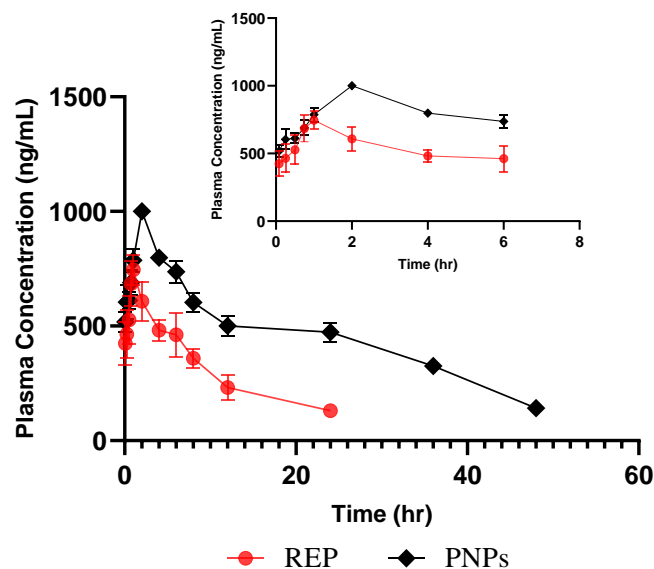


Fig.5.35: Plasma concentration-time profile of REP, and PNPs. Values were represented in mean \pm SEM, n=4.

Table.5.16: Pharmacokinetic parameters of REP and PNPs

Parameters		REP	PNPs
t_{max}	(h)	0.81 ± 0.19	2.00 ± 0.00
C_{max}	(ng/mL)	800.76 ± 26.57	1001.09 ± 25.80
AUC	(ng.h/mL)	7441.69 ± 763.75	21960.01 ± 907.09
CL	(mL/h/kg)	163.84 ± 17.39	129.98 ± 27.152
$t_{1/2}$	(h)	2.65 ± 1.54	15.91 ± 4.73
MRT	(h)	8.24 ± 0.32	20.25 ± 0.21

5.3.12 Biodistribution study

A biodistribution study was carried out to identify the potential of nanoformulation for brain targeting efficiency following oral administration. The distribution pattern of PNPs was quantified in major organs (brain, heart, lungs, liver, kidney) and depicts the concentration-time profiles (Fig. 5.36). In the brain, the concentration levels of REP were detected for 12 h, whereas PNPs persisted for more than 24 hours. Though a similar pattern was observed in other organs, especially in the heart where the REP reaches maximum concentration in 2h and is observed for 12 h and PNPs persist for more than 24 h. Moreover, in the liver, the metabolic rate of REP is very high, but REP-loaded PNPs represent a decrease in metabolic rate due to sustain release of the nanocarriers. In addition, the elimination rate of REP is very low thus PNPs were observed for a longer period compared to the free drug due to the presence of PEGylated polymer which increases the circulation half-life and reduces the protein binding.

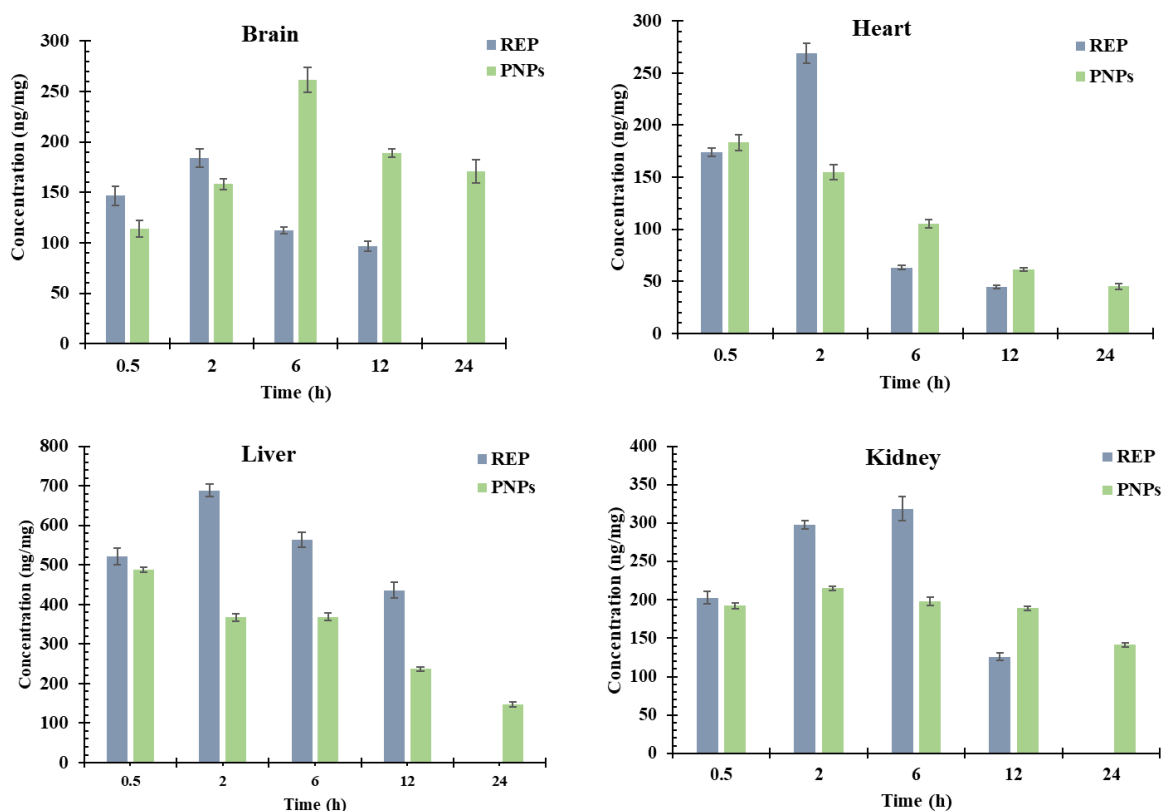


Fig. 5.36: Biodistribution study of REP and PNPs in major organs after oral administration (4mg/kg) in wistar rats

5.3.13 Pharmacodynamic study

5.3.13.1 Estimation of neurochemical parameters

The effect of REP and PNPs on neurochemical parameters (BDNF, A β , and tau protein) were estimated on HFD+STZ-induced wistar rats after the 4 weeks of treatment as represented in Fig.5.37. The BDNF level was significantly reduced in DC group rats than the NC group. When treated with REP and PNPs a significant amelioration in the level of BDNF was observed and PNPs resulted in more consistent amelioration of BDNF levels in comparison with REP. However, it has been well reported that A β deposition and hyperphosphorylation of tau proteins are the characteristic feature of neurodegeneration and plays a key role in AD pathogenesis. Therefore, the potential effect of REP and PNPs was also studied and observed in the DC group rats a significant ($p < 0.001$) upregulation in the levels of A β and tau proteins than in the NC group rats. On treatment with REP and PNPs, a significant attenuation in the A β levels and p-tau levels was noticed in comparison with the DC group. Moreover, PNPs exhibited consistent improvement in the clearance of A β levels and p-tau levels than REP only.

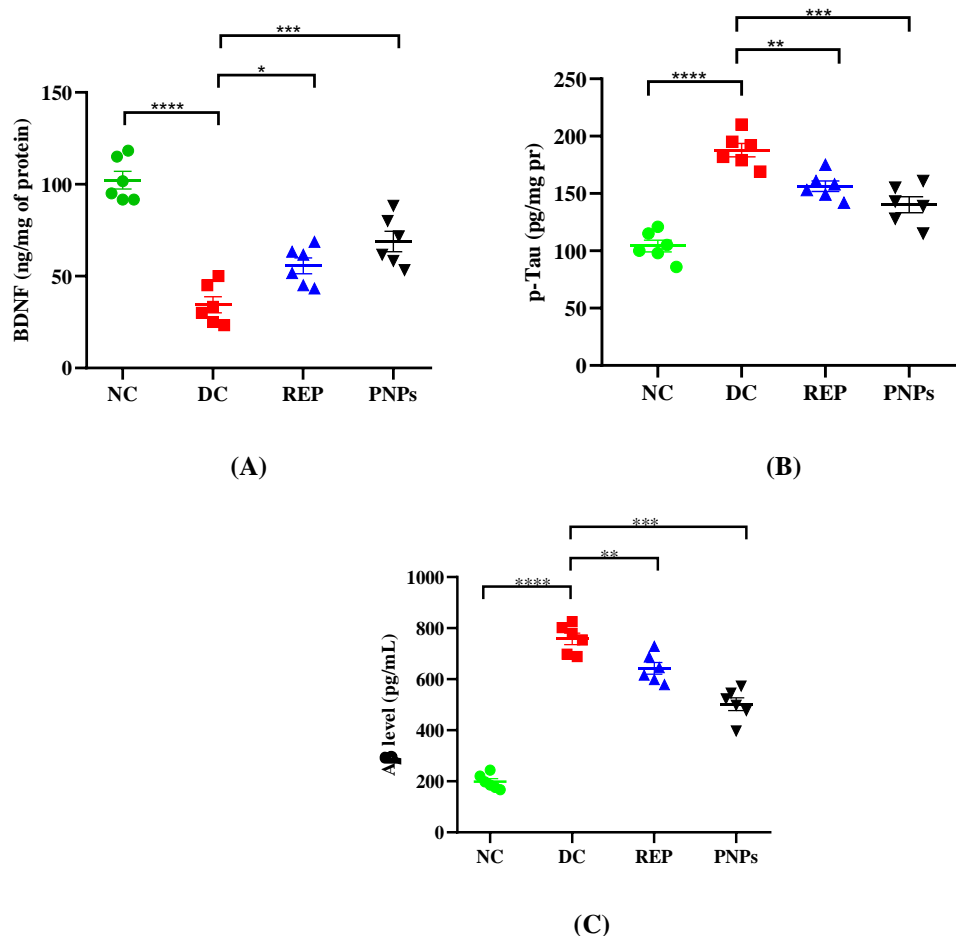


Fig.5.37: *In vivo* estimation of neurochemical parameters to understand the effect of REP and PNPs after the treatment (A) BDNF; (B) p-Tau; (C) A β level in brain homogenate of HFD+STZ induced wistar rats, data are

represented in (mean \pm SEM, n=6 rats per group). * Indicates $P < 0.05$; ** $P < 0.01$, *** $P < 0.001$, **** $P < 0.0001$ by one-way ANOVA followed by Tukey's post hoc multiple comparison test

5.3.13.2 Estimation of inflammatory cytokines

The level of inflammatory cytokines (TNF- α and IL-6) were observed (Fig.5.38) and found a significant ($p < 0.0001$) upregulation in the DC group when compared to NC rats. After the treatment with REP and PNPs, a decrease in these levels was observed but PNPs showed a significant ($p < 0.001$) suppression as compared to REP.

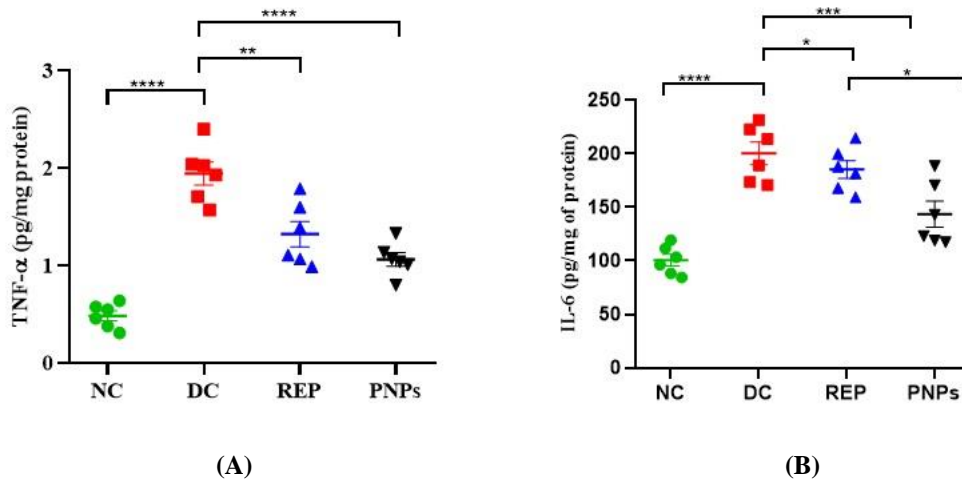


Fig.5.38: *In vivo* estimation of neurochemical parameters to understand the effect of REP and PNPs after the treatment (A) TNF- α ; and (B) IL-6 level in brain homogenate of HFD+STZ induced wistar rats, data are represented in (mean \pm SEM, n=6 rats per group). * Indicates $P < 0.05$; ** $P < 0.01$, *** $P < 0.001$, **** $P < 0.0001$ by one-way ANOVA followed by Tukey's post hoc multiple comparison test

5.3.13.3 Estimation of Oxidative stress parameters

In this study, the level of GSH (antioxidant) MDA, and nitrite (oxidative markers) were determined to understand the role of nanoparticles. The ROS generation (oxidative stress) and neuroinflammation are the molecular mechanisms involved in neurodegeneration. The hippocampus and neocortex regions of the brain were the most vulnerable to oxidative stress-induced impairment. Though the results showed that DC group rats significantly ($p < 0.001$) increase the levels of oxidative markers (MDA and nitrite) and decreased the levels of endogenous antioxidants (GSH) in Fig.5.39. However, the REP and PNPs lower the level of MDA and nitrite whereas the level of GSH increases after treatment. Moreover, PNPs resulted in significant attenuation of oxidative markers (MDA and nitrite) in comparison to REP. The level of GSH significantly ($p < 0.001$) depleted in the DC group than the NC and PNPs significantly ($p < 0.01$) prevented the fall of the defensive enzymes and exhibited more consistent restoration than the REP.

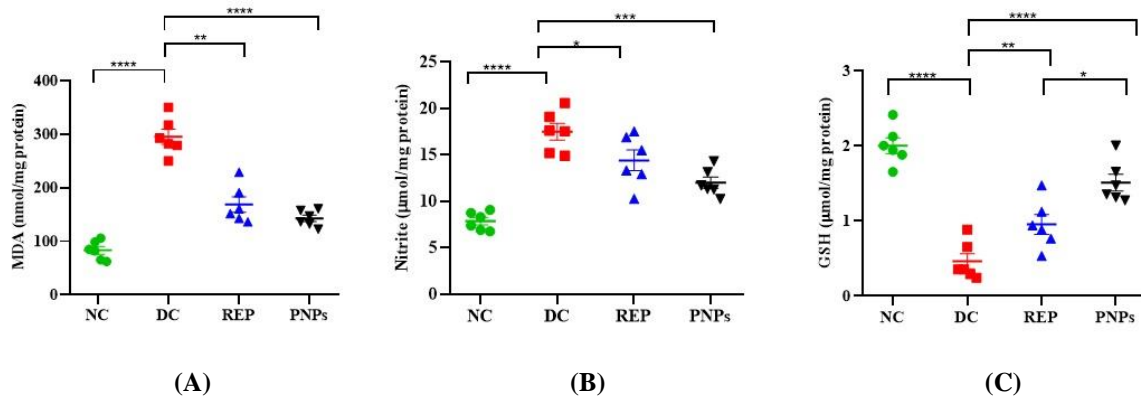


Fig.5.39: Effect of oxidative stress parameters (A) MDA; (B) Nitrite; (C) GSH on REP and PNPs. The data are represented in (mean \pm SEM, n=6 rats per group). * Indicates $P < 0.05$; ** $P < 0.01$, *** $P < 0.001$, **** $P < 0.0001$ by one-way ANOVA followed by Tukey’s post hoc multiple comparison test.

5.3.13.4 Passive avoidance task

A task in which rodents learn to abstain from a response to avoid the aversive stimulus. The test is used to evaluate the learning and memory in cognitive dysfunctions of the central nervous system. During the acquisition trial, no significant ($P > 0.05$) differences in the initial latency time of all the groups were observed. Whereas in retention latency (after 24h of acquisition trial) analysis a significant ($P < 0.01$) decrease was observed in the HFD+STZ group as compared with the NC group (Fig.5.40). However, rats treated with REP, and PNPs showed a significant amelioration in the retention latency which indicates improvement in retention memory.

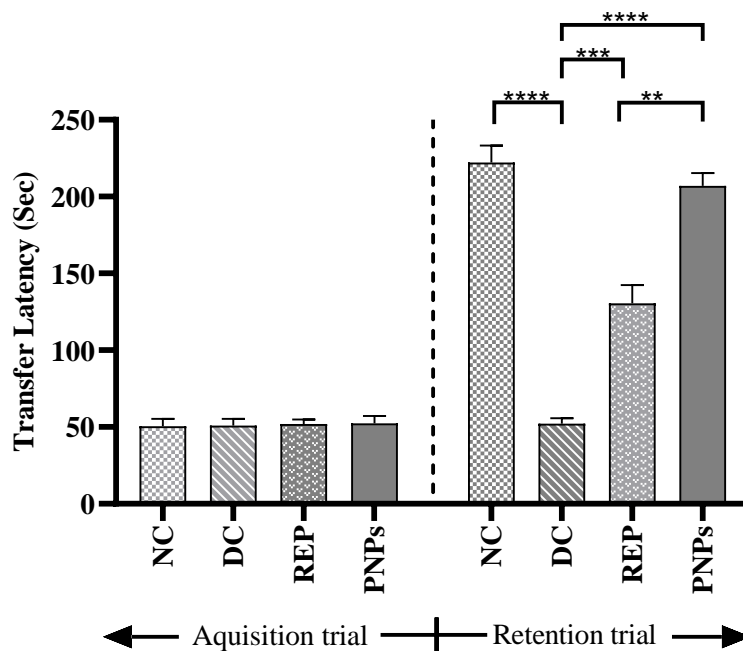


Fig.5.40: Estimation of transfer latency by performing behavioral parameters using passive avoidance task. data are represented in (mean \pm SEM, n=6 rats per group). * Indicates $P < 0.05$; ** $P < 0.01$, *** $P < 0.001$, **** $P < 0.0001$ by one-way ANOVA followed by Tukey’s post hoc multiple comparison test

5.3.13.5 Novel object recognition test

The NORT is used to evaluate the cognition of rodents and investigate changes in memory, particularly recognition memory. The test is primarily based on the spontaneous tendency of rats to spend more time exploring novel objects than familiar ones (Fig.5.41). During the NORT training session, no significant differences in the exploratory preferences of rats were observed. In the retention session, rats in the HFD+STZ group spent significantly less time in exploring novel objects than familiar objects. In the case of REP and PNP, however, an improvement in exploring time was observed, and PNP exhibited a significantly greater improvement than REP.

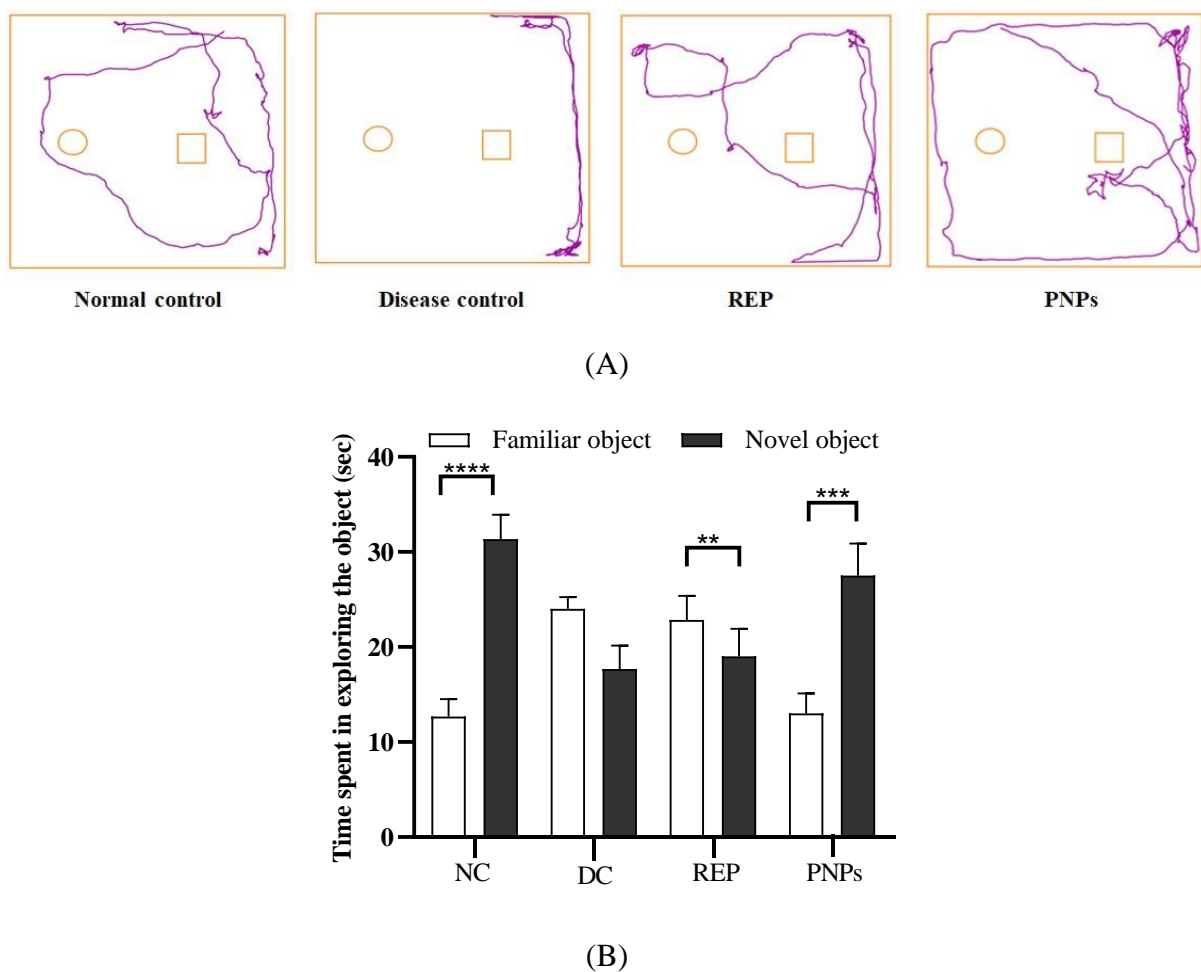


Fig.5.41: (A)Representation of track plot for the novel object recognition task and (B) Time spent in exploring the object. The data are represented in (mean \pm SEM, n=6 rats per group). * Indicates $P < 0.05$; ** $P < 0.01$, *** $P < 0.001$, **** $P < 0.0001$ by one-way ANOVA followed by Tukey's post hoc multiple comparison test.

5.3.13.6 Morri's water maze (MWM)

After four days of training, the mean escape latency in all groups decreased gradually in MWM analysis. However, in the DC group, the mean escape latency was significantly higher in comparison with the NC group. Although there was a decrease in escape latency was observed

after treatment with REP and PNPs. Furthermore, the PNPs significantly attenuated the effect of REP, as shown in Fig.5.42. The hidden platform was removed in the probe trial test, DC group rats were unable to identify the exact location of the platform and spent less time in that quadrant than the NC group rats. The DC group rats were administered with REP and PNPs for 4 weeks and were able to recall the exact position of the platform quadrant. Furthermore, the PNPs group rats spent more time in the platform quadrant than the REP group rats, indicating memory improvement. These findings indicate that PNPs can reduce cognitive behavior in rats. In the probe trial test, the hidden platform was removed in the probe trial test, DC group rats were unable to identify the exact location of the platform and spent less time in that quadrant than the NC group rats. The DC group rats were administered with REP and PNPs for 4 weeks and were able to recall the exact position of the platform quadrant. Furthermore, the PNPs group rats spent more time in the platform quadrant than the REP group rats, indicating memory improvement (Fig.5.42). These findings indicate that PNPs can reduce cognitive behavior in rats.

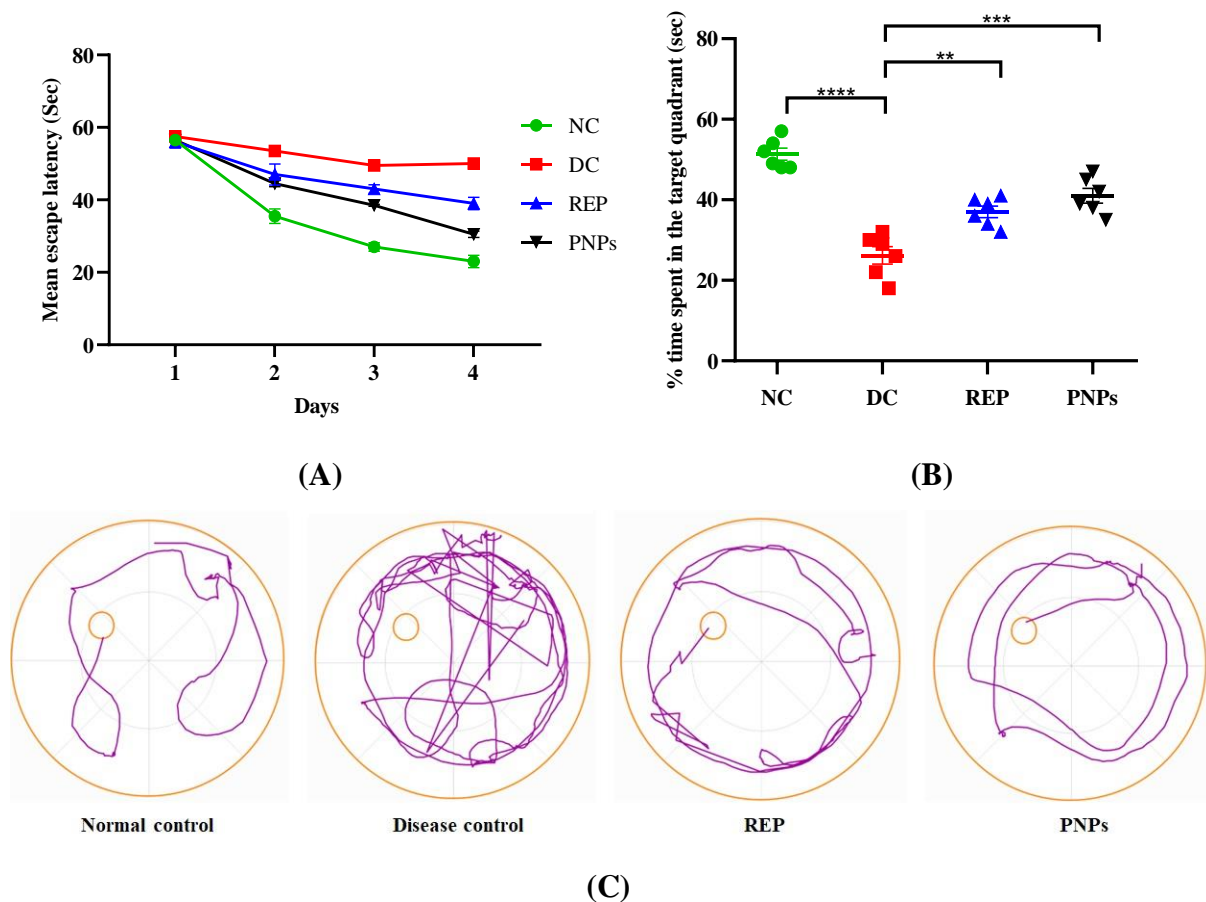
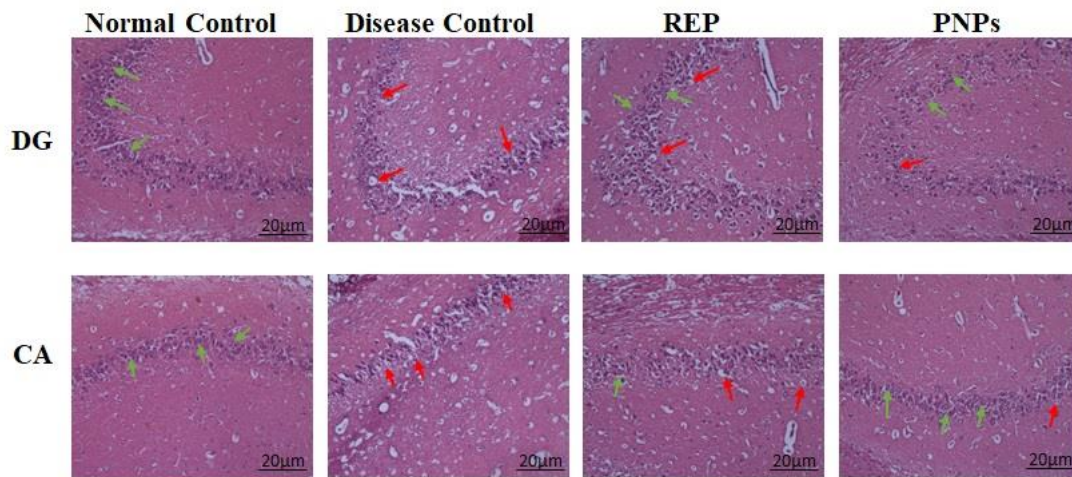


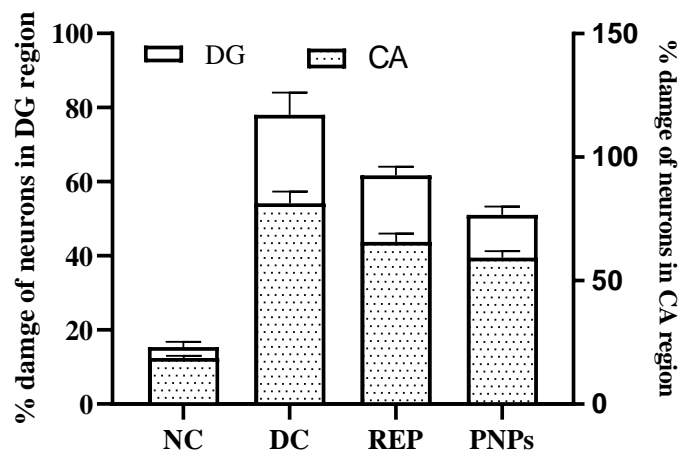
Fig.5.42: Estimation of (A) mean escape latency, (B) time spent in the same quadrant, and (C) representation of track plot for Morri's water maze task. Data are represented in (mean \pm SEM, n=6 rats per group).

5.3.13.7 Histopathological analysis

In this analysis, the HFD+STZ-induced neuronal changes (viable cells, % damaged neuron, pyknotic neurons) in the hippocampus region were investigated by H&E staining. The HFD+STZ group shows a significant change in DG and CA1 region whereas the NPD group shows a healthy nucleus with robust shapes and clear cytoplasm. The HFD+STZ group also represents degeneration, loss of cell bodies, and increase pyknotic neurons in the DG or CA1 region. These pyknotic neurons were shrunken and darkly stained with damaged nuclei and nucleolus. Treatment with REP and PNPs reduced neuronal damage and % of pyknotic neurons were observed (Fig.5.43). However, significant changes were noticed in PNPs compared to REP and represent reduced neuronal loss with improved neuroprotection.



(A)



(B)

Fig.5.43: (A)Neuronal regeneration on HFD+STZ rats at dentate gyrus (DG) and Cornus ammonis (CA) region of hippocampus and (B) % neuronal count in DG and CA region. Data are represented in (mean \pm SEM, n=6 rats per group).

In summary, a multifunctional drug delivery nano platform was fabricated which improves efficacy and promotes the brain delivery of the REP after oral administration. The REP-loaded PNPs were formulated by di-block bio-degradable copolymer mPEG-PCL using the nanoprecipitation method. The developed and optimized PNPs provide stability in GIT, enhance effective intestinal absorption, brain permeability, and improve cellular activities. Further, PNPs improve the pharmacokinetic profile and showed a significant increase in brain levels, indicating an improvement in REP uptake. Likewise, in pharmacodynamic studies, the REP-loaded PNPs significantly ($p<0.01$) attenuated the A β , tau proteins, TNF- α , IL-6, MDA, NO levels and improves the BDNF, SOD, GSH levels compared to REP. Furthermore, the behavioral studies (PAT, MWZ, NORT) also showed a significant ($p<0.01$) improvement in the retention, spatial and recognition memory after treated with REP-loaded PNPs compared to REP. Also, improvement in health neuronal count was observed in the REP-loaded PNPs compared to REP after performing hematoxylin and eosin (H&E) staining in the cornu ammonis (CA) and dentate gyrus (DG) regions of hippocampal. Therefore, it is evident that REP in PNPs ameliorates the activities and shows a neuroprotective effect.

5.4 Development and biological evaluation of Polymer lipid hybrid nanoparticles (PLHNPs)

5.4.1 Preparation of polymeric lipid hybrid nanoparticles (PLHNPs)

The PLHNPs were formulated by different phospholipids in combination with four different stabilizers. The amount of lipids used was 20% w/w of the amount of PLGA and the stabilizer concentration was 0.5% w/v for all the trial experiments. Firstly, the stabilizers including Tween 80, PVA, Pluronic F127, and TPGS were screened, and characteristic parameters were evaluated. Based on the PS, PDI, and EE, it was observed that Pluronic F127 showed comparatively the smallest PS with the highest EE and was graded the best among all. Pluronic F127 is the grade of poloxamer which is a triblock copolymer of ethylene oxide (EO) and propylene oxide (PO), that aids to form a self-assembled hydrophilic outer shell of polymer lipid surface. Through reports, it was ascertained that Pluronic F127 enhances EE and reduces PS. Although the phospholipids were screened (Phospholipon-90 H, Soy lecithin, Egg Phosphatidylcholine, Soy Phosphatidylcholine) to assess the effect of different phospholipids. It was observed that PLHNPs with SPC show good characteristic properties among all such as smaller PS, less PDI, and high EE (Table.5.17). Further, PLGA, SPC, DSPE-PEG₂₀₀₀, and Pluronic F127, were used in the preparation of PLHNPs, due to their biodegradable, biocompatible properties, and approved by the Food and Drug Administration (FDA) as drug carriers for clinical use. The PLGA is a hydrophobic polymer that precipitates to form a hydrophobic core for the encapsulation of drug and SPC a phospholipid, which forms the lipid monolayer at the interface of the PLGA core. The PEGylated lipid (DSPE-PEG₂₀₀₀) helps to form the “stealth” shell of the PLHNPs. However, SPC and DSPE-PEG₂₀₀₀ conjugate and self-assemble around the hydrophobic core to form a lipid monolayer.

Table.5.17: Preliminary Screening of phospholipids & stabilizers for preparation PLHNPs. Data are represented as mean \pm SEM (n=3)

Formulation No.	Phospholipids	Stabilizers	Particle size (nm)	Polydispersity index	Entrapment efficiency (%)
F1	Phospholipon-90 H	Tween 80	166.55 \pm 3.41	0.125 \pm 0.07	10.72 \pm 2.97
F2		PVA	188.00 \pm 2.94	0.133 \pm 0.08	32.22 \pm 3.86
F3		Pluronic- 127	178.86 \pm 1.76	0.186 \pm 0.09	31.23 \pm 5.96
F4		TPGS	251.15 \pm 2.87	0.212 \pm 0.10	6.53 \pm 3.37
F5	Soy lecithin	Tween 80	178.10 \pm 4.12	0.140 \pm 0.06	25.37 \pm 3.18
F6		PVA	174.10 \pm 3.49	0.146 \pm 0.14	56.68 \pm 4.61
F7		Pluronic- 127	186.76 \pm 3.56	0.249 \pm 0.11	41.65 \pm 2.71
F8		TPGS	191.33 \pm 2.97	0.262 \pm 0.15	23.71 \pm 2.97

F9		Tween 80	185.53 ± 1.65	0.238 ± 0.21	45.94 ± 2.98
F10	Egg Phosphatidylcholine	PVA	163.03 ± 2.76	0.168 ± 0.23	41.24 ± 5.90
F11		Pluronic- 127	175.30 ± 3.94	0.160 ± 0.26	50.84 ± 3.97
F12		TPGS	173.86 ± 2.45	0.153 ± 0.09	24.69 ± 3.76
F13		Tween 80	183.60 ± 4.76	0.144 ± 0.16	37.50 ± 3.87
F14	Soy Phosphatidylcholine	PVA	178.53 ± 3.87	0.188 ± 0.17	50.53 ± 4.29
F15		Pluronic- 127	164.56 ± 2.95	0.158 ± 0.19	60.90 ± 4.76
F16		TPGS	170.13 ± 2.78	0.166 ± 0.11	9.59 ± 4.57

5.4.2 Optimization of PLHNPs by QbD approach

The optimization of PLHNPs by the QbD approach was done by selecting QTPPs and CQAs to ensure the safety and efficacy of the product. However, CQAs were evaluated, and based on the parameters of the sequential model sum of the square, model summary statistic the model was suggested (Table.5.18).

Table.5.18: The Statistical values for each of the model sources for both the responses, along with remarks generated by the Design-Expert® software (version 13.0, Stat-Ease Inc.) under the heading of summary of fitness of each model.

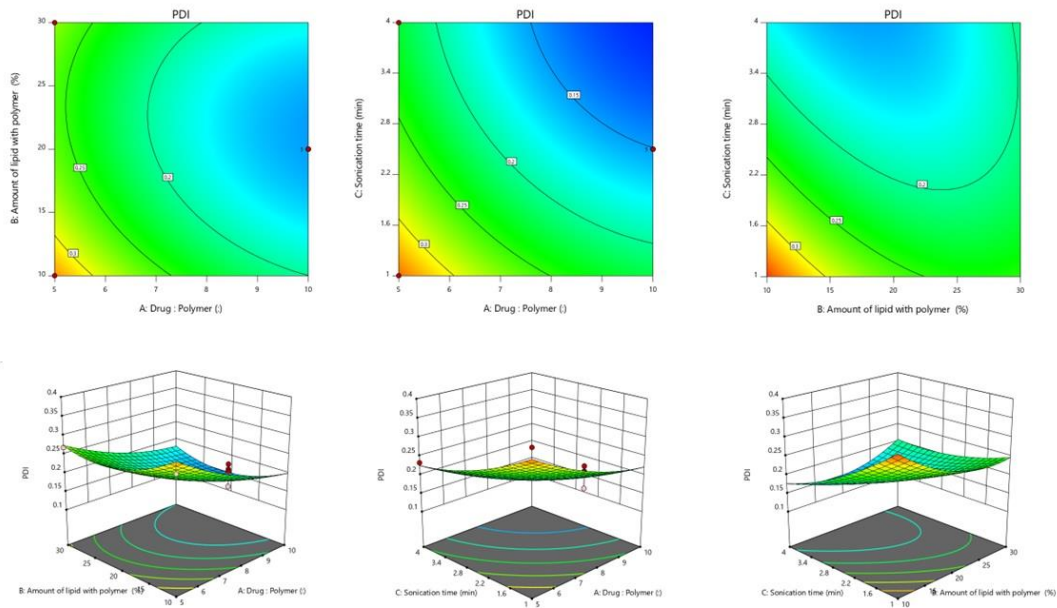
Response	Source	Sequential p value	R ²	Adjusted R ²	Predicted R ²	Press	Remarks
Particle size	Liner	<0.0001	0.8598	0.8279	0.7489	1807.24	Suggested
	2FI	0.7592	0.8747	0.7995	0.5322	3367.04	-
	Quadratic	0.5368	0.9064	0.7860	0.0574	6784.36	-
	Cubic	0.2691	0.9615	0.8461	-	-	Aliased
PDI	Liner	0.1068	0.3643	0.2176	0.1748	0.0869	-
	2FI	0.7402	0.4360	0.0976	-0.3036	0.1373	-
	Quadratic	0.0025	0.9188	0.8406	0.0726	0.0977	Suggested
	Cubic	0.2111	0.9708	0.9479	-	-	Aliased
Entrapment efficiency	Liner	0.6488	0.1150	-0.0892	-0.4667	11330.01	-
	2FI	0.5835	0.2652	-0.1757	-1.1717	16775.86	-
	Quadratic	< 0.0001	0.9746	0.9420	0.8133	1442.03	Suggested
	Cubic	0.5170	0.9848	0.9393	-	-	Aliased

The linear model was suggested for Response 1(PS) whereas the quadratic model was recommended for Response 2 (PDI) and Response 3(EE) based on the applied ANOVA test to evaluate the factors which affect the response in quadratic equations (Table.5.19).

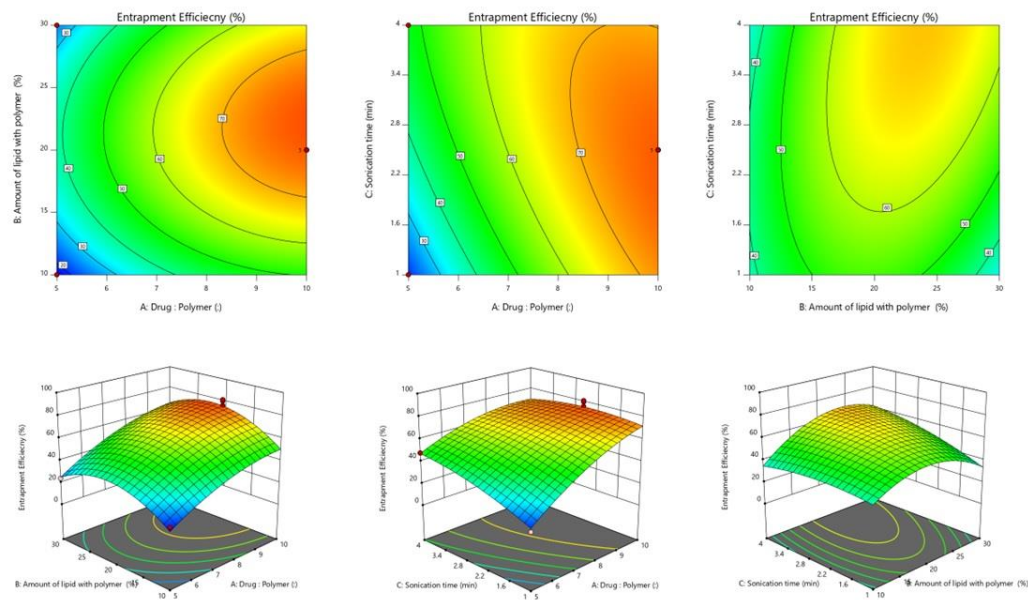
Table.5.19: Statistical validation parameters of the selected models for individual responses

Response	Equation	Adequate precision	F-value	p-value Prob >F
Particle size	+133.20-0.17A-0.35B-27.81C	13.18	26.58	0.0001
PDI	+0.18+0.05A+0.01B-0.05C+0.008AB+0.002AC+0.033BC+0.02A ² +0.34B ² +0.01C ²	8.69	13.88	0.0045
Entrapment	+64.21+18.56A+5.82B+6.36C+1.64AB-7.36AC+7.90BC-7.44A ² -17.51B ² -4.56C ²	14.49	65.28	0.0001

It was observed that the selected factors i.e., drug-polymer ratio (Factor 1), amount of lipid (Factor 2), and sonication time (Factor 3) significantly affect PS, PDI, and EE in PLHNPs. The BBD provides information on polynomial equations involving the interaction, effects, and responses of independent variables. Attentively observing the polynomial equations and surface plots (2d or 3d) results in emphasizing the effects of each variable independently and in combination with other variables on each response.



(A)



(B)

Fig. 5.44: The 2D and 3D-response surface plot showing the relationship among the factors on (A)PDI, and (B) entrapment efficiency of Drug: polymer; Surfactant amount (AB factor), Drug: polymer; Sonication time (AC factor), Surfactant, sonication time (BC factor) of the PLHNPs

The 2D and 3D response surface plots of PS, PDI, and % EE on PLHNPs were generated (Fig.5.44 A-B) and showed a dependency on selected independent variables. It was observed that the PS, PDI, and % EE increase as the drug: polymer ratio increases. However, the drug amount was kept constant while the amount of polymer was varied (increased) resulting in a decrease PS and PDI due to the change in concentration of hydrophilic moiety of the polymer. Moreover, an increase in the amount of lipid enhances the EE due to an increase in the viscosity of the medium resulting in rapid solidification which prevents drug diffusion and leads to a greater or speedy encapsulation. In addition, sonication time increased, PS, PDI, and percent EE were observed to decrease. An increase in sonication time breaks up the particles and decreases the dispersion size. The overlay plot was obtained using numerical and graphical methods to predict the optimal composition for PLHNPs [235]. The composition of factors was selected from the design space in the overlay plot (Fig.5.45) and the minimum PS, PDI, and maximum EE% were kept for the selected criterion for the optimized region.

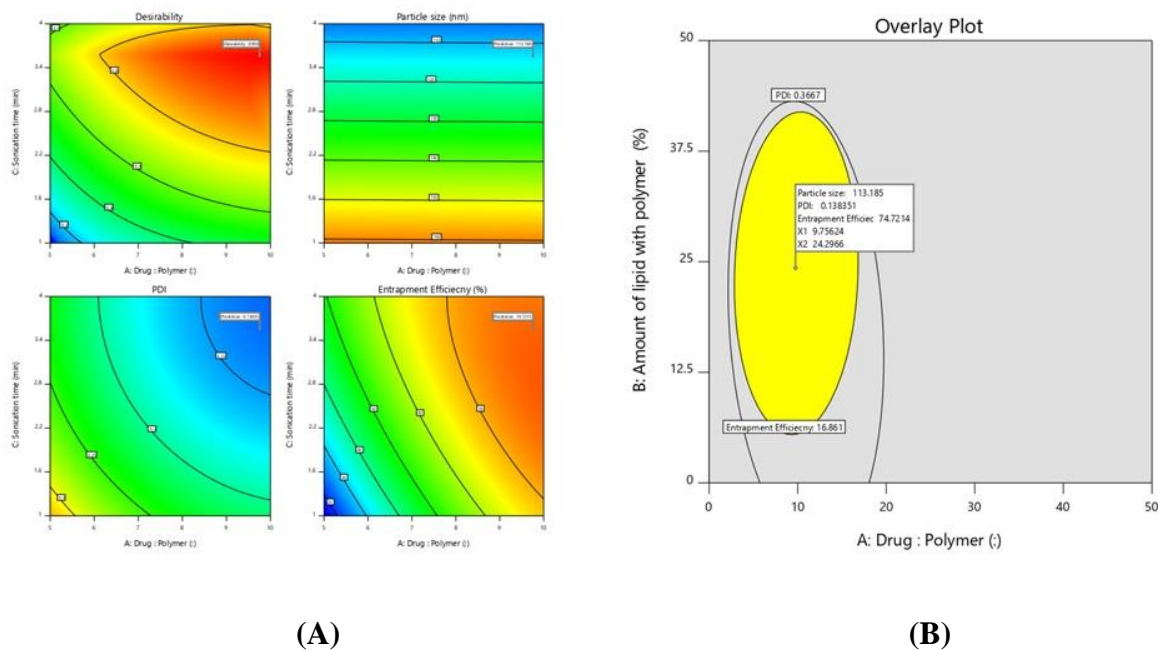


Fig.5.45: The (A) desirability index and (B) overlay plot of PNP with Drug: polymer; Surfactant amount

In addition, the predicted results were verified by comparing them with the actual experimental values derived from the responses (Table.5.20). In PLHNPs, the deviation between predicted and experimental values varied from -1.86 to 4.91. The obtained results demonstrated that the generated design space can reduce the risk of failure and thus indicated that the models are reliable.

Table.5.20: Experimental design model validation of PLHNPs by QbD.

Responses	Polymeric lipid hybrid nanoparticles		
	Predicted value	Experimental value	% Residual
Particle size (nm)	130.01	125.09 ± 3.21	4.91
Polydispersity index	0.16	0.18 ± 0.05	-0.02
Entrapment efficiency (%)	73.37	75.23 ± 1.94	-1.86

5.4.3 Physicochemical Characterization of nanoparticles

5.4.3.1 Compatibility study

The ATIR spectra analysis of REP, BPLHNPs, and PLHNPs depicts the appearance of no new peaks and the disappearances of existing peaks which eliminates the probability of any chemical interactions (Fig.5.46 A). The ATIR spectra of REP showed a peak at 3310 cm^{-1} (NH stretching), 2952 cm^{-1} (-CH stretch), 1684 cm^{-1} (-C=O) and C-O stretch at 1040 cm^{-1} , 1209 cm^{-1} respectively. Whereas in PLHNPs sharp peak were obtained at 1071 cm^{-1} (C-O stretch), 1734 cm^{-1} (-C=O), 2934 cm^{-1} (-CH stretch). Though a slight shift was seen in IR fingerprint region peaks and the absence of an extra peak confirmed no interaction between the excipients used in the formulation.

DSC a thermo analytical technique for studying the thermal properties and/or phase transitions that can be produced or absorb heat as a function of time and temperature. DSC also evaluates the material properties, inertness, melting point and determines the content and degradation of the substance. The thermogram of REP shows an endothermic peak at 135 °C whereas BPLHNPs thermogram represented peaks at 53 °C, 128 °C, 211 °C, 272 °C and PLHNPs at 53 °C, 98 °C, 128 °C, 257 °C respectively. The thermograms depict the shift of the peaks in PLHNPs which represents the proper incorporation of guest moiety into the host cavity. The absence of characteristic peaks of components indicates the amorphous nature of PLHNPs (Fig.5.46 B).

pXRD, a non-destructive technique was used to identify phase transition and measured the diffraction pattern of crystalline material. The crystallinity of REP, BPLHNPs, and PLHNPs was investigated by pXRD. The patterns of REP revealed the distinguishable diffraction peaks at diffraction angle 2θ of 7.65°, 10.11°, 12.40°, 13.24°, 13.76°, 14.58°, 16.67°, 17.50°, 18.56°, 20.22°, 22.91°, 23.33°, 25.67°, 26.60°, and 30.88° which confirmed the highly crystalline nature whereas PLHNPs and BPLHNPs exhibited an additional peak at 23.78°, signify the presence of shell with the lipid core at the interface. Furthermore, the results of pXRD confirmed the REP was incorporated within the matrix core and leading to a change in its crystallinity (Fig.5.46.C).

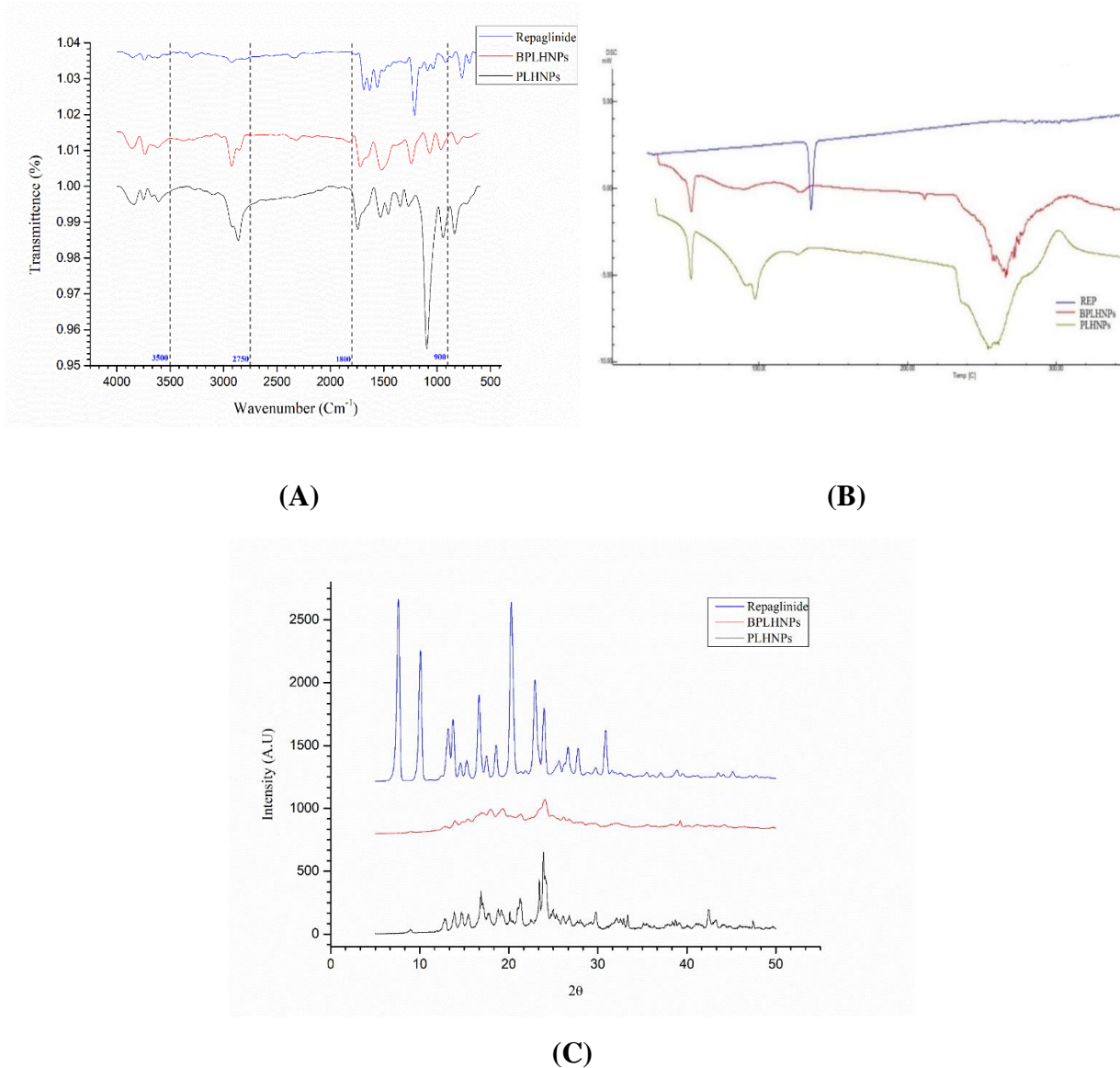


Fig. 5.46: The compatibility study of REP, BPLHNPs, and PLHNPs performed by (A) ATIR, (B) DSC, and (C) pXRD.

s5.4.3.2 Particle size and morphological evaluation

PS is a crucial parameter that influences the release, stability, *in vitro* and *in-vivo* pattern. The absolute size of PNP was found to be 125.09 ± 3.21 nm with a PDI of 0.18 ± 0.05 and ZP of -16.4 ± 0.53 mV (Fig.5.47 A-B).

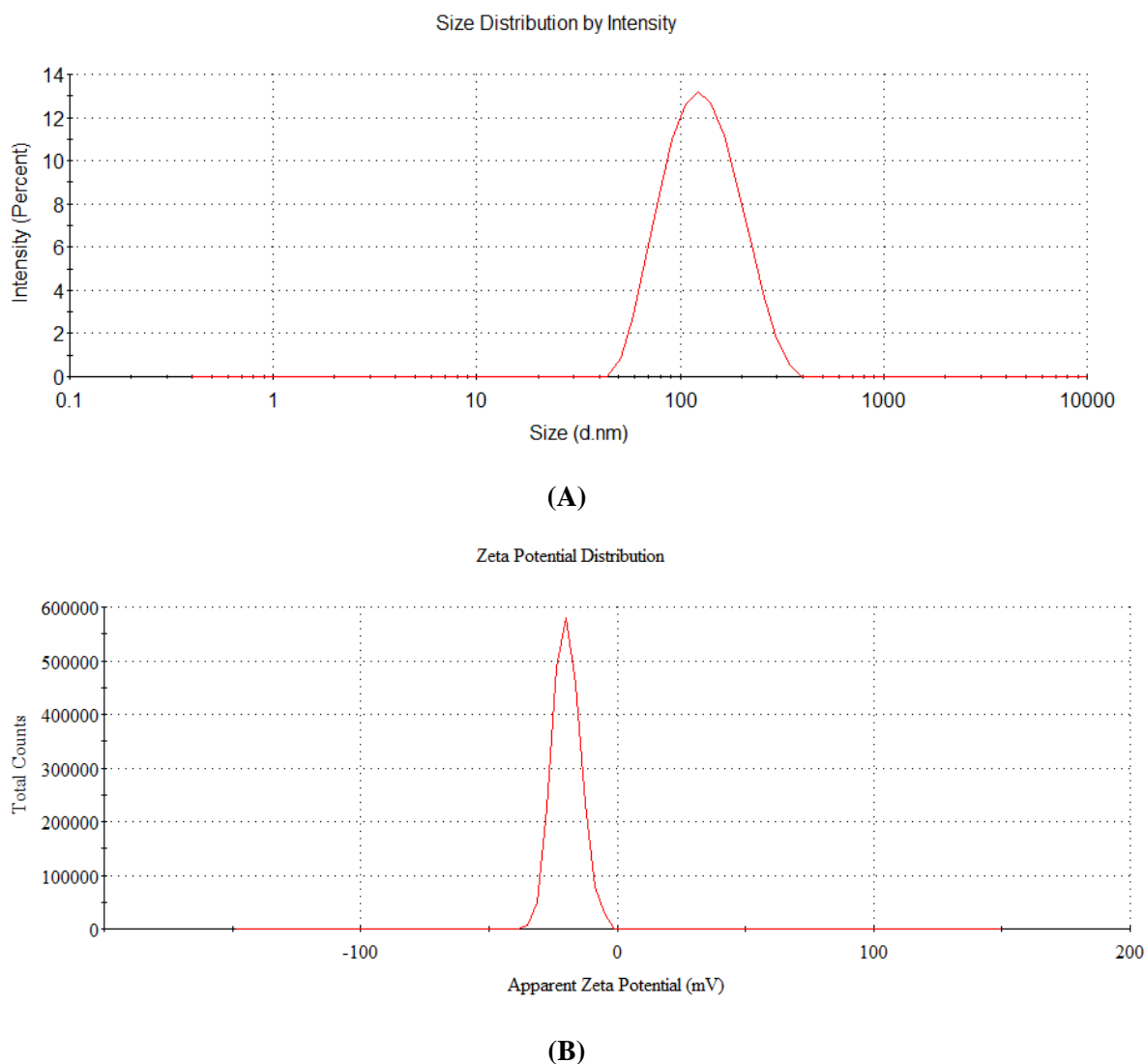


Fig.5.47: Characterization of polymer lipid hybrid nanoparticles by (A) PS and (B) ZP.

Moreover, particle morphology significantly influences the percent drug loading, entrapment efficiency, drug release profile, pharmacokinetics, and biodistribution pattern of the nanoparticles. It also has a role in cellular uptake, cellular internalization, receptor binding, and molecular interactions. The FE-SEM and TEM analysis showed that most nanoparticles were isometric, with smooth surfaces and the average size of nanoparticles was the same as obtained by DLS. However, in TEM the PLHNPs showed a spherical core-shell structure in which the core (PLGA) was properly surrounded by lipid monolayer at the interface (Fig.5.48. A&B).

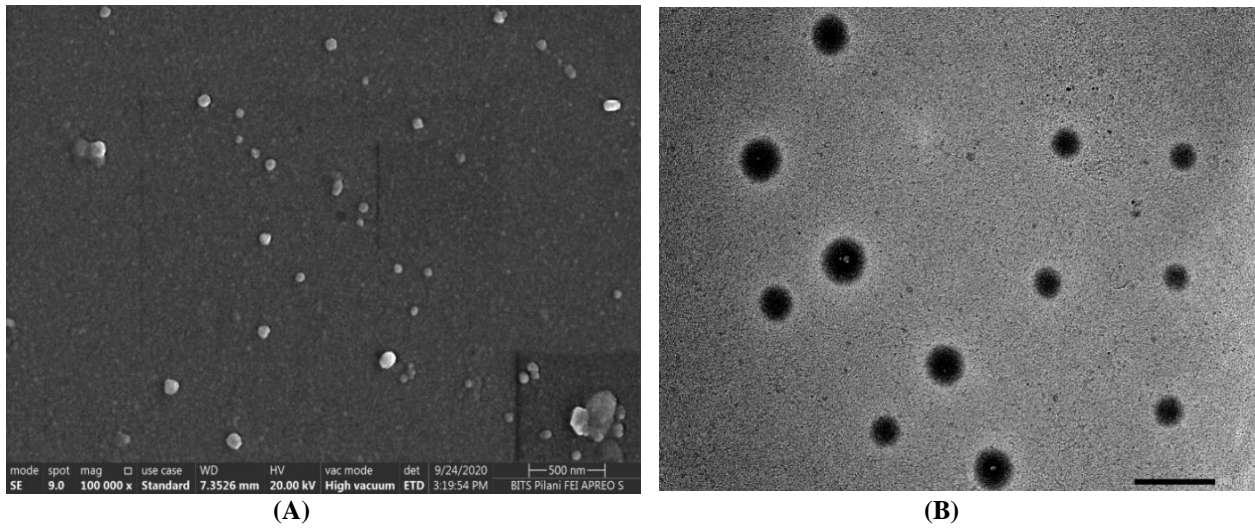


Fig.5.48: Morphological characterization of polymer lipid hybrid nanoparticles by (a) SEM and (b) TEM

5.4.4 Lyophilization process optimization

In preliminary studies, cryoprotectants such as sucrose, trehalose, lactose, and mannitol were examined based on dispersibility (Fig.5.49. A). Through the screening process, trehalose was found the most suitable cryoprotectant due to its excellent redispersibility index, and 5% w/v of trehalose was selected for the cryoprotection of PNPs due to the formation of a poor network, which undue the stress of freeze-drying (Fig.5.49. B).

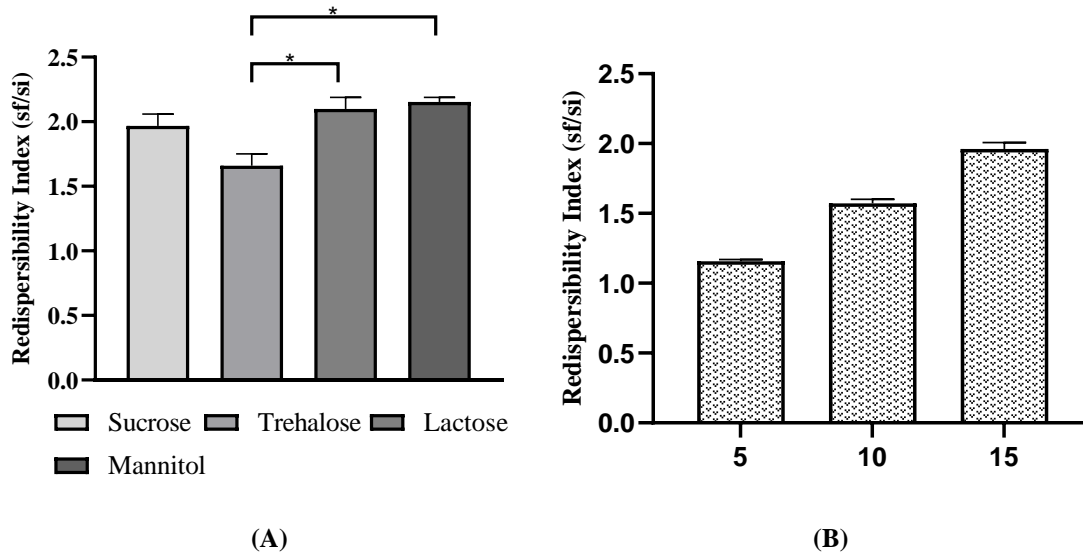


Fig.5.49: Graphical representation of (A) cryoprotectant screening; (B) amount (% w/v) of selected cryoprotectant.

5.4.5 *In vitro* drug release study

The estimation of the release profile of REP and PLHNPs is important to understand the rate and extent of the drug present at the site of action. The controlled release of drugs is essential to maintain the therapeutic window. Herein, the release of REP and PLHNPs was studied using the dialysis bag method, and the drug release profile is shown in Fig.5.50.

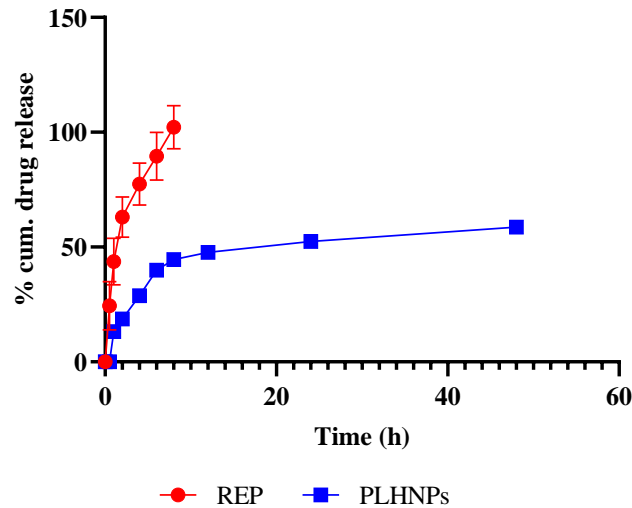


Fig.5.50: *In vitro* release profile of REP and PLHNPs using dialysis bag method for 48h.

The PLHNPs showed a cumulative drug release of ~58% within 48h, and REP showed a burst release profile with 100% release in ~2h (Fig.5.50). Although, various mathematical models were measured to determine the release pattern of REP using DD-Solver (Table.5.21). It was observed that the REP follows the first order kinetics whereas PNP's featured with low AIC value with high regression coefficient and fitted to the Korsmeyer-Peppas model which indicates that PLHNPs imply the degradation by creating fine pores with diffusion.

Table.5.21: Mathematic release models for the estimation of *in vitro* release parameters

Model	Parameters	Test Sample	
		REP	PLHNPs
Zero	K_0	9.03	3.48
	R^2	0.69	0.80
	AIC	108.37	74.63
First	K_1	2.16	0.07
	R^2	0.94	0.91
	AIC	84.90	67.05
Higuchi	K_H	39.52	14.92
	R^2	0.85	0.92
	AIC	96.41	58.58
Korsmeyer-Peppas	k_{KP}	81.82	20.62
	R^2	0.93	0.95
	AIC	73.76	55.01

5.4.6 Protein binding assay

The hydrophobic surface of nanoparticles has the propensity to adsorb protein, which enhances opsonization and macrophage recognition. Thus, it increased the rate of elimination and diminished therapeutic efficacy. Utilizing lipophobic moieties such as polyethylene glycol (PEG) or poly (ethylene oxide) (PEO) on the surface of nanoparticles could reduce protein adsorption. Typically, PEG and PEO increase the probability that a drug molecule will be pre-dispersed at the target site by resisting interactions with bloodstream components. Formulating PNPs with PEG and PEO decreases the clearance and increases blood circulation. Though the observed data also show protein adsorption of $3.58 \pm 2.7\%$.

5.4.7 Stability studies

5.4.7.1 Stability study in simulated biological fluids

Nano formulations for the controlled delivery of drugs are receiving considerable attention, but the stability of nanoparticles has been a source of concern. Particularly, the size and dispersity of nanoparticles that facilitates target-specific delivery, rapid gastric emptying, and reproducible GIT transit. In addition, it safeguards the encapsulated drug, controlled release profile, decreased toxicity, and immunogenic potential more effectively than the conventional system. In the preparation of nanoparticles, surface-capping or stabilizing ligands were used to regulate particle dimensions. As depicted in Fig.5.51, the PLHNPs were found to be stable in simulated gastrointestinal fluids, and a significant change in their quality attributes was observed. As the formulation contains a stabilizing or capping agent (Poloxamer), van der Waals forces are diminished, and repulsive forces are established between the colloidal particles. These forces ultimately diminished particle aggregation and precipitation. The PLHNPs were comprised of biodegradable polymers and DSPE-PEG2k a PEG-Lipid which aims to improve the stability and mobility of the complexes in the harsh gastrointestinal environment.

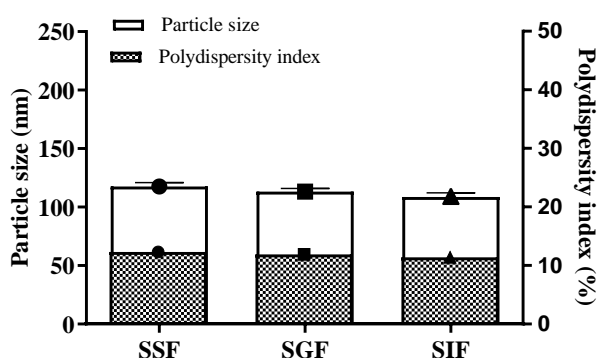


Fig:5.51: Stability study of PLHNPs in simulated gastrointestinal fluids

5.4.7.2 Stability of lyophilized nanoformulation

The most important factor to consider is the nanocarrier's stability, which should thoroughly characterize its resuspension. The long-term stability study was conducted for three months in accordance with ICH guidelines, and PS, PDI, ZP, and EE% were evaluated. The PLHNPs were discovered to be stable and not significantly different from the initial (Table 5.22). In addition, the redispersion time for lyophilized PLHNPs was less than one minute, and the designed lyophilized PLHNPs were stable at 25 ± 2 °C, 60 ± 5 % RH.

Table 5.22: Stability studies of PLHNPs*

Parameters	Initial	after 1 month	after 2 months	after 3 months
PS (nm)	123.5 ± 5.91	125.2 ± 2.15	122.4 ± 4.03	128.7 ± 2.91
PDI	0.17 ± 0.04	0.16 ± 0.02	0.15 ± 0.05	0.17 ± 0.03
ZP (mV)	-16.13 ± 0.65	-16.36 ± 0.41	-16.38 ± 0.27	-17.05 ± 0.11
% EE	75.42 ± 2.51	76.29 ± 3.10	76.89 ± 4.12	75.04 ± 3.13

*Results were represented as mean ± SEM, n=3

5.4.8 *In situ* absorption study by Single pass intestinal perfusion (SPIP) model

The estimation of intestinal absorption plays an important role in identifying the transport mechanisms (p-glycoprotein) for improvement of drug profile, safety, and efficacy. Initially, the steady state of REP with intestinal tissue was evaluated for permeation through the intestine and confirmed by the determination of C_{out}/C_{in} ratios (Fig.5.52). Throughout the experiment, no nonspecific binding of REP to the tubing was observed, and the concentration of REP in the perfusion solution remained stable. In the study, it was observed that the P_{eff} value of PLHNPs increased by ~3.3 fold and the K_a value increased by ~3.9 fold that of REP, indicating that the nanoformulations increased the permeation/absorption rate of REP in wistar rats. Though the PLHNPs show significant enhancement due to more GIT stability or can be attributed to the core-shell structure of PLHNPs which helps to maintain the controlled release of the drug and PEG enhances the permeation rate.

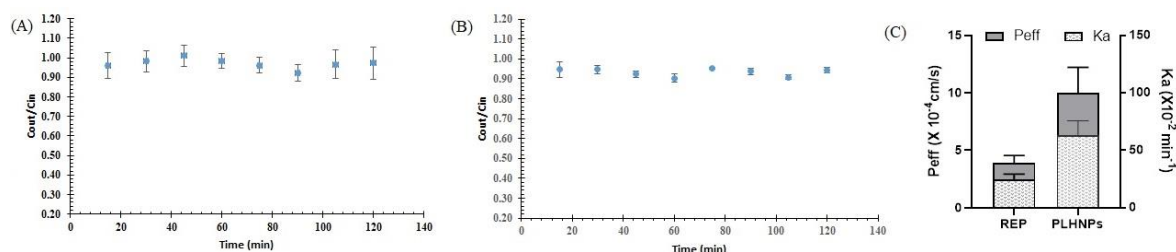


Fig.5.52: Representative plots of the steady-state concentration (c_{out}/c_{in}) VS time for (a) REP, (b) PLHNPs, and (c) Effective permeability coefficient and apparent absorption rate constant. Values were represented as mean ± SEM ($n=3$)

5.4.9 Parallel artificial membrane permeability assay-blood brain barrier

The PAMPA-BBB is the most used method to predict brain permeability due to its high throughput and is designed to precisely mimic the physicochemical microenvironment of the barrier. PAMPA is a limited method because it is modeled by an artificial membrane and thus is neither used for active transport nor P-gp efflux. Herein, REP and PLHNPs were examined to determine the effective permeability (P_e) using measured concentrations and it was observed that the PLHNPs achieve ~ 1.6 folds more permeability to the brain than REP due to the core-shell structure of the nanoparticles which enhanced the selective tissue targeting and sustain the release profile [229,230,234].

5.4.10 *In vitro* cell culture study

5.4.10.1 Cell viability assay

The cell viability assay examines the physical or cellular health in response to chemical agents, or extracellular stimuli and reflects the amount of live and/or healthy cells in a sample. MTT assay, a colorimetric test used to detect cellular oxidative metabolic activities based on NAD(P)H-dependent dehydrogenase enzyme activity. Initially, concentrations of REP (0.10 to 200 $\mu\text{g}/\text{mL}$) were tested on the viability of SHSY-5Y cells to assess concentration-dependent toxicity. In order to determine the potential of nanoparticles, the effects of REP, BPLHNPs, and PLHNPs were tested between 0.25 and 40 $\mu\text{g}/\text{mL}$ (Fig.5.53). The cell viability of BPLHNPs over $\sim 70\%$ indicates the biocompatibility and nontoxicity nature of nanocarrier. However, the higher concentration of PLHNPs and BPLHNPs showed $\sim 90\%$ cell viability in SH-SY5Y cells and indicates the nontoxic nature of REP-loaded nanoformulations.

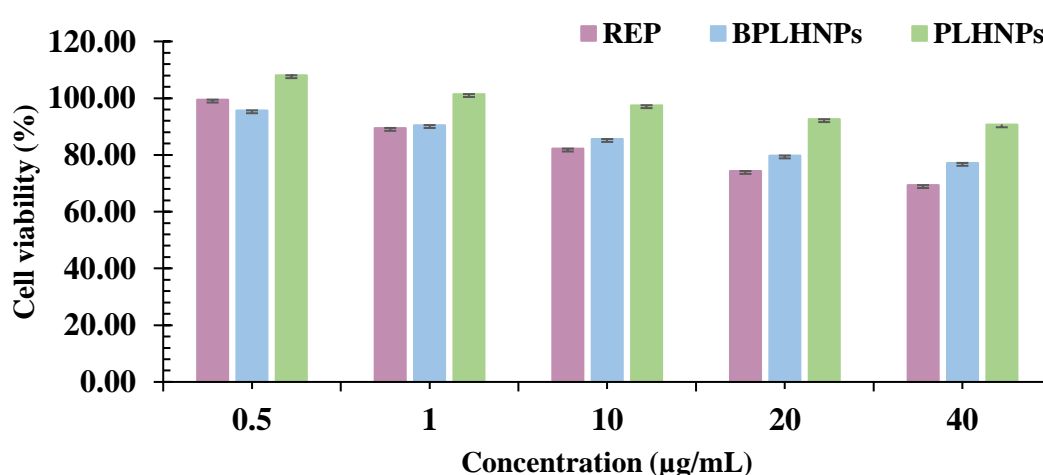


Fig.5.53: Cell viability assay of REP, BPLHNPs, and PLHNPs on neuroblastoma SH-SY5Y cell line.

5.4.10.2 Cellular uptake

In drug delivery systems, nanoparticles are utilized to reduce systemic toxicity, prolong blood circulation, and enhance intracellular uptake. The cellular uptake is affected by the shape, size, hydrophobicity, and charge of the nanoparticles. Herein, C6 as a model drug and the cellular uptake of PLHNPs were investigated using confocal microscopy, and flow cytometry in SHSY-5Y cell lines. Although the cellular uptake of C6-loaded PLHNPs was significantly ($p < 0.001$) greater than that of free C6 in SH-SY5Y cells at 4h and 8h (Fig.5.54). The uptake of C6-loaded PLHNPs in SHSY-5Y cells increased by ~ 28.81 -fold at 4h and ~ 32.24 -fold at 8h compared to C6-free cells. The PLHNPs exhibited greater intercellular uptake than free C6, which may be a result of drug loading into a hydrophobic polymer matrix and a strong interaction between the negative charge on the cell membrane. Additionally, it was also noticed that the c6-loaded PLHNPs showed higher uptake due to the size-independent lipid trafficking pathway. The lipid density in the cellular membrane increases the sustained drug release compared to free c6. The PLHNPs easily affect the biological barriers and efficiently enhance circulation. In spite of the fact that increased cellular uptake increases the amount of drug available at the site of action for therapeutic activity, indicating the potential for dose reduction and enhanced efficacy.

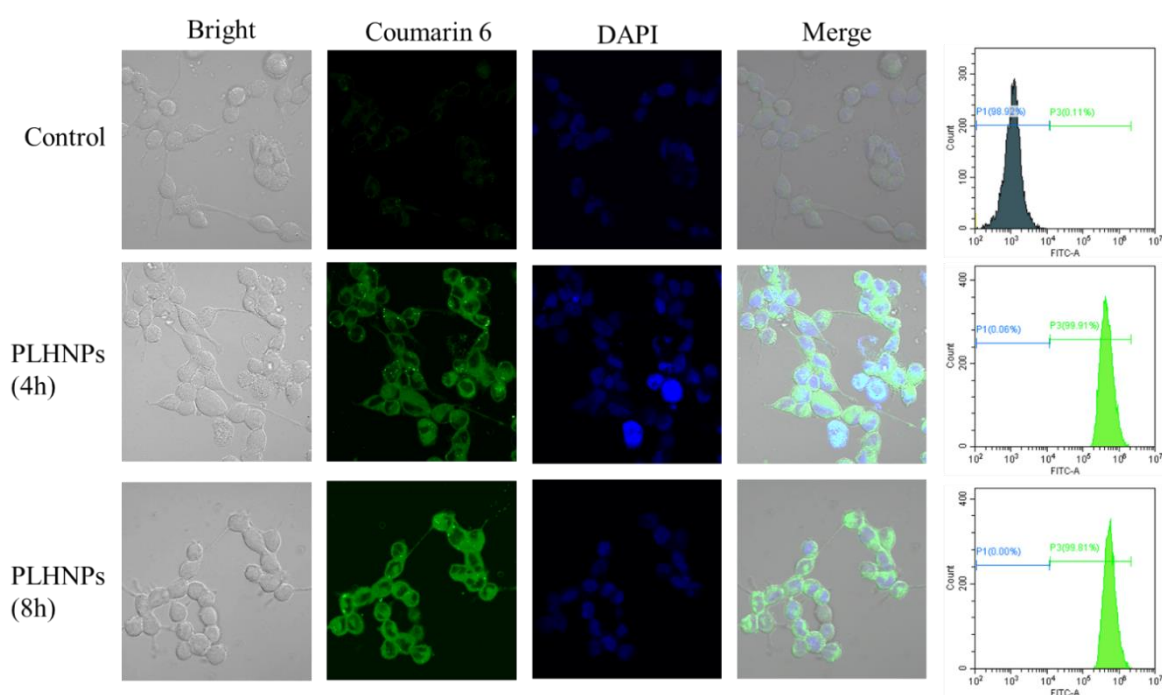


Fig. 5.54: The quantitative estimation of coumarin 6, and coumarin 6 loaded PNP in cellular uptake study by confocal microscopy at 4h and 8h.

5.4.10.3 STZ treated SHSY-5Y cell-based study

The effect of REP and PLHNPs on metabolic stress induced in cells was measured by performing an STZ cell study (Fig.5.55). Initially, the concentration of STZ was standardized and observed that at 2.5mM approximately 60-65% of the cell was viable (section 3). Further, the SHSY-5Y cells were treated with REP and PLHNPs and incubated for 12 h. Though it was found that the PLHNPs represent an increment of ~1.67 fold in cell viability which represents a significant effect compared to only STZ-induced cells. However, REP enhances the viability of cells but after loading into PLHNPs the ~1.20-fold improvement was also observed compared to REP in the STZ-induced SHSY-5Y cells.

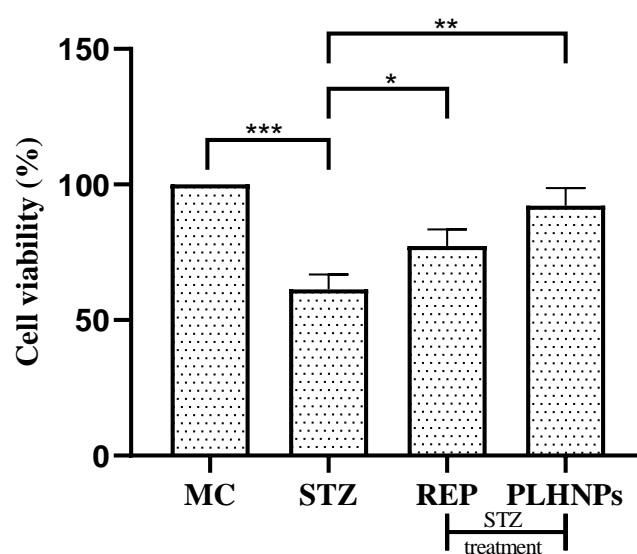


Fig.5.55: The effect of REP and PLHNPs on STZ-treated SHSY-5Y neuroblastoma cell lines Data are represented in (mean \pm SEM, n=8 rats per group). * Indicates ** $P < 0.05$; *** $P < 0.01$, **** $P < 0.001$, by one-way ANOVA followed by Tukey's post hoc multiple comparison test

5.4.10.4 Reactive oxygen species-scavenging activity by hydrogen peroxide

The scavenging assay was performed to estimate the effect of REP and PLHNPs on SHSY-5Y cells after being treated with 1 mM H_2O_2 for 12 h. Though from initial studies the optimal concentration of H_2O_2 for inducing ~40% cell death (Fig.5.56). Further, cells treated with 1mM H_2O_2 were incubated with REP and PLHNPs and the study indicates that the REP shows a ~1.3-fold increase in cell viability, while PLHNPs show a significant ($p < 0.01$) effect compared to H_2O_2 and enhance the effect by ~1.52-fold (Fig.5.56). The increase in cell viability indicates that the REP predominates the activity, whereas PLHNPs simultaneously enhance the protective effect.

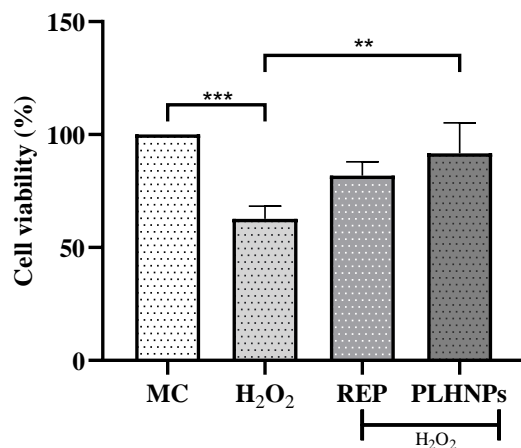


Fig.5.56: Neuroprotective effect of REP and PLHNPs on H₂O₂ treated SH-SY5Y neuroblastoma cell lines. Data are represented in (mean \pm SEM, n=8 rats per group). * Indicates ** $P < 0.01$, *** $P < 0.001$, by one-way ANOVA followed by Tukey's post hoc multiple comparison test

5.4.11 Pharmacokinetic study

The pharmacokinetic studies for REP and PLHNPs were investigated on wistar rats and the plasma concentration versus time profiles were plotted in Fig.5.57. The oral administration of PLHNPs results in good absorption, and peak plasma concentration reached in ~ 3.6 h approximately (Table.5.23). It was observed that the PLHNPs exhibited ~ 6.4 -fold increase in $t_{1/2}$ than REP solution, indicating slow distribution and elimination. However, AUC was observed to be higher in PLHNPs (32625.07 ± 3167.49 ng. h/ml) than in pure REP solution, which indicates the long-circulating ability of the nanoformulation in plasma. The clearance (Cl) of PNP's indicates ~ 1.8 fold, a decrease to pure REP solution. The increment in the PK parameters might be due to the core-shell of the lipid which influences the kinetic properties and DSPC-PEG₂₀₀₀ helps to increase the circulation time, protecting against immune recognition.

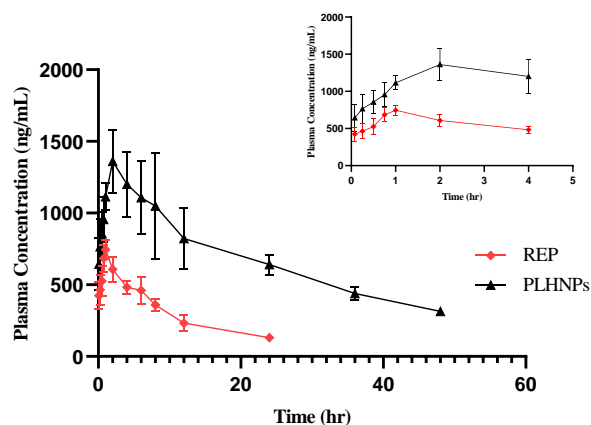


Fig.5.57: Plasma concentration-time profile of REP, and PLHNPs. Values were represented in mean \pm SEM,

Table.5.23.: Pharmacokinetic parameters of REP and PLHNPs

Parameters		REP	PLHNPs
t_{max}	(h)	0.81 ± 0.19	3.60 ± 1.16
C_{max}	(ng/mL)	800.76 ± 26.57	1547.16 ± 165.72
AUC	(ng.h/mL)	7441.69 ± 763.75	32625.07 ± 3167.49
CL	(mL/h/kg)	163.84 ± 17.39	88.87 ± 4.67
t_{1/2}	(h)	2.65 ± 1.54	24.16 ± 2.19
MRT	(h)	8.24 ± 0.32	38.633 ± 1.02

5.4.12 Biodistribution study

Biodistribution studies were performed to identify the potential nano-formulation for the brain targeting efficiency after oral administration. The REP distribution pattern was quantified in all the major organs (brain, heart, liver & kidney) and concentration-time profiles were represented in Fig.5.58. In the brain, the concentration levels of REP have observed for 12 h but for the PLHNPs it continued for more than 24 h and exhibited ~3.5 fold ($p < 0.05$) increases in the brain uptake due to the presence of PEGylation on the outer surface of the nanoparticles. A similar pattern was observed in the heart where the REP shows the maximum concentration in 2h and observed for 12 h though PLHNPs were still present for more than 24 h. As per the literature survey, REP was completely metabolized (98%) by oxidative biotransformation and direct conjugation with glucuronic acid. Interestingly, REP-loaded PLHNPs show a significant decrease in the metabolism of REP than the free REP which might be due to the presence of a core-shell structure that consists of biodegradable polymer and target moieties attached over the surface. Moreover, REP has a very fast elimination rate and PLHNPs lower the concentration of REP in the kidney and showed a sustained release thus the amount of REP in the kidney maintains till 24 h. Additionally, the amount of REP was significantly reduced in the tissues than PLHNPs. On the other side, PLHNPs exhibit more selective distribution to the brain due to surface modifications (PEGylation). Moreover, these findings of the biodistribution studies were in complementary relation to the systemic pharmacokinetic data as well as cellular uptake studies.

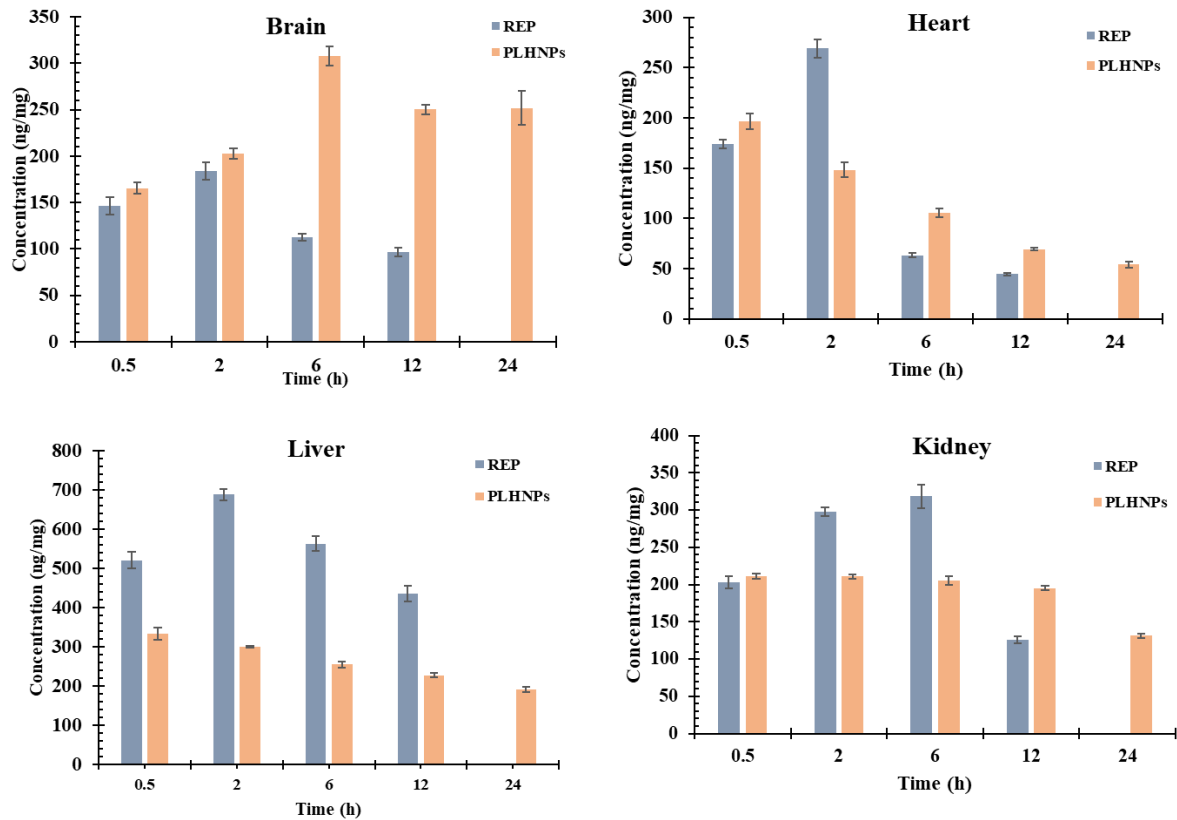


Fig.5.58: Biodistribution study of REP and PLHNPs in major organs after oral administration (4mg/kg) in wistar rats

5.4.13 Pharmacodynamic study

5.4.13.1 Estimation of neurochemical parameters

After the treatment period on HFD+STZ-induced wistar rats, the effect of REP and PLHNPs was measured on neurochemical parameters such as BDNF, $A\beta$, and tau protein as shown in Fig.5.59 A-C. The BDNF level in the DC group was significantly ($p < 0.001$) decreased than the NC group but after the treatment with REP and PLHNPs a significant ($p < 0.05$) amelioration was observed. The consistent amelioration of BDNF levels has resulted more in PLHNPs than REP. Moreover, $A\beta$ deposition and hyperphosphorylation of tau proteins are the hallmarks of neurodegeneration and are crucial to the pathogenesis of AD. Thus, the potential effect of REP and PLHNPs was studied and measured a significant ($p < 0.001$) upregulation in the levels of $A\beta$ and tau proteins in DC than the NC group. After treatment with REP and PLHNPs, a significant attenuation was observed in comparison with the DC group.

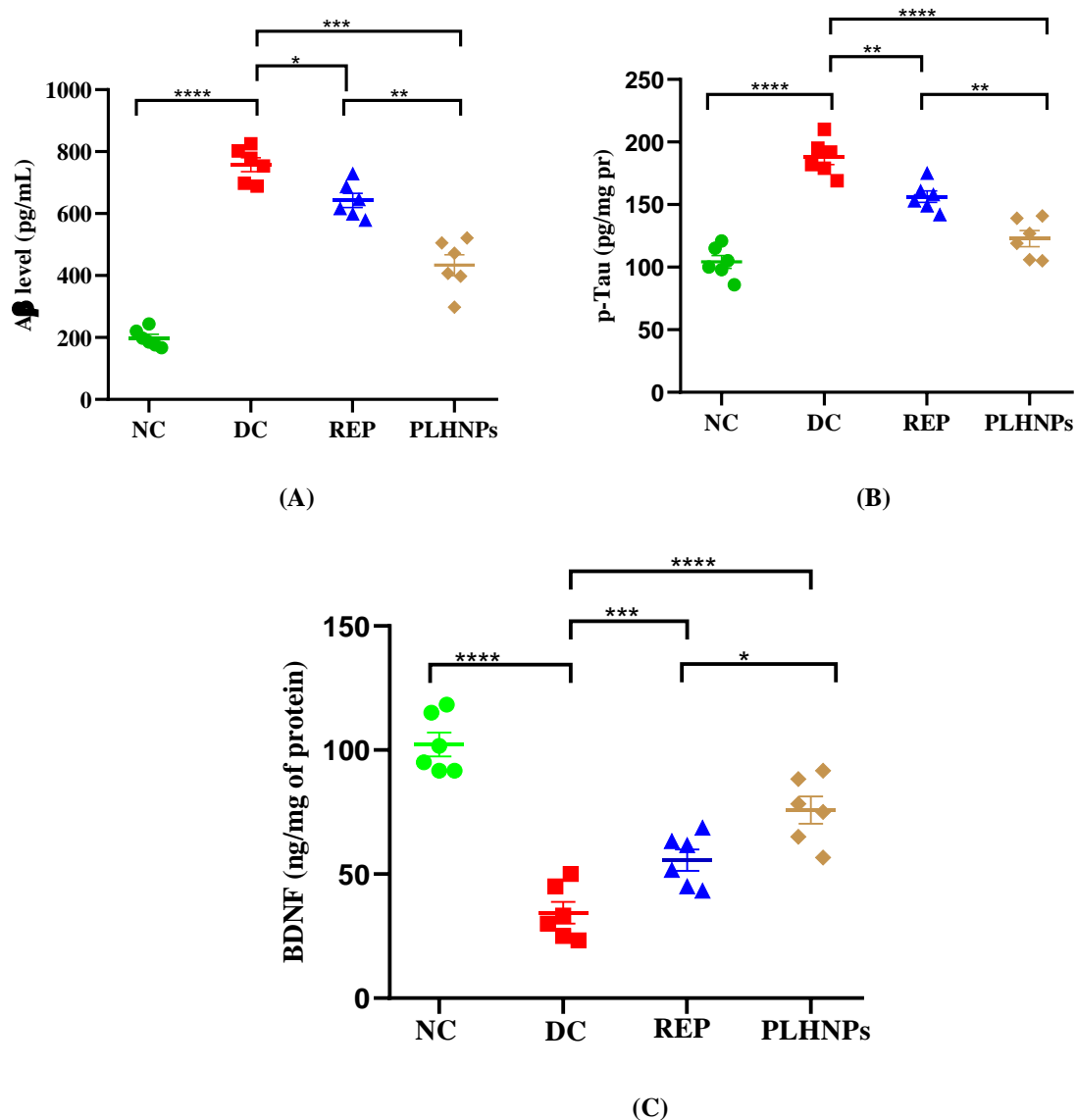


Fig.5.59: *In vivo* estimation of neurochemical parameters to understand the effect of REP and PLHNPs after the treatment (A) A β level; (B) p-Tau; (C) BDNF level in brain homogenate of HFD+STZ induced wistar rats, data are represented in (mean \pm SEM, n=6 rats per group). * Indicates $P < 0.05$; ** $P < 0.01$, *** $P < 0.001$, **** $P < 0.0001$ by one-way ANOVA followed by Tukey's post hoc multiple comparison test

5.4.13.2 Estimation of inflammatory cytokines

The effect of REP and PLHNPs on inflammatory cytokines (TNF- α and IL-6) was estimated in HFD+STZ-induced wistar rats (Fig.5.60. A&B). The significant ($p < 0.0001$) upregulation of levels was observed in DC compared to NC rats. Moreover, the REP and PNP administration for 4 weeks reduces the levels than the DC group but PLHNPs showed a significant ($p < 0.001$) suppression as compared to REP.

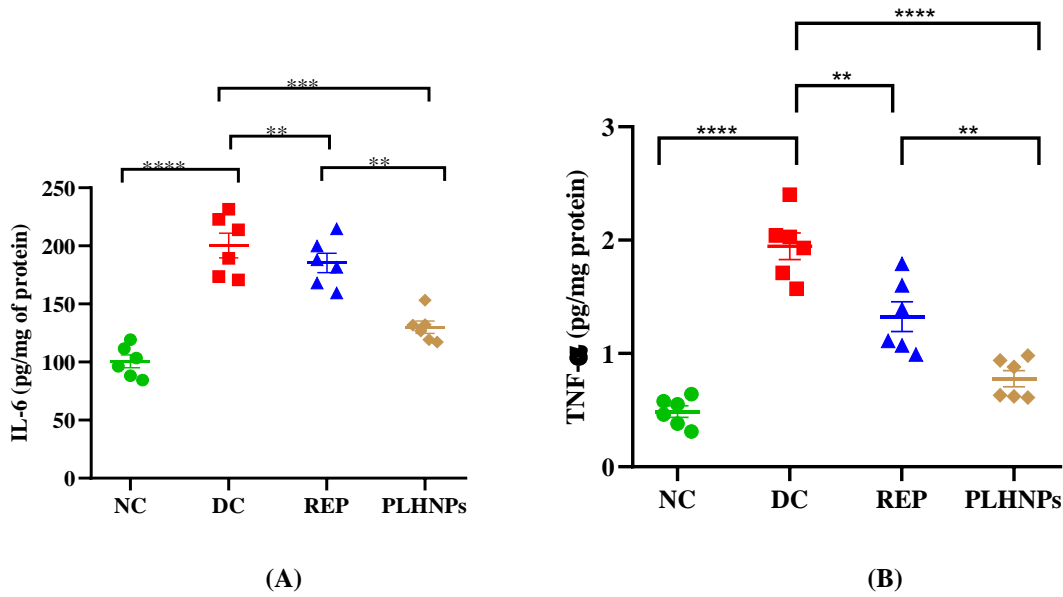
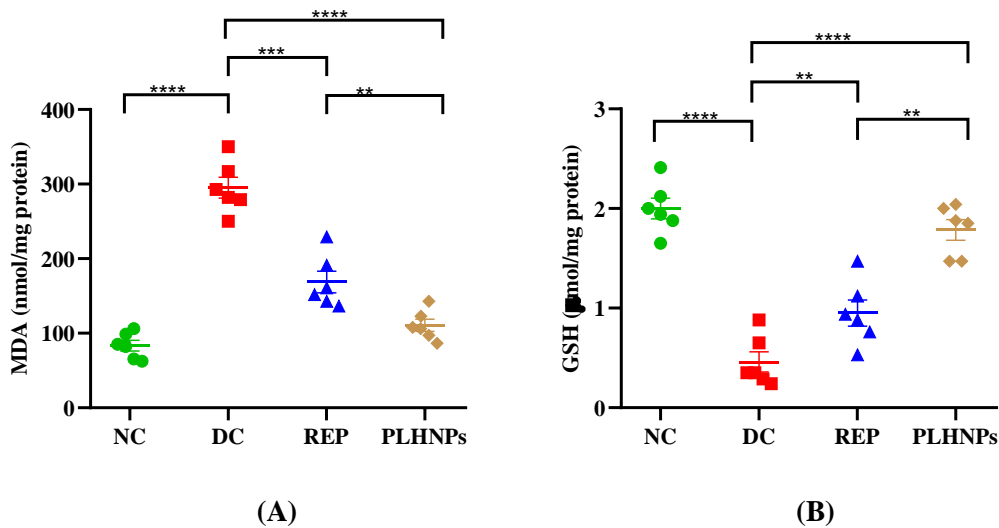
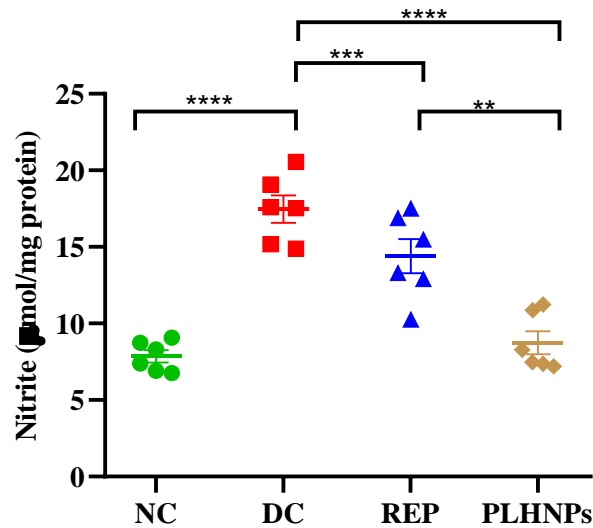


Fig.5.60: *In vivo* estimation of neurochemical parameters to understand the effect of REP and PLHNPs after the treatment (A) IL-6; and (B) TNF- α level in brain homogenate of HFD+STZ induced wistar rats, data are represented in (mean \pm SEM, n=6 rats per group). * Indicates $P < 0.05$; ** $P < 0.01$, *** $P < 0.001$, **** $P < 0.0001$ by one-way ANOVA followed by Tukey's post hoc multiple comparison test

5.4.13.3 Estimation of Oxidative stress parameters

The level of MDA, nitrite (oxidative markers), and GSH (antioxidant) were measured to understand the effect of REP and PLHNPs. Though the levels of oxidative markers (MDA and nitrite) were resulted in significant ($p < 0.001$) elevation of level in DC compared to NC whereas a decrement in levels of endogenous antioxidants (GSH) was observed in Fig 5.61. Furthermore, the REP and PLHNPs lower the level of MDA, nitrite and enhance the GSH level after the treatment. The PLHNPs resulted in significant ($p < 0.001$) attenuation of oxidative markers (MDA, nitrite) and significant ($p < 0.001$) enhancement of GSH compared to REP.





(C)

Fig.5.61: Effect of oxidative stress parameters (A) MDA; (B) GSH; (C) Nitrite on REP and PLHNPs. The data are represented in (mean \pm SEM, n=6 rats per group). * Indicates $P < 0.05$; ** $P < 0.01$, *** $P < 0.001$, **** $P < 0.0001$ by one-way ANOVA followed by Tukey's post hoc multiple comparison test.

5.4.13.4 Passive avoidance task

A passive avoidance task is a test in which rodents learn to abstain from a response in order to avoid the aversive stimulus. The test was used to evaluate the learning and memory in cognitive dysfunctions of the central nervous system. During the acquisition trial, no significant ($P > 0.05$) differences in the initial latency time of all the groups were observed. Whereas in retention latency (after 24h of acquisition trial) analysis a significant ($P < 0.01$) decrease was observed in the HFD+STZ group as compared with the NPD group (Fig.5.62). However, rats treated with REP and PLHNPs showed a significant amelioration in the retention latency which indicates improvement in retention memory. In HFD+ STZ PLHNPs treated group significant ($P < 0.01$) changes in retention memory were observed more than REP.

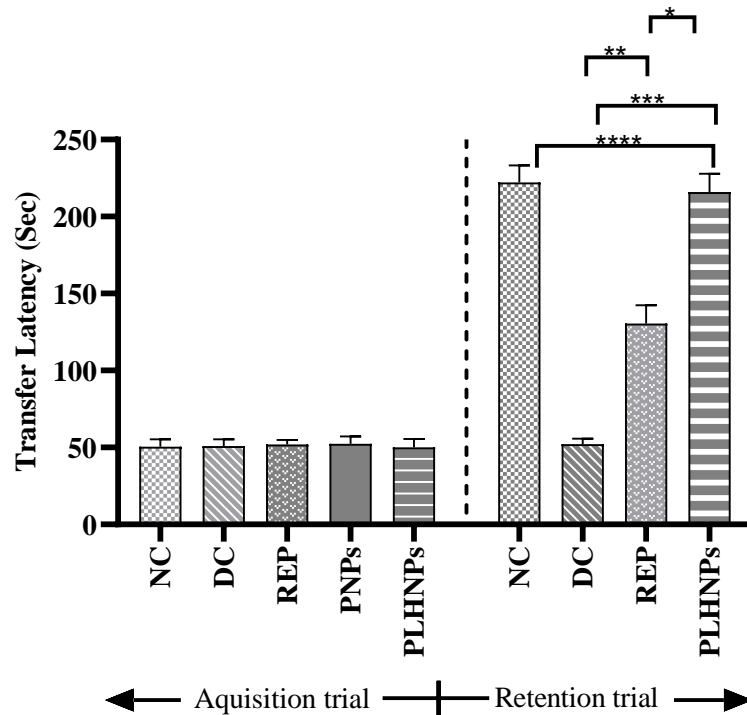
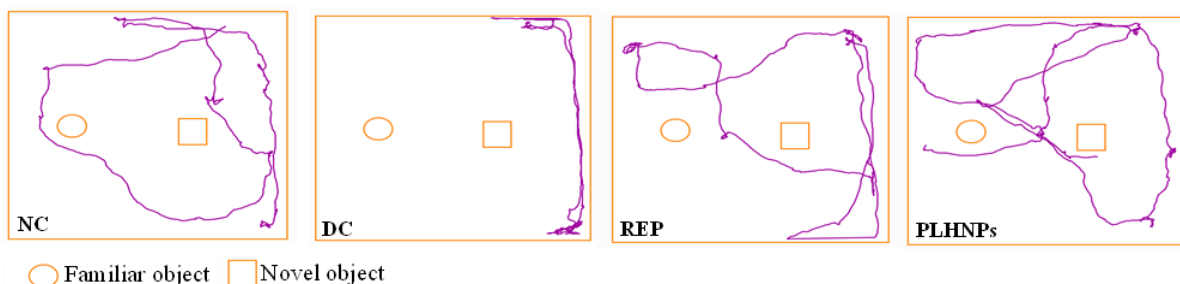


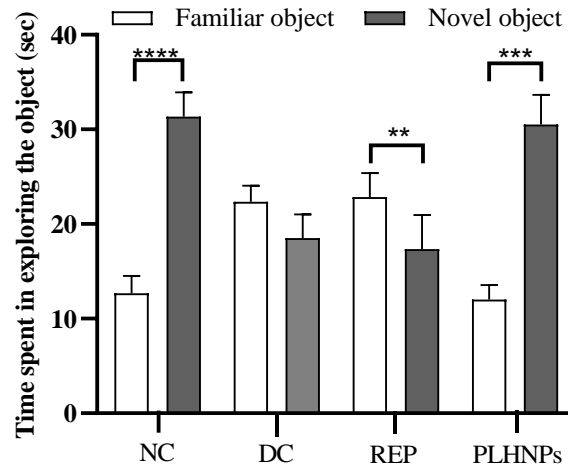
Fig.5.62: Estimation of transfer latency by performing behavioral parameters using passive avoidance task. Data are represented in (mean \pm SEM, n=6 rats per group). * Indicates $P < 0.05$; ** $P < 0.01$, *** $P < 0.001$, **** $P < 0.0001$ by one-way ANOVA followed by Tukey’s post hoc multiple comparison test

5.4.13.5 Novel object recognition test

The NORT is used to investigate the alterations in memory, particularly in recognition memory. The test is based on the spontaneous tendency of rats to spend more time exploring a novel object than familiar objects (Fig.5.63. A). In NORT during the training session, no significant difference was measured in the exploratory preferences of the rats. However, in the retention session, the HFD+STZ group rats spent significantly lesser time in exploring the novel object compared to the familiar object (Fig.5.63. B). But in the case of REP and PLHNPs amelioration in the exploring time was observed, especially in PLHNPs a significant change in the exploring time was measured compared with the REP.



(A)



(B)

Fig.5.63: (A) Representation of track plot for the novel object recognition task and (B) Time spent in exploring the object. The data are represented in (mean \pm SEM, n=6 rats per group). * Indicates $P < 0.05$; ** $P < 0.01$, *** $P < 0.001$, **** $P < 0.0001$ by one-way ANOVA followed by Tukey's post hoc multiple comparison test

5.4.13.6 Morri's water maze (MWM)

The effect of REP and PLHNPs was measured for the estimation of spatial memory. The mean escape latency in all groups was recorded after the 4 days of training and observed a gradual attenuation in MWM analysis. Though in the DC group, the mean escape latency was significantly ($p < 0.001$) higher with the NC group and decrement was observed after treatment with REP and PLHNPs as shown in Fig.5.64. A. In the second part of the analysis, the hidden platform was removed to perform a probe trial test, where DC group rats were unable to identify the exact location of the platform and spent less time in that quadrant than the NC group rats. However, after the treatment with REP and PLHNPs, rats were able to recall the exact position of the platform and spend more time in that quadrant which indicates memory improvement (Fig.5.64. B).

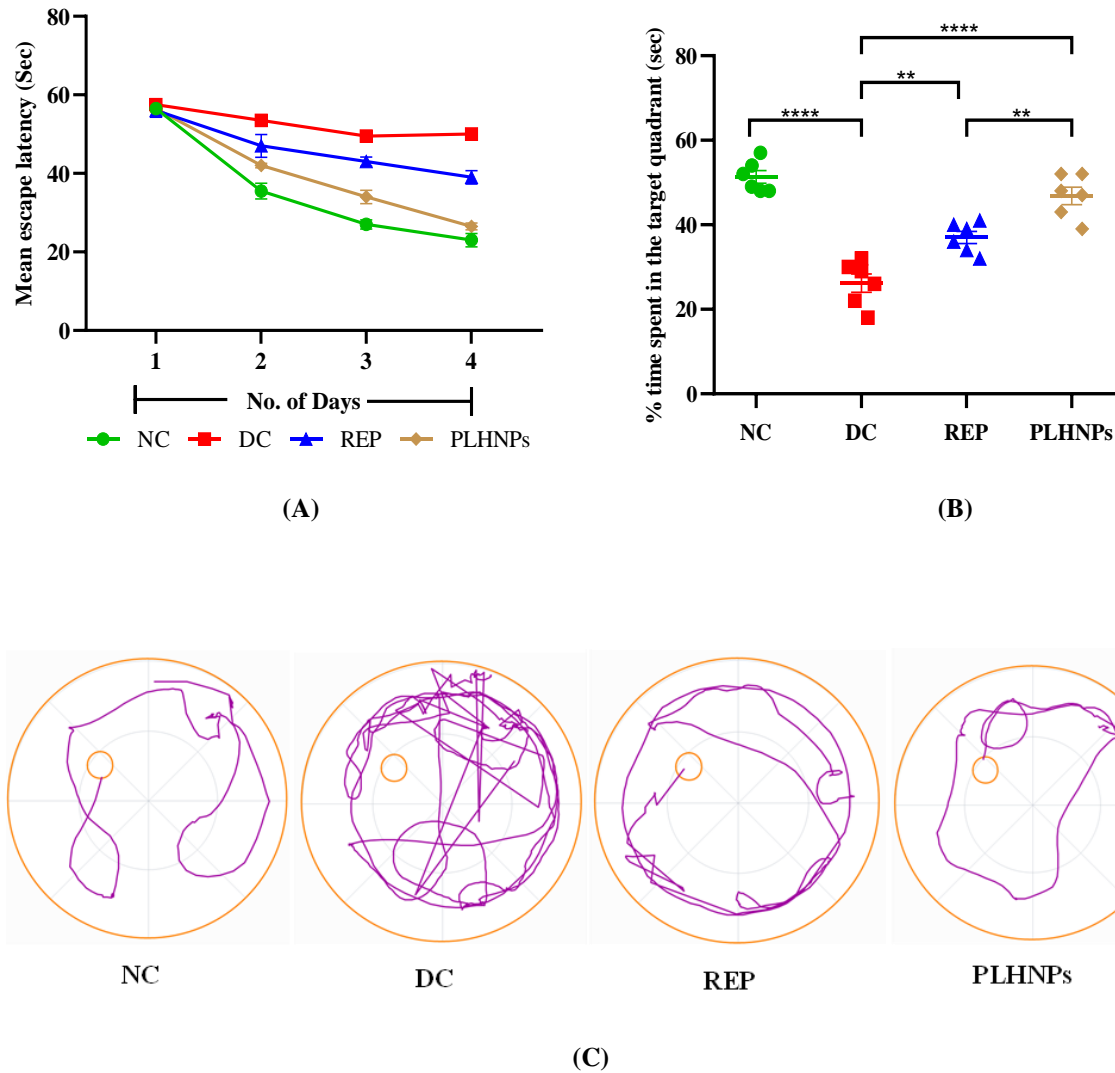
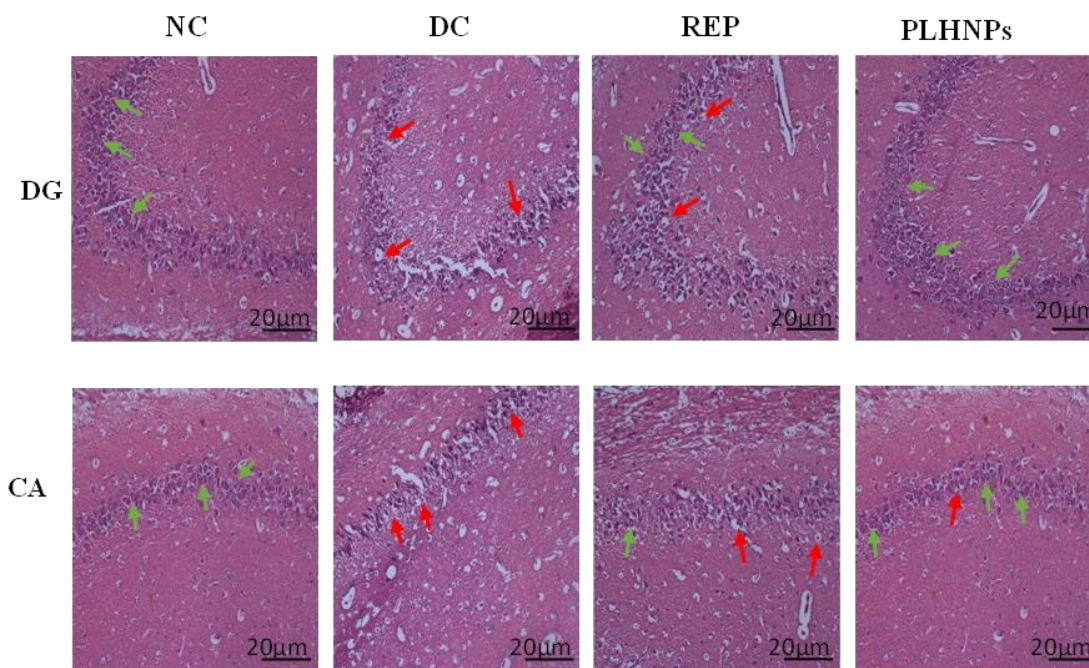


Fig.5.64: Estimation of (A) mean escape latency, (B) time spent in the same quadrant, and (C) representation of track plot for Morri's water maze task. Data are represented in (mean \pm SEM, n=6 rats per group). data are represented in (mean \pm SEM, n=6 rats per group). * Indicates $P < 0.05$; ** $P < 0.01$, *** $P < 0.001$, **** $P < 0.0001$ by one-way ANOVA followed by Tukey's post hoc multiple comparison test

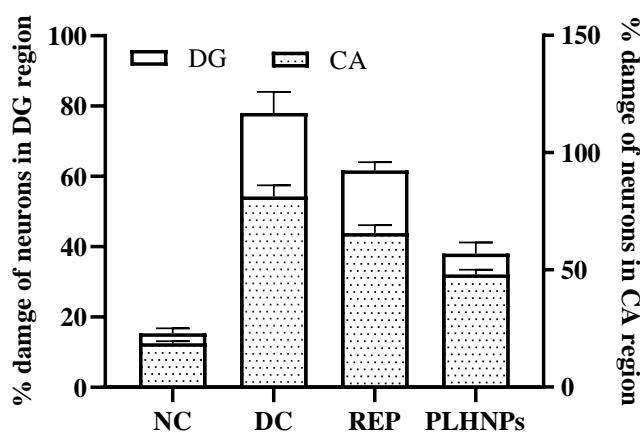
5.4.13.7 Histopathological analysis

H&E staining was used to investigate the HFD+STZ-induced neuronal changes (viable cells, percent damaged neuron, pyknotic neurons) in the hippocampus region. The DG and CA1 regions of the brain are significantly altered in the HFD+STZ group, whereas the NPD group has healthy nuclei with robust shapes and clear cytoplasm. The HFD+STZ group also displays degeneration, cell body loss, and an increase in pyknotic neurons in the DG or CA1 regions. These pyknotic neurons were shrunken, darkly stained, and their nucleus and nucleolus were damaged. On treatment with REP and PLHNPs, neuronal damage and the proportion of pyknotic neurons diminished (Fig.5.65. A). However, significant differences were observed

between PLHNPs and REP, with PLHNPs representing reduced neuronal loss and enhanced neuroprotection (Fig.5.65. B).



(A)



(B)

Fig.5.65: (A) Neuronal regeneration on HFD+STZ rats at dentate gyrus (DG) and Cornus ammonis (CA) region of hippocampus and (B) %neuronal count in DG and CA region. Data are represented in (mean \pm SEM, n=6 rats per group).

In the current study, PEGylated PLHNPs were formulated for the delivery of REP, an insulinotropic agent. However, owing to its short action, poor absorption, and brain permeation it falls short in the race of clinical transitions. Nanocarriers have many advantages to overcome these problems and deliver the drug to the brain after oral administration, which itself a challenging process due to the presence of physiological barriers such as GIT, and BBB. Hence,

PLHNPs were developed and optimized to provide stability in GIT, improve absorption characteristic in the intestine and enhance permeation in the brain through passive transport. Further, the efficacy of REP has also been identified in the diabetes-linked neurodegenerative animals' model (HFD+STZ model) by estimating the biochemical and behavioral parameters. The report suggested that PLHNPs promote the characteristic properties and show a more significant effect compared to REP due to the presence of a core-shell structure. PLHNPs lipid shell protects the core from gastric secretions and controls the release of the drug. The presence of a hybrid lipid polymer (DSPE-PEG_{2k}) prolongs the systemic circulation time and reduces immunogenicity.

5.5 Comparative evaluation of PNPs and PLHNPs

The PNPs were fabricated by in-house synthesized mPEG-PCL polymer whereas PLHNPs were prepared using PLGA as a polymer, SPC as a phospholipid, and DSPC-PEG₂₀₀₀ as a lipid/PEG molecule. Both the formulations were optimized using quality by design approach with Box-Behnken response surface methodology, the particles were characterized using the dynamic light scattering method to estimate the PS, PDI, and ZP though no significant changes were observed between PNPs and PLHNPs (Fig.5.66). All the characteristics parameters were in the nano range with PS <150 nm, PDI <0.3, and ZP in between ± 30 mV[236].

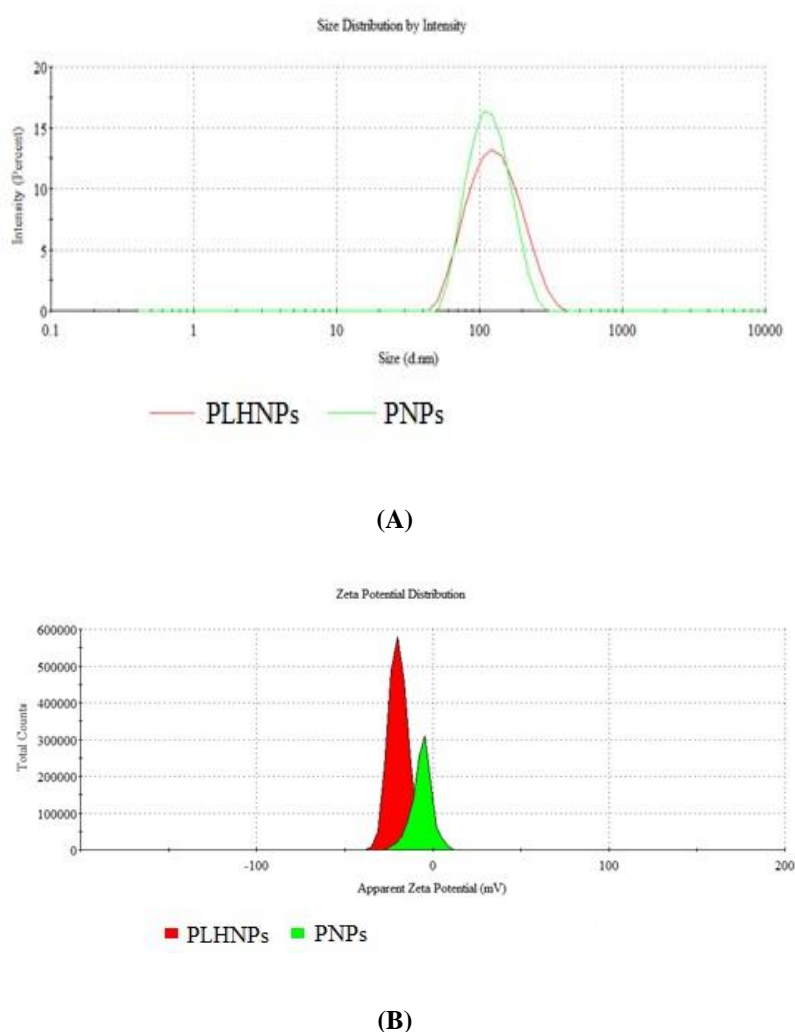


Fig.5.66: Characterization of Polymeric nanoparticles and polymer lipid hybrid nanoparticles by (a) particle size, (b) zeta potential

As the estimation of *in vitro* drug release is important for the nano formulation to understand the rate and extent of active ingredients present at the site of action. Hence a sustained/controlled release of drug from nanoparticle is suitable to maintain the therapeutic

window. The release profile of, PNP and PLHNPs were estimated (Fig.5.67) and showed a cumulative drug release of ~ 70% and ~58% respectively within 48h. The observed release profile data represent that PLHNPs have more sustainability than the PNP due to the core-shell structure of PLHNPs which decreases the diffusion rate and is sustained for a longer period of time[213].

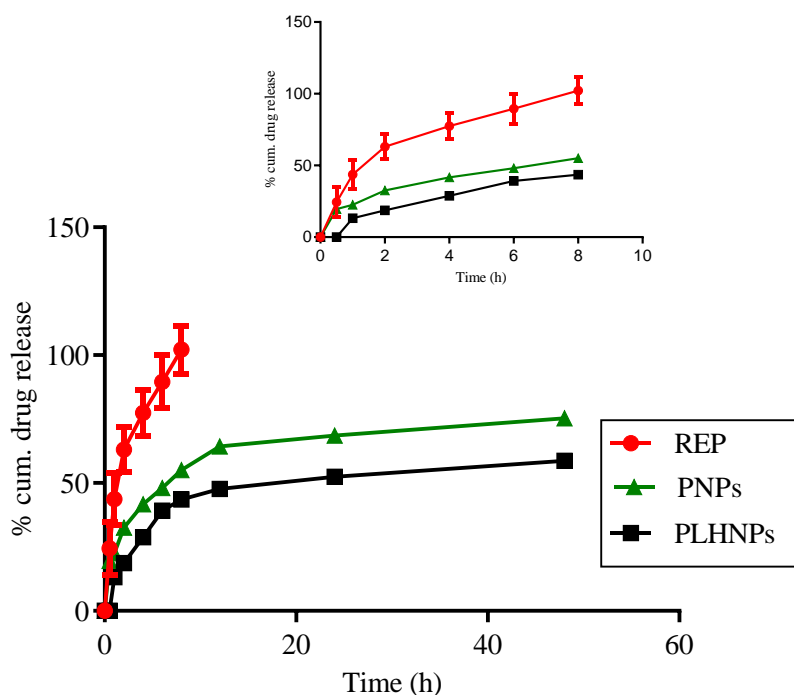


Fig.5.67: *In vitro* release profile of Polymeric nanoparticles and polymer lipid hybrid nanoparticles

Nano formulations are getting much consideration for the controlled delivery of drugs, but the stability of nanoparticles has been a source of concern. Thus, the effect of different simulated gastrointestinal fluids on nanoparticles was measured, and observed that the PLHNPs were found stable as no changes in the quality attributes were observed in simulated gastrointestinal fluids whereas PNP shows nonsignificant changes with REP. Due to the presence of DSPE-PEG2k a PEG-Lipid in PLHNPs aims to improve the stability and mobility of the complexes in the harsh gastrointestinal environment[237]. Intestinal absorption is a crucial factor for defining the bioavailability of oral drugs, as there are many transporters that are available on the intestine which are involved in the pharmacokinetic profile of drugs.[224,227] Thus, intestinal absorption plays a critical role in their improvement, safety, and effectiveness.[233] In the study, it was observed that the P_{eff} value increased around ~ 2.3 folds of PNP and ~ 3.3 folds PLHNPs compared to free REP and showed a significant change in intestinal permeation rate (Fig.5.68). Additionally, the K_a is also increased by ~2.3folds in PNP and ~3.9 fold in

PLHNPs with respect to REP indicating that the nano formulations enhanced the permeation/absorption rate of REP in wistar rats. Though the PLHNPs show more significant enhancement (~ 3.13 -fold P_{eff} & ~ 1.69 -fold K_a) in comparison to PNPs, it may be due to more GIT stability or can be attributed to the core-shell structure of PLHNPs which helps to maintain the controlled release of the drug and also enhance permeation [238].

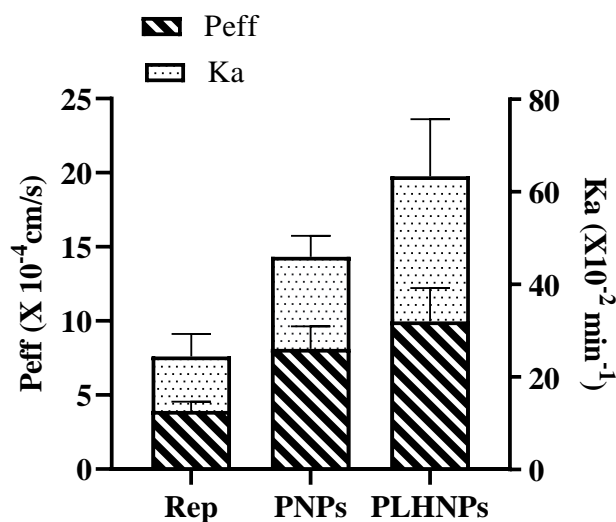


Fig.5.68: Effective permeability coefficient and apparent absorption rate constant of PNPs and PLHNPs after using SPIP wistar rat model

Further, *in vitro* PAMPA-BBB assay was performed to estimate the effective brain permeability of REP-loaded PNPs and PLHNPs and it was observed that the PNPs achieved ~ 1.3 folds and PLHNPs ~ 1.6 folds more permeability to the brain than REP [229,230,234].

Additionally, *in vitro* cell culture studies were performed on neuroblastoma SHSY-5Y cells to measure the effect of both the formulations (PNPs and PLHNPs) on cell viability, cellular uptake, etc. As viability assay indicates the number of live and/or healthy cells in a sample to measure the physical or cellular health in response to chemical agents, therapeutic treatments, or extracellular stimuli. It was revealed that more than 70% of cells were viable in the blank formulation which indicates that both the formulations were biocompatibility and nontoxicity (Fig.5.69). Moreover, the PLHNPs show ~ 90 - 95% cell viability whereas PNPs has cell viability of ~ 80 - 85% indicating the effectiveness of PLHNPs[239].

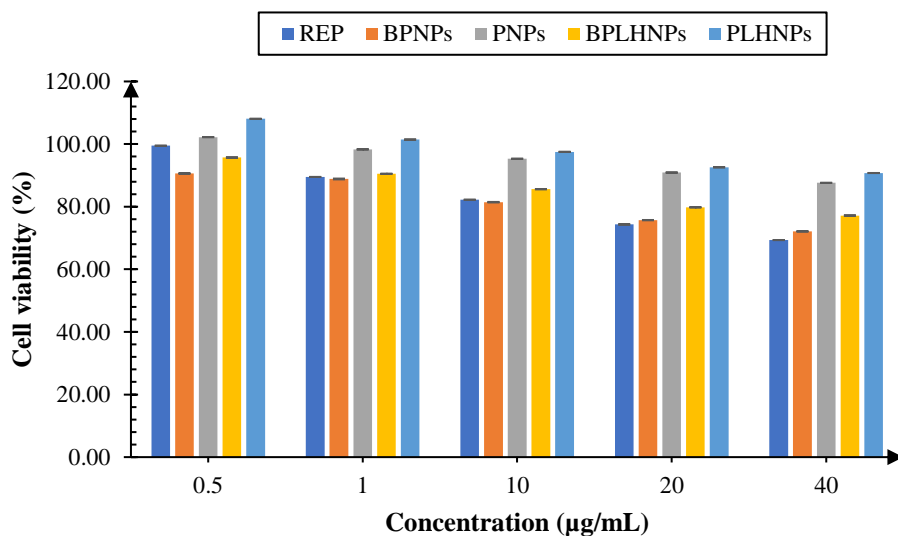
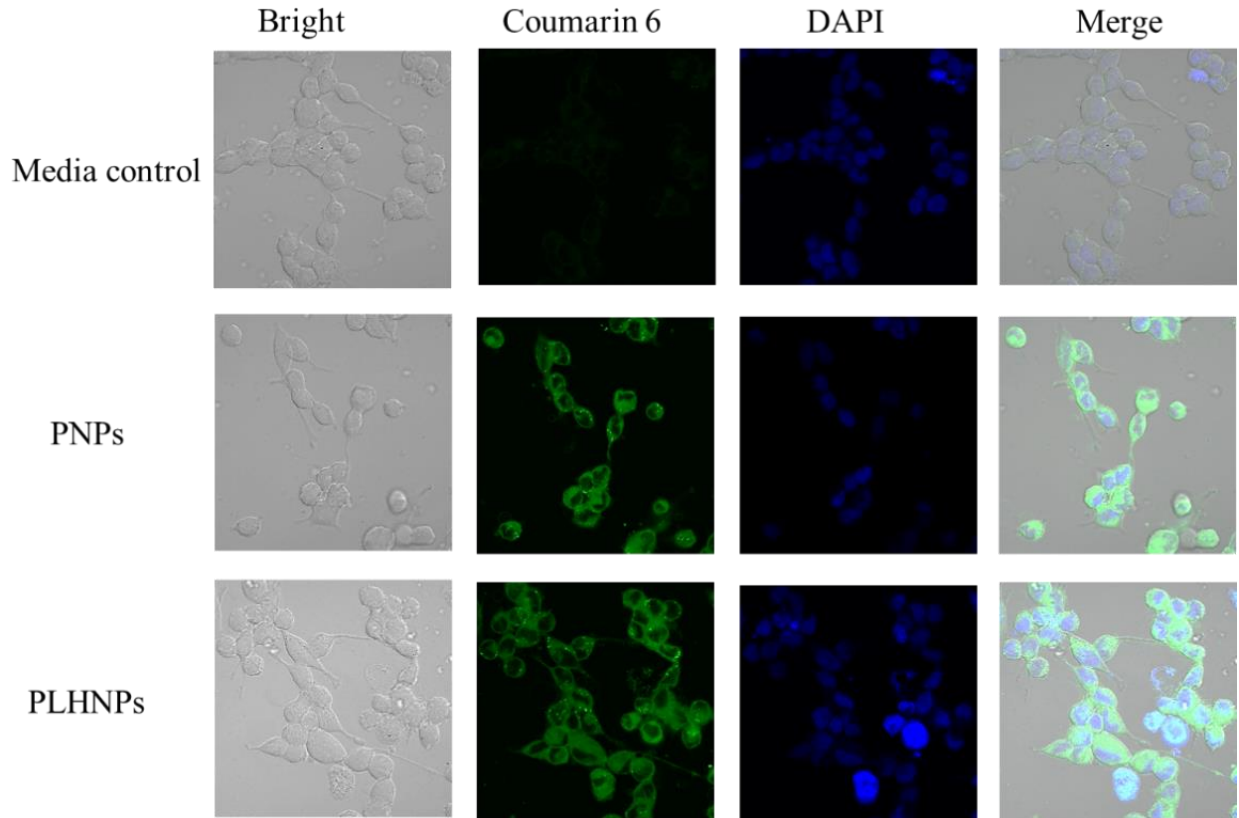
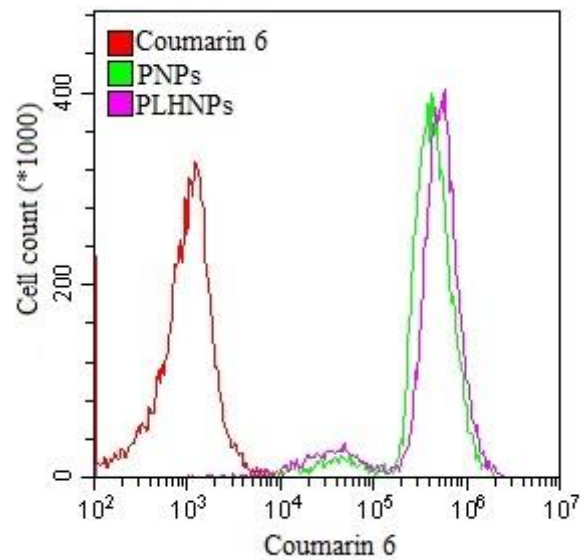


Fig. 5.69: *In vitro* cell culture studies on neuroblastoma cell line SHSY-5Y for estimation of cell viability by MTT cytotoxicity assay

Further, the cellular uptake of both the formulations was quantified, and observed that the PLHNPs showed ~ 1.2 % more uptake than the PNP which could be due to the size-independent lipid trafficking pathway (Fig.5.70.) The lipid density in the cellular membrane increases the sustained drug release compared to PNP. The PLHNPs easily affect the biological barriers and efficiently enhance circulation. Moreover, negative charge also exhibits a strong interaction with the cell membrane and therefore enhances the intercellular uptake. Though more uptake into the cells ensures more amount of the drug is available at the site of action for therapeutic activity indicating the possibility for reduction of dose and improvement in efficacy. Furthermore, the SHSY-5Y cells were treated with STZ and H₂O₂ to estimate the effect of PNP and PLHNPs as both STZ and H₂O₂ generate oxidative stress, increase apoptosis, and reduce the glucose uptake. Though the results revealed that both the formulations significantly ameliorated the effect of REP but PLHNPs enhance the REP activity by 0.97-fold more than PNP which might be due to the presence of DSPC-PEG₂₀₀₀ on the outer corona that reduces the cytotoxicity and phospholipids exhibits antioxidant activity.



(A)



(B)

Fig.5.70: The quantitative estimation of coumarin 6, coumarin 6 loaded PNP, and coumarin 6 loaded PLHNPs in cellular uptake study by (A) confocal microscope, (B) flow cytometer and the cell sorter. Moreover, in *in vivo* studies on the wistar rats i.e., pharmacokinetic, biodistribution, and pharmacodynamic studies, a significant ($p < 0.05$) difference between both formulations were observed. In the pharmacokinetic profile of PNP and PLHNPs the significant ($p < 0.05$) fold

changes in the parameters were observed (Table 5.23 & Fig.5.71) due to the core-shell of lipid which influences the kinetic properties and DSPC-PEG increases the circulation time, protecting against immune recognition.

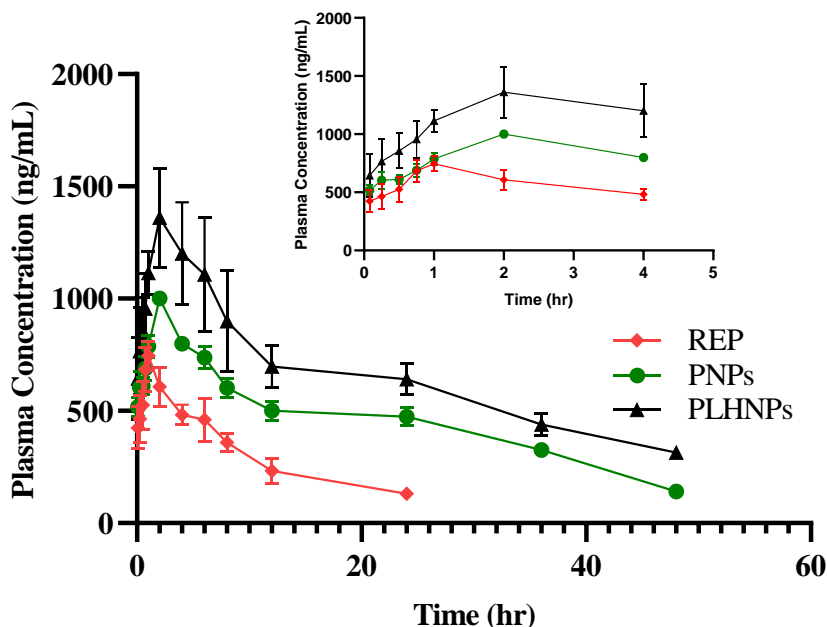


Fig. 5.71: Plasma concentration-time profile of REP, PNPs, and PLHNPs. Values were represented in mean \pm SEM.

Table.5.24.: Comparative analysis of Pharmacokinetic parameters of PNPs and PLHNPs

Parameters	Difference between PNPs and PLHNPs
t_{max} (h)	1.81
C_{max} (ng/mL)	1.54
AUC (ng.h/mL)	1.48
CL (mL/h/kg)	1.49
MRT (h)	1.90

Similarly, in biodistribution studies, the distribution pattern of PNPs and PLHNPs was quantified and compared in major organs (brain, heart, lungs, liver, and kidney), depicting the concentration-time profiles response (Fig.5.72). The results revealed that the concentration levels of both formulations were observed till 24 h whereas REP is detected only up to 12h. The concentration level of PLHNPs was increasing 1.4-fold in the brain, 1.1-fold in the heart, 1.3-fold in the liver, and 0.9-fold in the kidney then PNPs.

Thought, it suggests that PLHNPs improve the ability of REP to penetrate across BBB, decrease the metabolism, and elimination rate and enhance the circulation life compared to

PNPs. The characteristic features of PLHNPs combine the benefits of lipid-based carrier systems such as better loading, and biomimetic nature along with the architectural benefits of the polymeric system. Moreover, the outer layer of PLHNPs i.e., the polyethylene glycol layer provides a stealth effect and increases the mean residence time in addition to stearic stabilization. Furthermore, high structure integrity, mechanical stability, controlled release profile, and biocompatibility made the PLHNPs more efficient.

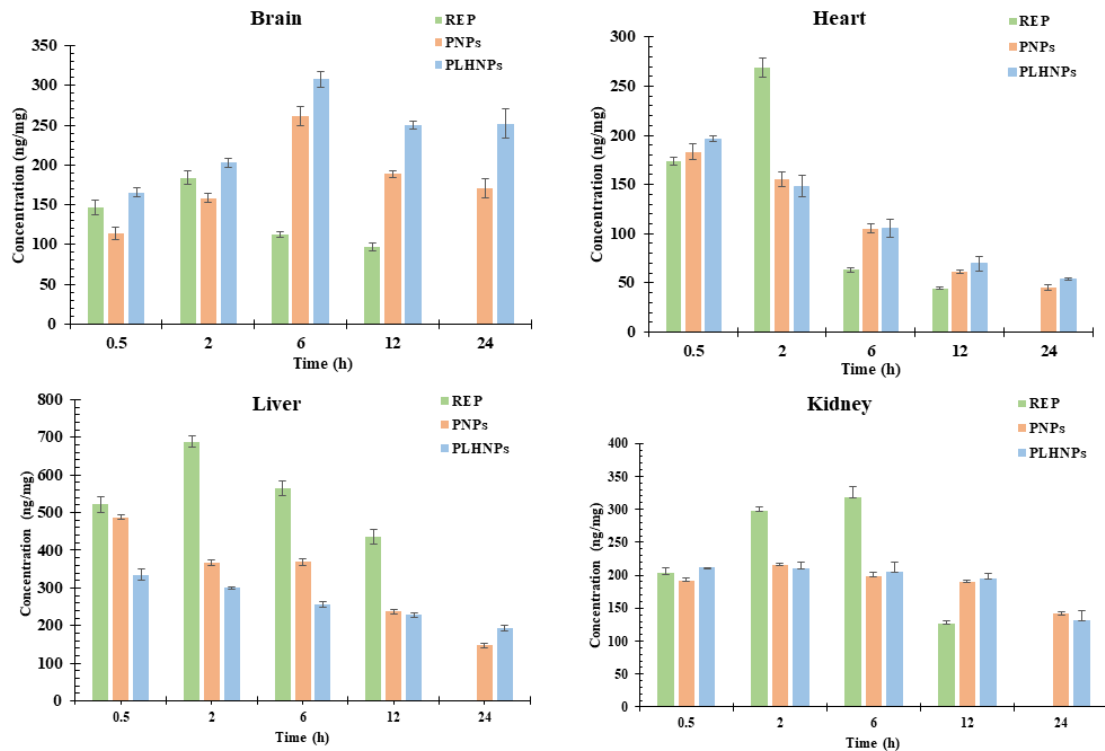


Fig.5.72 Biodistribution study of REP, PNPs, and PLHNPs on brain, heart, liver, and kidney.

Additionally, the pharmacodynamic study revealed a significant ($P < 0.001$) amelioration in the biochemical parameters such as neurotropic (Fig.5.73), inflammatory (Fig.5.74), and oxidative (Fig.5.75) of PLHNPs and PNPs group compared to DC and REP group in HFD+STZ administered rats. Although, PLHNPs resulted in consisted significant changes in $A\beta$, tau protein, and BDNF in comparison to REP and PNPs. However, in the case of pro-inflammatory cytokines (IL-6, TNF- α) identification the HFD+STZ rats significantly elevates ($P < 0.001$) the level of IL-6, TNF- α compared to NPD rats. It was observed that after treatment of REP, PNPs, and PLHNPs the level of inflammatory cytokinin reduces ($P < 0.05$) and PLHNPs show significant differences compared to REP and PNPs. Similarly, in the case of MDA, GSH, NO, and SOD, PLHNPs represent a significant improvement compared to PNPs and REP.

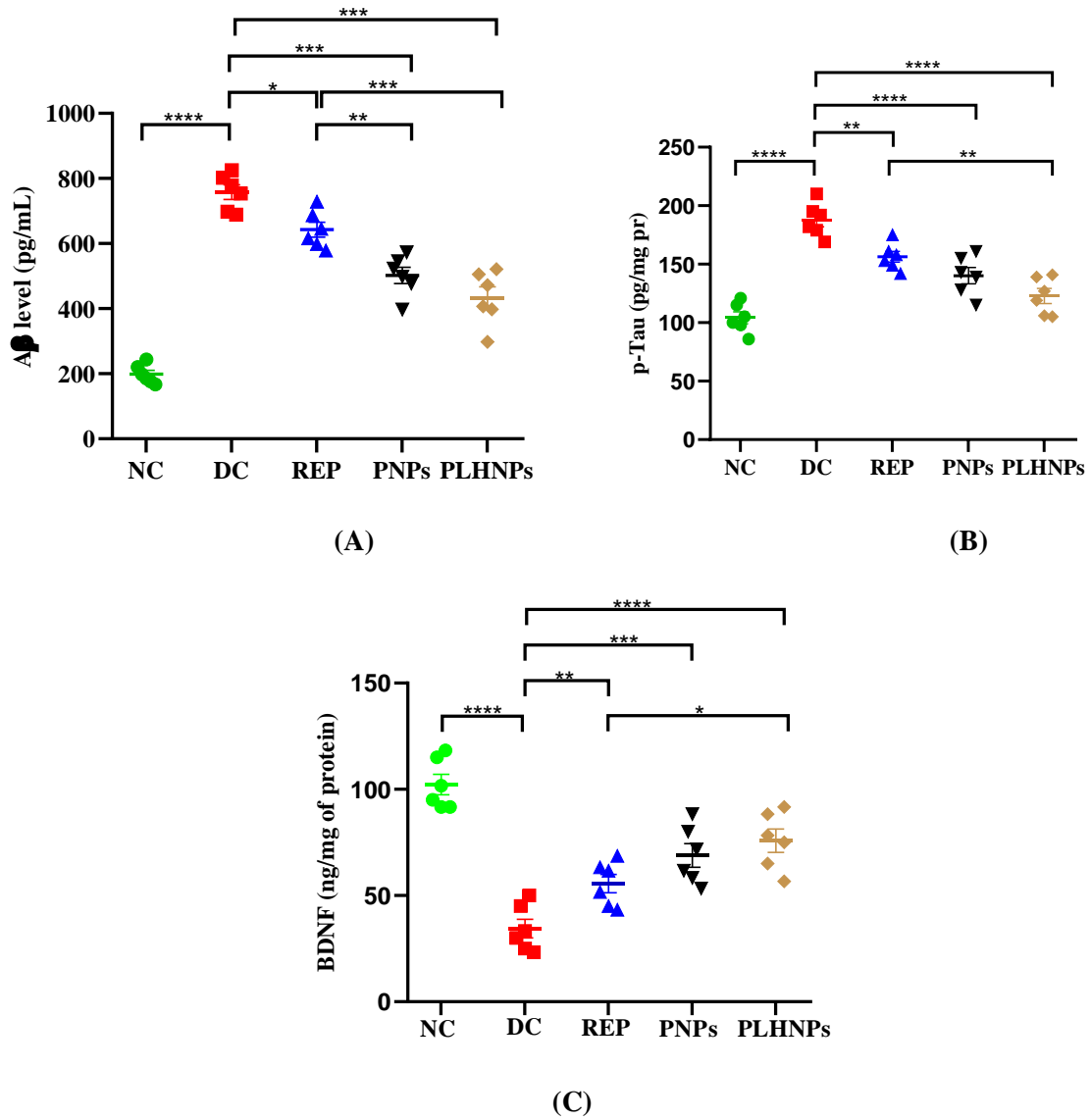


Fig.5.73: Neurobiochemical parameters improvement on HFD+STZ induced animal model on the treatment of REP, PNP and PLHNPs, (A) A β level, (B) p-Tau level and (C) BDNF level, data are represented in (mean \pm SEM, n=6 rats per group). * Indicates $P < 0.05$; ** $P < 0.01$, *** $P < 0.001$, **** $P < 0.0001$ by one-way ANOVA followed by Tukey’s post hoc multiple comparison test.

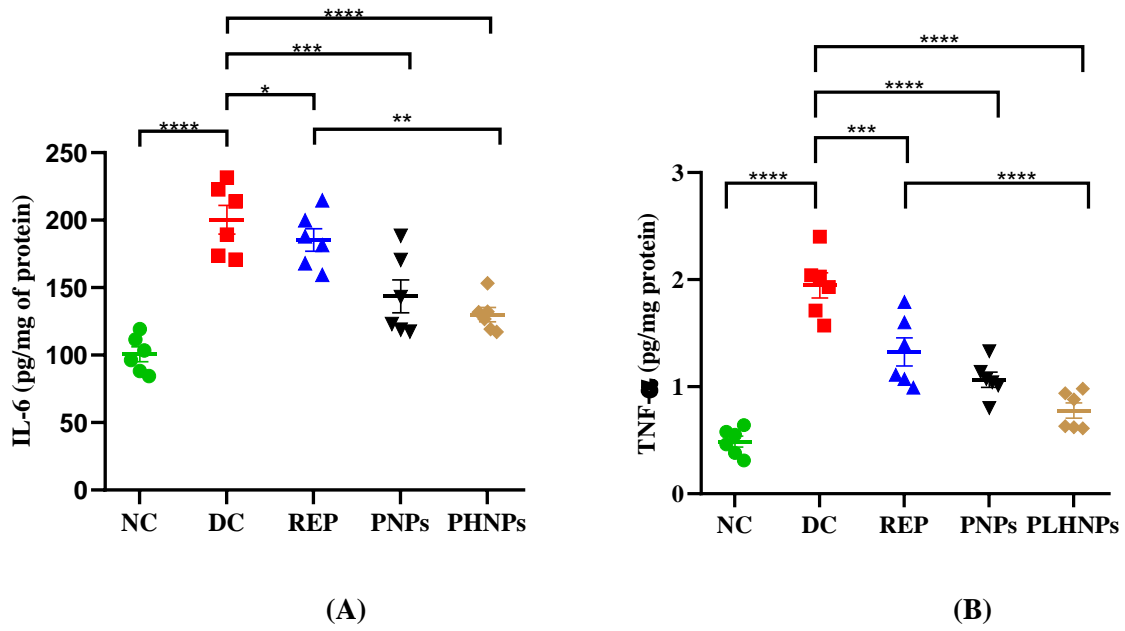
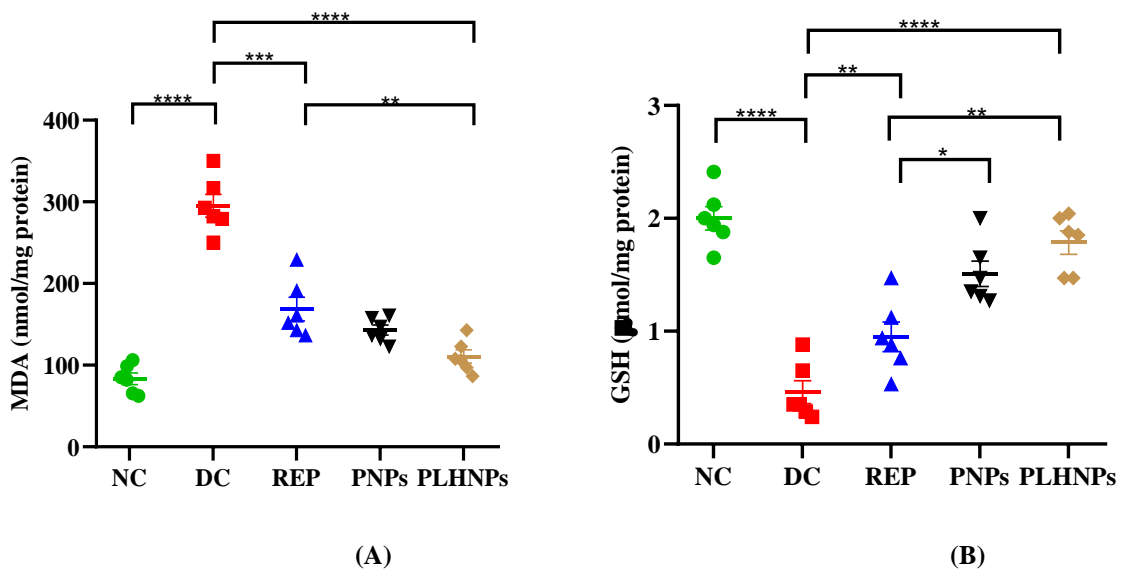


Fig.5.74: Effect of inflammatory parameters on HFD+STZ induced animal model on the treatment of REP, PNP, and PLHN. (A) IL-6, and (B) TNF- α . The data are represented in (mean \pm SEM, n=6 rats per group). * Indicates $P < 0.05$; ** $P < 0.01$, *** $P < 0.001$, **** $P < 0.0001$ by one-way ANOVA followed by Tukey's post hoc multiple comparison test.



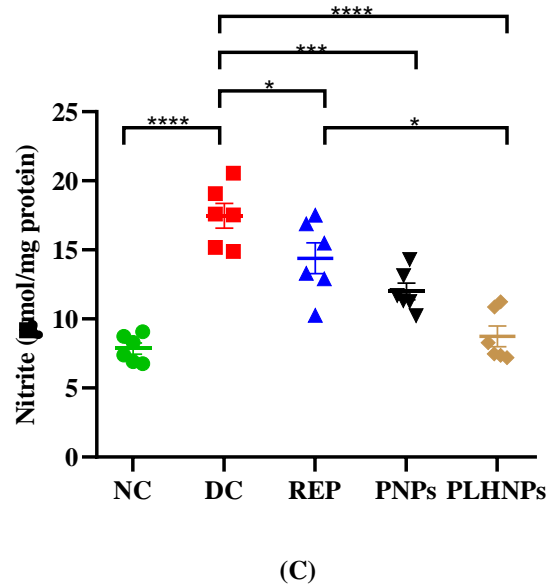


Fig.5.75: Effect of oxidative stress parameters on HFD+STZ induced animal model on the treatment of REP, PNP, and PLHNPs, (A) MDA, (B) GSH, and (C) nitrite. The data are represented in (mean \pm SEM, n=6 rats per group). * Indicates $P < 0.05$; ** $P < 0.01$, *** $P < 0.001$, **** $P < 0.0001$ by one-way ANOVA followed by Tukey's post hoc multiple comparison test.

Moreover, behavioral tasks were also performed to evaluate the retention, reference, and spatial memory by performing a passive avoidance task (Fig.5.76), a novel object recognition task (Fig.5.77), and Morri's water maze test (Fig.5.78). Though results indicate amelioration in memory loss, it was observed that PLHNPs show significant ($P < 0.01$) changes in the HFD+STZ group as compared with REP and PNP treated rats.

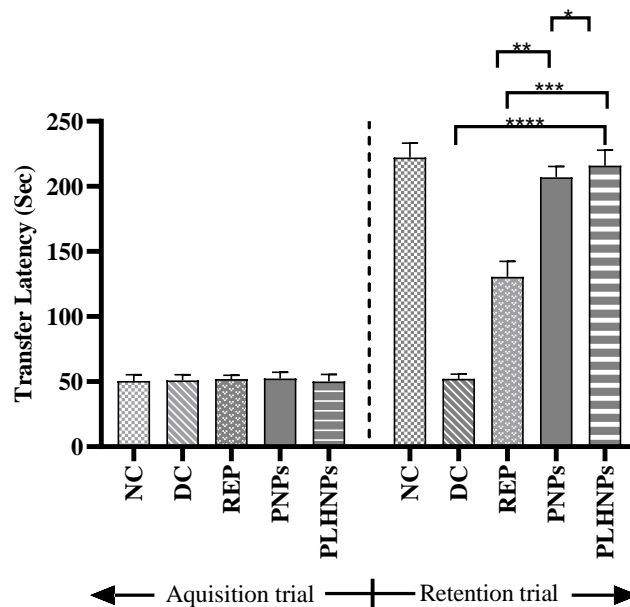
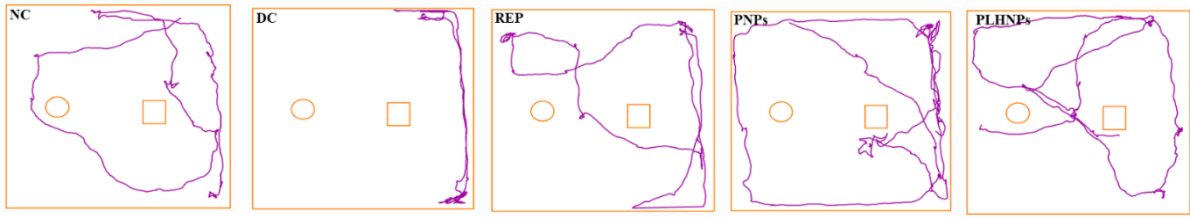
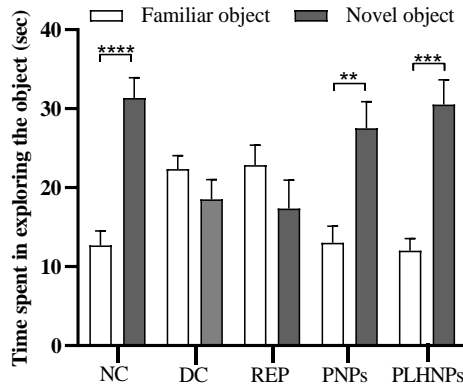


Fig.5.76: The estimation of transfer latency by performing behavioral parameters using passive avoidance task.



(A)



(B)

Fig.5.77: (A)The representation of the track plot for the novel object recognition task and (B) Time spent in exploring the object



Normal control

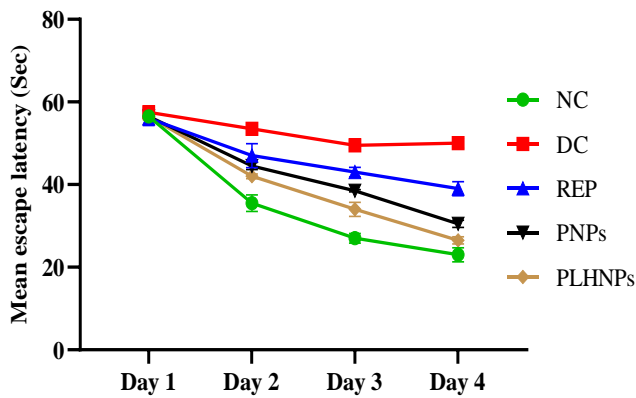
Disease control

REP

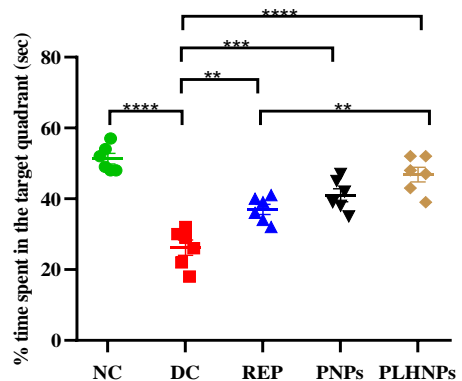
PNP

PLHNP

(A)



(B)



(C)

Fig.5.78: (A) The representation of track plot for Morri's water maze task; (B) mean escape latency and (C) Estimation of time spent in the same quadrant

In summary, the conventional preparations suffer from certain limitations and do not provide sustained effects therefore novel carriers were developed which could meet requirements for drug delivery systems. A nanoparticulate drug delivery system has been proposed to improve the limitations of the conventional system. PNPs and PLHNPs were formulated and evaluated as effective nanocarrier systems for the brain delivery of REP via oral administration. The evaluation of both nanoparticles was done by performing various physicochemical, *in vitro*, and *in vivo* studies. Though from physicochemical studies no significant differences were observed as both have PS < 150nm, PDI < 0.3, and fulfill the morphological criteria of shape, and size. However, through the results, it was observed that PLHNPs released REP in a controlled manner, with high effective permeability in the intestine and brain. Moreover, in cellular studies, the PLHNPs were found to be more effective than PNPs and have a significant effect on pharmacokinetic parameters. In biodistribution and pharmacodynamic studies of PLHNPs, a significant effect on the neurochemicals, inflammatory biomarkers, and oxidative parameters was observed as compared to PNPs. The core-shell structure of PLHNPs which efficiently loads the poorly water-soluble active ingredient and lipid monolayer reduces the outward diffusion of the drug and provides stability. Further, the outer layer of lipid PEG enhances systemic circulation and protects against immune recognition. Hence, it was revealed that PLHNPs were more efficient for the brain delivery of REP by oral administration than the PNPs.

5.6 In vivo studies

5.6.1 Estimation of Neurochemicals bio markers

The effect of REP, REP +MEM, and PLHNPs on neurochemical parameters (BDNF, A β , and tau protein) was estimated in HFD+STZ-induced wistar rats after the 4 weeks of treatment (Fig.5.79). It was observed that in DC group rats shows a significant ($p < 0.001$) upregulation in the levels of A β and tau proteins than the NC group rats. Whereas the BDNF level was significantly ($p < 0.001$) reduced in DC group rats than the NC group. Though after the treatment with REP for 4 weeks a significant ($p < 0.01$) reduction in the level of A β and tau proteins was observed however the BDNF level also improved significantly ($p < 0.01$) compared to DC group rats. Moreover, significant ($p < 0.01$) changes in the level of A β , tau proteins, and BDNF were also observed in the REP+MEM group compared to REP but when compared with PLHNPs, the nonsignificant ($p > 0.05$) change in the parameters were observed. Thus, the results suggest that the REP+MEM and PLNPs showed a similar effect and both enhance the effect of REP in an additive manner.

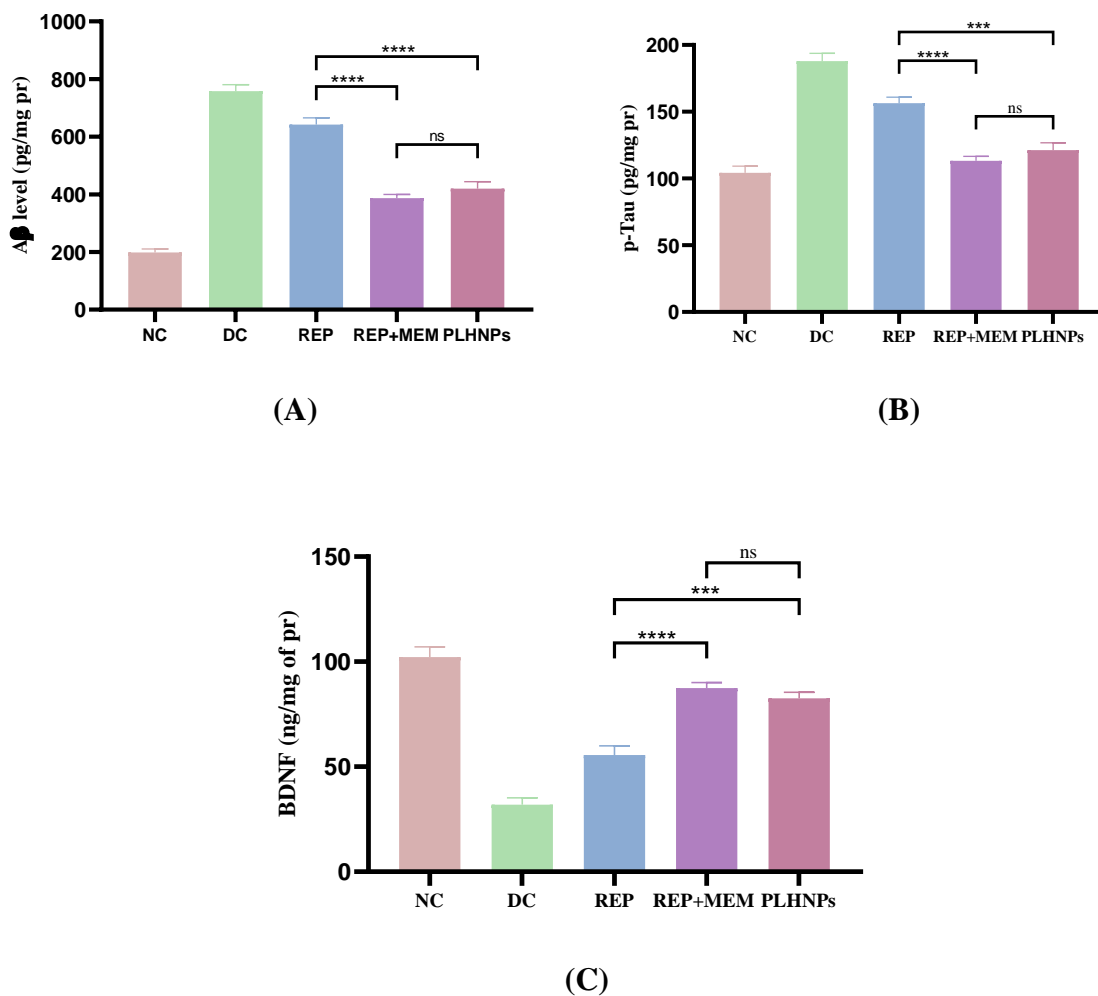


Fig.5.79: *In vivo* estimation of neurochemical parameters to understand the effect of REP after the treatment (A) BDNF; (B) p-Tau; (C) A β level in brain homogenate of HFD+STZ induced wistar rats, data are represented in (mean \pm SEM, n=6 rats per group). ^{ns} $P > 0.05$; * $P < 0.05$; ** $P < 0.01$, *** $P < 0.001$, **** $P < 0.0001$ by one-way ANOVA followed by Tukey's post hoc multiple comparison test

5.6.2 Estimation of Proinflammatory cytokines

The level of inflammatory cytokines (TNF- α and IL-6) were observed (Fig.5.80) and found a significant ($p < 0.001$) upregulation in the DC group compared to NC rats. After the treatment with REP, a decrement in these levels was observed and showed a significant ($p < 0.001$) suppression as compared to DC. Moreover, in the REP+MEM group, a significant ($p < 0.001$) attenuation in the level of pro-inflammatory cytokines was observed compared to free REP. Further, no significant change in the level of TNF- α and IL-6 was observed in the REP+MEM group when compared to PLHNPs. Therefore, it was observed that the PLHNPs showed similar action as that of REP +MEM.

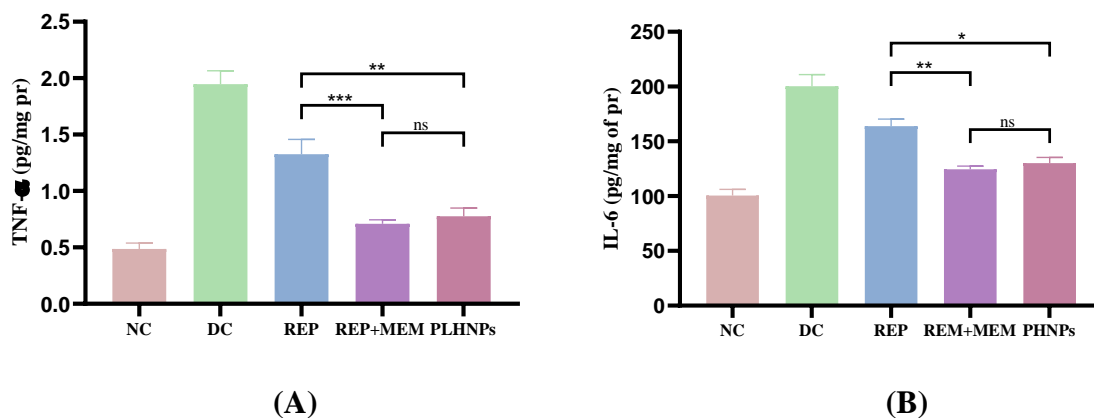


Fig.5.80: *In vivo* estimation of proinflammatory cytokines to understand the effect of REP on (A) TNF- α ; (B) IL-6 level in brain homogenate of HFD+STZ induced wistar rats, data are represented in (mean \pm SEM, n=6 rats per group). * Indicates $P < 0.05$; ** $P < 0.01$, *** $P < 0.001$, **** $P < 0.0001$ by one-way ANOVA followed by Tukey's post hoc multiple comparison test

5.6.3 Estimation of Oxidative stress parameters

In this study, the level of GSH, SOD (antioxidant) MDA, and nitrite (oxidative markers) were determined to understand the role of REP. The ROS generation (oxidative stress) and neuroinflammation are the molecular mechanisms involved in neurodegeneration. The hippocampus and neocortex regions of the brain were the most vulnerable to oxidative stress-induced impairment. Though the results showed that DC group rats significantly ($p < 0.001$) increase the levels of oxidative markers (MDA and nitrite) and decreased the levels of endogenous antioxidants (GSH, SOD) compared to the NC group as shown in Fig.5.81 However, after the treatment with REP+MEM a significant reduction in the level of MDA and

nitrile was observed compared to REP. Moreover, REP+MEM showed similar action as that of PLHNPs and no significant attenuation in oxidative markers was observed when compared REP+MEM to PLHNPs.

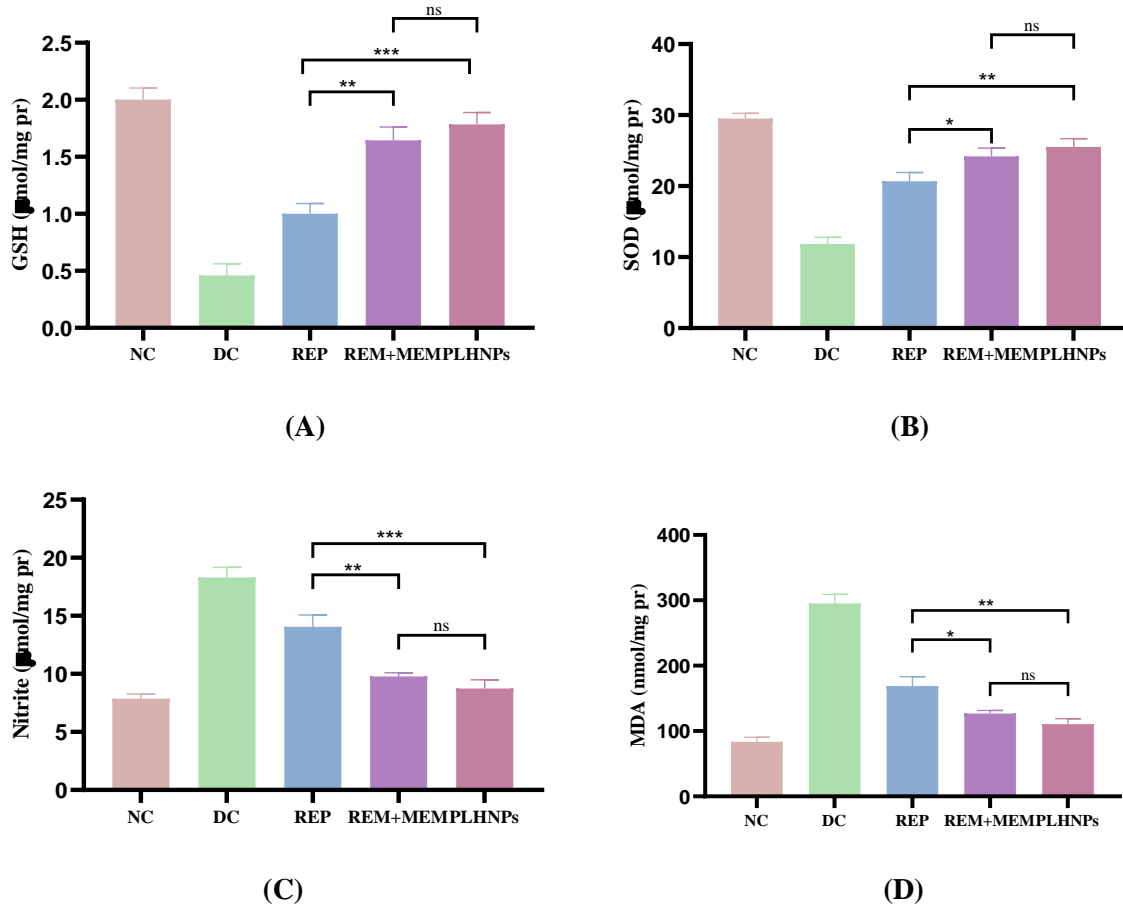


Fig.5.81: *In vivo* estimation of proinflammatory cytokines to understand the effect of REP on (A) GSH; (B) SOD; (C) Nitrite; (D) MDA level in brain homogenate of HFD+STZ induced wistar rats, data are represented in (mean \pm SEM, n=6 rats per group). * Indicates $P < 0.05$; ** $P < 0.01$, *** $P < 0.001$, **** $P < 0.0001$ by one-way ANOVA followed by Tukey's post hoc multiple comparison test

In summary, the effect of REP was measured when co administered with a low dose of MEM in HFD-STZ-induced rats. The neurochemical biomarkers, proinflammatory cytokines, and oxidative stress markers were estimated to understand the effect of REP+MEM and compared to REP, and PLHNPs. The results suggest that REP in combination with a low dose of MEM produces an additive effect when compared with free REP group. In addition, the PLHNPs was also compared to the combination of REP and MEM to estimate the improvement in the efficacy to REP. Surprisingly, it was found that the REP-loaded PLHNPs exerted therapeutic responses similar to REP and MEM combination, indicating the developed formulation as an effective approach in the management of AD.

6. Summary and Conclusions

- In this work, we have addressed various important questions regarding the role of REP in the treatment of MetS-linked neurodegenerative disorder i.e., AD. We have demonstrated for the first time the mechanistic insights of REP to control MetS (T2DM, BIR) comorbid with AD. The mechanism of REP was identified by assessing *in vitro* parameters (cell viability, & ROS) and the *in vivo* studies (pharmacokinetic & pharmacodynamic) using HFD fed STZ treated animal model. We have observed that the REP significantly increased the cell viability in STZ and H₂O₂-treated neuroblastoma SHSY-5Y cells, indicating the neuroprotective potential of REP. Based on *in vitro* data we further tested REP in HFD fed STZ treated animal model and observed a strong attenuation of AD pathogenesis by accessing the AD biomarkers i.e. A β , hyperphosphorylated tau proteins, and pro-inflammatory cytokines (TNF- α , IL-6), oxidative marker (MDA, NO) and increased BDNF, antioxidants (GSH, SOD) enzymes level as compared to HFD fed STZ rats. Similarly, in behavioral studies a significant improvement ($p < 0.01$) in the retention memory and spatial memory was observed with the REP treatment (4mg/kg) when compared to the HFD-fed STZ-treated group. Additionally, a significant ($p < 0.05$) increase in the Bcl-2 (anti-apoptotic marker), ATF-6 gene expression, and decrement in Bax, Caspase-3 expression (proapoptotic markers) were observed that indicates a reduction in neuronal cell death when compared with HFD+STZ disease rats. Moreover, H&E staining also indicates an increase in healthy neuronal cell count in REP as compared to the HFD-fed STZ-treated group. However, we have observed pharmacokinetic problems with REP i.e., short half-life ($t_{1/2}$) 2.65 ± 1.54 h), high clearance rate (163.84 ± 17.39 mL/h/kg), and low volume of distribution (2209.63 ± 603.29 mL/kg) based on the PK study.
- Therefore, to circumvent the observed PK problems *i.e.*; low absorptivity, high protein binding, first-pass metabolism, and to improve the efficacy of REP, the brain-targeted nano drug delivery systems have been designed and evaluated. Herein, the two types of PEGylated nanocarrier systems, *i.e.*, PNPs, and PLHNPs were developed, optimized, and characterized. Primarily, an amphiphilic di-block co-polymer (mPEG-PCL) was successfully synthesized and characterized using NMR, and GPC. The REP was successfully loaded into the mPEG-PCL polymer using nanoprecipitation and formulate REP-loaded PNPs. Further, the optimization of PNPs was done by the QbD approach, and the characteristic parameters *i.e.*, morphological evaluation (SEM,

TEM), compatibility with excipients (AT-IR, pXRD &DSC), *in vitro* release, GIT stability of PNPs were successfully evaluated. Additionally, SPIP and PAMPA-BBB assays were performed and improvement in the intestinal absorption, brain permeation of REP-loaded PNPs were observed as compared to free REP. Furthermore, *in vitro* cellular studies confirmed that REP-loaded PNPs significantly enhance cell viability, and cell uptake, decrease STZ induce neurodegeneration and oxidative stress in SHSY-5Y cells when compared to free REP. The *in vivo* pharmacokinetic and biodistribution study also confirmed that PNPs loaded with REP significantly improved the PK parameters and enhance the mean residence time when compared to free REP. Likewise, in pharmacodynamic studies, it was confirmed that the REP-loaded PNPs significantly ($p < 0.01$) attenuated the A β , tau proteins, proinflammatory cytokines (TNF- α , IL-6), oxidative markers (MDA, NO) levels while improved the BDNF, anti-oxidants enzymes (SOD, GSH) levels as compared to REP. Furthermore, the behavioral studies (PAT, MWZ, NOR) also showed a significant ($p < 0.01$) improvement in the retention, spatial, and recognition memory after being treated with REP-loaded PNPs compared to free REP. Also, improvement in the healthy neuronal count was observed in the REP-loaded PNPs compared to REP after performing H&E staining in the CA and dentate gyrus DG regions of the hippocampus.

- Likewise, the other formulation i.e., PLHNPs was successfully formulated using the nanoprecipitation self-assemble method and optimized by QbD approach response surface methodology (Box Behnken) with PS, PDI, EE as a response factors. The morphological characterization of REP-loaded PLHNPs was carried out by SEM, and TEM techniques, which clearly represented that PLHNPs have a core-shell structure with a spherical shape. Further, the *in vitro* release study of REP-loaded PLHNPs represented a delayed release and also showed good stability in the GIT environment. Moreover, REP-loaded PLHNPs confirmed an improvement in brain permeation, intestinal permeation, and absorption rate as compared to free REP. The *in vitro* cellular studies of REP-loaded PLHNPs exhibit significant improvement in cellular uptake, cell viability, and decreased oxidative stress in neuroblastoma SHSY-5Y cells when compared to free REP. Furthermore, *in vivo* pharmacokinetic studies, also confirmed a significant ($p < 0.05$) improvement in the PK parameters as compared to free REP. Likewise, in pharmacodynamic studies, the REP-loaded PLHNPs significantly ($p < 0.01$) attenuated the A β , tau proteins, TNF- α , IL-6, MDA, NO levels and improves the BDNF, SOD, GSH levels when compared to free REP. Furthermore, the behavioral

studies (PAT, MWZ, NOR) also showed a significant ($p < 0.01$) improvement in the retention, spatial, and recognition memory after treated with REP-loaded PLHNPs as compared to REP. Also, improvement in the neuronal count was observed in the REP-loaded PLHNPs compared to REP after performing H&E staining in the CA and DG regions of the hippocampus.

- Based on conducted *in vitro* and *in vivo* studies, both the REP-loaded PNP and PLHNP formulations confirmed the efficient delivery of REP in the brain but to check the better nanocarrier system among both of them, a comparative evaluation study was conducted for the delivery of REP to the brain after oral administration. We found that PLHNPs exhibit better changes like delaying the release of REP and better stability in the simulated GIT fluids when compared with PNP. Additionally, PLHNPs showed significant enhancement in effective intestinal permeability (~3.13-fold), absorption rate (~1.69-fold), and brain permeability when compared to PNP. The *in vitro* cellular uptake study of PLHNPs also showed ~ 1.2 % more uptake than PNP. Furthermore, PLHNP formulation significantly prevents the neuronal cell death induced by STZ and H₂O₂ in SHSY-5Y cells as evidenced by increased cell viability by 0.97-fold than the PNP. Moreover, pharmacokinetic studies also indicated the significant improvement of t_{max} by 1.8-fold, C_{max} by 1.4-fold, $t_{1/2}$ by 1.5-fold, and CL 1.4-fold by PLHNPs when compared to PNP. Likewise, in pharmacodynamic studies, PLHNPs strongly attenuated the level of A β , tau-protein, pro-inflammatory cytokines (IL-6, TNF- α), MDA, NO and increased the antioxidant enzyme (GSH, SOD), and BDNF levels when compared with PNP. Furthermore, behavioral studies (PA, MWM, and NOR test) also indicated significant improvement in memory and cognitive dysfunctions in PLHNPs as compared to PNP. The H&E staining also confirmed the improvement in healthy neuronal count in PLHNPs when compared with PNP. Hence, it is confirmed that oral administration of PLHNPs efficiently promotes the brain delivery of REP more than that of the PNP, which may be due to its core-shell nanoparticulate structure which imparts GIT stability, enhanced permeation, and reduced immunogenicity. The polymeric core in PLHNPs encapsulates the REP and SPC monolayer surrounding the core which reduces the outward diffusion and enhances the stability of REP. The outer layer of DSPE-PEG 2000 prolongs the circulation time of nanocarriers by avoiding reticuloendothelial system uptake, which is indispensable for increasing the brain's uptake of nanocarriers. PEGylation is also known to facilitate the ligand-receptor interactions at the brain endothelium to ease the entry of REP into the brain.

- Additionally, to examine the mechanistic co-delivery and the additive/synergistic benefits of REP in AD comorbid with MetS, the REP was co-administered with a low dose of MEM in HFD-fed STZ rats. We observed that the REP in combination with a low dose of MEM produces an additive effect when compared with REP. In addition, we also compared the REP-loaded PLHNPs whether it may produce the response similar to the combination of REP and MEM. Interestingly, we found that the REP-loaded PLHNPs exerted therapeutic responses similar to REP and MEM combination, indicating the strong translational possibility of our developed formulation for effective clinical management of AD.

7.1 Salient findings from the current study

- First time, we explored the efficiency of REP as a neuroprotective agent, suggesting the clinical translation of REP for AD management.
- To circumvent the observed pharmacokinetic problems and to improve the efficacy of REP, the two types of PEGylated formulations i.e., PNPs and PLHNPs were developed, optimized, characterized, and biologically evaluated.
- The PNPs were formulated with the synthesized di block amphiphilic co-polymer i.e., mPEG-PCL, and characterized for the delivery of REP in the brain to treat AD and AD comorbid with MetS.
- Similarly, PEGylated PLHNPs were developed and evaluated to enhance the *in vitro* and *in vivo* efficacy of REP for the treatment of AD comorbid with BIR.
- Based on comparative studies of PEGylated nanocarrier systems, the best nanocarrier i.e., polymer lipid hybrid nanoparticles were explored for effective brain delivery of REP via oral administration.
- Explored the additive effect of REP combined with a low dose of MEM in the BIR animal model.

7.2. Future scope of this work

The current research work confirmed that the REP has a neuroprotective potential and also proved that REP is an effective agent for the treatment of AD co-morbid with MetS (BIR, T2DM). Based on these findings, utilizing the obtained evidence future research can be performed as:

- Studying the benefits of other anti-diabetic drugs i.e, DPP-4, SGLT-2, HMGA-CoA inhibitors, and thiazolidinediones during BIR condition that may further open new avenues for therapeutic management of neurodegenerative disorders.
- Combining two different classes of drugs may be evaluated for checking the synergistic potential in BIR conditions
- The synthesized di-block polymer can be further modified for selective delivery to the brain.
- The formulation can be modified using alternative strategies of nanoparticle formation such as fabrication techniques, and choice of excipients to increase the entrapment efficiency, and loading capacity that may eventually reduce the cost.
- The process control parameters can be further optimized for the scale-up and manufacturing of the formulation.
- The developed formulations can be further processed for dosage form design for patient compliance.
- The pre-clinical and clinical toxicity and safety investigations can be performed for long-term usage.

8. References

- [1] Y. Rochlani, N.V. Pothineni, S. Kovelamudi, J.L. Mehta, Metabolic syndrome: pathophysiology, management, and modulation by natural compounds, *Ther. Adv. Cardiovasc. Dis.* 11 (2017) 215. <https://doi.org/10.1177/1753944717711379>.
- [2] L. Keltikangas-Järvinen, Metabolic Syndrome, *Encycl. Stress.* (2007) 717–721. <https://doi.org/10.1016/B978-012373947-6.00230-0>.
- [3] <https://www.nhlbi.nih.gov/health/metabolic-syndrome>
- [4] M.B. Lanktree, R.A. Hegele, Metabolic Syndrome, *Genomic Precis. Med. Cardiovasc. Dis.* Third Ed. (2018) 47–63. <https://doi.org/10.1016/B978-0-12-801812-5.00015-9>.
- [5] N. Wang, B. Yang, J. Zhang, Y. Zheng, S. Wang, X. Zhang, H. Situ, Y. Lin, Z. Wang, Metabolite profiling of traditional Chinese medicine XIAOPI formula: An integrated strategy based on UPLC-Q-Orbitrap MS combined with network pharmacology analysis, *Biomed. Pharmacother.* 121 (2020) 109569. <https://doi.org/10.1016/j.biopha.2019.109569>.
- [6] V. Cassano, A. Leo, M. Tallarico, V. Nesci, A. Cimellaro, T.V. Fiorentino, R. Citraro, M.L. Hribal, G. De Sarro, F. Perticone, G. Sesti, E. Russo, A. Sciacqua, Metabolic and cognitive effects of ranolazine in type 2 diabetes mellitus: Data from an in vivo model, *Nutrients.* 12 (2020). <https://doi.org/10.3390/nu12020382>.
- [7] A. Engin, The definition and prevalence of obesity and metabolic syndrome, *Adv. Exp. Med. Biol.* 960 (2017) 1–17. https://doi.org/10.1007/978-3-319-48382-5_1/COVER.
- [8] (<https://www.who.int/news-room/fact-sheets/detail/obesity-and-overweight>).
- [9] P.L. Huang, A comprehensive definition for metabolic syndrome, *DMM Dis. Model. Mech.* 2 (2009) 231–237. <https://doi.org/10.1242/dmm.001180>.
- [10] R.A. DeFronzo, E. Ferrannini, L. Groop, R.R. Henry, W.H. Herman, J.J. Holst, F.B. Hu, C.R. Kahn, I. Raz, G.I. Shulman, D.C. Simonson, M.A. Testa, R. Weiss, Type 2 diabetes mellitus, *Nat. Rev. Dis. Prim.* 1 (2015) 15019. <https://doi.org/10.1038/nrdp.2015.19>.
- [11] K. Mittal, R.J. Mani, D.P. Katare, Type 3 Diabetes: Cross Talk between Differentially Regulated Proteins of Type 2 Diabetes Mellitus and Alzheimer's Disease, *Sci. Reports* 2016 61. 6 (2016) 1–8. <https://doi.org/10.1038/srep25589>.

- [12] IDF Diabetes Atlas, (n.d.).
- [13] R. Nishimura, R.E. LaPorte, J.S. Dorman, N. Tajima, D. Becker, T.J. Orchard, Mortality Trends in Type 2 Diabetes, *Diabetes Care*. 24 (2018) 823–827. <https://doi.org/10.2337/diacare.24.5.823>.
- [14] Y. Krishnamoorthy, S. Rajaa, S. Murali, J. Sahoo, S.S. Kar, Association Between Anthropometric Risk Factors and Metabolic Syndrome Among Adults in India: A Systematic Review and Meta-Analysis of Observational Studies, *Prev. Chronic Dis*. 19 (2022) E24. <https://doi.org/10.5888/PCD19.210231>.
- [15] A.D. American Diabetes Association, Diagnosis and classification of diabetes mellitus., *Diabetes Care*. 33 Suppl 1 (2010) S62-9. <https://doi.org/10.2337/dc10-S062>.
- [16] G. Verdile, S.J. Fuller, R.N. Martins, The role of type 2 diabetes in neurodegeneration, *Neurobiol. Dis*. 84 (2015) 22–38. <https://doi.org/10.1016/j.nbd.2015.04.008>.
- [17] S. Cetinkalp, I. Simsir, S. Ertek, Insulin resistance in brain and possible therapeutic approaches, *Curr. Vasc. Pharmacol*. 12 (2014) 553–564. <https://doi.org/10.2174/1570161112999140206130426>.
- [18] R.U. Margolis, N. Altszuler, Insulin in the cerebrospinal fluid, *Nature*. 215 (1967) 1375–1376. <https://doi.org/10.1038/2151375A0>.
- [19] J. Havrankova, D. Schmechel, J. Roth, M. Brownstein, Identification of insulin in rat brain., *Proc. Natl. Acad. Sci. U. S. A*. 75 (1978) 5737. <https://doi.org/10.1073/PNAS.75.11.5737>.
- [20] F. Bagaméry, K. Varga, K. Kecsmár, I. Vincze, É. Szökő, T. Tábi, Lack of insulin resistance in response to streptozotocin treatment in neuronal SH-SY5Y cell line, *J. Neural Transm*. 127 (2020) 71–80. <https://doi.org/10.1007/S00702-019-02118-5>.
- [21] R.U. Margolis, N. Altszuler, Effect of intracisternally administered insulin-131-I in normal and vagotomized dogs, *Proc. Soc. Exp. Biol. Med*. 127 (1968) 1122–1125. <https://doi.org/10.3181/00379727-127-32887>.
- [22] S. Kang, C.H. Kim, H. Jung, E. Kim, H.T. Song, J.E. Lee, Agmatine ameliorates type 2 diabetes induced-Alzheimer’s disease-like alterations in high-fat diet-fed mice via reactivation of blunted insulin signalling, *Neuropharmacology*. 113 (2017) 467–479. <https://doi.org/10.1016/j.neuropharm.2016.10.029>.

- [23] K. Mittal, R.J. Mani, D.P. Katare, Type 3 Diabetes: Cross Talk between Differentially Regulated Proteins of Type 2 Diabetes Mellitus and Alzheimer's Disease, *Sci. Reports* 2016 61. 6 (2016) 1–8. <https://doi.org/10.1038/srep25589>.
- [24] J.M. van der Harg, L. Eggels, S.R. Ruigrok, J.J. Jeroen, S.E. La Fleur, W. Scheper, Neuroinflammation is not a prerequisite for diabetes-induced Tau phosphorylation, *Front. Neurosci.* 9 (2015). <https://doi.org/10.3389/fnins.2015.00432>.
- [25] R. Agrawal, C.M. Reno, S. Sharma, C. Christensen, Y. Huang, S.J. Fisher, Insulin action in the brain regulates both central and peripheral functions, *Am. J. Physiol. - Endocrinol. Metab.* 321 (2021) 156–163. https://doi.org/10.1152/AJPENDO.00642.2020/ASSET/IMAGES/LARGE/AJPENDO.00642.2020_F001.JPEG.
- [26] L.S.S. Ferreira, C.S. Fernandes, M.N.N. Vieira, F.G. De Felice, Insulin Resistance in Alzheimer's Disease, *Front. Neurosci.* 12 (2018) 830. <https://doi.org/10.3389/fnins.2018.00830>.
- [27] S.M. De La Monte, M. Tong, Brain metabolic dysfunction at the core of Alzheimer's disease, *Biochem. Pharmacol.* 88 (2014) 548–559. <https://doi.org/10.1016/J.BCP.2013.12.012>.
- [28] A.A.M. Rensink, I. Otte-Höller, R. De Boer, R.R. Bosch, H.J. Ten Donkelaar, R.M.W. De Waal, M.M. Verbeek, B. Kremer, Insulin inhibits amyloid β -induced cell death in cultured human brain pericytes, *Neurobiol. Aging.* 25 (2004) 93–103. [https://doi.org/10.1016/S0197-4580\(03\)00039-3](https://doi.org/10.1016/S0197-4580(03)00039-3).
- [29] T.T. Nguyen, Q.T.H. Ta, T.K.O. Nguyen, T.T.D. Nguyen, V. Van Giau, Type 3 Diabetes and Its Role Implications in Alzheimer's Disease, *Int. J. Mol. Sci.* 2020, Vol. 21, Page 3165. 21 (2020) 3165. <https://doi.org/10.3390/IJMS21093165>.
- [30] D. Kellar, S. Craft, Brain insulin resistance in Alzheimer's disease and related disorders: mechanisms and therapeutic approaches, *Lancet Neurol.* 19 (2020) 758–766.
- [31] S.E. Arnold, Z. Arvanitakis, S.L. Macauley-Rambach, A.M. Koenig, H.Y. Wang, R.S. Ahima, S. Craft, S. Gandy, C. Buettner, L.E. Stoeckel, D.M. Holtzman, D.M. Nathan, Brain insulin resistance in type 2 diabetes and Alzheimer disease: Concepts and conundrums, *Nat. Rev. Neurol.* 14 (2018) 168–181.

- <https://doi.org/10.1038/NRNEUROL.2017.185>.
- [32] S.E. Arnold, Z. Arvanitakis, S.L. Macauley-Rambach, A.M. Koenig, H.-Y. Wang, R.S. Ahima, S. Craft, S. Gandy, C. Buettner, L.E. Stoeckel, D.M. Holtzman, D.M. Nathan, Brain insulin resistance in type 2 diabetes and Alzheimer disease: concepts and conundrums, *Nat. Rev. Neurol.* 14 (2018) 168–181. <https://doi.org/10.1038/nrneurol.2017.185>.
- [33] A. Guven, O. Yavuz, M. Cam, C. Comunoglu, O. Sevinc, Central nervous system complications of diabetes in streptozotocin-induced diabetic rats: A histopathological and immunohistochemical examination, *Int. J. Neurosci.* 119 (2009) 1155–1169. <https://doi.org/10.1080/00207450902841723>.
- [34] S. Chatterjee, A. Mudher, Alzheimer’s Disease and Type 2 Diabetes: A Critical Assessment of the Shared Pathological Traits, *Front. Neurosci.* 12 (2018) 383. <https://doi.org/10.3389/fnins.2018.00383>.
- [35] S. Jeong, Molecular and Cellular Basis of Neurodegeneration in Alzheimer’s Disease, *Mol. Cells.* 40 (2017) 613. <https://doi.org/10.14348/MOLCELLS.2017.0096>.
- [36] M. Agrawal, Molecular basis of chronic neurodegeneration, *Clin. Mol. Med. Princ. Pract.* (2020) 447–460. <https://doi.org/10.1016/B978-0-12-809356-6.00026-5>.
- [37] R.K. Sodhi, N. Singh, Defensive Effect of Lansoprazole in Dementia of AD Type in Mice Exposed to Streptozotocin and Cholesterol Enriched Diet, *PLoS One.* 8 (2013). <https://doi.org/10.1371/journal.pone.0070487>.
- [38] J.S. Birks, R.J. Harvey, Donepezil for dementia due to Alzheimer’s disease, *Cochrane Database Syst. Rev.* (2018).
- [39] Alzheimer’s Facts and Figures Report | Alzheimer’s Association, (n.d.). <https://www.alz.org/alzheimers-dementia/facts-figures> (accessed February 23, 2023).
- [40] A.A.-N. rinsho. J. journal of clinical medicine, undefined 2010, Dementia and insulin resistance in patients with diabetes mellitus, *Europepmc.Org.* (n.d.). <https://europepmc.org/article/med/20229808> (accessed February 27, 2023).
- [41] L. Frölich, D. Blum-Degen, P. Riederer, S. Hoyer, A disturbance in the neuronal insulin receptor signal transduction in sporadic Alzheimer’s disease, *Ann. N. Y. Acad. Sci.* 893 (1999) 290–293. <https://doi.org/10.1111/J.1749-6632.1999.TB07839.X>.

- [42] M. Aschner, M. Culbreth, GSK-3 β , a double-edged sword in Nrf2 regulation: Implications for neurological dysfunction and disease [version 1; referees: 2 approved], *F1000Research*. 7 (2018). <https://doi.org/10.12688/F1000RESEARCH.15239.1>.
- [43] E.M. Blalock, J.W. Geddes, K.C. Chen, N.M. Porter, W.R. Markesbery, P.W. Landfield, Incipient Alzheimer's disease: Microarray correlation analyses reveal major transcriptional and tumor suppressor responses, *Proc. Natl. Acad. Sci. U. S. A.* 101 (2004) 2173–2178. <https://doi.org/10.1073/PNAS.0308512100>.
- [44] C.J. Phiel, C.A. Wilson, V.M.Y. Lee, P.S. Klein, GSK-3 α regulates production of Alzheimer's disease amyloid- β peptides, *Nat.* 2003 4236938. 423 (2003) 435–439. <https://doi.org/10.1038/nature01640>.
- [45] S. M. de la Monte, Brain Insulin Resistance and Deficiency as Therapeutic Targets in Alzheimers Disease, *Curr. Alzheimer Res.* 9 (2012) 35–66. <https://doi.org/10.2174/156720512799015037>.
- [46] D. Muylaert, A. Kremer, T. Jaworski, P. Borghgraef, H. Devijver, S. Croes, I. Dewachter, F. Van Leuven, Glycogen synthase kinase-3 β , or a link between amyloid and tau pathology?, *Genes, Brain Behav.* 7 (2008) 57–66. <https://doi.org/10.1111/J.1601-183X.2007.00376.X>.
- [47] X. jia Zhai, K. Hu, F. Chen, Y. ning Lu, Comparative Bioavailability and Tolerability of a Single 2-mg Dose of 2 Repaglinide Tablet Formulations in Fasting, Healthy Chinese Male Volunteers: An Open-Label, Randomized-Sequence, 2-Period Crossover Study, *Curr. Ther. Res. - Clin. Exp.* 75 (2013) 48–52. <https://doi.org/10.1016/j.curtheres.2013.08.001>.
- [48] C.R. Culy, B. Jarvis, Repaglinide: A review of its therapeutic use in type 2 diabetes mellitus, *Drugs*. 61 (2001) 1625–1660. <https://doi.org/10.2165/00003495-200161110-00008>.
- [49] L.J. Scott, Repaglinide, *Drugs* 2012 722. 72 (2012) 249–272. <https://doi.org/10.2165/11207600-000000000-00000>.
- [50] X. Li, Z.Q. Liu, Pharmacogenetic Factors That Affect Drug Metabolism and Efficacy in Type 2 Diabetes Mellitus, *Drug Metab. Dis.* (2017) 157–179. <https://doi.org/10.1016/B978-0-12-802949-7.00007-9>.

- [51] L.F. Van Gaal, K.L. Van Acker, I.H. De Leeuw, Repaglinide improves blood glucose control in sulphonylurea-naive type 2 diabetes, *Diabetes Res. Clin. Pract.* 53 (2001) 141–148. [https://doi.org/10.1016/S0168-8227\(01\)00253-4](https://doi.org/10.1016/S0168-8227(01)00253-4).
- [52] V. Hatorp, W.C. Huang, P. Strange, Repaglinide pharmacokinetics in healthy young adult and elderly subjects, *Clin. Ther.* 21 (1999) 702–710. [https://doi.org/10.1016/S0149-2918\(00\)88321-6](https://doi.org/10.1016/S0149-2918(00)88321-6).
- [53] T.K. Motawi, R.H. Al-Kady, M.A. Senousy, S.M. Abdelraouf, Repaglinide Elicits a Neuroprotective Effect in Rotenone-Induced Parkinson’s Disease in Rats: Emphasis on Targeting the DREAM-ER Stress BiP/ATF6/CHOP Trajectory and Activation of Mitophagy, *ACS Chem. Neurosci.* (2022). https://doi.org/10.1021/ACSCHEMNEURO.2C00656/ASSET/IMAGES/MEDIUM/CN2C00656_0011.GIF.
- [54] R. Naranjo, P. González, A. Lopez-Hurtado, X.M. Dopazo, B. Mellström, J.R. Naranjo, Inhibition of the neuronal calcium sensor DREAM modulates presenilin-2 endoproteolysis, *Front. Mol. Neurosci.* 11 (2018) 1–9. <https://doi.org/10.3389/fnmol.2018.00449>.
- [55] J.R. Naranjo, H. Zhang, D. Villar, P. González, X.M. Dopazo, J. Morón-Oset, E. Higuera, J.C. Oliveros, M.D. Arrabal, A. Prieto, P. Cercós, T. González, A. De La Cruz, J. Casado-Vela, A. Rábano, C. Valenzuela, M. Gutierrez-Rodriguez, J.Y. Li, B. Mellström, Activating transcription factor 6 derepression mediates neuroprotection in Huntington disease, *J. Clin. Invest.* 126 (2016) 627–638. <https://doi.org/10.1172/JCI82670>.
- [56] J.K. Patra, G. Das, L.F. Fraceto, E.V.R. Campos, M.D.P. Rodriguez-Torres, L.S. Acosta-Torres, L.A. Diaz-Torres, R. Grillo, M.K. Swamy, S. Sharma, S. Habtemariam, H.S. Shin, Nano based drug delivery systems: recent developments and future prospects, *J. Nanobiotechnology* 2018 161. 16 (2018) 1–33. <https://doi.org/10.1186/S12951-018-0392-8>.
- [57] M.J. Mitchell, M.M. Billingsley, R.M. Haley, M.E. Wechsler, N.A. Peppas, R. Langer, Engineering precision nanoparticles for drug delivery, *Nat. Rev. Drug Discov.* 2020 202. 20 (2020) 101–124. <https://doi.org/10.1038/s41573-020-0090-8>.
- [58] Metabolic Syndrome - What Is Metabolic Syndrome? | NHLBI, NIH, (n.d.).

- <https://www.nhlbi.nih.gov/health/metabolic-syndrome> (accessed February 25, 2023).
- [59] V. Rani, G. Deep, R.K. Singh, K. Palle, U.C.S. Yadav, Oxidative stress and metabolic disorders: Pathogenesis and therapeutic strategies, *Life Sci.* 148 (2016) 183–193. <https://doi.org/10.1016/j.lfs.2016.02.002>.
- [60] Diagnosis and classification of diabetes mellitus, *Diabetes Care.* 33 (2010). <https://doi.org/10.2337/DC10-S062>.
- [61] H.W. Baynes, Classification, pathophysiology, diagnosis and management of diabetes mellitus, *J Diabetes Metab.* 6 (2015) 1–9.
- [62] W.R. Yamamoto, R.N. Bone, P. Sohn, F. Syed, C.A. Reissaus, A.L. Mosley, A.B. Wijeratne, J.D. True, X. Tong, T. Kono, C. Evans-Molina, Endoplasmic reticulum stress alters ryanodine receptor function in the murine pancreatic cell, *J. Biol. Chem.* 294 (2019) 168–181. <https://doi.org/10.1074/JBC.RA118.005683>.
- [63] S. Del Prato, Role of glucotoxicity and lipotoxicity in the pathophysiology of Type 2 diabetes mellitus and emerging treatment strategies, *Diabet. Med.* 26 (2009) 1185–1192. <https://doi.org/10.1111/J.1464-5491.2009.02847.X>.
- [64] U. Galicia-Garcia, A. Benito-Vicente, S. Jebari, A. Larrea-Sebal, H. Siddiqi, K.B. Uribe, H. Ostolaza, C. Martín, Pathophysiology of type 2 diabetes mellitus, *Int. J. Mol. Sci.* 21 (2020) 1–34. <https://doi.org/10.3390/IJMS21176275>.
- [65] S. Lim, J.H. Bae, H.S. Kwon, M.A. Nauck, COVID-19 and diabetes mellitus: from pathophysiology to clinical management, *Nat. Rev. Endocrinol.* 17 (2021) 11–30. <https://doi.org/10.1038/S41574-020-00435-4>.
- [66] X.F. Huang, P. Arvan, Intracellular transport of proinsulin in pancreatic β -cells: structural maturation probed by disulfide accessibility, *J. Biol. Chem.* 270 (1995) 20417–20423.
- [67] D.F. Steiner, The biosynthesis of insulin, *Pancreat. Beta Cell Heal. Dis.* (2008) 31–49.
- [68] Z. Fu, E. R. Gilbert, D. Liu, Regulation of Insulin Synthesis and Secretion and Pancreatic Beta-Cell Dysfunction in Diabetes, *Curr. Diabetes Rev.* 9 (2012) 25–53. <https://doi.org/10.2174/157339913804143225>.
- [69] P.A. Halban, Proinsulin processing in the regulated and the constitutive secretory

- pathway, *Diabetologia*. 37 (1994). <https://doi.org/10.1007/BF00400828>.
- [70] S.B. Choi, C.H. Park, M.K. Choi, D.W. Jun, S. Park, Improvement of insulin resistance and insulin secretion by water extracts of *Cordyceps militaris*, *Phellinus linteus*, and *Paecilomyces tenuipes* in 90% pancreatectomized rats, *Biosci. Biotechnol. Biochem.* 68 (2004) 2257–2264. <https://doi.org/10.1271/BBB.68.2257>.
- [71] J. Lee, P.F. Pilch, The insulin receptor: Structure, function, and signaling, *Am. J. Physiol. - Cell Physiol.* 266 (1994). <https://doi.org/10.1152/AJPCELL.1994.266.2.C319>.
- [72] C.C. Lee, C.C. Huang, M.Y. Wu, K. Sen Hsu, Insulin stimulates postsynaptic density-95 protein translation via the phosphoinositide 3-kinase-Akt-mammalian target of rapamycin signaling pathway, *J. Biol. Chem.* 280 (2005) 18543–18550. <https://doi.org/10.1074/jbc.M414112200>.
- [73] M.F. White, Insulin Signaling in Health and Disease, *Science* (80-.). 302 (2003) 1710–1711. <https://doi.org/10.1126/SCIENCE.1092952>.
- [74] M.F. White, S.E. Shoelson, H. Keutmann, C.R. Kahn, A cascade of tyrosine autophosphorylation in the β -subunit activates the phosphotransferase of the insulin receptor, *J. Biol. Chem.* 263 (1988) 2969–2980. [https://doi.org/10.1016/s0021-9258\(18\)69163-x](https://doi.org/10.1016/s0021-9258(18)69163-x).
- [75] B.D.- Diabetes, undefined 2006, Molecular mechanisms of insulin resistance: serine phosphorylation of insulin receptor substrate-1 and increased expression of p85 α : the two sides of a coin, *Am Diabetes Assoc.* (2006). <https://doi.org/10.2337/db06-0391>.
- [76] T. Pederson, D. Kramer, C.R.- Diabetes, undefined 2001, Serine/threonine phosphorylation of IRS-1 triggers its degradation: possible regulation by tyrosine phosphorylation, *Am Diabetes Assoc.* (2001). <https://doi.org/10.2337/diabetes.50.1.24>.
- [77] S.E. Arnold, Z. Arvanitakis, S.L. Macauley-Rambach, A.M. Koenig, H.-Y. Wang, R.S. Ahima, S. Craft, S. Gandy, C. Buettner, L.E. Stoeckel, D.M. Holtzman, D.M. Nathan, Brain insulin resistance in type 2 diabetes and Alzheimer disease: concepts and conundrums, *Nat. Rev. Neurol.* 14 (2018) 168–181. <https://doi.org/10.1038/nrneurol.2017.185>.
- [78] V.K. Sharma, T.G. Singh, Insulin resistance and bioenergetic manifestations: Targets

- and approaches in Alzheimer's disease, *Life Sci.* 262 (2020). <https://doi.org/10.1016/j.lfs.2020.118401>.
- [79] D. Bosco, A. Fava, M. Plastino, T. Montalcini, A. Pujia, Possible implications of insulin resistance and glucose metabolism in Alzheimer's disease pathogenesis, *J. Cell. Mol. Med.* 15 (2011) 1807–1821. <https://doi.org/10.1111/J.1582-4934.2011.01318.X>.
- [80] S. Craft, G.S. Watson, Insulin and neurodegenerative disease: Shared and specific mechanisms, *Lancet Neurol.* 3 (2004) 169–178. [https://doi.org/10.1016/S1474-4422\(04\)00681-7](https://doi.org/10.1016/S1474-4422(04)00681-7).
- [81] A. Akhtar, S.P. Sah, Insulin signaling pathway and related molecules: Role in neurodegeneration and Alzheimer's disease, *Neurochem. Int.* 135 (2020). <https://doi.org/10.1016/j.neuint.2020.104707>.
- [82] Y. Tang, B. Huang, L. Sun, X. Peng, X. Chen, X. Zou, Ginkgolide B promotes proliferation and functional activities of bone marrow-derived endothelial progenitor cells: involvement of Akt/eNOS and MAPK/p38 signaling pathways, *Eur Cell Mater.* 21 (2011) 459–469.
- [83] C.M. Griffith, T. Eid, G.M. Rose, P.R. Patrylo, Evidence for altered insulin receptor signaling in Alzheimer's disease, *Neuropharmacology.* 136 (2018) 202–215. <https://doi.org/https://doi.org/10.1016/j.neuropharm.2018.01.008>.
- [84] Y. Hu, S.J. Russek, BDNF and the diseased nervous system: A delicate balance between adaptive and pathological processes of gene regulation, *J. Neurochem.* 105 (2008) 1–17. <https://doi.org/10.1111/J.1471-4159.2008.05237.X>.
- [85] L. Munoz, A.J. Ammit, Targeting p38 MAPK pathway for the treatment of Alzheimer's disease, *Neuropharmacology.* 58 (2010) 561–568. <https://doi.org/10.1016/J.NEUROPHARM.2009.11.010>.
- [86] A.R. Saltiel, C.R. Kahn, Insulin signalling and the regulation of glucose and lipid metabolism, *Nature.* 414 (2001) 799–806. <https://doi.org/10.1038/414799A>.
- [87] G. Thomas, M.N. Hall, TOR signalling and control of cell growth, *Curr. Opin. Cell Biol.* 9 (1997) 782–787. [https://doi.org/https://doi.org/10.1016/S0955-0674\(97\)80078-6](https://doi.org/https://doi.org/10.1016/S0955-0674(97)80078-6).
- [88] M. Miron, J. Verdú, P.E.D. Lachance, M.J. Birnbaum, P.F. Lasko, N. Sonenberg, The translational inhibitor 4E-BP is an effector of PI(3)K/Akt signalling and cell growth in

- Drosophila*, Nat. Cell Biol. 2001 36. 3 (2001) 596–601. <https://doi.org/10.1038/35078571>.
- [89] V.W. Ding, R.-H. Chen, F. McCormick, Differential Regulation of Glycogen Synthase Kinase 3 β by Insulin and Wnt Signaling*, J. Biol. Chem. 275 (2000) 32475–32481. <https://doi.org/https://doi.org/10.1074/jbc.M005342200>.
- [90] C. Hooper, R. Killick, S. Lovestone, The GSK3 hypothesis of Alzheimer's disease, J. Neurochem. 104 (2008) 1433–1439. <https://doi.org/https://doi.org/10.1111/j.1471-4159.2007.05194.x>.
- [91] F. Hernández, E. Gómez de Barreda, A. Fuster-Matanzo, J.J. Lucas, J. Avila, GSK3: A possible link between beta amyloid peptide and tau protein, Exp. Neurol. 223 (2010) 322–325. <https://doi.org/10.1016/J.EXPNEUROL.2009.09.011>.
- [92] H. Koepsell, Glucose transporters in brain in health and disease, Pflugers Arch. Eur. J. Physiol. 472 (2020) 1299–1343. <https://doi.org/10.1007/S00424-020-02441-X>.
- [93] B. Thorens, GLUT2, glucose sensing and glucose homeostasis, Diabetologia. 58 (2015) 221–232. <https://doi.org/10.1007/S00125-014-3451-1>.
- [94] L. Chang, S.H. Chiang, A.R. Saltiel, Insulin signaling and the regulation of glucose transport, Mol. Med. 10 (2004) 65–71. <https://doi.org/10.2119/2005-00029.SALTIEL>.
- [95] A. Zisman, O.D. Peroni, E.D. Abel, M.D. Michael, F. Mauvais-Jarvis, B.B. Lowell, J.F.P. Wojtaszewski, M.F. Hirshman, A. Virkamaki, L.J. Goodyear, C.R. Kahn, B.B. Kahn, Targeted disruption of the glucose transporter 4 selectively in muscle causes insulin resistance and glucose intolerance, Nat. Med. 2000 68. 6 (2000) 924–928. <https://doi.org/10.1038/78693>.
- [96] V.H. Maier, G.W. Gould, Long-term insulin treatment of 3T3-L1 adipocytes results mis-targeting of GLUT4: Implications for insulin-stimulated glucose transport, Diabetologia. 43 (2000) 1273–1281. <https://doi.org/10.1007/S001250051523/METRICS>.
- [97] W. Farris, S. Mansourian, Y. Chang, L. Lindsley, E.A. Eckman, M.P. Frosch, C.B. Eckman, R.E. Tanzi, D.J. Selkoe, S. Guénette, Insulin-degrading enzyme regulates the levels of insulin, amyloid beta-protein, and the beta-amyloid precursor protein intracellular domain in vivo, Proc. Natl. Acad. Sci. U. S. A. 100 (2003) 4162–4167.

- <https://doi.org/10.1073/PNAS.0230450100>.
- [98] L.B. Hersh, The insulysin (insulin degrading enzyme) enigma, *Cell. Mol. Life Sci.* 63 (2006) 2432–2434. <https://doi.org/10.1007/S00018-006-6238-9>.
- [99] M. Kouach, B. Desbuquois, F. Authier, Endosomal proteolysis of internalised [ArgA0]-human insulin at neutral pH generates the mature insulin peptide in rat liver in vivo, *Diabetologia.* 52 (2009) 2621–2632. <https://doi.org/10.1007/S00125-009-1551-0>.
- [100] H. Chen, Y. Qian, X. Chen, Z. Ruan, Y. Ye, H. Chen, L.A. Babiuk, Y.-S. Jung, J. Dai, HDAC6 Restricts Influenza A Virus by Deacetylation of the RNA Polymerase PA Subunit, *J. Virol.* 93 (2019). <https://doi.org/10.1128/JVI.01896-18>.
- [101] J. Fawcett, P.A. Permana, J.L. Levy, W.C. Duckworth, Regulation of protein degradation by insulin-degrading enzyme: Analysis by small interfering RNA-mediated gene silencing, *Arch. Biochem. Biophys.* 468 (2007) 128–133. <https://doi.org/10.1016/J.ABB.2007.09.019>.
- [102] G.M. Reaven, Insulin Resistance/Compensatory Hyperinsulinemia, Essential Hypertension, and Cardiovascular Disease, *J. Clin. Endocrinol. Metab.* 88 (2003) 2399–2403. <https://doi.org/10.1210/JC.2003-030087>.
- [103] P.A. Sarafidis, G.L. Bakris, Insulin Resistance, Hyperinsulinemia, and Hypertension: An Epidemiologic Approach, *J. Cardiometab. Syndr.* 1 (2006) 334–344. <https://doi.org/10.1111/J.1559-4564.2006.05795.X>.
- [104] Y. Nakatani, H. Kaneto, D. Kawamori, K. Yoshiuchi, M. Hatazaki, T.A. Matsuoka, K. Ozawa, S. Ogawa, M. Hori, Y. Yamasaki, M. Matsuhisa, Involvement of endoplasmic reticulum stress in insulin resistance and diabetes, *J. Biol. Chem.* 280 (2005) 847–851. <https://doi.org/10.1074/jbc.M411860200>.
- [105] Y.J. Jung, J.E. Lee, A.S. Lee, K.P. Kang, S. Lee, S.K. Park, S.Y. Lee, M.K. Han, D.H. Kim, W. Kim, SIRT1 overexpression decreases cisplatin-induced acetylation of NF- κ B p65 subunit and cytotoxicity in renal proximal tubule cells, *Biochem. Biophys. Res. Commun.* 419 (2012) 206–210. <https://doi.org/10.1016/j.bbrc.2012.01.148>.
- [106] S.M. de la Monte, Contributions of Brain Insulin Resistance and Deficiency in Amyloid-Related Neurodegeneration in Alzheimer's Disease, *Drugs.* 72 (2012) 49–66. <https://doi.org/10.2165/11597760-000000000-00000>.

- [107] S.M. de la Monte, Therapeutic targets of brain insulin resistance in sporadic Alzheimer's disease, *Front. Biosci. E4* (2012) 1582–1605. <https://doi.org/10.2741/E482>.
- [108] S.B. Wheatcroft, I.L. Williams, A.M. Shah, M.T. Kearney, Pathophysiological implications of insulin resistance on vascular endothelial function, *Diabet. Med.* 20 (2003) 255–268. <https://doi.org/10.1046/j.1464-5491.2003.00869.x>.
- [109] K. Talbot, H.-Y. Wang, H. Kazi, L.-Y. Han, K.P. Bakshi, A. Stucky, R.L. Fuino, K.R. Kawaguchi, A.J. Samoyedny, R.S. Wilson, Z. Arvanitakis, J.A. Schneider, B.A. Wolf, D.A. Bennett, J.Q. Trojanowski, S.E. Arnold, Demonstrated brain insulin resistance in Alzheimer's disease patients is associated with IGF-1 resistance, IRS-1 dysregulation, and cognitive decline, *J. Clin. Invest.* 122 (2012) 1316–1338. <https://doi.org/10.1172/JCI59903>.
- [110] S.M. de la Monte, Insulin Resistance and Neurodegeneration: Progress Towards the Development of New Therapeutics for Alzheimer's Disease, *Drugs*. 77 (2017) 47–65. <https://doi.org/10.1007/S40265-016-0674-0>.
- [111] T. Matsuzaki, K. Sasaki, Y. Tanizaki, J. Hata, K. Fujimi, Y. Matsui, A. Sekita, S.O. Suzuki, S. Kanba, Y. Kiyohara, T. Iwaki, Insulin resistance is associated with the pathology of Alzheimer disease: The Hisayama study, *Neurology*. 75 (2010) 764–770. <https://doi.org/10.1212/WNL.0B013E3181EEE25F>.
- [112] S. Frere, I. Slutsky, Alzheimer's Disease: From Firing Instability to Homeostasis Network Collapse, *Neuron*. 97 (2018) 32–58. <https://doi.org/https://doi.org/10.1016/j.neuron.2017.11.028>.
- [113] F. Yin, H. Sancheti, I. Patil, E. Cadenas, Energy metabolism and inflammation in brain aging and Alzheimer's disease, *Free Radic. Biol. Med.* 100 (2016) 108–122. <https://doi.org/https://doi.org/10.1016/j.freeradbiomed.2016.04.200>.
- [114] W.R. Miles, H.F. Root, Psychologic tests applied to diabetic patients, *Arch. Intern. Med.* 30 (1922) 767–777. <https://doi.org/10.1001/ARCHINTE.1922.00110120086003>.
- [115] L.C. Perlmutter, M.K. Hakami, C. Hodgson-Harrington, J. Ginsberg, J. Katz, D.E. Singer, D.M. Nathan, Decreased cognitive function in aging non-insulin-dependent diabetic patients, *Am. J. Med.* 77 (1984) 1043–1048. [https://doi.org/10.1016/0002-9343\(84\)90186-4](https://doi.org/10.1016/0002-9343(84)90186-4).

- [116] R.O. Roberts, D.S. Knopman, R.H. Cha, M.M. Mielke, V.S. Pankratz, B.F. Boeve, K. Kantarci, Y.E. Geda, C.R. Jack, R.C. Petersen, V.J. Lowe, Diabetes and elevated hemoglobin a1c levels are associated with brain hypometabolism but not amyloid accumulation, *J. Nucl. Med.* 55 (2014) 759–764. <https://doi.org/10.2967/JNUMED.113.132647>.
- [117] L.D. Baker, D.J. Cross, S. Minoshima, D. Belongia, G.S. Watson, S. Craft, Insulin resistance and Alzheimer-like reductions in regional cerebral glucose metabolism for cognitively normal adults with prediabetes or early type 2 diabetes, *Arch. Neurol.* 68 (2011) 51–57.
- [118] A.A. Willette, B.B. Bendlin, E.J. Starks, A.C. Birdsill, S.C. Johnson, B.T. Christian, O.C. Okonkwo, A. La Rue, B.P. Hermann, R.L. Kosciak, Association of insulin resistance with cerebral glucose uptake in late middle-aged adults at risk for Alzheimer disease, *JAMA Neurol.* 72 (2015) 1013–1020.
- [119] M. Heni, P. Schöpfer, A. Peter, T. Sartorius, A. Fritsche, M. Synofzik, H.U. Häring, W. Maetzler, A.M. Hennige, Evidence for altered transport of insulin across the blood-brain barrier in insulin-resistant humans, *Acta Diabetol.* 51 (2014) 679–681. <https://doi.org/10.1007/S00592-013-0546-Y>.
- [120] D.Y. Yoo, H.S. Yim, H.Y. Jung, S.M. Nam, J.W. Kim, J.H. Choi, J.K. Seong, Y.S. Yoon, D.W. Kim, I.K. Hwang, Chronic type 2 diabetes reduces the integrity of the blood-brain barrier by reducing tight junction proteins in the hippocampus, *J. Vet. Med. Sci.* 78 (2016) 957–962. <https://doi.org/10.1292/JVMS.15-0589>.
- [121] J.M. Starr, J.M. Wardlaw, K. Ferguson, A. MacLulich, I.J. Deary, I. Marshall, Increased blood–brain barrier permeability in type II diabetes demonstrated by gadolinium magnetic resonance imaging, *J. Neurol. Neurosurg. Psychiatry.* 74 (2003) 70. <https://doi.org/10.1136/JNNP.74.1.70>.
- [122] B. Van Harten, F.E. De Leeuw, H.C. Weinstein, P. Scheltens, Brain imaging in patients with Diabetes Mellitus. A systematic review, *Asp. Subcortical Ischaem. Vasc. Dis.* 29 (2006) 39.
- [123] A.M. Moloney, R.J. Griffin, S. Timmons, R. O’Connor, R. Ravid, C. O’Neill, Defects in IGF-1 receptor, insulin receptor and IRS-1/2 in Alzheimer’s disease indicate possible resistance to IGF-1 and insulin signalling, *Neurobiol. Aging.* 31 (2010) 224–243.

- <https://doi.org/10.1016/J.NEUROBIOLAGING.2008.04.002>.
- [124] T.R. Bomfim, L. Forny-Germano, L.B. Sathler, J. Brito-Moreira, J.-C. Houzel, H. Decker, M.A. Silverman, H. Kazi, H.M. Melo, P.L. McClean, An anti-diabetes agent protects the mouse brain from defective insulin signaling caused by Alzheimer's disease-associated A β oligomers, *J. Clin. Invest.* 122 (2012) 1339–1353.
- [125] A. Karpova, P.P. Sanna, T. Behnisch, Involvement of multiple phosphatidylinositol 3-kinase-dependent pathways in the persistence of late-phase long term potentiation expression, *Neuroscience.* 137 (2006) 833–841. <https://doi.org/10.1016/J.NEUROSCIENCE.2005.10.012>.
- [126] Á. Kelly, M.A. Lynch, Long-term potentiation in dentate gyrus of the rat is inhibited by the phosphoinositide 3-kinase inhibitor, wortmannin, *Neuropharmacology.* 39 (2000) 643–651. [https://doi.org/https://doi.org/10.1016/S0028-3908\(99\)00169-0](https://doi.org/https://doi.org/10.1016/S0028-3908(99)00169-0).
- [127] M. Mizuno, K. Yamada, N. Takei, M.H. Tran, J. He, A. Nakajima, H. Nawa, T. Nabeshima, Phosphatidylinositol 3-kinase: a molecule mediating BDNF-dependent spatial memory formation, *Mol. Psychiatry.* 8 (2003) 217–224. <https://doi.org/10.1038/sj.mp.4001215>.
- [128] S.R. Kopf, C.M. Baratti, Effects of posttraining administration of insulin on retention of a habituation response in mice: Participation of a central cholinergic mechanism, *Neurobiol. Learn. Mem.* 71 (1999) 50–61. <https://doi.org/10.1006/nlme.1998.3831>.
- [129] D.P. Figlewicz, P. Szot, P.A. Israel, C. Payne, D.M. Dorsa, Insulin reduces norepinephrine transporter mRNA in vivo in rat locus coeruleus, *Brain Res.* 602 (1993) 161–164. [https://doi.org/10.1016/0006-8993\(93\)90258-O](https://doi.org/10.1016/0006-8993(93)90258-O).
- [130] S.M. De La Monte, J.R. Wands, Alzheimer's disease is type 3 diabetes—evidence reviewed, *J. Diabetes Sci. Technol.* 2 (2008) 1101–1113.
- [131] L. Haataja, T. Gurlo, C.J. Huang, P.C. Butler, Islet Amyloid in Type 2 Diabetes, and the Toxic Oligomer Hypothesis, *Endocr. Rev.* 29 (2008) 303–316. <https://doi.org/10.1210/er.2007-0037>.
- [132] K. Nowotny, T. Jung, A. Höhn, D. Weber, T. Grune, Advanced glycation end products and oxidative stress in type 2 diabetes mellitus. *Biomolecules.* 2015; 5 (1): 194–222, (n.d.).

- [133] S. Bhatia, R. Rawal, P. Sharma, T. Singh, M. Singh, V. Singh, Mitochondrial Dysfunction in Alzheimer's Disease: Opportunities for Drug Development, *Curr. Neuropharmacol.* 20 (2021) 675–692. <https://doi.org/10.2174/1570159X19666210517114016>.
- [134] R. Ramasamy, S.J. Vannucci, S.S. Du Yan, K. Herold, S.F. Yan, A.M. Schmidt, Advanced glycation end products and RAGE: a common thread in aging, diabetes, neurodegeneration, and inflammation, *Glycobiology*. 15 (2005) 16R-28R.
- [135] Alzheimer Association, 2022 Alzheimer's disease facts and figures, *Alzheimer's Dement.* 15 (2022) 321–387.
- [136] S. Bhatia, M. Singh, T. Singh, V. Singh, Scrutinizing the Therapeutic Potential of PROTACs in the Management of Alzheimer's Disease, *Neurochem. Res.* (2022) 1–13.
- [137] S. Bhatia, P. Sharma, S. Mujwar, M. Singh, Scaffold morphing and in-silico studies of potential BACE1 (β -secretase) inhibitors: A hope for newer dawn in anti-Alzheimer therapeutics, (2022).
- [138] R. Shri, V. Singh, R. Kaur, S. Bhatia, Natural BACE1 Inhibitors: Promising Drugs for the Management of Alzheimer's Disease, in: 2021: pp. 137–171. <https://doi.org/10.2174/9781681089041121090007>.
- [139] R. Vassar, P.C. Kandalepas, The β -secretase enzyme BACE1 as a therapeutic target for Alzheimer's disease, *Alzheimers. Res. Ther.* 3 (2011) 20. <https://doi.org/10.1186/alzrt82>.
- [140] S.M. Son, M.Y. Cha, H. Choi, S. Kang, H. Choi, M.S. Lee, S.A. Park, I. Mook-Jung, Insulin-degrading enzyme secretion from astrocytes is mediated by an autophagy-based unconventional secretory pathway in Alzheimer disease, *Autophagy*. 12 (2016) 784–800. <https://doi.org/10.1080/15548627.2016.1159375>.
- [141] L. Xie, E. Helmerhorst, B. Plewright, W. Van Bronswijk, R. Martins, Alzheimer's beta-amyloid peptides compete for insulin binding to the insulin receptor, *J. Neurosci.* 22 (2002) 1–5.
- [142] L. Gasparini, G.K. Gouras, R. Wang, R.S. Gross, M.F. Beal, P. Greengard, H. Xu, Stimulation of β -amyloid precursor protein trafficking by insulin reduces intraneuronal β -amyloid and requires mitogen-activated protein kinase signaling, *J. Neurosci.* 21

- (2001) 2561–2570.
- [143] A.A. Willette, S.C. Johnson, A.C. Birdsill, M.A. Sager, B. Christian, L.D. Baker, S. Craft, J. Oh, E. Statz, B.P. Hermann, E.M. Jonaitis, R.L. Kosciak, A. La Rue, S. Asthana, B.B. Bendlin, Insulin resistance predicts brain amyloid deposition in late middle-aged adults, *Alzheimer's Dement.* 11 (2015) 504-510.e1. <https://doi.org/10.1016/J.JALZ.2014.03.011>.
- [144] Y. Chen, Y. Zhao, C. ling Dai, Z. Liang, X. Run, K. Iqbal, F. Liu, C.X. Gong, Intranasal insulin restores insulin signaling, increases synaptic proteins, and reduces A β level and microglia activation in the brains of 3xTg-AD mice, *Exp. Neurol.* 261 (2014) 610–619. <https://doi.org/10.1016/J.EXPNEUROL.2014.06.004>.
- [145] A.A.M. Rensink, I. Otte-Höller, R. de Boer, R.R. Bosch, H.J. ten Donkelaar, R.M.W. de Waal, M.M. Verbeek, B. Kremer, Insulin inhibits amyloid β -induced cell death in cultured human brain pericytes, *Neurobiol. Aging.* 25 (2004) 93–103. [https://doi.org/https://doi.org/10.1016/S0197-4580\(03\)00039-3](https://doi.org/https://doi.org/10.1016/S0197-4580(03)00039-3).
- [146] P. Rodriguez-Rodriguez, A. Sandebring-Matton, P. Merino-Serrais, C. Parrado-Fernandez, A. Rabano, B. Winblad, J. Ávila, I. Ferrer, A. Cedazo-Minguez, Tau hyperphosphorylation induces oligomeric insulin accumulation and insulin resistance in neurons, *Brain.* 140 (2017) 3269–3285. <https://doi.org/10.1093/BRAIN/AWX256>.
- [147] C.H. Reynolds, C.J. Garwood, S. Wray, C. Price, S. Kellie, T. Perera, M. Zvelebil, A. Yang, P.W. Sheppard, I.M. Varndell, D.P. Hanger, B.H. Anderton, Phosphorylation Regulates Tau Interactions with Src Homology 3 Domains of Phosphatidylinositol 3-Kinase, Phospholipase C γ 1, Grb2, and Src Family Kinases, *J. Biol. Chem.* 283 (2008) 18177–18186. <https://doi.org/10.1074/JBC.M709715200>.
- [148] E. Marciniak, A. Leboucher, E. Caron, T. Ahmed, A. Tailleux, J. Dumont, T. Issad, E. Gerhardt, P. Pagesy, M. Vileno, Tau deletion promotes brain insulin resistance, *J. Exp. Med.* 214 (2017) 2257–2269.
- [149] R.A. Gonçalves, N. Wijesekara, P.E. Fraser, F.G. De Felice, The link between tau and insulin signaling: Implications for alzheimer's disease and other tauopathies, *Front. Cell. Neurosci.* 13 (2019). <https://doi.org/10.3389/FNCEL.2019.00017/FULL>.
- [150] G.K. Kuga, V.R. Muñoz, R.C. Gaspar, S.C.B.R. Nakandakari, A.S.R. da Silva, J.D.

- Botezelli, J.A.C. de A. Leme, R.J. Gomes, L.P. de Moura, D.E. Cintra, E.R. Ropelle, J.R. Pauli, Impaired insulin signaling and spatial learning in middle-aged rats: The role of PTP1B, *Exp. Gerontol.* 104 (2018) 66–71. <https://doi.org/10.1016/J.EXGER.2018.02.005>.
- [151] M. Lesort, G.V.W. Johnson, Insulin-like growth factor-1 and insulin mediate transient site-selective increases in tau phosphorylation in primary cortical neurons, *Neuroscience*. 99 (2000) 305–316.
- [152] M. Lesort, R.S. Jope, G.V.W. Johnson, Insulin Transiently Increases Tau Phosphorylation, *J. Neurochem.* 72 (1999) 576–584. <https://doi.org/https://doi.org/10.1046/j.1471-4159.1999.0720576.x>.
- [153] R.J. Mullins, T.C. Diehl, C.W. Chia, D. Kapogiannis, Insulin resistance as a link between amyloid-beta and tau pathologies in Alzheimer’s disease, *Front. Aging Neurosci.* 9 (2017). <https://doi.org/10.3389/FNAGI.2017.00118/FULL>.
- [154] T.K. Silzer, N.R. Phillips, Etiology of type 2 diabetes and Alzheimer’s disease: Exploring the mitochondria, *Mitochondrion*. 43 (2018) 16–24. <https://doi.org/10.1016/J.MITO.2018.04.004>.
- [155] C. Carvalho, M.S. Santos, C.R. Oliveira, P.I. Moreira, Alzheimer’s disease and type 2 diabetes-related alterations in brain mitochondria, autophagy and synaptic markers, *Biochim. Biophys. Acta - Mol. Basis Dis.* 1852 (2015) 1665–1675. <https://doi.org/10.1016/j.bbadis.2015.05.001>.
- [156] J. Szendroedi, E. Phielix, M. Roden, The role of mitochondria in insulin resistance and type 2 diabetes mellitus, *Nat. Rev. Endocrinol.* 8 (2012) 92–103. <https://doi.org/10.1038/nrendo.2011.138>.
- [157] E. Calvo-Ochoa, C. Arias, Cellular and metabolic alterations in the hippocampus caused by insulin signalling dysfunction and its association with cognitive impairment during aging and Alzheimer’s disease: Studies in animal models, *Diabetes. Metab. Res. Rev.* 31 (2015) 1–13. <https://doi.org/10.1002/DMRR.2531>.
- [158] C. M Wilson, A. Magnaudeix, C. Yardin, F. Terro, Autophagy dysfunction and its link to Alzheimer’s disease and type II diabetes mellitus, *CNS Neurol. Disord. Targets (Formerly Curr. Drug Targets-CNS Neurol. Disord.)* 13 (2014) 226–246.

- [159] K. Ohta, A. Mizuno, S. Li, M. Itoh, M. Ueda, E. Ohta, Y. Hida, M. xing Wang, M. Furoi, Y. Tsuzuki, M. Sobajima, Y. Bohmoto, T. Fukushima, M. Kobori, T. Inuzuka, T. Nakagawa, Endoplasmic reticulum stress enhances γ -secretase activity, *Biochem. Biophys. Res. Commun.* 416 (2011) 362–366. <https://doi.org/10.1016/J.BBRC.2011.11.042>.
- [160] A.P. Arruda, B.M. Pers, G. Parlakgöl, E. Güney, K. Inouye, G.S. Hotamisligil, Chronic enrichment of hepatic endoplasmic reticulum–mitochondria contact leads to mitochondrial dysfunction in obesity, *Nat. Med.* 20 (2014) 1427–1435. <https://doi.org/10.1038/nm.3735>.
- [161] C. Hetz, K. Zhang, R.J. Kaufman, Mechanisms, regulation and functions of the unfolded protein response, *Nat. Rev. Mol. Cell Biol.* 21 (2020) 421–438. <https://doi.org/10.1038/S41580-020-0250-Z>.
- [162] R. Iurlaro, C. Muñoz-Pinedo, Cell death induced by endoplasmic reticulum stress, *FEBS J.* (2016) 2640–2652. <https://doi.org/10.1111/febs.13598>.
- [163] 020741_S030_PRANDIN_TABS_AP.pdf, (n.d.).
- [164] P. Strange, S.L. Schwartz, R.J. Graf, W. Polvino, I. Weston, T.C. Marbury, W.C. Huang, R.B. Goldberg, Pharmacokinetics, pharmacodynamics, and dose-response relationship of repaglinide in type 2 diabetes, *Diabetes Technol. Ther.* 1 (1999) 247–256. <https://doi.org/10.1089/152091599317143>.
- [165] J.A. Palma-Aguirre, J.A. Absalón-Reyes, G. Novoa-Heckel, A. de Lago, I. Oliva, Z. Rodríguez, M. González-de la Parra, V. Burke-Fraga, S. Namur, Bioavailability of two oral suspension and two oral tablet formulations of acyclovir 400 mg: Two single-dose, open-label, randomized, two-period crossover comparisons in healthy Mexican adult subjects, *Clin. Ther.* 29 (2007) 1146–1152. <https://doi.org/10.1016/j.clinthera.2007.06.007>.
- [166] X. Li, Z.Q. Liu, Pharmacogenetic Factors That Affect Drug Metabolism and Efficacy in Type 2 Diabetes Mellitus, *Drug Metab. Dis.* (2017) 157–179. <https://doi.org/10.1016/B978-0-12-802949-7.00007-9>.
- [167] A.P. Li, D.L. Kaminski, A. Rasmussen, Substrates of human hepatic cytochrome P450 3A4, *Toxicology.* 104 (1995) 1–8. [https://doi.org/10.1016/0300-483X\(95\)03155-9](https://doi.org/10.1016/0300-483X(95)03155-9).

- [168] R. Taliyan, V. Kakoty, K.C. Sarathlal, S.S. Kharavtekar, C.R. Karennavar, Y.K. Choudhary, G. Singhvi, Y. Riadi, S.K. Dubey, P. Kesharwani, Nanocarrier mediated drug delivery as an impeccable therapeutic approach against Alzheimer's disease, *J. Control. Release.* 343 (2022) 528–550. <https://doi.org/10.1016/J.JCONREL.2022.01.044>.
- [169] J.K. Patra, G. Das, L.F. Fraceto, E.V.R. Campos, M.D.P. Rodriguez-Torres, L.S. Acosta-Torres, L.A. Diaz-Torres, R. Grillo, M.K. Swamy, S. Sharma, S. Habtemariam, H.S. Shin, Nano based drug delivery systems: recent developments and future prospects, *J. Nanobiotechnology* 2018 161. 16 (2018) 1–33. <https://doi.org/10.1186/S12951-018-0392-8>.
- [170] L.H. Madkour, Nanoparticle and polymeric nanoparticle-based targeted drug delivery systems, *Nucleic Acids as Gene Anticancer Drug Deliv. Ther.* (2019) 191–240. <https://doi.org/10.1016/B978-0-12-819777-6.00013-5>.
- [171] A. Alexander, M. Agrawal, A. Uddin, S. Siddique, A.M. Shehata, M.A. Shaker, S.A.U. Rahman, M.I.M. Abdul, M.A. Shaker, Recent expansions of novel strategies towards the drug targeting into the brain, *Int. J. Nanomedicine.* 14 (2019) 5895. <https://doi.org/10.2147/IJN.S210876>.
- [172] L. Zhang, J.M. Chan, F.X. Gu, J.-W. Rhee, A.Z. Wang, A.F. Radovic-Moreno, F. Alexis, R. Langer, O.C. Farokhzad, Self-Assembled LipidPolymer Hybrid Nanoparticles: A Robust Drug Delivery Platform, (2008). <https://doi.org/10.1021/nn800275r>.
- [173] M. Agrawal, S. Saraf, S. Saraf, S.K. Dubey, A. Puri, R.J. Patel, Ajazuddin, V. Ravichandiran, U.S. Murty, A. Alexander, Recent strategies and advances in the fabrication of nano lipid carriers and their application towards brain targeting, *J. Control. Release.* 321 (2020) 372–415. <https://doi.org/10.1016/J.JCONREL.2020.02.020>.
- [174] G. Wadhwa, K.V. Krishna, S.K. Dubey, R. Taliyan, Development and validation of RP-HPLC method for quantification of repaglinide in mPEG-PCL polymeric nanoparticles: QbD-driven optimization, force degradation study, and assessment of in vitro release mathematic modeling, *Microchem. J.* 168 (2021) 106491. <https://doi.org/10.1016/J.MICROC.2021.106491>.
- [175] P.S. Sandhu, S. Beg, R. Kumar, O.P. Katare, B. Singh, Analytical QbD-based systematic

- bioanalytical HPLC method development for estimation of quercetin dihydrate, *J. Liq. Chromatogr. Relat. Technol.* 40 (2017) 506–516. <https://doi.org/10.1080/10826076.2017.1329744>.
- [176] H. Hashem, H.M. El-Sayed, Quality by design approach for development and validation of a RP-HPLC method for simultaneous determination of co-administered levetiracetam and pyridoxine HCl in prepared tablets, *Microchem. J.* 143 (2018) 55–63. <https://doi.org/10.1016/j.microc.2018.07.031>.
- [177] G. Sharma, K. Thakur, K. Raza, O.P. Katare, Stability kinetics of fusidic acid: Development and validation of stability indicating analytical method by employing Analytical Quality by Design approach in medicinal product(s), *J. Chromatogr. B Anal. Technol. Biomed. Life Sci.* 1120 (2019) 113–124. <https://doi.org/10.1016/j.jchromb.2019.05.001>.
- [178] P.B. Prajapati, K. Radadiya, S.A. Shah, Quality Risk Management Based: Analytical Quality by Design Approach to Eco-Friendly and Versatile Chromatography Method for Simultaneous Estimation of Multiple Fixed-Dose-Combination Products of Anti-Diabetic Drugs, *J. Pharm. Innov.* (2020) 1–18. <https://doi.org/10.1007/s12247-020-09506-5>.
- [179] G. Wadhwa, K.V. Krishna, R. Taliyan, N. Tandon, S.S. Yadav, C. Katiyar, S.K. Dubey, Pre-clinical pharmacokinetic and pharmacodynamic modelling study of 4-hydroxyisoleucine using validated ultra-performance liquid chromatography-tandem mass spectrometry, *RSC Adv.* 10 (2020) 5525–5532. <https://doi.org/https://doi.org/10.1039/c9ra08121f>.
- [180] T. Sharma, A. Jain, S. Saini, O. Katare, B. Singh, Implementation of analytical quality-by-design and green analytical chemistry approaches for the development of robust and ecofriendly UHPLC analytical method for quantification of chrysin, *Sep. Sci. PLUS.* 3 (2020) 384–398. <https://doi.org/10.1002/sscp.202000028>.
- [181] S.K. Dubey, S. Duddelly, H. Jangala, R. Saha, Rapid and sensitive reverse-phase high-performance liquid chromatography method for estimation of ketorolac in pharmaceuticals using weighted regression, *Indian J. Pharm. Sci.* 75 (2013) 89–93. <https://doi.org/10.4103/0250-474X.113535>.
- [182] N. Žigart, Z. Časar, Development of a Stability-Indicating Analytical Method for

- Determination of Venetoclax Using AqBd Principles, ACS Omega. 5 (2020) 17726–17742. <https://doi.org/10.1021/acsomega.0c02338>.
- [183] C.D. Herzfeldt, R. Kümmel, Dissociation constants, solubilities and dissolution rates of some selected nonsteroidal antiinflammatories, Drug Dev. Ind. Pharm. 9 (1983) 767–793.
- [184] S.H. Yalkowsky, Y. He, P. Jain, Handbook of aqueous solubility data, CRC press, 2016.
- [185] G. Wadhwa, K.V. Krishna, R. Taliyan, N. Tandon, S.S. Yadav, D. Banerjee, A. Narwaria, C. Katiyar, S.K. Dubey, A novel UPLC–MS/MS method for simultaneous quantification of trigonelline, 4-hydroxyisoleucine, and diosgenin from Trigonella foenum-graecum extract: Application to pharmacokinetic study in healthy and type 2 diabetic rats, Biomed. Chromatogr. 36 (2022) e5275. <https://doi.org/10.1002/BMC.5275>.
- [186] Fda, Cder, Bioanalytical Method Validation Guidance for Industry Biopharmaceutics Bioanalytical Method Validation Guidance for Industry Biopharmaceutics Contains Nonbinding Recommendations, 2018. <http://www.fda.gov/Drugs/GuidanceComplianceRegulatoryInformation/Guidances/default.htm> and/or <http://www.fda.gov/AnimalVeterinary/GuidanceComplianceEnforcement/GuidanceforIndustry/default.htm> (accessed September 15, 2020).
- [187] E. Medicines Agency, ICH guideline M10 on bioanalytical method validation 4 Step 2b 5, 2019. www.ema.europa.eu/contact (accessed September 15, 2020).
- [188] P. Singh, V. Bajpai, A. Gupta, A.N. Gaikwad, R. Maurya, B. Kumar, Identification and quantification of secondary metabolites of Pterocarpus marsupium by LC–MS techniques and its in-vitro lipid lowering activity, Ind. Crops Prod. 127 (2019) 26–35. <https://doi.org/10.1016/j.indcrop.2018.10.047>.
- [189] S.K. Dubey, R.N. Saha, H. Jangala, S. Pasha, Rapid sensitive validated UPLC-MS method for determination of venlafaxine and its metabolite in rat plasma: Application to pharmacokinetic study., J. Pharm. Anal. 3 (2013) 466–471. <https://doi.org/10.1016/j.jpha.2013.05.002>.
- [190] G. Wadhwa, K.V. Krishna, R. Taliyan, N. Tandon, S.S. Yadav, D. Banerjee, A. Narwaria, C.K. Katiyar, S.K. Dubey, Preclinical pharmacokinetics of trigonelline using

- ultra-performance liquid chromatography–tandem mass spectrometry and pharmacological studies targeting type 2 diabetes, *Sep. Sci. Plus.* 4 (2021) 185–194. <https://doi.org/10.1002/SSCP.202000118>.
- [191] J.H. Jo, J.H. Kim, H.S. Lee, G.S. Jeong, J.M. Lee, S. Lee, Investigation of pharmacokinetic parameters of bakuchicin isolated from *Psoralea corylifolia* in mice, *Fitoterapia.* 120 (2017) 194–198. <https://doi.org/10.1016/j.fitote.2017.06.007>.
- [192] Jyotshna, P. Gaur, D.K. Singh, S. Luqman, K. Shanker, Validated method for quality assessment of henna (*Lawsonia inermis* L.) leaves after postharvest blanching and its cosmetic application, *Ind. Crops Prod.* 95 (2017) 33–42. <https://doi.org/10.1016/j.indcrop.2016.10.010>.
- [193] A. Khosa, K. V. Krishna, R.N. Saha, S.K. Dubey, S. Reddi, A simplified and sensitive validated RP-HPLC method for determination of temozolomide in rat plasma and its application to a pharmacokinetic study, *J. Liq. Chromatogr. Relat. Technol.* 41 (2018) 692–697. <https://doi.org/10.1080/10826076.2018.1511803>.
- [194] M. Zamani, M. Sadeghizadeh, M. Behmanesh, F. Najafi, Dendrosomal curcumin increases expression of the long non-coding RNA gene MEG3 via up-regulation of epimRNAs in hepatocellular cancer, *Phytomedicine.* 22 (2015) 961–967. <https://doi.org/10.1016/j.phymed.2015.05.071>.
- [195] J. Wang, J. Yin, Y. Song, L. Zhang, ... Y.R.-J. of D., undefined 2014, Brain aging and AD-like pathology in streptozotocin-induced diabetic rats, *Hindawi.Com.* (n.d.). <https://www.hindawi.com/journals/jdr/2014/796840/> (accessed December 26, 2022).
- [196] P. Sun, G. Ortega, Y. Tan, Q. Hua, P.F. Riederer, J. Deckert, A.G. Schmitt-Böhrer, Streptozotocin impairs proliferation and differentiation of adult hippocampal neural stem cells in vitro–correlation with alterations in the expression of proteins associated with the insulin system, *Front. Aging Neurosci.* 10 (2018). <https://doi.org/10.3389/FNAGI.2018.00145/FULL>.
- [197] N.G. Hattangady, M.S. Rajadhyaksha, A brief review of in vitro models of diabetic neuropathy, *Int. J. Diabetes Dev. Ctries.* 29 (2009) 143–149. <https://doi.org/10.4103/0973-3930.57344>.
- [198] Z. Karavelioglu, R. Cakir-koc, *International Journal of Biological Macromolecules*

- Preparation of chitosan nanoparticles as Ginkgo Biloba extract carrier: In vitro neuroprotective effect on oxidative stress-induced human, *Int. J. Biol. Macromol.* 192 (2021) 675–683. <https://doi.org/10.1016/j.ijbiomac.2021.10.023>.
- [199] E. Wesén, G.D.M. Jeffries, M.M. Dzebo, E.K. Esbjörner, Endocytic uptake of monomeric amyloid- β peptides is clathrin- and dynamin-independent and results in selective accumulation of A β (1-42) compared to A β (1-40), *Sci. Rep.* 7 (2017). <https://doi.org/10.1038/S41598-017-02227-9>.
- [200] K.A. Park, Z. Jin, J.Y. Lee, H.S. An, E.B. Choi, K.E. Kim, H.J. Shin, E.A. Jeong, K.A. Min, M.C. Shin, G.S. Roh, Long-lasting exendin-4 fusion protein improves memory deficits in high-fat diet/streptozotocin-induced diabetic mice, *Pharmaceutics.* 12 (2020) 1–18. <https://doi.org/10.3390/pharmaceutics12020159>.
- [201] T. Narender, A. Puri, Shweta, T. Khaliq, R. Saxena, G. Bhatia, R. Chandra, 4-Hydroxyisoleucine an unusual amino acid as antidyslipidemic and antihyperglycemic agent, *Bioorg. Med. Chem. Lett.* 16 (2006) 293–296. <https://doi.org/10.1016/J.BMCL.2005.10.003>.
- [202] S. Sharma, R. Taliyan, Epigenetic modifications by inhibiting histone deacetylases reverse memory impairment in insulin resistance induced cognitive deficit in mice, *Neuropharmacology.* 105 (2016) 285–297. <https://doi.org/10.1016/J.NEUROPHARM.2016.01.025>.
- [203] K.V. Krishna, R.N. Saha, S.K. Dubey, Biophysical, Biochemical, and Behavioral Implications of ApoE3 Conjugated Donepezil Nanomedicine in a A β 1-42Induced Alzheimer's Disease Rat Model, *ACS Chem. Neurosci.* 11 (2020) 4139–4151. <https://doi.org/10.1021/acchemneuro.0c00430>.
- [204] K.C.S. Sarathlal, V. Kakoty, K.V. Krishna, S.K. Dubey, D. Chitkara, R. Taliyan, Neuroprotective Efficacy of Co-Encapsulated Rosiglitazone and Vorinostat Nanoparticle on Streptozotocin Induced Mice Model of Alzheimer Disease, *ACS Chem. Neurosci.* 12 (2021) 1528–1541. https://doi.org/10.1021/ACSCHEMNEURO.1C00022/ASSET/IMAGES/MEDIUM/CN1C00022_M001.GIF.
- [205] S. Sharma, R. Taliyan, Epigenetic modifications by inhibiting histone deacetylases reverse memory impairment in insulin resistance induced cognitive deficit in mice,

- Neuropharmacology. 105 (2016) 285–297.
<https://doi.org/10.1016/J.NEUROPHARM.2016.01.025>.
- [206] V. Kakoty, S. K C, S.K. Dubey, C.H. Yang, R. Taliyan, Neuroprotective Effects of Trehalose and Sodium Butyrate on Preformed Fibrillar Form of α -Synuclein-Induced Rat Model of Parkinson's Disease, *ACS Chem. Neurosci.* 12 (2021) 2643–2660.
<https://doi.org/10.1021/ACSCHEMNEURO.1C00144>.
- [207] V. Kakoty, K.C. Sarathlal, C.H. Yang, S. Kumari, S.K. Dubey, R. Taliyan, Neuroprotective Effect of Lentivirus-Mediated FGF21 Gene Delivery in Experimental Alzheimer's Disease is Augmented when Concerted with Rapamycin, *Mol. Neurobiol.* 59 (2022) 2659–2677. <https://doi.org/10.1007/S12035-022-02741-6>.
- [208] M.R. Aslani, H. Ghobadi, H. Panahpour, M. Ahmadi, M. Khaksar, M. Heidarzadeh, Modification of lung endoplasmic reticulum genes expression and NF-kB protein levels in obese ovalbumin-sensitized male and female rats, *Life Sci.* 247 (2020).
<https://doi.org/10.1016/J.LFS.2020.117446>.
- [209] L. Pillai-Kastoori, A.R. Schutz-Geschwender, J.A. Harford, A systematic approach to quantitative Western blot analysis, *Anal. Biochem.* 593 (2020) 113608.
<https://doi.org/10.1016/J.AB.2020.113608>.
- [210] K. Lee, J. Lee, J. Park, ... T.H.-E.& molecular, undefined 2008, Low energy proton beam induces tumor cell apoptosis through reactive oxygen species and activation of caspases, *Nature.Com.* (n.d.). <https://www.nature.com/articles/emm200814> (accessed January 3, 2023).
- [211] K.V. Krishna, R.N. Saha, A. Puri, M. Viard, B.A. Shapiro, S.K. Dubey, Pre-clinical compartmental pharmacokinetic modeling of 2-[1-hexyloxyethyl]-2-devinyl pyropheophorbide-a (HPPH) as a photosensitizer in rat plasma by validated HPLC method, *Photochem. Photobiol. Sci.* (2019). <https://doi.org/10.1039/C8PP00339D>.
- [212] L. Jiang, H. Wee Lee, S. Chye Joachim Loo, Therapeutic lipid-coated hybrid nanoparticles against bacterial infections, (2020). <https://doi.org/10.1039/c9ra10921h>.
- [213] J. Zhang, D. Wang, Y. Wu, W. Li, Y. Hu, G. Zhao, C. Fu, S. Fu, L. Zou, Lipid–Polymer Hybrid Nanoparticles for Oral Delivery of Tartary Buckwheat Flavonoids, (2018).
<https://doi.org/10.1021/acs.jafc.8b00714>.

- [214] T.E. Yalcin, S. Ilbasimis-Tamer, S. Takka, Development and characterization of gemcitabine hydrochloride loaded lipid polymer hybrid nanoparticles (LPHNs) using central composite design, *Int. J. Pharm.* 548 (2018) 255–262. <https://doi.org/10.1016/j.ijpharm.2018.06.063>.
- [215] E. Pallagi, R. Ismail, T.L. Paál, I. Csóka, Initial Risk Assessment as part of the Quality by Design in peptide drug containing formulation development, *Eur. J. Pharm. Sci.* 122 (2018) 160–169. <https://doi.org/10.1016/J.EJPS.2018.07.003>.
- [216] J.C. Kasper, G. Winter, W. Friess, Recent advances and further challenges in lyophilization, *Eur. J. Pharm. Biopharm.* 85 (2013) 162–169. <https://doi.org/10.1016/J.EJPB.2013.05.019>.
- [217] L. Wu, L. Zhao, X. Su, P. Zhang, G. Ling, Repaglinide-loaded nanostructured lipid carriers with different particle sizes for improving oral absorption: preparation, characterization, pharmacokinetics, and in situ intestinal perfusion, <https://doi.org/10.1080/10717544.2019.1689313>. 27 (2019) 400–409.
- [218] J.N. Eriksen, A.Y. Luu, L.O. Dragsted, E. Arrigoni, Adaption of an in vitro digestion method to screen carotenoid liberation and in vitro accessibility from differently processed spinach preparations Adaption of an in vitro digestion method to screen carotenoid liberation and in vitro accessibility from di, *Food Chem.* (2016). <https://doi.org/10.1016/j.foodchem.2016.11.146>.
- [219] Z. Li, S. Peng, X. Chen, Y. Zhu, L. Zou, W. Liu, Pluronic modified liposomes for curcumin encapsulation: Sustained release, stability and bioaccessibility, 108 (2018) 246–253. <https://doi.org/10.1016/j.foodres.2018.03.048>.
- [220] ICH Q1A (R2) Stability testing of new drug substances and drug products | European Medicines Agency, (n.d.). <https://www.ema.europa.eu/en/ich-q1a-r2-stability-testing-new-drug-substances-drug-products> (accessed September 21, 2021).
- [221] C. Nehate, A.A.M. Raynold, V. Haridas, V. Koul, Comparative Assessment of Active Targeted Redox Sensitive Polymersomes Based on pPEGMA-S-S-PLA Diblock Copolymer with Marketed Nanoformulation, *Biomacromolecules.* 19 (2018) 2549–2566. <https://doi.org/10.1021/ACS.BIOMAC.8B00178>.
- [222] V. Hlady, J. Buijs, H.P. Jennissen, *Methods for Studying Protein Adsorption*, n.d.

- [223] S. Strindberg, J. Plum, M.B. Stie, M.L. Christiansen, L. Hagner Nielsen, T. Rades, A. Müllertz, Effect of supersaturation on absorption of indomethacin and tadalafil in a single pass intestinal perfusion rat model, in the absence and presence of a precipitation inhibitor, *Eur. J. Pharm. Biopharm.* 151 (2020) 108–115. <https://doi.org/10.1016/J.EJPB.2020.03.019>.
- [224] T.M. Dezani, A.B. Dezani, J.B.D.S. Junior, C.H.D.R. Serra, Single-Pass Intestinal Perfusion (SPIP) and prediction of fraction absorbed and permeability in humans: A study with antiretroviral drugs, *Eur. J. Pharm. Biopharm.* 104 (2016) 131–139. <https://doi.org/10.1016/J.EJPB.2016.04.020>.
- [225] T.M. Dezani, A.B. Dezani, J.B.D.S. Junior, C.H.D.R. Serra, Single-Pass Intestinal Perfusion (SPIP) and prediction of fraction absorbed and permeability in humans: A study with antiretroviral drugs, *Eur. J. Pharm. Biopharm.* 104 (2016) 131–139. <https://doi.org/10.1016/J.EJPB.2016.04.020>.
- [226] R. Konsoula, M. Jung, In Vitro Plasma Stability, Permeability and Solubility of Mercaptoacetamide Histone Deacetylase Inhibitors, (n.d.). <https://doi.org/10.1016/j.ijpharm.2008.05.001>.
- [227] S. Strindberg, J. Plum, M.B. Stie, M.L. Christiansen, L. Hagner Nielsen, T. Rades, A. Müllertz, Effect of supersaturation on absorption of indomethacin and tadalafil in a single pass intestinal perfusion rat model, in the absence and presence of a precipitation inhibitor, *Eur. J. Pharm. Biopharm.* 151 (2020) 108–115. <https://doi.org/10.1016/J.EJPB.2020.03.019>.
- [228] L. Wu, L. Zhao, X. Su, P. Zhang, G. Ling, Repaglinide-loaded nanostructured lipid carriers with different particle sizes for improving oral absorption: preparation, characterization, pharmacokinetics, and *in situ* intestinal perfusion, *Drug Deliv.* (2019) 1–10. <https://doi.org/10.1080/10717544.2019.1689313>.
- [229] G. Graverini, V. Piazzini, E. Landucci, D. Pantano, P. Nardiello, F. Casamenti, D.E. Pellegrini-Giampietro, A.R. Bilia, M.C. Bergonzi, Solid lipid nanoparticles for delivery of andrographolide across the blood-brain barrier: in vitro and in vivo evaluation, *Colloids Surfaces B Biointerfaces.* 161 (2018) 302–313. <https://doi.org/10.1016/j.colsurfb.2017.10.062>.
- [230] M. Radan, T. Djikic, D. Obradovic, K. Nikolic, Application of in vitro PAMPA

- technique and in silico computational methods for blood-brain barrier permeability prediction of novel CNS drug candidates, *Eur. J. Pharm. Sci.* 168 (2022) 106056. <https://doi.org/10.1016/J.EJPS.2021.106056>.
- [231] J. Park, J. Won, J. Seo, H.-G. Yeo, K. Kim, Y.G. Kim, C.-Y. Jeon, M.K. Kam, Y.-H. Kim, J.-W. Huh, S.-R. Lee, D.-S. Lee, Y. Lee, Streptozotocin Induces Alzheimer's Disease-Like Pathology in Hippocampal Neuronal Cells via CDK5/Drp1-Mediated Mitochondrial Fragmentation, *Front. Cell. Neurosci.* 14 (2020). <https://doi.org/10.3389/FNCEL.2020.00235/FULL>.
- [232] K.V. Krishna, G. Wadhwa, A. Alexander, N. Kanojia, R.N. Saha, R. Kukreti, G. Singhvi, S.K. Dubey, Design and Biological Evaluation of Lipoprotein-Based Donepezil Nanocarrier for Enhanced Brain Uptake through Oral Delivery, *ACS Chem. Neurosci.* 10 (2019) 4124–4135. <https://doi.org/10.1021/acschemneuro.9b00343>.
- [233] H. Yang, B. Zhai, Y. Fan, J. Wang, J. Sun, Y. Shi, D. Guo, Intestinal absorption mechanisms of araloside A in situ single-pass intestinal perfusion and in vitro Caco-2 cell model, *Biomed. Pharmacother.* 106 (2018) 1563–1569. <https://doi.org/10.1016/J.BIOPHA.2018.07.117>.
- [234] A. Simon, A. Darcsi, Á. Kéry, E. Riethmüller, Blood-brain barrier permeability study of ginger constituents, *J. Pharm. Biomed. Anal.* 177 (2020) 112820. <https://doi.org/10.1016/J.JPBA.2019.112820>.
- [235] N.K. Garg, R.K. Tyagi, G. Sharma, A. Jain, B. Singh, S. Jain, O.P. Katare, Functionalized Lipid–Polymer Hybrid Nanoparticles Mediated Codelivery of Methotrexate and Aceclofenac: A Synergistic Effect in Breast Cancer with Improved Pharmacokinetics Attributes, (2017). <https://doi.org/10.1021/acs.molpharmaceut.6b01148>.
- [236] G. Adamo, S. Campora, G. Ghersi, Functionalization of nanoparticles in specific targeting and mechanism release, *Nanostructures Nov. Ther. Synth. Charact. Appl.* (2017) 57–80. <https://doi.org/10.1016/B978-0-323-46142-9.00003-7>.
- [237] P. Ma, T. Li, H. Xing, S. Wang, Y. Sun, X. Sheng, K. Wang, Local anesthetic effects of bupivacaine loaded lipid-polymer hybrid nanoparticles: In vitro and in vivo evaluation, *Biomed. Pharmacother.* 89 (2017) 689–695. <https://doi.org/10.1016/j.biopha.2017.01.175>.

- [238] N.K. Garg, B. Singh, G. Sharma, V. Kushwah, R.K. Tyagi, S. Jain, O.P. Katare, Development and characterization of single step self-assembled lipid polymer hybrid nanoparticles for effective delivery of methotrexate, *RSC Adv.* 5 (2015) 62989–62999. <https://doi.org/10.1039/c5ra12459j>.
- [239] B. Mandal, N.K. Mittal, P. Balabathula, L.A. Thoma, G.C. Wood, Development and in vitro evaluation of core-shell type lipid-polymer hybrid nanoparticles for the delivery of erlotinib in non-small cell lung cancer, Elsevier B.V., 2016. <https://doi.org/10.1016/j.ejps.2015.10.021>.

List of Publications

➤ Publications from thesis work

1. **Wadhwa G**, Dubey SK, Taliyan R. Mechanistic investigation of Repaglinide as a potential therapeutic agent for Metabolic Syndrome Linked Alzheimer's Disease: In vitro and In vivo Analysis. (Under revision)
2. **Wadhwa G**, Krishna KV, Dubey SK, Taliyan R. Design and biological evaluation of Repaglinide loaded polymeric nanocarriers for diabetes linked neurodegenerative disorder: QbD-driven optimization, in situ, in vitro and in vivo investigation. *International Journal of Pharmaceutics*. 2023 Apr 5;636:122824.
3. **Wadhwa G**, Krishna KV, Dubey SK, Taliyan R. PEGylated Polymer–Lipid Hybrid Nanoparticles to Enhance In Vivo Exposure and Uptake of Repaglinide in Brain Cells to Treat Diabetes-Linked Neurodegenerative Disorders. *ACS Applied Nano Materials*. 2023 Feb 8;6(5):3497-512.
4. **Wadhwa G**, Krishna KV, Dubey SK, Taliyan R. Development and validation of RP-HPLC method for quantification of repaglinide in mPEG-PCL polymeric nanoparticles: QbD-driven optimization, force degradation study, and assessment of in vitro release mathematic modeling. *Microchem J*. 2021 Sep 1;168:106491.
5. Gorantla S, **Wadhwa G**, Jain S, Sankar S, Kshitij Nuwal ·, Mahmood A, et al. Recent advances in nanocarriers for nutrient delivery. *Drug Deliv Transl Res*.2021;1:3.
6. Krishna KV, **Wadhwa G**, Alexander A, Kanojia N, Saha RN, Kukreti R, et al. Design and Biological Evaluation of Lipoprotein-Based Donepezil Nanocarrier for Enhanced Brain Uptake through Oral Delivery. *ACS Chem Neurosci*. 2019 Sep;10(9):4124–35.

➤ Other Publications

1. **Wadhwa G**, Krishna KV, Taliyan R, Tandon N, Yadav SS, Banerjee D, et al. A novel UPLC–MS/MS method for simultaneous quantification of trigonelline, 4-hydroxyisoleucine, and diosgenin from *Trigonella foenum-graecum* extract: Application to pharmacokinetic study in healthy and type 2 diabetic rats. *Biomed Chromatogr*.2022 Feb 1 ;36(2):e5275.
2. **Wadhwa G**, Krishna KV, Taliyan R, Tandon N, Yadav SS, Banerjee D, et al. Preclinical pharmacokinetics of trigonelline using ultra-performance liquid chromatography–tandem mass spectrometry and pharmacological studies targeting type 2 diabetes. *Sep Sci Plus*. 2021 Apr 1;4(4):185–94.

3. **Wadhwa G**, Krishna KV, Taliyan R, Tandon N, Yadav SS, Katiyar C, et al. Preclinical pharmacokinetic and pharmacodynamic modelling study of 4-hydroxyisoleucine using validated ultra-performance liquid chromatography-tandem mass spectrometry. *RSC Adv.* 2020 Feb;10(10):5525–32.
4. Pradhan R, Krishna K V., **Wadhwa G**, Taliyan R, Khadgawat R, Kachhawa G, et al. QbD-driven development and validation of HPLC method for determination of Bisphenol A and Bis-sulphone in environmental samples. *Int J Environ Anal Chem.* 2020 Jan 2;100(1):42–54.

List of Conference

➤ **Conference Proceedings**

1. **Wadhwa G**, Taliyan Rajeev. Preclinical investigation of Repaglinide Nanoparticles in High Fat Diet with Streptozotocin-Induced Memory Impaired Rats. *Alzheimer's Association International Conference-July,2022*.
2. **Wadhwa G**, Dubey S K, Taliyan Rajeev. Repaglinide Loaded Hybrid Nanocarrier for the Management of Diabetes Mellitus Induced Neuronal Complications. *AAIC neuroscience next-November,2020*.

➤ **Oral Presentations**

1. Wadhwa Geetika, Taliyan Rajeev. Oral Delivery of Insulinotropic Agent Loaded Nanocarrier to Enhanced Brain Uptake for Diabetes Linked Neurodegenerative Disorder in Wistar Rats. *Oral Presentation at NIPER-PHARMACON- November 2022*.

➤ **Poster Presentations**

1. Wadhwa Geetika, Dubey S K, Taliyan Rajeev. Repaglinide Loaded Hybrid Nanocarrier for the Management of Diabetes Mellitus Induced Neuronal Complications, *Presented at Alzheimer's Association International Conference Neuroscience next- (AAIC neuroscience next)-November 2020*.
2. Wadhwa Geetika, Dubey S K, Taliyan Rajeev. Preclinical Investigation of Developed Lipid Hybrid Nanocarrier for the Treatment of Diabetes Induce Neuronal Complications, *Presented at Annual conference of Society for the study of Xenobiotics (SSX), India- July 2021*.
3. Wadhwa Geetika, Dubey S K, Taliyan Rajeev, *In vitro* Release Study of Insulinotropic Agent for the Treatment of Diabetes Induce Neuronal Complications, *Presented at Dissolution Research Presentation India (DRPI), India -June 2021*.
4. Wadhwa Geetika, Taliyan Rajeev. Development of PEGylated Hybrid Nanocarrier for the treatment of Diabetes induced neuronal complications. *Presented at 20th international e-symposium by control released society (CRS India chapter)-February 2022*.

5. Wadhwa Geetika, Taliyan Rajeev. Preclinical investigation of Repaglinide Nanoparticles in High Fat Diet with Streptozotocin-Induced Memory Impaired Rats. *Presented at Alzheimer's Association International Conference-July,2022.*

Biography of Prof. Rajeev Taliyan

Prof. Rajeev Taliyan is a Professor in the Department of Pharmacy, Birla Institute of Technology and Science (BITS), Pilani. He earned his M.Pharm. (Pharmacology) from Punjabi University-Patiala, Punjab, and Ph. D in Pharmacology with Prof. P.L Sharma (Emeritus, Prof. PGIMER) and Late Prof. Manjeet Singh (Ex-Head, Dean, Punjabi University) from ISF college, Punjab Technical University, Punjab. He has extensive research experience in the area of cardiovascular pharmacology, neuropharmacology, and nanomedicines. He was also invited as a Visiting Assistant Research Professor in Landon (2014), Dubai (2018), and Taiwan (2018). Prof. R. Taliyan. Dubey has about 26 years of teaching, research, and administrative experience. He has supervised 11 Ph. D, and several postgraduate and undergraduate students. He has published numerous research papers, review papers, and book chapters in renowned journals and presented papers at conferences in India and abroad besides that he also delivered an invited talk at several national and international conferences including Massachusetts Institute of Technology (MIT-USA). He is a member of the editorial board and reviewer of many reputed journals. He is also an Ex- executive member of the Indian Pharmacological Society (IPS) and is actively involved in the regional conference of IPS. Many prizes and awards are also in his credit including the prestigious NAMS membership award. He has successfully completed various projects and is presently handling several projects funded by government and industrial agencies like ICMR, UGC, DST, Etica, Zeon, etc.

Biography of Geetika

Geetika is a research scholar at the Department of Pharmacy, BITS Pilani, with an ICMR-SRF fellowship for pursuing doctoral research. She has completed his Bachelor of Pharmacy from the Postgraduate Institute of Medical Science, Haryana, and her Master of Pharmacy from Guru Jambheshwar University of Science and Technology, Haryana. She has published articles in peer-reviewed journals and delivered various oral and poster presentations at international and national conferences. She has qualified for the national-level competitive exam (GPAT). She also received a senior research fellowship from the Indian Council of Medical Research (ICMR) for doctoral research. She is a professional member of the Alzheimer's Association: International Society to Advance Alzheimer's Research and Treatment (ISTAART) and Control release society (CRS). She was awarded travel grants from DST-SERB, ICMR and CSIR and best Abstract Award from AAPS Pharma 360.